GKSS
FORSCHUNGSZENTRUM
in der HELMHOLTZ-GEMEINSCHAFT

GeNF – Experimental Report 2005

GeNF

Geesthacht Neutron Facility



Editors:

A. Schreyer
J. Vollbrandt
R. Willumeit

GKSS 2006/4

ISSN 0344-9629

HELMHOLTZ GEMEINSCHAFT
GKSS ist Mitglied der Helmholtz-Gemeinschaft Deutscher Forschungszentren e.V.

GKSS 2006/4

GeNF – Experimental Report 2005

Editors:

A. Schreyer
J. Vollbrandt
R. Willumeit
(Institute for Materials Research)

GKSS-Forschungszentrum Geesthacht GmbH • Geesthacht • 2006

Die Berichte der GKSS werden kostenlos abgegeben.
The delivery of the GKSS reports is free of charge.

Anforderungen/Requests:

GKSS-Forschungszentrum Geesthacht GmbH
Bibliothek/Library
Postfach 11 60
D-21494 Geesthacht
Germany
Fax.: (49) 04152/871717

Als Manuskript vervielfältigt.
Für diesen Bericht behalten wir uns alle Rechte vor.

ISSN 0344-9629

GKSS-Forschungszentrum Geesthacht GmbH · Telefon (04152)87-0
Max-Planck-Straße 1 · D-21502 Geesthacht / Postfach 11 60 · D-21494 Geesthacht

GKSS 2006/4

GeNF – Experimental Report 2005

Andreas Schreyer, Jürgen Vollbrandt, Regine Willumeit (Editors)

254 pages with 213 figures and 8 tables

Abstract

At the Geesthacht Neutron Facility GeNF about 180 experiments were performed in 2005 by GKSS and by or for external users, partners or contractors. In most cases the measurements were performed and analysed in cooperation by the guests and by the GKSS staff or by the permanent external user group staff. The activities, which are based on a proposal procedure and on the in house R&D program, are reported in 67 contributions in the present annual experimental report for the year 2005. The contributions may contain one or also several combined experiments.

During 2005 the GKSS research reactor FRG-1 achieved an operation time of 199 days at the full 5 MW reactor power providing a neutron flux of ca. $1.4 \cdot 10^{14}$ thermal neutrons/cm^2 s. The cold neutron source was available during the complete operation time.

The focus of the in house R&D work at GeNF instruments was the characterisation of metal alloys, the analysis of stresses in welds and technical structures at ARES, FSS, DCD and SANS-2, the structural investigation of hydrogen containing substances such as polymers, colloids and biological macromolecules at SANS-1 as well as the characterisation of magnetic thin films at PNR, POLDI and RÖDI. The thoroughly upgraded reflectomer NeRo went in full operation. It now offers state of the art new measurement possibilities.

In appendices the progress of the project REFSANS at FRM-II is reported as well as the experimental activities of the GKSS outstation HARWI-II at DESY where in 2005 first experiments were performed.

Jahresbericht 2005 über die Experimente an GeNF

Zusammenfassung

An der Geesthachter Neutronenforschungseinrichtung GeNF wurden von GKSS und von oder für externe Nutzer, Partner oder Auftraggeber etwa 180 Experimente in 2005 durchgeführt. In den meisten Fällen wurden die Messungen gemeinschaftlich von den Gastwissenschaftlern und dem GKSS-Personal vorgenommen und ausgewertet. Die Experimente, die in der Regel über das Antragsverfahren und über das GKSS-eigene F&E-Programm abgewickelt wurden,

werden in diesem Jahresbericht in Form von 67 Experimentierberichten dargestellt. Dabei können die Berichte einzelne Experimente oder auch mehrere zusammengefasst beschreiben.

Während 2005 erreichte der Forschungsreaktor FRG-1 119 Volllasttage bei 5 MW und bei einem Fluss von $1{,}4 \cdot 10^{14}$ thermischen Neutronen je cm^2 und s. Die kalte Neutronenquelle war während der gesamten Betriebszeit verfügbar.

Der Schwerpunkt der GKSS-eigenen Forschungsarbeiten lag in 2005 im Bereich der Charakterisierung von Metalllegierungen, der Analyse von Eigenspannungen in Schweißverbindungen und technischen Strukturen an ARES, FSS, DCD und SANS-2, im Bereich der Strukturanalyse von wasserstoffhaltigen Substanzen wie Polymere, Kolloide und Biomolekülen an der SANS-1 sowie im Bereich der Charakterisierung magnetischer Schichtstrukturen an PNR, POLDI und RÖDI. Nach dem gründlichen Umbau wurde das Reflektometer NeRo voll in Betrieb genommen. NeRo bietet nun erweiterte Messmöglichkeiten auf neuestem Standard.

In Anhängen wird auch über den Fortschritt des Projekts REFSANS am FRM-II sowie über die experimentellen Arbeiten der jungen GKSS-Außenstation HARWI-II bei DESY berichtet, wo in 2005 der Messbetrieb aufgenommen werden konnte.

Manuscript received / Manuskripteingang in TDB: 30. März 2006

CONTENTS

Preface

- GeNF Operation
- Operation of FRG-1
- GeNF Instruments (overview)

SANS-1 **21**

V. M. Nadutov
Small-angle polarized neutron scattering in f.c.c. Fe-Ni alloys 23

S. Gerber
Mixed micelles formed by SDS and a bolaamphiphile with carbohydrate headgroups 25

G. Milkereit
Influence of small ethoxy-spacers on the micellar structure of alkyl β-maltosides 29

V. Abetz, A. Boschetti,M. Gradzielski
Micelles of amphiphilic triblock terpolymers 31

M. V. Avdeev
SANS Study of Dispersed Ultrananocrystalline Diamond 33

M. Knaapila, L. Almasy, H. Burrows
A SANS study of water soluble polyfluorene-surfactant systems 35

P. Claesson
Conformational change of the polyelectrolyte in presence of surfactant studied using SANS 37

R. Perzynski, E. Dubois, V. Haramus
Study of the magnetic scattering in magnetic fluids and solids: dilute samples 39

R. Perzynski, E. Dubois, V. Haramus
Study of the magnetic scattering in magnetic fluids and solids: concentrated samples 41

P. Claesson
Solution Conformation of comb copolymers containing different degree of graft PEO and its interaction with the anionic detergent (SDS) 43

H. Kawasaki
Protonation-Induced Vesicle Formation in di-n-Decylmethylamine Oxide Surfactant 45

M. Almgren
Variable contrast study of coexisting fluorocarbon-rich and hydrocarbon-rich micelles 47

S. V. Grigoriev, G.P. Kopitsa
The study of the orbital part of the magnetic scattering amplitude in the heavy-fermion compound $CeRu_2Si_2$ by means of SAPNS 49

L. Vekas
SANSPOL study of organic non-polar ferrofluids stabilized by mixed surfactants 51

L. He, A. Middelberg
Conformation investigation of hen egg white lysozyme conjugated with poly(ethylene glycol) 53

L. He, A. Middelberg, H.-J. Gabius
Comparison of conformation of new growth/adhesion-regulating effector galectin-3 and its carbohydrate-recognition domains 55

SANS-2 **57**

M. Bischof, H. Clemens, P. Staron
The precipitation sequences of a novel steel during varied heat treatments 59

H. Leitner, H. Clemens, P. Staron
Characterization of precipitates in a high-strength low-alloy steel 63

S. Mühlbauer
Polarised SANS measurements of the FLL of Niobium 65

I. Skorvánek, J. Marcin
SANS study of the early stages of crystallization in the Fe-Zr-B-Cu nanocrystalline alloys 67

S. Gruner, I. Kaban, W. Hoyer
SANS study of amorphous and annealed $Ni_{36.5}Pd_{36.5}P_{27}$ glass 69

A. Manescu, A. Giuliani, F. Fiori
SANS investigation of Cu alloys for applications to technology for the restoration of ancient organs 71

R. Triolo, F. Lo Cels0, I. Ruffo
Fingerprinting Marbles of Archeological Interest 73

M. Fally, I. Drevenšek-Olenik
Light-induced phase separation in polymer dispersed liquid crystals (PDLC) 75

M. Dornheim, P. K. Pranzas, T. Klassen, A. Schreyer
Investigation of structural changes of nanocrystalline MgH_2/Cr_2O_3 for reversible storage of hydrogen 79

P. Mayrhofer, H. Clemens, P. Staron
Characterisation of coherent precipitates in a hard coating 81

H.P. Degischer, A. Pyzalla
The effect of heat treatment on the precipitation of Al-Si alloys 83

S.V. Grigoriev, N. Grigorieva
Investigation of magnetic and structural properties of nanosystems with cobalt embedded into mesoporous silica and alumo-silicate matrices 87

S.V. Grigoriev, A.I. Okorokov
Low temperature properties of the helix structure in MnSi under applied field 89

S.V. Grigoriev, A.I. Okorokov
Investigation of the structural instability of the spin helix in MnSi under applied field near T_c 91

S.V. Grigoriev, N. Grigorieva
SAPNS study of system of nickel nanoparticles embedded into Al_2O_3 93

D. Chernyshov, S.V. Grigoriev, K.W. Törnroos, B. Vangdal
Temperature induced spin conversion in a molecular complex as seen by SANS 95

S.V. Grigoriev, Y. Chetverikov, A.I. Okorokov
SANS study of the magnetic structure of $Tb_xY_{1-x}Mn_6Sn_6$ compounds 97

S. Pouget, S.V. Grigoriev, N. van Dijk
Investigation of the magnetic structure of the ferromagnet $ZrZn_2$ 101

S.V. Grigoriev, N. Grigorieva
SANS study of new magnetic nanocomposites based on mesoporous silica with embedded Fe-particles 103

D. Lamago, C. Pfleiderer, P.Böni
Bulk Properties and Neutron Diffraction of the Phase Diagram of MnSi 105

A. Ulbricht, F. Bergner
SANS investigation of neutron-irradiated RPV steels with special emphasis on Ni effect 107

DCD **109**

V. Ryukhtin, P. Stepanek,
USANS investigations of organized nanostructures of diblock copolymers in immiscible Solvents 111

PNR **113**

F. Klose, D. Lott, P. Mani
Polarized neutron reflectivity studies on $CoPt_3/FePt_3$ multilayers 115

D. Lott, M. Almokhtar, A. Schreyer
Polarized neutron reflectivity studies on Fe/Cr/Sn/Cr multilayer 117

NeRo **119**

D.Solina, D. Lott, U. Tietze, O. Frank, V.Leiner, A. Schreyer
The New Neutron Reflectometer-NeRo 121

A. Grünwald, A. Wildes, W. Schmidt, H. Tartakowskaya, A. Schreyer
Neutron diffraction and reflectivity studies on Gd/Y 123

ARES **125**

U. Cihak, P. Staron
Residual stresses in a water-quenched IN 718 plate 127

U. Cihak, M. Stockinger
Residual Strain Measurements within forged engineering components and model parts 129

H. P. Degischer, A. Pyzalla
Evolution of internal stresses during isothermal creep of an Al-Si piston alloy 133

H. Wohlfahrt, P. Staron
Residual stresses in an austenitic steel plate with a weld 135

M. Kocak, F. Bayraktar
Residual stresses in laser beam welded T-joint Al sheets 137

FSS **141**

H. G. Priesmeyer
Simultaneous Positron Annihilation and Neutron TOF – diffraction Investigation of fcc – Iron under Compression 143

H. G. Priesmeyer
On the correlation between the linear coefficient of thermal expansionand the diffraction – elastic constants for polycrystalline copper 145

J. Bohlen
Residual stresses in a rolled sheet of magnesium alloy AZ31 147

H. G. Priesmeyer
Positron annihilation and neutron diffraction experiments on aluminium alloys 149

H. G. Priesmeyer
Combined positron annihilation and neutron diffraction investigation on welds 151

H. G. Priesmeyer
Positron annihilation investigation of a quenched steel cylinder 153

TEX-2 **155**

W. Skrotzki, B. Klöden
Global textures of ECAP deformed nickel 157

M. Y. Zheng, W. M. Gan, S. W. Xu, K. Wu, H.-G. Brokmeier
Texture development in Mg-Zn-Y alloy under different deformation processes 161

J. Bohlen, D. Letzig
Influence of temperature and aluminium content on the texture formation of extruded Mg-alloys 165

J. Bohlen, D. Letzig
Influence of cooling conditions on microstructure and texture during extrusion of magnesium alloys 167

S.-J. Jin, H.-G. Brokmeier
Initial texture of a friction welded Ti64 – TiAl – rod 169

R. E. Bolmaro, H.-G. Brokmeier
Measurement of Textures in Low-Carbon Steels 171

R. E. Bolmaro, H.-G. Brokmeier
Textures on FeMn Shape Memory Alloys 173

R. E. Bolmaro, H.-G. Brokmeier
Measurement of textures in geological structures of Pie de Palo sierra, Córdoba, Argentina 175

W. Klauber, R. Schnitzer, H. Chladil
Texture characterisation of extruded TiAl 177

S. Lenser, H.-G. Brokmeier
Texture analysis of laser beam welded Al-alloys (AA5083H111 and AA6013T6) 179

POLDI **181**

P. Mikula
Multiple reflection monochromator 183

P. Mani, D. Lott
Neutron diffraction studies on a $Fe_{50}Pt_{40}Rh_{10}$ thin film 187

GENRA-3 **189**

R. Willumeit, S. Nunes, E. Spohr
Insights of a methanol fuel cell – a feasibility study 191

F. Beckmann, J. Vollbrandt, H.-W. Schmitz, T. Donath, A. Schreyer
The New Setup for Neutron Tomography (NCT) at GENRA-3 193

Note: EU support **197**

APPENDIX I **199**

REFSANS Progress Report

R. Kampmann, M. Haese-Seiller, V. Kudryashov, C. Daniel, B. Nickel, J. Rädler, A. Schreyer, E. Sackmann
Horizontal ToF-Neutron Reflectometer REFSANS at FRM-II Munich / Germany: First Tests and Status 201

APPENDIX II **205**

Reports of experiments carried out at HASYLAB/DESY by GKSS personel – GKSS outstation HARWI-II at DESY – as responsible experimenters in support of external users

P.K. Pranzas, M. Dornheim, K.-F. Aguey-Zinsou, S. Roth, R. Gehrke, G. Goerigk, T. Klassen, A. Schreyer
ASAXS and SAXS/USAXS Investigations of Metal Hydrides for Reversible Hydrogen Storage

T. Lippmann, F. Beckmann, R. V. Martins, L. Lottermoser, T. Dose, A. Schreyer:
Commissioning and first experiments at the Materials Science Beamline HARWI II

Celebrating the first experiments the new high-energy beamline HARWI II

U. Garbe, J. Fischer, T. Lippmann, H.-G. Brokmeier, F. Beckmann, F. Witte:
Characterization of MgCa-bone screws by high energy texture analysis

S. Irsen, C.Tille, H. Seitz, B. Leukers, F. Beckmann, B. Müller:
Comparison of conventional and synchrotron-radiation-based micro computed tomography of 3D printed scaffolds for bone augmentation

H.-G. Brokmeier, S.-J. Jin, S. Lenser, B. Schwebke, U. Garbe, T. Lippmann:
Crystallographic texture of an Al90-Cu10 cold extruded composite

J. Fischer, T. Donath, F. Beckmann, F. Witte:
Direct corrosion measurement of Mg-alloys by SRµCT

H.-A. Crostack, J. Nellesen, G. Fischer, F. Beckmann, T. Donath, J. Fischer:
High Energy µCT at HARWI-II and SEM of Cobalt / Diamond Composite

T. Donath, R. Zettler, F. Beckmann, J. Fischer, J.F. dos Santos, D. Lohwasser, A. Schreyer:
Investigation of material flow in friction stir welds using high energy synchrotron radiation at HARWI II

T. Vugrin, F. Beckmann, T. Donath, J. Fischer, A. Schreyer:
Investigation of Root Flaws in Friction Stir Welds

F. Despang, R. Bernhardt, E. Mund, R. Dittrich, F. Beckmann, G. Tomandt, W. Pompe, M. Gelinsky
Investigations of aIginate/calciurn phosphate scaffolds with oriented tube-like pores by microcomputed tomography

F. *Witte,* J. *Fischer, J. Nellesen, H-A. Crostack, T. Donath, F. Beckmann*
In-vivo corrosion rates of magnesium alloys determined by synchrotron-radiation based microtomography (SRμCT)

K. Haldrup, S. F: Nielsen, H.F. Poulsen, F. Beckmann, J. A. *Wert*
Measuring 3D Plastic Strain Fields Inside Metallic Materials

T. Walther, T. Donath, K. Terzic, H. Meine, H. Thömen, F. Beckmann
Microstructural Investigations on Natural Fiber Composites and Medium Density Fiberboard (MDF)

S. Peth, F. Beckmann, T. Donath, J. Fischer, A.J.M. Smucker, R. Horn
Pore space analysis of soil aggregates investigated by microtomography using synchrotron radiation

M. Kuehbacher, J. Fischer, B. *Gruenewald, T. Donath, D. Behne,* A. *Kyriakopoulos, F. Beckmann*
Honeybee in 3D - Neuroimaging with μ-Tomography

O. Prymak, C. Schiller, H. Tiemann, I. Soetje,. J. Marxen, T. Donath, F. Beckmann, M. Epple
Mikrotomographie an Biomineralien

M. Nickel, J. U. Hammel, T. Donath, F. Beckmann
Quantitative morphometrics and contraction analysis of the marine sponge *Tethya wilhelma* using synchrotron radiation based x-ray microtomography and *in vivo* x-ray imaging

O. Brunke, S. Odenbach, R. Jurgons, C. Alexiou, I. Hilger, F. Beckmann
Synchrotron tomography as a tool for the analysis of magnetic particle distribution in tumor tissue

W. Freysinger, R. Stoffner, F. Kral, A.P. Gunkel, A. Schrott-Fischer. R. Glückert, J. Fischer, F. Beckmann, B. Müller
Synchrotron-radiation-based micro computed tomographic imaging of the human Organ of Corti

M. Germann. A. Morel, F. Beckmann, B. Müller
Three-dimensional characterization *of* brain tissue using synchrotron-radiation-based micro computed tomography

G. Taton, T. Rok, E. Rokita, Z. Tabor, M. Karwala-Szytula, F. Beckmann, T. Donath, J. Fischer
3D Bone Architecture in Osteoporosis

PREFACE

GeNF Operation

The Geesthacht Neutron Facility (GeNF) is operated as an open facility for external users for about 2/3 of the available beam time and it is used for GKSS in house research within its materials science programme for the remaining 1/3. The external users come either from national and international scientific research institutions, universities and industry, or they own and operate experiments at GeNF as permanent external partners.

The beam time allocations for GeNF instruments are established on the base of a proposal procedure which can react in a flexible and fast way on new proposals. Proposals can be submitted at any time. In 2005 about 180 experiments were performed at GeNF by or for external users, partners or contractors as well as for the in house research programmes. A part of these activities – mainly the part of external use based on proposals – is reported in the present annual experimental report for the year 2005. In many cases several experiments are concentrated in one experimental report.

Operation of FRG-1

In 2005 the FRG-1 was operated routinely interrupted by the two planned major shut downs in January/February and in July. The total FRG operation time was 208 days providing neutrons, from these 199 days at its full 5 MW power providing a neutron flux of ca. $1.4 \cdot 10^{14}$ thermal neutrons/cm^2 s. The cold neutron source was always available during FRG operation.

GeNF Instruments

The current set of instruments at GeNF is shown in figure A and listed in table A. The available sample environment is listed in table B.

In 2005 the installation of the modern experiment control hardware and software based on LabView was continued for SANS-2 and ARES. An additional option to integrate a magnet into the sample position system was added at DCD. A thorough upgrade of the complete secondary spectrometer of ARES was started. The POLDI experiment was modified for research on magnetic nanostructures. PTB continues to use the neutron dosimetry option of POLDI, since PTB has qualified POLDI as the best thermal neutron reference field in Europe. Last but not least, the new neutron tomography camera on GENRA-3 has successfully commenced operation.

The focus of the GKSS in-house research at GeNF is the investigation of metal alloys, the analysis of stresses in welds and technical structures at ARES, FSS, DCD and SANS-2, the structural investigation of hydrogen containing substances such as polymers, colloids and biological macromolecules at SANS-1 as well as the characterisation of magnetic and polymer thin films at PNR, NeRo, POLDI and RÖDI.

In the autumn of 2005 the GKSS high-energy synchrotron beam line HARWI-II at DESY went in operation with its diffractometer and tomography parts. For details see the report in Appendix II.

The construction of the REFSANS instrument of GKSS at FRM-II as a highly sophisticated instrument for the research on solid and fluid films and nanostructures by combining small angle scattering and reflectometry was completed and also began operation. In 2005 GKSS

began to contribute to the operation of the Strain/Texture diffractometer STRESS-SPEC at FRM-II together with HMI and the Technical University of Munich (TUM). Furthermore a collaboration was started with the TUM to construct a new small angle scattering machine at the FRM-II.

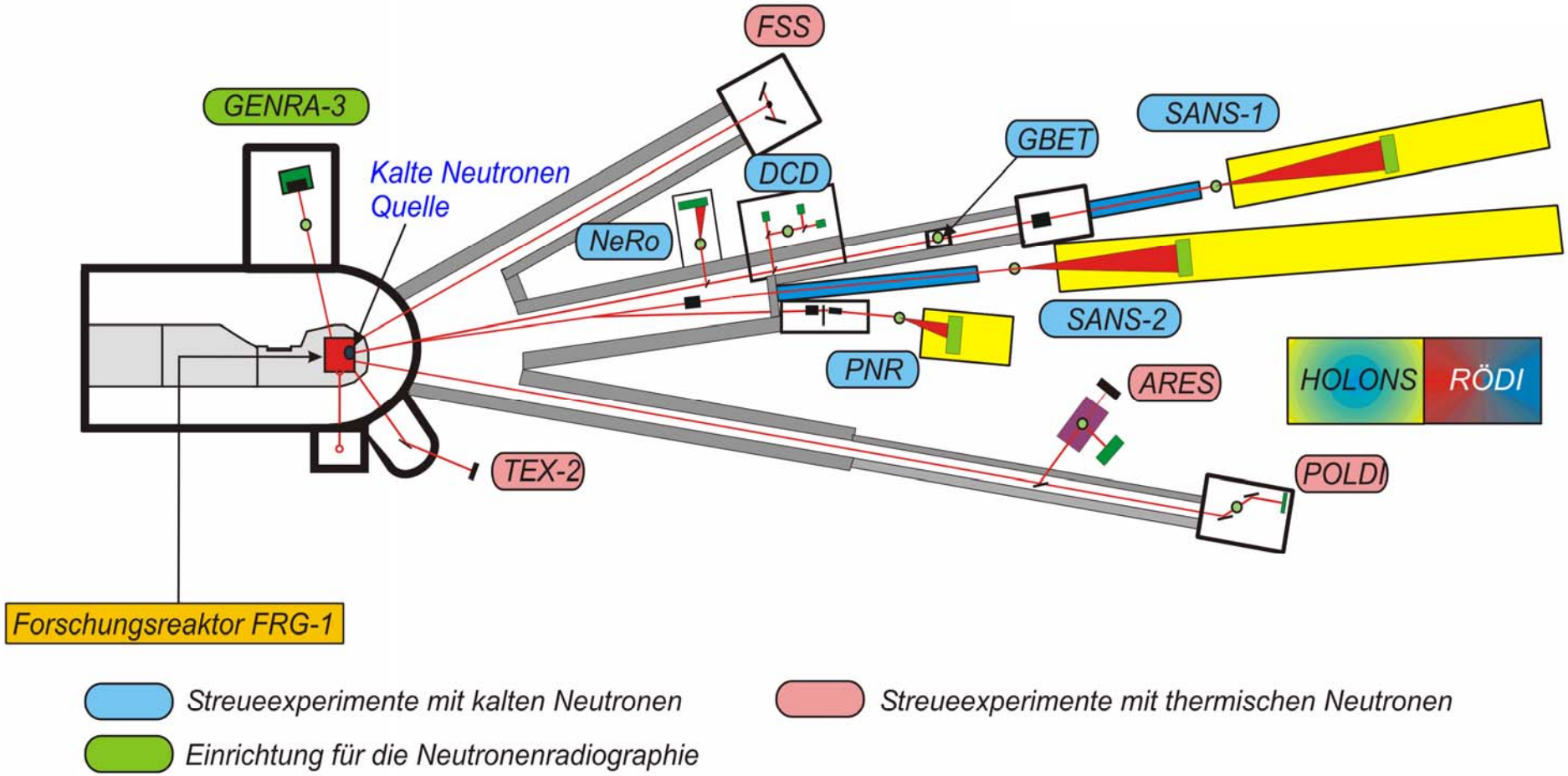


Figure A: **Arrangement of the Instruments at GeNF.**

Table A: **List of GeNF Instruments.**

Instrument	Short Instrument Description /Main Tasks	Characteristic Data	Operator / Local Contact
SANS-1	Small Angle Neutron Scattering using cold non-polarised/polarised neutrons primarily to investigate molecular biology, colloids and polymers	$\Phi_{max} = 6 \cdot 10^5$ cm^{-2} s^{-1} (coll.2 m,λ=0.8nm) $\Delta\lambda/\lambda = 0.1$ ($\lambda = 0.85$ nm) Particle sizes: 2−80 nm 2-D position-sens. ^{3}He- detector	GKSS / Regine Willumeit Vasyl Haramus
SANS-2	Small Angle Neutron Scattering using cold non-polarised/polarised neutrons to characterise precipitates, clusters, interfaces, grain sizes, magnetic structures etc. in materials (metals, polymers, colloids a.o.)	$\Phi_{max} = 2 \cdot 10^7$ cm^{-2} s^{-1} (coll.1 m,λ=0.5nm) $\Delta\lambda/\lambda = 0.1$ Particle sizes: 1−100 nm 2-D position-sens. ^{3}He- detector	GKSS / Helmut Eckerlebe P. Klaus Pranzas
DCD	Double Crystal Diffractometer for ultra small angle neutron scattering (USANS) using non-polarised cold neutrons to characterise large creep pores, fatigue and sintering cavities, precipitates, voids, bubbles, etc. in materials	$\Phi \approx 0.5 \cdot 10^3$ cm^{-2} s^{-1} $\Delta\lambda/\lambda = 1 \cdot 10^{-5}$ ($\lambda = 0.443$ nm) Particle sizes: 30 nm−24 μm 3 x ^{3}He- detectors	GKSS / Dieter Bellmann
ARES	Diffractometer for the Analysis of REsidual Stresses in specimens with technical sizes (up to 100 kg) using thermal non-polarised neutrons	$\Phi \approx 3 \cdot 10^5$ cm^{-2} s^{-1} (perfect Si-Monochr.) $\Delta d/d \approx 4 \cdot 10^{-3}$ take-off angle: 57°−120° 2-D position-sens. ^{3}He-detector	GKSS / Peter Staron
FSS	Time of flight Fourier Strain Spectrometer to investigate residual stresses in specimens with technical sizes using thermal neutrons	$\Phi = 5.5 \cdot 10^6$ cm^{-2} s^{-1} timing res. ca. $4 \cdot 10^{-3}$ ($\lambda = 0.1$−0.4 nm) Analyser: 2 x 3072 TOF channels 2 detector banks (90° & 270°)	CAU - Universität Kiel / Hans-Georg Priesmeyer
NeRo	Neutronen Reflectometer to study magnetic and other surfaces, layers, thin films and membranes using cold non-polarised/polarised neutrons with high resolution	$\Phi = 5 \cdot 10^4$ cm^{-2} s^{-1} (standard collimation) $\Delta\lambda/\lambda = 0.02$ ($\lambda = 0.435$ nm) 2-D position-sens. ^{3}He-detector, ^{3}He-pencil counter	GKSS / Dieter Lott
PNR	Polarised Neutron Reflectometer to study magnetic and other surfaces, layers, thin films and membranes using cold non-polarised/polarised neutrons at high fluxes	$\Phi_{nonpol} = 1 \cdot 10^5$ cm^{-2} s^{-1} $\Phi_{nonpol} / \Phi_{pol} = 3 / 1$ $\Delta\lambda/\lambda = 0.05$ ($\lambda \geq 0.635$ nm) 2-D position-sens. ^{3}He-detector	GKSS / Danica Solina

Table A: **List of GeNF Instruments** (continued).

Instrument	Short Instrument Description /Main Tasks	Characteristic Data	Operator / Local Contact
RÖDI	X-ray (RÖntgen) DIffractometer to investigate residual stresses, textures and thin films	Seifert XRD 3003 PTS Heavy load goniometer	GKSS / Peter Staron
TEX-2	Four circle neutron TEXture diffractometer to characterise textures in metallic, ceramic and geologic materials using thermal non-polarised neutrons	$\Phi = 0.3 - 2 \cdot 10^6$ cm^{-2} s^{-1} take-off angle: 17°–57° (in 10°-steps) λ-range: 0.08–0.27 nm ^{3}He-single detect., 38° JULIOS-PSD, 2-D position-sens. ^{3}He- detector	TUC – Technische Universität Clausthal / Heinz-Günter Brokmeier
POLDI	POLarised DIffractometer; 3-D depolarisation analysis is used to investigate magnetic properties and correlations in magnetic materials; additional time of flight option in non-polarised mode	$\Phi_{max} = 0.8 \cdot 10^5$ cm^{-2} s^{-1} (polarized) take-off angle: $10° < 2\,\Theta_M < 65°$ λ-range: 0.1 nm–0.36 nm ^{3}He-single detector	PTB – Physikalisch Technische Bundesanstalt / Volker Wagner
HOLONS	HOLOgraphy and Neutron Scattering to investigate the properties in functional materials of photonics (e.g. photopolymers and photorefractive crystals) and to study light-induced changes simultaneously by light and neutron diffraction	holographic setup in SANS-2: angular resol. ≤ 0.01°; angul.setting acc = 0.001° lasers (excitation & diffract.): Ar^+-laser (single&multi line mode: 25 W /visible, 5.5 W / UV), HeNe-lasers (green, red)	Universities of Vienna and Osnabrück / Romano Rupp
GENRA-3	GEesthacht Neutron RAdiography facility for non-destructive analysis of materials by static and dynamic imaging	$\Phi_{therm} / \Phi_{epi} = 1.4 \cdot 10^6 / 8 \cdot 10^3$ [cm^{-2} s^{-1}] image: 15 x 15 to 45 x 45 cm^2 max. size of specimen: 100 x 200 cm^2	GKSS / Jürgen Vollbrandt
GBET	Geesthachter Boron- capture (Einfang) Therapy originally designed to study cell cultures in tumours with enriched boron; now available as a cold neutron irradiation facility	$\Phi = 1.6 \cdot 10^8$ cm^{-2} s^{-1} (λ_m= 0.6 nm) irrad. area : 30 x 40 mm^2 E_m = 2.3 meV	GKSS / Hans-Ulrich Ruhnau
ICI	In Core Irradiation - service for industry and others, different core positions, pneumatic dispatch system available	$\Phi_{therm} = 2$ to $8 \cdot 10^{13}$ cm^{-2} s^{-1} $\Phi_{fast} = 0.02$ to $0.06\ \Phi_{therm}$ max. sample size: 40 mm∅ x 100 mm	GKSS / Wolfgang Knop

Table B: **GeNF Sample Environment.**

Instrument	Cryostat	Magnets	Temp. Conditioning	Other Devices
SANS-1	^{3}He / ^{4}He – Cryostat: horizontal dilution-refrigerator with NMR sample coil and microwave source: T-range: 120 mK - RT; NMR: 106 and 16 MHz; Microwave: tunable: 68 to 74 GHz sample dimension: 2,8 x 17 x 19 mm^3 (optimum design for NMR coil), NMR is made for ^{1}H and ^{2}H resonance in 2.5 Tesla continuous wave mode;	2.5 Tesla magnet	heater up to 80 °C	
SANS-2	refrigerator cryostat Model Leybold RGD 210, temp.-range: 12−475 K flexible operation in various instruments	• **B-E 25**: up to 2 Tesla with closed cycle refrigerator (T: 8−300 K • **B-E 15**: up to 1.5 Tesla with closed cycle refrigerator (T: 8−300 K) • **B-E 10**: up to 1 Tesla with closed cycle refrigerator (T: 8−300 K), alternative furnace (T: 300−900 K), usable for polarised neutrons, • **superconducting magnet:** up to 5 Tesla with closed cycle refrigerator (T: 8−300 K) usable for polarised neutrons	heater (electric) / cooler (thermostat liquid circuit): T-range: -30−400 °C vacuum or inert gas atmosphere	− sample container for big samples − lasers;
DCD	refrigerator cryostat Model Leybold RGD 210, temp.-range: 12−475 K flexible operation in various instruments			
ARES	refrigerator cryostat Model Leybold RGD 210, temp.-range: 12−475 K flexible operation in various instruments			

Table B: **GeNF Sample Environment** (continued).

Instrument	Cryostat	Magnets	Temp. Conditioning	Other Devices
FSS	refrigerator cryostat Model Leybold RGD 210, temp.-range: 12 −475 K flexible operation in various instruments		heater (up to 1000 °C)	−stress rig max. force: 30 t
PNR	refrigerator cryostat Model Leybold RGD 210, temp.-range: 12−475 K flexible operation in various instruments	• **electro magnet:** up to 0.9 Tesla • **superconducting magnet:** up to 5 Tesla with closed cycle refrigerator (T: 8−300 K) usable for polarised neutrons	• heater / cooler (thermostat liquid circuit): T-range: -30−250 °C	
NeRo	refrigerator cryostat Model Leybold RGD 210, temp.-range: 12−475 K flexible operation in various instruments	• **electro magnet:** up to 0.9 Tesla	• 2 x vacuum furnaces: T-range: RT - 200 °C - one especially. for annealing purposes under PC control • heater / cooler (thermostat liquid circuit): T-range: -30−250 °C	
TEX-2			mirror furnace up to 2000 °C	− loading device: tension up to 1.5 t, compression up to 2.0 t − sophisticated set of sample holders
POLDI	− refrigerator T > 10 K − Orange cryostat T > 1.5 K	DC magnetic field < 160 A/cm pulsed field < 6.5 kA/cm		

GKSS FORSCHUNGSZENTRUM in der HELMHOLTZ-GEMEINSCHAFT	EXPERIMENTAL REPORT	GeNF SANS-1
Small-angle scattering instrument SANS-1		

Short Instrument Description:

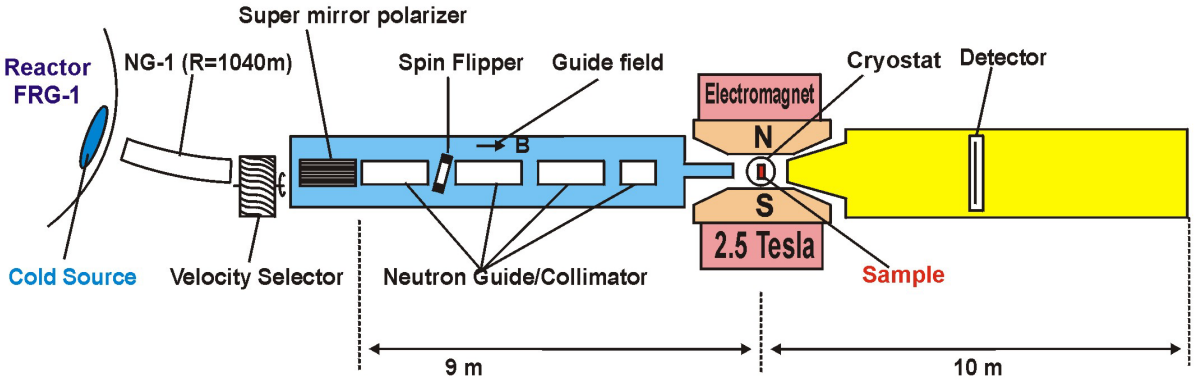
The small angle neutron scattering instrument SANS-1 using cold non-polarised/polarised neutrons serves primarily to investigate molecular biology, colloids and polymers.

Local Contact:

Dr. Regine Willumeit
Phone/Fax : +49 (0)4152 87–1291 / +49 (0)4152 87–1356
e-mail: regine.willumeit@gkss.de

Dr. Vasyl Haramus
Phone/Fax : +49 (0)4152 8 –1290 / +49 (0)4152 87–1356
e-mail: vasyl.haramus@gkss.de

Schematic View of SANS-1:



Instrument Details:

Beamline:	Beamline 8 - NG-1, radius of curvature R = 1040 m, cross section 3 x 4 cm^2, cold neutrons
Monochromator	helical slot selector
Wavelength range behind polariser and selector:	≥ 0.45 nm;
Wavelength resolution	$\Delta\lambda / \lambda = 0.1$ ($\lambda = 0.85$ nm)
Length L of collimation:	1 m, 3 m, 5 m, 7 m, 9 m
Flux at specimen:	$\Phi = 0.04 - 6 \cdot 10^5$ cm^{-2} s^{-1} see table

Instrument Details (continued):

Range of momentum transfer:	$0.05 \leq Q \leq 3$ nm^{-1}
Distance sample to detector:	0.7 m $\leq$ d $\leq$ 9m
Detector: active area: effective pixel size: background:	2-dim position-sensitive ^{3}He-counter 55 **x** 55 cm^2 0.7 x 0.7 cm^2 1 cps
Polarized target station:	dilution refrigerator (120 mK) 2.5 T C-shaped electro-magnet microwave emitter (68–74 GHz) NMR circuit for protons and deuterons selective nuclear spin depolarisation
Other sample environment	thermostat (5 °C to +200 °C) automatic sample change

Flux of polarized cold neutrons at the sample position:

length of collimator [m]	**1**	**3**	**5**	**7**	**9**
Φ [10^3 n cm^{-2} s^{-1}] (λ= 0.85 nm)	600	360	120	72	40

GKSS FORSCHUNGSZENTRUM in der HELMHOLTZ-GEMEINSCHAFT	**EXPERIMENTAL REPORT**	**GeNF SANS-1**

Small-angle polarized neutron scattering in f.c.c. Fe-Ni alloys

Proposer:	**V. M. Nadutov[1],** [1]G.V. Kurdyumov Institute for Metal Physics of the N.A.S. of Ukraine, Kyiv, Ukraine
Experimental Team:	**V. M. Haramus[2]**, **R. Willumeit[2]**, [2]GKSS, **D. V. Semenov[1]**
User Group Leader:	**V. M. Nadutov[1]**
Date(s) of Experiment:	November–December 2004

Scientific Objective

The small-angle neutron scattering experiment (SANS) in the Fe–30,5%Ni-0,4%C, Fe–30,5%Ni-1,5%C (wt.%) alloys has shown the existence of chemical and magnetic inhomogeneities. The average sizes of the inhomogeneities of 20–300 Å were estimated and they were described in terms of a fractal-like structures [1, 2]. The applied magnetic field of 2.5 T reduced the scattering intensity by approximately one order due to exclusion partially of the magnetic component in SANS. We assumed that the predominantly small length-scale magnetic inhomogeneities in the Fe-Ni-C alloys were not destroyed even by 2.5 T. However, the use of nonpolarized neutrons did not reveal difference between SANS curves [3]. In this work the SANS was measured in Fe–Ni alloys containing 29,2, 30,3, 34,1 % Ni with using polarized neutron beam and applied magnetic field in order to determine the effect of Ni and to separate nuclear and magnetic contributions in scattering excluding effect of carbon.

Experimental

The alloys with different Ni concentration, Fe–29.2 % Ni, Fe–30.3 % Ni, Fe–34.1 % Ni, were melted in a vacuum induction furnace in protective Ar environment. The ingots were annealed at 1273 K in vacuum for 3 hours. The concentration of Ni was obtained by means of X–ray fluorescence analysis. The samples were the 2–2.5 mm thick plates which were solution treated at 1373 K in vacuum and subsequently quenched in water. The phase content of samples was controlled with X–ray analysis. The polarized neutron beam and applied magnetic field of 2.5 T was used in SANS experiment.

Results and Main Achievements

The differential cross-section of SANS in the f.c.c. Fe–Ni alloys for H = 0 and H = 2.5 T are presented in Fig. 1 *a*. At small and average values of q the applied magnetic field decreases the scattering intensities ($d\Sigma(q)/d\Omega$) of two-one order of magnitude. The largest effect is related to the Fe–29.2 % Ni alloy. The difference of scattering at large q for all alloys is negligible small.

The decreasing of $d\Sigma(q)/d\Omega$ is due to magnetic ordering under the field. In this case the scattering is as almost from nuclear structure of the alloys $F_N(q)$. We can support our suggestion by negligible difference between SANS curves which represent different spin direction $I^-(q, H)$ *and* $I^+(q, H)$ (Fig. 1 *b*). Similar reaction on polarized neutrons was observed in the Fe-Ni-C alloys [3]. Under the field the behavior and slopes of curves for all Fe-Ni alloys is similar. However, the intensity of scattering simultaneously reduces with increasing Ni concentration

(fig. 1 *a*). The power-law exponent α in the power-law $I(q) = Aq^{-\alpha} + B$ charac-terizing the structure of nuclear inhomogeneities was estimated. The values of α at low and large q point to existence of nuclear inhomogeneities in the Fe-Ni alloys with the fractal-like properties [5]
The sizes of aggregates in the Fe–Ni alloys (for $q > 0.05$ Å^{-1}) was estimated using the Indirect Fourier Transformation method, 16–200 Å (it belongs to Fe–30,3 % Ni [3], what about Fe–29,2 % Ni, Fe–34,1 % N), which appeared to be less than in the Fe–Ni–C alloys, 20–300 Å [3].
Thus, the increase of Ni concentration in the austenitic Fe-Ni alloys reduces both nuclear and magnetic fraction in SANS varying magnetic structure ambiguously in given q range.

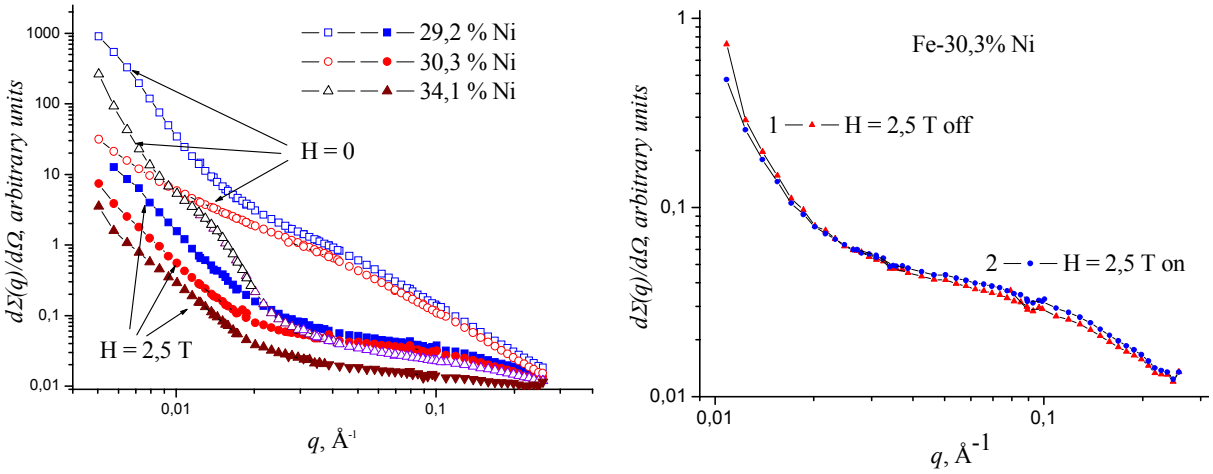


Figure 1. The φ-averaged small-angle nonpolarized neutron scattering intensity in the Fe–29,2 % Ni, Fe–30,3 % Ni, Fe–34,1 % Ni (wt. %) alloys in magnetic field 2.5 T and without field (*a*) and SANS in the Fe–30.3 % Ni alloy by different direction of polarization of neutron beam (averaged by φ-angle) (*b*).

Acknowledgments. This study was carried out under support of GKSS Research Centre and the Science and Technology Center in Ukraine (the project #2412).

References

1. V.M. Nadutov, V.M. Garamus, R. Willumeit, Ye.O. Svystunov: Metallofizika i noveishie tekhnologii, 24(5), 717 (2002).
2. Nadutov V.M., Garamus V.M., Willumeit R., Svystunov Ye.O. Small-Angle Neuton Scattering in F.C.C. Fe-Ni and Fe-Ni-C alloys, Materials Science Forum vol. 443-444, 2004 pp. 251–254.
3. V.M. Nadutov, V.M. Garamus, R. Willumeit, D.V. Semenov. Small-angle neutron scattering in Invar Fe-Ni-C alloys in magnetic field. Functional Materials 2004, v. 11, pp. 501–505.
4. W. Wagner, A. Wiedenmann, W. Petry, et. al, *J. Mater. Res*. 6 (1991) 2305.; A. Wiedenmann, *J. Met. Nanocryst. Mater*. 2-6 (1999) 315.
5. P.W. Schmidt: Use of scattering to determine the fractal dimension. in D. Avnir (Ed.), *The fractal approach to Heterogeneous Chemistry* (Wiley, New York 1989), p. 67.

GKSS FORSCHUNGSZENTRUM in der HELMHOLTZ-GEMEINSCHAFT	**EXPERIMENTAL REPORT**	**GeNF SANS-1**

Mixed micelles formed by SDS and a bolaamphiphile with carbohydrate headgroups

Proposer:	**Sven Gerber,** [1]Universität Hamburg, Inst. für Organische Chemie, Martin-Luther-King-Platz 6, 20146 Hamburg
Experimental Team:	**Götz Milkereit**[1]
User Group Leader:	**Sven Gerber**[1]
Date(s) of Experiment:	11–19 March 2005

Objectives

In this work we investigated the interaction of a carbohydrate-based bolaamphiphile with sodium dodecyl sulfate (**SDS**) (figure 1). **SDS**-mixtures in particular gained much interest in mixed surfactant systems, therefore much data is available that can be compared with results from our studies. It is known that **SDS** shows synergism in mixtures with non ionic surfactants [1]. Mixtures of **SDS** with glucosides (octyl glucosides) favour the formation of mixed micelles also [2]. From these and other studies synergetic interactions between a bolaamphiphile and **SDS** and formation of mixed micelles can be expected. In this work the mixtures were investigated by small-angle neutron scattering (SANS) and surface tension measurements, using deuterated and protonated **SDS** to obtain information about mixing with the bolaamphiphile and it's location in mixed micelles.

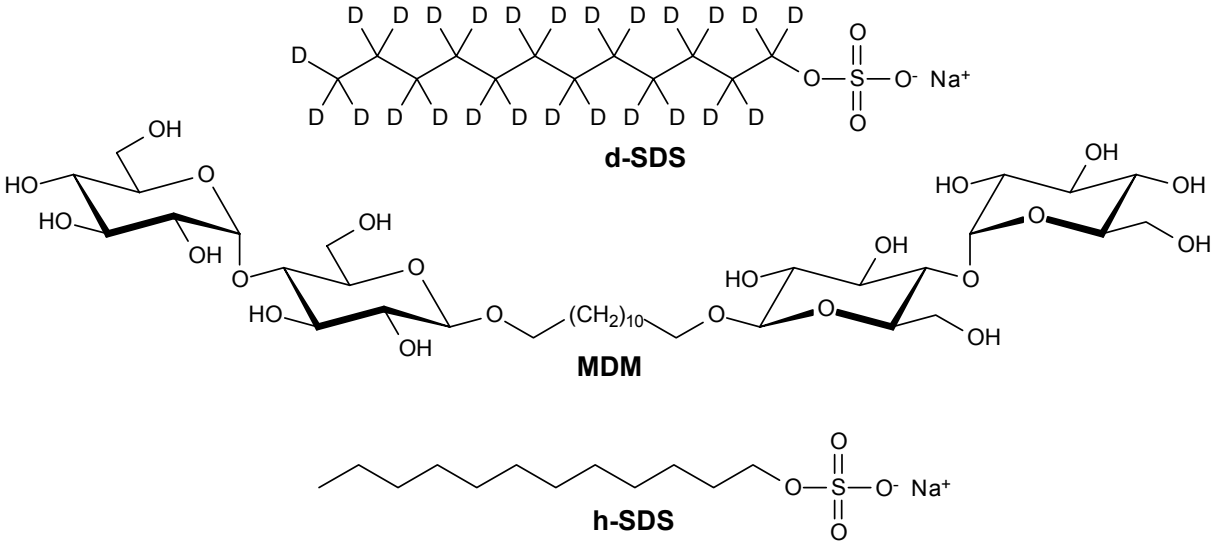


Figure 1: Investigated compounds: 1,12-bis-[4''-*O*-(α-D-glucopyranosyl)-β-D-glucopyrano-syl]-dodecane (**MDM**), sodium dodecylsulphate (h-**SDS**) and sodium dodecyl-sulphate-D_{25} (d-**SDS**).

Experiment

Figure 2a shows the CMC values of the mixtures together with the theoretical curve for the CMC's of an ideal mixing of surfactants which was calculated within the regular solution theory (RST) using [1,2].

It is easy to see that the experimental values of the CMC are always lower than the values expected for an ideal mixing. It shows that there is a synergism pointing on the formation of mixed micelles in solution of **SDS/MDM**. It can be expected that the parameters f_1 and f_2 are lower than 1 and the corresponding parameter β ($f_1=\exp\beta(1-x_1)^2$ and $f_2=\exp\beta x_1^2$) which is related to an interaction between surfactants in mixed micelles, is negative [3,4].

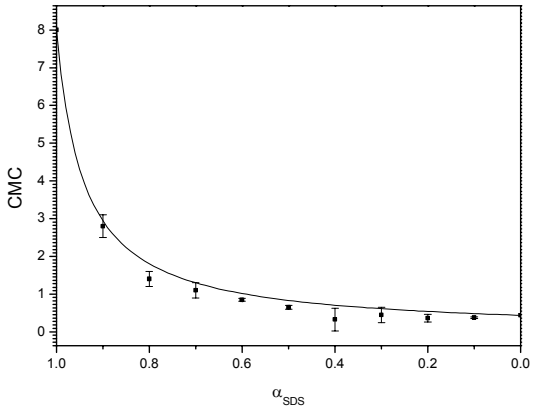


Figure 2a: CMC as a function of surfactant composition of **SDS** and **MDM** mixtures (symbols) and ideal mixing curve (solid line). α is the molar fraction of **SDS**.

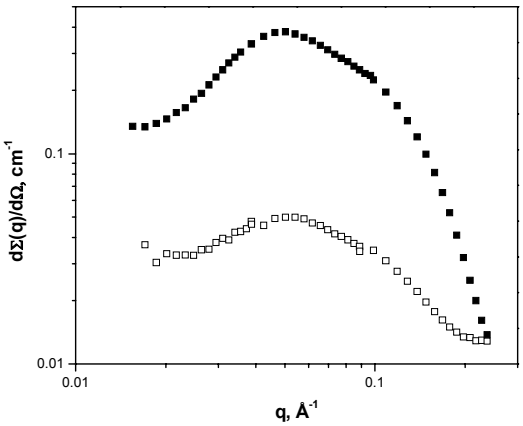


Figure 2b: Small angle neutron scattering data from solutions of **SDS**/**MDM**/D_2O, α=0.7 (filled symbols – protonated **SDS** and empty symbols – deuterated **SDS**).

SANS measurements were performed in two solutions: first **SDS**/**MDM**/D_2O and second **SDS** was substituted by deuterated **SDS**. The total concentration of surfactant was the same in both cases (0.1 M, ~4.5 wt%, and composition α = 0.7). The use of deuterated **SDS** instead of protonated gives us the possibility to decrease the scattering contrast from **SDS** ~ 200 times. It can be concluded that most scattering in the second solution should be mainly from **MDM**.

SANS data are shown in Figure 2b. For both solutions an interference maximum is clearly visible which points on a significant repulsion between the aggregates due to a strong electrostatic interaction between micelles. The main feature, which has to be compared for both curves, is the position of the maximum. The position of the maximum is connected with the average distance between aggregates $q_{max} \sim 1/d^{1/3}$ which is determined by the concen-tration of aggregates. The constant value of q_{max} supports the idea that the concentration of aggregates, there we observe **SDS** and **MDM** (solution with protonated **SDS**) and there we can observe only **MDM** (solution with deuterated **SDS**), is the same. It means that we observe the same aggregates i.e., mixed micelles of **SDS** and **MDM**. It is well-known for non-ionic/ionic mixtures [5].

The experimental data were analyzed via fitting of the scattering intensities by the model of two-shell ellipsoids of rotation, interacting screened Coulomb potential (α>0). This approach was successfully applied for many micellar solutions [6,7].

Some obtained fitting parameters and other geometric features (semi-axis values) are presented in Table 1. Analysis of solutions with h-**SDS** and d-**SDS** gives the same parameters of aggregates. It points that the chosen model of one population of mixed micelles (without demixing within the micelle) is correct for the length scale $l > \pi/q > 10$ Å. Aggregates are of a

non-spherical (oblate) shape which is in accordance with pure **SDS** micelles [8]. The total aggregation number is 30 % less than for pure **SDS** micelles but it should be taken into account that **MDM** molecules are significant larger than **SDS** ones.
The observed oblate shape (mostly planar) shape of aggregates is in agreement with a preferably planar geometry of bola amphiphiles [9]. The values of smaller semi axis suggest a tilted direction of **SDS** molecules in mixed micelles.

Achievements and Main Results
Synergetic interactions between a carbohydrated bolaamphiphile and **SDS** are observed (parameter β is negative; with a minimum in the cmc vs composition plot). SANS data are collected for mixtures containing protonated and deuterated **SDS** which give us the possibility to conclude the formation of mixed micelles with a homogeneous distribution of surfactants within the micelle. The shape of micelles is non-spherical (oblate).

Table 1: Results of fitting SANS data by a model of a two-shell ellipsoid of rotation (*a,a,b*) for solutions of **SDS**/**MDM**/D_2O containing h-**SDS** and d-**SDS** (N_a – total aggregation number, $N_{a,SDS}$ and $N_{a,MDM}$ - number of SDS and MDM molecules in micelles, γ - axis ratio, total charge, semi axis values *a* and *b*).

	N_a	$N_{a,SDS}$	$N_{a,MDM}$	γ	Total charge, e	*a*, Å	*b*, Å
h-**SDS**	46±3	32±2	14±1	0.85±0.05	10±1	25±2	21±2
d-**SDS**	42±3	29±2	13±1	0.89±0.05	8±1	24±2	21±2

References

[1] Jönsson, B.; Lindman, B.; Holmberg, K.; Kronberg, B. *Surfactants and Polymers in Aqueous Solution*; John Wiley & Sons: New York, 1998; p. 95.
[2] Kameyama, K.; Muroya, A.; Takagi, T. *J. Colloid Interface Sci.* 1997, *196*, 4852.
[3] Clint, J. *J. Chem. Soc., Faraday Trans I* 1975, *71*, 1327–1334.
[4] P.M. Holland, *Adv. Colloid Interface Sci.* 1986, *26*, 111–129.
[5] Hines, J.D. *Curr. Opinion Colloid Interf. Sci.* 2001, *6*, 350–356.
[6] Chen, S. H. *Ann. Rev. Phys. Chem.* 1986, *37,* 351–370.
[7] Chevalier, Y.; Zemb, T. *Rep. Prog. Phys.* 1990, *53*, 279–371.
[8] Bergström, M.; Pedersen, J. S. *Phys. Chem. Chem. Phys.* 1999, *1*, 4437–4446.
[9] Fuhrhop J.-H.; Wang T.Y. *Chem. Rev*. 2004, *104*, 2901–2937.

GKSS FORSCHUNGSZENTRUM in der HELMHOLTZ-GEMEINSCHAFT	EXPERIMENTAL REPORT	GeNF SANS-1

Influence of small ethoxy-spacers on the micellar structure of alkyl β-maltosides

Proposer: **Co-Proposers:**	**Götz Milkereit**[1], [1]Universität Hamburg, Inst. für Organische Chemie, Martin-Luther-King-Platz 6, 20146 Hamburg
Experimental Team:	**Stephan Hauschild** [1],
User Group Leader:	**Götz Milkereit**[1]
Date(s) of Experiment:	12–14, 22–24 April 2005

Objetives

The effect of spacer and alkyl chain length on the formation of micelles in aqueous solutions of synthetic alkyloxyethyl β-maltosides containing ethyl spacer was investigated. The lipophilic part consists of dodecyl or tetradecyl chains (Figure 1). The adsorption at the liquid air-interface was investigated by surface tension measurements. The micellar phase region (L_1) was studied using small-angle neutron scattering. The results were compared with the micellar structures reported for the corresponding n-alkyl β-maltosides with different chain length (C12 and C14).

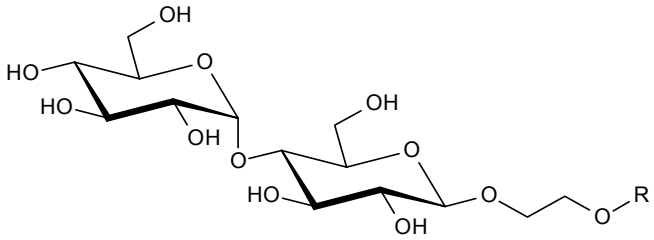


Figure 1:
Chemical structures of the investi-gated amphiphiles.

Mal-EG-12: R = $C_{12}H_{25}$

Mal-EG-14: R = $C_{14}H_{29}$

Experiment

For **Mal-EG-12** solutions at 6 x 10^{-4} and 1 x 10^{-3} g/mL (three and five times the CMC) were measured. For **Mal-EG-14** a concentration of 1 x 10^{-4} g/mL was measured (two times the CMC). The concentration range near the CMC was chosen for measurements to get information about the growth and a possible change in the shape of the aggregates near the CMC. As reported for the micelle formation of some simple alkyl glycosides the size and shape of micelles does not change with the concentration in a concentration range well above CMC [1]. In the measured concentration range (close to CMC) no change of the structure was observed on increase of the concentration.

We did not observe a significant difference in the shape of SANS curves for the maltose compounds **Mal-EG-12** and **Mal-EG-14** (Figure 2a). The increasing of the alkyl chain from 12 to 14 carbon atoms results in a slightly higher scattering but does not change main features of the scattering patterns (size and shape of formed aggregates).

The application of the IFT analysis shows that micelles formed by **Mal-EG-14** are slightly larger than the ones formed by **Mal-EG-12**. The corresponding values of radius of gyration are 27.6±0.3 Å and 24.7±0.2 Å. The shapes of the pair distance distribution functions (Figure 2b) show a shift of the maximum to larger *r*. The shape of the p(r) function is also more symmetrical in the case of the long chain compound. Although the same maximum distance

of 90 Å was required to get reasonable fits; it can be explained as a hydrocarbon core of micelles and hydrated shell of the polar groups.
The application of the two-shell spherical model gives a good fit of the scattering data (Figure 2a) and the structural parameters of the formed micelles: Similar radius of the hydrocarbon core R_c = 20±1 Å (**MaI-EG-12**) and R_c = 22±1 Å (**MaI-EG-14**) for both compounds, similar total radius R_t = 38±2 Å (**MaI-EG-12**) and R_t = 40±2 Å (**MaI-EG-14**) but different values for the contrast ratio between the shell and the core: 0.15±0.01 (**MaI-EG-12**) and 0.20±0.01 (**MaI-EG-14**). The increase of the contrast ratio of the shell/core values can be connected to a higher fraction of methylene groups, which are located in the shell of the micelles and/or a different degree of hydration of the polar groups.

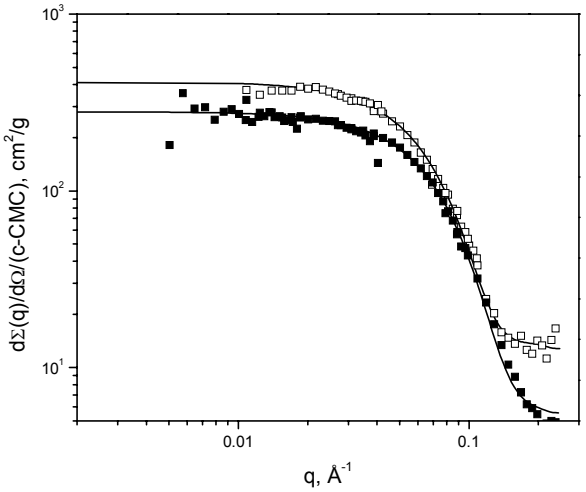


Figure 2a: Scattering data for **MaI-EG-12** (filled squares) and **MaI-EG-14** (empty squares) together with the model fits (solid lines).

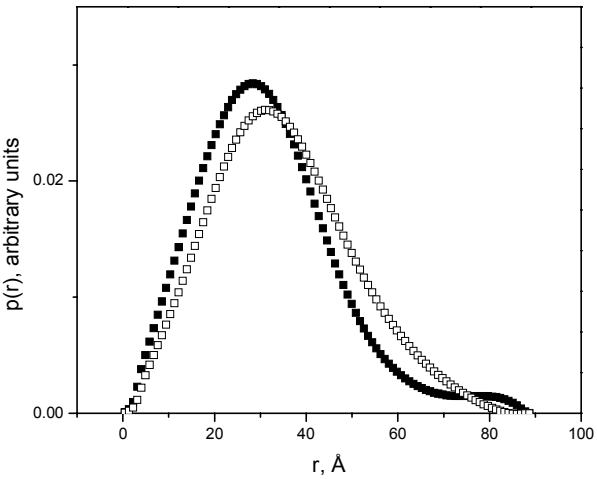


Figure 2b: Pair distance distribution functions, p(r) for **MaI-EG-12** (filled squares) and **MaI-EG-14** (empty squares).

Achievements and Main Results

The CMC value of **MaI-EG-12** is two times higher than the corresponding value of the non-spacer Maltoside **MaI-C12** [2]. This result shows that the equilibrium between micelles and monomers in solution is shifted to the monomer side, if the hydrophilic part of the molecule is increased by a hydrophilic spacer. This also changes the shape of micelles.
The formation of ellipsoidal micelles by **MaI-C12** and cylindrical micelles for **MaI-C14** was already reported [2,3]. In present studies we have observed that only spherical aggregates were formed. This observation can be connected to a lower surfactant concentration (10 times) compared to previous studies and with the influence on the polarity of the ethylenoxid spacer. The overall size of micelles formed by alkyl glycosides with short alkyl chains and with and without spacer is in the case of the maltosides very similar (r~35–40 Å).
The main difference in the micellisation behaviour of maltosides with spacer and without spacer was observed with an increasing of the alkyl chain from 12 to 14 carbon atoms. For maltosides without spacer the micellar shape changes from a ellipsoidal to a rod-like geometry while increasing of the alkyl chain from 12 to 14 carbon atoms [3]. On the other hand the maltosides with a spacer form the same type of micelles (spherical) with increasing chain length (12 to 14 carbon atoms). The addition of spacer results in a higher rigidity of the polar group, which resists the transformation of the micelles with increasing chain length.

References

[1] He, L., Garamus, V.M., Funari, S.S., Malfois, M., Willumeit, R., Niemeyer, B., *J. Phys. Chem. B*, 2002, *106*, 7598–7604.
[2] Dupuy, C., Auvray, X., Pepitay, C., Rico-Lattes, I., Lattes, A., *Langmuir*, 13, 1997, 39653967.
[3] Heerklotz, H., Tsamaloukas, A., Kita-Tokarczyk, K., Strunz, P., Gutberlet, T., *J. Am. Chem. Soc.*, 126, 2004, 16544–16552.

GKSS FORSCHUNGSZENTRUM in der HELMHOLTZ-GEMEINSCHAFT	**EXPERIMENTAL REPORT**	**GeNF SANS-1**

Micelles of amphiphilic triblock terpolymers

Proposer:	**Volker Abetz**, [1]Institut für Polymerforschung, GKSS Forschungszentrum Geesthacht, 21502 Germany.
Co-Proposers:	**Adriana Boschetti**[1], **Michael Gradzielski**, [2]Physikalische Chemie, TU Berlin, Berlin, Germany
Experimental Team:	**Vasyl Haramus**, GKSS
	Daniel Fierro[1],
User Group Leader:	**Adriana Boschetti**[1]

Date(s) of Experiment:	6–8, 18–21 April 2005

Objectives

A novel type of water-soluble triblock terpolymer of polybutadiene-*b*-polystyrene-*b*-poly(ethylene oxide) has been synthesized. These terpolymers form well-defined micellar aggregates in aqueous solution. During the performed experiments, the main goal was to study the impact of dioxane on the aggregation behavior of the amphiphilic triblock terpolymers, by means of varying the concentration of dioxane in the dioxane/water mixture.

Experiment

In general the morphology of amphiphilic block copolymers in aqueous solution is currently a topic of intensive research [1-4]. We have recently synthesized a novel type of water-soluble triblock terpolymer of polybutadiene-*b*-polystyrene-*b*-poly(ethylene oxide). Such terpolymers can become dispersed in aqueous solution by different techniques, e. g. by vigorous shaking, ultrasonification or aqueous dilution of a concentrated solution dissolved in dioxane or THF [5].

These aqueous solutions were characterized by means of dynamic light scattering and it is interesting to note that for identical total concentration of copolymer we found similar values of the hydrodynamic radii, e. g. about 50–65 nm for $B_{19}S_{34}EO_{47}^{142}$ [5]. Evidently the terpolymer is aggregated in these solutions and the aggregates are only little affected by the way of preparation. This is surprising as the polymer contains an extended block of polystyrene, which is below the glass transition temperature, and accordingly one should expect formation of non-equilibrium aggregates ("frozen micelles"), which normally display a strong dependence on their way of formation.

The sample used in our experiments was a polybutadiene-*b*-polystyrene-*b*-poly(ethylene oxide) triblock terpolymer, $B_{19}S_{34}EO_{47}^{142}$. In the notation here employed, B stands for polybutadiene, S for polystyrene and EO for poly(ethylene oxide). In the $A_xB_yC_z^m$, the subscript numbers stand for the mass fraction in percent and the superscript indicates the overall number-averaged molecular weight M_n in kg/mol of the block copolymer.

The influence of the d_8-dioxane:water ratio on the micelles formed was studied. In order to do so, the polymer was dissolved in deuterated dioxane. The dispersion of the particles was achieved by adding deuterated water slowly and drop-wise to the polymer solution under stirring. The final polymer concentration was kept constant at 0.1 wt.-%.

Achievements and Main Results

The aggregation behavior of the triblock terpolymer was successfully studied. Figure 1 shows the scattering patterns obtained for the different solvent/non-solvent ratios employed. The results of the corresponding fittings are shown in Table 1.

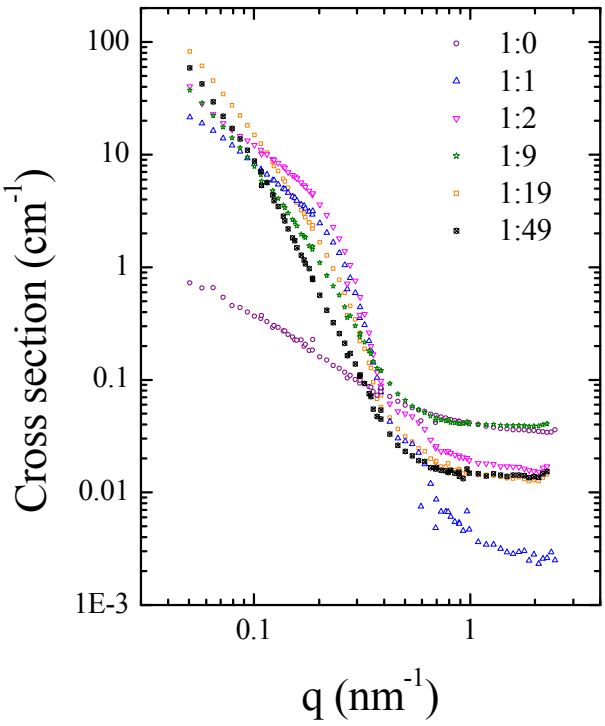


Figure 1:
Neutron scattering of $B_{19}S_{34}EO_{47}$[142] triblock terpolymer in deuterated dioxane:deuterated water mixtures with different mixture ratios.

Table 1: Results from the data analysis.

d_8-Dioxane: D_2O ratio	*Slope, q = 0.05–0.15 nm^{-1}*	*Slope, q = 0.5–2.5 nm^{-1}*	*Shape*
1:0	1.12±0.02	1.18±0.02	Rod like
1:1	1.58±0.01		Random walk chains
1:2	1.43±0.01		Random walk chains
1:9	2.48±0.01	α=4.0	Structure volume fractal-like with smooth and sharp interface
1:19	2.70±0.01	α=4.6±0.1	Some structure volume fractal like
1:49	2.74±0.01	α=4.4±0.1	Some structure volume fractal like

As can be observed in table 1, at low content of D_2O (ratios of 1:0, 1:1 and 1:2) rod like aggregates have been found, with radius of cross section is around 90–100 Å. At higher content of the non-solvent (ratios of 1:9, 1:19 and 1:49) volume fractal aggregates are formed, which size of primary particles is ~ 100 Å. Specifically for the case of a d_8-Dioxane: D_2O ratio of 1:9, a smooth surface was found, and the average size of the aggregates was calculated to be ~ 5000 Å.

References

[1] V. Balsamo, G. Gil, C. Urbina de Navarro, I.W. Hamley, F. von Gyldenfeldt, V. Abetz, E. Canizales, *Macromolecules* 36, 4515 (2003)
[2] D.E. Discher, A. Eisenberg, *Science* 297, 967 (2002)
[3] S. Förster, V. Abetz, A.H.E. Müller, *Adv. Polym. Sci.* 166, 173, (2004)
[4] D.V. Pergushov, E.V. Remizova, M. Gradzielski, P. Lindner, J. Feldthusen, A.B. Zezin, A.H.E. Müller, V.A. Kabanov, *Polymer* 45, 367 (2004)
[5] A. Boschetti, V. Abetz, M. Drechsler, M. Drechsel, M. Gradzielski, in preparation

GKSS FORSCHUNGSZENTRUM in der HELMHOLTZ-GEMEINSCHAFT	EXPERIMENTAL REPORT	GeNF SANS-1

SANS Study of Dispersed Ultrananocrystalline Diamond

Proposer:	**M.V. Avdeev** Frank Laboratory of Neutron Physics, Joint Institute for Nuclear Research, 141980 Dubna, Moscow region, Russia
Experimental Team:	**E. Osawa[1], N.N. Rozhkova[2], V.M. Haramus[3]** [1]NanoCarbon Research Institute, Chiba, Japan; [2]Institute of Geology, Petrozavodsk, Russia; [3]GKSS
User Group Leader:	**M.V. Avdeev**
Date(s) of Experiment:	April 9–17, October 10–15, 2005

Objectives

Detonation nanodiamond (DND) was discovered in 1963 [1] and, then, rediscovered in 1988 [2,3] as an excellent alternative to the well-developed shock diamond. DND was found in the soot from explosion of oxygen-imbalanced explosives exploded in the absence of any extra carbon source. DND particles are ultra-fine single crystals of cubic diamond with diameters of 4–5 nm as estimated from the half widths of powder X-ray diffraction peaks, thus offering the smallest known diamond, apparently a highly attractive material in nanotechnology. However, until very recently DND has never been successfully purified. The most crucial was the lack of knowledge on the remarkable tendency of nanoparticles to form tight aggregates, primarily because of large surface area relative to bulk inside. The particles in DND powders available now are assumed to be of a complex structure, which is conglomerates of variously sized aggregates containing the agglutinates (extremely tight aggregates) in the core. In 2002 a way to decompose the agglutinates by stirred-media milling technique using ultrafine ceramic beads of 30 micron zirconia was developed [4]. Dispersed in liquids, primary particles of DND result in surprisingly stable colloid - dispersed ultrananocrystalline diamond (DUNCD). Especially favorable are water and polar aprotic solvents like dimethyl sulfoxide (DMSO). The mechanism of stabilization of DUNCD is unclear for the moment. We believe that it can be connected with the interaction of surface atoms different from carbon (O, N, H) with the solvent. According to dynamic light scattering, the size of the agglutinated core ranges between 60 to 200 nm.

Experiment and main results

In the given experiments small-angle neutron scattering was applied to DUNCD in water and DMSO to reveal features of the aggregates and their interaction at the scale of 1-100 nm. The concentration effect in the range of 0.1–10 wt. % was followed by dilution of initial samples with the maximal fraction of diamond. SANS curves referred to one concentration are presented in Fig.1. One can see that for $q > 0.1$ nm^{-1} the curves coincide and show common two-scale organization: primary particles of ~6 nm size compose fractal-like aggregates with the mass fractal dimension ~ 2.3 found from the power-law scattering. The size-effect on the scattering from these aggregates is not seen in the curves reflecting the fact that their characteristic size is more than 120 nm. Instead, one can see the pronounced interaction effect between the aggregates at smallest q-value. It reveals an interesting observation that the correlation length of such interaction is less than the size of the interacting particles. This means that the large fractal aggregates penetrate each other when interacting, so that the length between their centers of mass is less than their characteristic size.

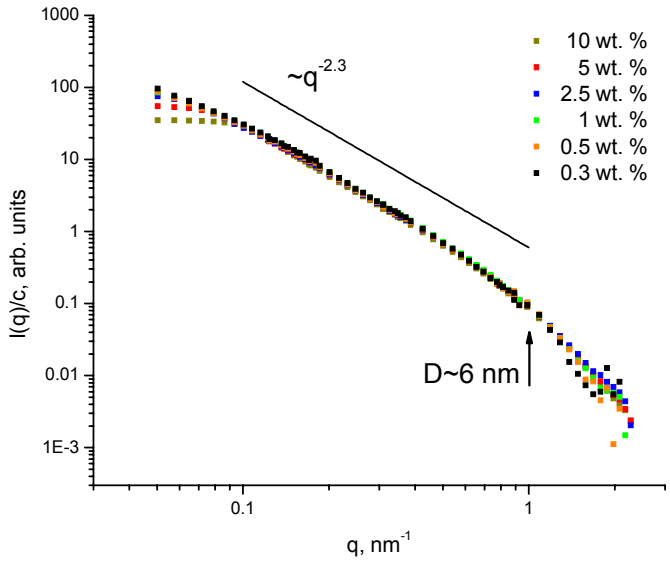


Figure 1. Experimental SANS curves from DUNCD in water referred to one concentration. Line denote the scattering of the power-law type corresponding to aggregates with mass fractal dimension of 2.3. Arrow points to the place where the power law of the experimental curves breaks used to estimate the characteristic size D of structural units of the aggregates.

The next step performed during the experiments was the contrast variation technique based on exchange of hydrogen with deuterium in liquid media. The change in the SANS curves with the contrast variation and determination of the match point of the particles are demonstrated in Fig.2. One can conclude that the studied aggregates are quite uniform at the scale of 10–100 nm. The match point of their structural basic units is determined with a good precision 1.62±0.04, and gives the value of the mean scattering length density of 10.6±0.3 cm^{-2}. It is less than that calculated for pure diamond, 11.8 cm^{-2}. It can be explained by the presence of other component in basic units. This component can form a shell around diamond crystallites, which is responsible, from the one hand, for aggregate formation during the synthesis and, then, for stabilization of the aggregates in liquid dispersions due to its specific interaction with polar solvents. Modelling of such shell is in progress.

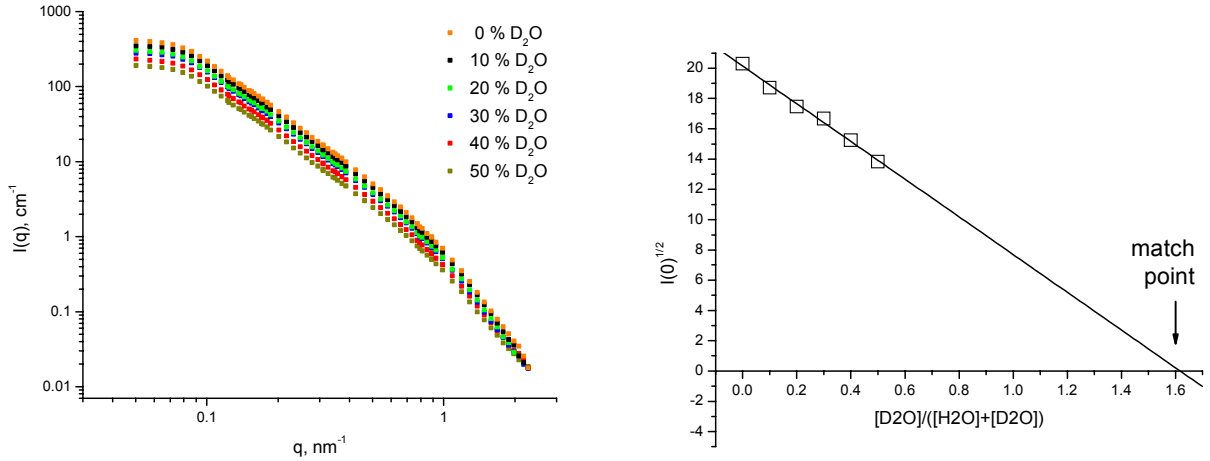


Figure 2. (**left**) Experimental SANS curves from DUNCD in water obtained with different content of D_2O in the carrier (contrast variation); (**right**) Determination of the match point of the system for the 5 wt.% dispersion.

References

[1] V.V. Danilenko, Phys. Solid State 46 (2004) 581
[2] N.R. Gneiner, D.S. Phillips, J.D. Johnson, F.Volk, Nature 333 (1988) 440
[3] V.L. Kuznetsov, et al. Carbon 29 (1991) 665.
[4] E. Osawa In book of abstracts of NATO ARW "UltraNanoCrystallineDiamond'2004", St-Petersburg, June 7–10 2004

GKSS FORSCHUNGSZENTRUM in der HELMHOLTZ-GEMEINSCHAFT	EXPERIMENTAL REPORT	GeNF SANS-1

A SANS study of water soluble polyfluorene-surfactant systems

Proposer:	**Matti Knaapila**[1], [1]Department of Physics & Durham Nanomaterials UIC, University of Durham, South Road, Durham DH1 3LE, UK
Co-Proposers:	**Laszlo Almasy**[2], [2]Research Institute of the Solid State Physics (Budapest, Hungary)
	Hugh Burrows[3], [3] Department of Chemistry, University of Coimbra (Coimbra, Portugal)
Experimental Team:	**Matti Knaapila**[1], **Laszlo Almasy**[2], **Vasyl Haramus**[4], [4]GKSS
User Group Leader:	**Matti Knaapila**[1]
Date(s) of Experiment:	23 April–03 May 2005

Objectives

Water soluble π-conjugated polymers form an option for interrogating biological substrates. Furthermore, control of the inkjet process and layer-by-layer self assembly – the major advantages of polymers over oligomers in organic light emitting device fabrication – would greatly benefit from versatile selection of water soluble electroluminescent materials. Unfortunately, conjugated polyfluorenes are scarcely water soluble as such but different co-solvents are needed [1]. In order to probe the water solubility of polyfluorene and its solubilization by $C_{12}E_5$ surfactant, a phase behavior study of the ternary D_2O-poly-{1,4-phenylene-[9,9-bis(4-phenoxy-butylsulfonate)]fluorene-2,7-diyl} (PBS-PFP) and pentao-xyethylene glycol ether ($C_{12}E_5$) system was realized.

Experiment

The solution formation was initially suggested by the transparency and a blue shift in photoluminescence spectrum upon mixing the constituents as well as changes in surface tension and contact angle. The micellar structure was then suggested to be studied using small-angle neutron scattering. As indicated by this consideration, the polymer itself is not water soluble. Then, a phase behavior study of a ternary D_2O-PBS-PFP$(C_{12}E_5)_x$ at 20 °C was per-formed. PBS-PFP and $C_{12}E_5$ concentrations were $5{\cdot}10^{-4}$ M and 2.5-75$\cdot 10^{-4}$ M, respec-tively. Surface tension, contact angle, and photoluminescence, measurements were per-formed at the University of Durham. The general phase behaviour was introduced as a function of surfactant fraction using the mentioned methods (see results below).

Achievements and Main Results

Under the studied conditions, ternary D_2O-PBS-PFP$(C_{12}E_5)_x$ shows three phase regimes phenomenologically corresponding to observed blue shifts in photoluminescence and changes in surface tension and contact angle. First, the solution turns isotropic, when the molar ratio of surfactant over monomer unit (x) is around 1, indicating dissolution and negligible polymer-surfactant interaction (association). Second, for x ~ 1-2, SANS patterns indicate elongated (polymer-surfactant) objects with elliptical cross-sectional and persistence length of 7-22 nm increasing with x. Third, for x ~ 4-15 the SANS curves show a concentration dependent interference maximum at q ~ 0.015 Å^{-1}, which is suggested to be due to the electrostatic repulsion between $C_{12}E_5$ micelles with adsorbed polymers [2]. The inteference maximum due to the intermicellar interaction is shown in Figure 1.

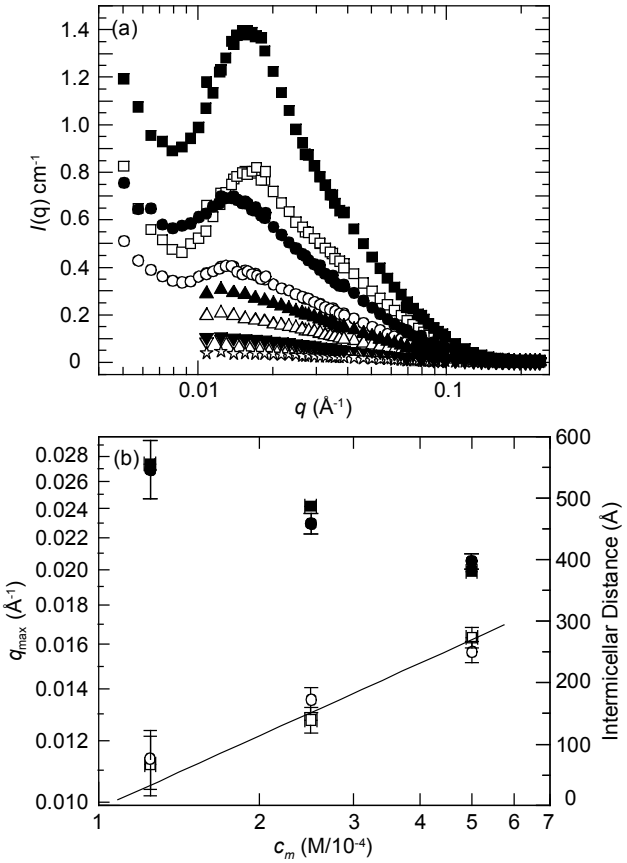


Figure 1.
(a) SANS data of D_2O-PBS-PFP($C_{12}E_5$)$_x$ for x=8 (open symbols) and x=10 (solid symbols) with PBS-PFP concentration of $5 \cdot 10^{-4}$ M (squares), $2.5 \cdot 10^{-4}$ M (spheres), $1.25 \cdot 10^{-4}$ M (upper triangels), $0.625 \cdot 10^{-4}$ M (lower triangles), and $0.3125 \cdot 10^{-4}$ M (stars).

(b) The q_{max} (open symbols) and intermicellar distance (solid symbols) vs. monomer concentration corresponding for x=8 (squares) and x=10 (spheres). A solid line is a of q_{max} for x =8. T=20 °C.

We found the results reasonable and important and they give us a base to develop ternary water soluble polyfluorene solutions. As we had made a preliminary study at the Budapest Neutron Centre, the experiment in Geestacht was straightforward and technically successful.

References

[1] H. Burrows et al. Fluorescence enhancement of the water soluble poly{1,4-phenylene-[9,9-bis(4-phenoxy-butylsulfonate)]fluorene-2,7-diyl} copolymer in n-dodecyl pentaoxyethylene glycol ether micelles Macromolecules 2004 37 7425.

[2] M. Knaapila, L. Almásy, V. M. Garamus et al. Rodlike micelles and ordered micellar phase of polyfluorene polyelectrolyte-$C_{12}E_5$ surfactant system in aqueous solution, submitted.

GKSS FORSCHUNGSZENTRUM in der HELMHOLTZ-GEMEINSCHAFT	**EXPERIMENTAL REPORT**	**GeNF SANS-1**

Conformational change of the polyelectrolyte in presence of surfactant studied using SANS

Proposer:	**Per Claesson**[1], [1]Chemistry Department, KTH, Stockholm, Sweden
Co-Proposers:	
Experimental Team:	**Joseph Iruthayaraj[1], Luis Bastardo Zambrano[1]**
User Group Leader:	**Per Claesson**
Date(s) of Experiment:	19–27 May 2005

Objectives

Polyelectrolyte-surfactant interactions can often lead to macroscopic phase separation thereby exhibiting diverse phase behaviours akin to pure surfactants in water. For example studies conducted on various polyelectrolyte/ surfactant systems revealed varied phases like cubic, hexagonal or lamellar[1-3]. Such interactions also lead to conformational change of the polyelectrolyte chain. It is possible to observe the change in chain conformation in SANS by performing the experiment under appropriate contrast. This study concerns the 100 % charged Poly (dimethylaminoethylmethacrylate.CH_3Cl) and its interaction with anionic surfactant (SDS). Addition of 4 mM of SDS to 0.2 % polyelectrolyte lead to phase separation which is a general phenomenon observed in most polyelectrolyte and oppositely charged surfactant systems. Also this phase is in equilibrium with dilute aqueous solution. Measurements in different contrast clearly show the change in chain conformation in presence of surfactant. The main objective is to study the interaction between the anionic surfactant (SDS) and the oppositely charged polyelectrolyte, poly (dimethylamino-ethylmethacrylate.CH_3Cl) under various contrasts.

Experiment

Dimethylaminoethylmethacrylate monomers were free radically polymerised using thermal initiator. The amine group in all segments were quarternized thereby providing us with a 100 % permanently charged polyelectrolyte. Represented as Poly (DMAEMA.CH_3Cl).

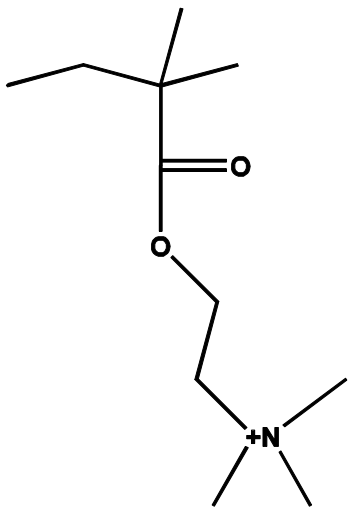


Figure1: Chemical structure of Poly (dimethylaminoethylmethacrylate CH_3Cl) used in this study.

Poly (DMAEMA.CH_3Cl)-SDS complexes were prepared at room temperature in D_2O. In this case both the surfactants and the polyelectrolyte contribute to the total scattering. In order to contrast match the surfactants complexes were prepared with dSDS in D_2O. In this case the polyelectrolyte alone contributes to the total scattering. Thus any change in the conformation of the polyelectrolyte chain can be readily observed.

Achievements and Main Results

SANS scattering curves of pure Poly (DMAEMA.CH_3Cl) and the Poly (DMAEMA.CH_3Cl)-SDS complexes in different contrasts are shown in figure 2. The peak at low q range, in the case of pure polyelectrolyte, is a consequence of electrostatic interaction between the chains. The change in the chain conformation upon addition of surfactant is observed in the case where the surfactant is contrast matched. Here a small peak is noted in the high q range. This indicates that the polyelectrolyte chain is interacting at larger q range (or smaller distances) in presence of surfactant. This interaction is due to well ordered structures adopted by the polyelectrolyte chain in presence of surfactant. However it is not possible to comment on what structure, for example lamellar, hexagonal, the polyelectrolyte adopts in presence of surfactant. For this additional SAXS measurements are needed.

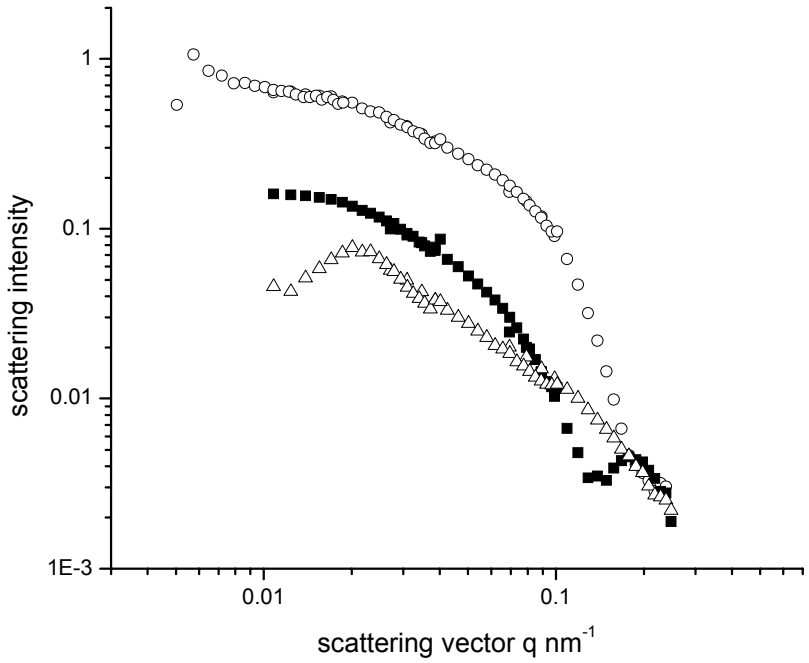


Figure 2: Effect of addition of 4 mM SDS to 0.2 % Poly (DMAEMA:CH_3Cl): only polyelectrolyte(Δ); in presence of 4 mM SDS in D_2O (○); in presence of 4 mM dSDS in D_2O (■)

References

(1) Chen, L. Y., S.; Kagami,Y.; Gong,J.;Osada,Y. *Macromolecules* 1998, *31*, 787.
(2) Hansson, P. *Langmuir* 1998, *14*, 4059.
(3) Juha, m. T., mika; Ikonen,Teemu; Serimaa, Ritva; Stenius, Per. *Macromolecules* 2001, *34*, 2937.

GKSS FORSCHUNGSZENTRUM in der HELMHOLTZ-GEMEINSCHAFT	EXPERIMENTAL REPORT	GeNF SANS-1

Study of the magnetic scattering in magnetic fluids and solids: dilute samples

Proposer:	**Régine Perzynski,** [1]LI2C, UPMC, UMR 7612 CNRS-UPMC-ESPCI, case 51, 4 place Jussieu, 75005 Paris, France
Co-Proposers:	**Emmanuelle Dubois,** [1] **Vasyl Haramus,** [2]GKSS
Experimental Team:	**Guillaume Mériguet [1], Elie Wandersman [1],**
User Group Leader:	**Michael Avdeev [3]** Joint Institute for Nuclear Research, Frank Laboratory of Neutron Physics, 141980 Dubna, Moscow region, Russia
Date(s) of Experiment:	13–24 June 2005

Objectives

The intensity scattered by magnetic fluids, which are dispersions of magnetic nanoparticles in a liquid, is the sum of the magnetic scattering I_M and the nuclear scattering I_N. With the aim of studying the structure of concentrated samples, dilute samples have been analyzed in order to separate and determine the magnetic and the nuclear contributions. Once separated, their contrasts can be determined, as well as the nuclear and magnetic sizes of the nanoparticles, and the contribution to the intensity of the stabilizing species adsorbed on their surface.

Experiment

Measurements have been performed on a biocompatible magnetic fluid, both on dilute and concentrated dispersions. They are constituted of maghemite (γ-Fe_2O_3) nanoparticles dispersed in water with a diameter d=8.3 nm and a polydispersity σ = 0.35 in order to obtain stable solutions with high enough magnetic dipolar interaction for concentrated samples. Citrate molecules adsorbed on the surface of the particles ensure a negative charge at pH = 7, thus an electrostatic stabilization of the biocompatible colloidal solutions.

The present report deals with the results on dilute samples. In this system, the nuclear scattering I_N can be modified by changing the nature of the solvent, and the magnetic scattering I_M is constant. I_N is high in H_2O and low in D_2O, however difficult to estimate precisely in D_2O because the contrast of maghemite is close to the contrast of D_2O, which introduces a large error. Moreover, in D_2O, I_N could be strongly influenced by the hydrogenated citrate shell around the particles, the contribution of which is also very difficult to estimate. Due to the complexity of the problem, we coupled two kinds of measurements: (i) polarized neutrons on samples with large proportions of D_2O and (ii) contrast variation with non polarized neutrons. The volume fraction of all the dispersions studied here was 1 %.

The measurements with polarized neutrons in D_2O allow separating I_N and I_M. Indeed, for such a dilute sample, the intensity scattered is only due to the shape of the particle and not to the structure, because the interparticle interactions are negligible, both without and with a magnetic field (1T here). The two contributions extracted are plotted in Figure 1 as well as the nuclear signal in H_2O. It shows that in D_2O $I_N \sim 0.2\ I_M$ although we expected $I_N \sim I_M$ from calculated estimations. It means that I_M dominates the signal in D_2O. In this system, the intensity is very low, therefore the nuclear signal is difficult to extract and very noisy. From these form factors, 2 mean radius of gyration can be determined: $R_{g\,N}$ = 11 ± 0.5 nm and $R_{g\,M}$ = 7.9 ± 0.5 nm. The shape of the nuclear signal in D_2O is the same as the shape of the nuclear signal in H_2O ($I_{N\,H2O}$ scaled by a constant is plotted as a solid line in Figure 1), which means that the contribution of the citrate molecules is negligible in D_2O.

The contrast variation (x_{D2O} = 0, 0.7, 0.8, 0.9, 0.95, 1) with non-polarized neutrons confirms these conclusions. In H_2O, the nuclear signal dominates while in D_2O, the magnetic signal dominates. The influence of the citrate molecules appears negligible in D_2O and the magnetic and nuclear sizes are clearly different. The apparent radius of gyration is plotted as a function of the fraction of D_2O in Figure 2. It shows that it decreases for large D_2O contents. In H_2O, the value of R_g corresponds to the mean nuclear size: $R_{g\,N}$ = 10 ± 0.5 nm and, in D_2O, it corresponds to the mean magnetic size $R_{g\,M}$ = 7.5 ± 0.5 nm, with the hypothesis that the nuclear signal is negligible in D_2O.

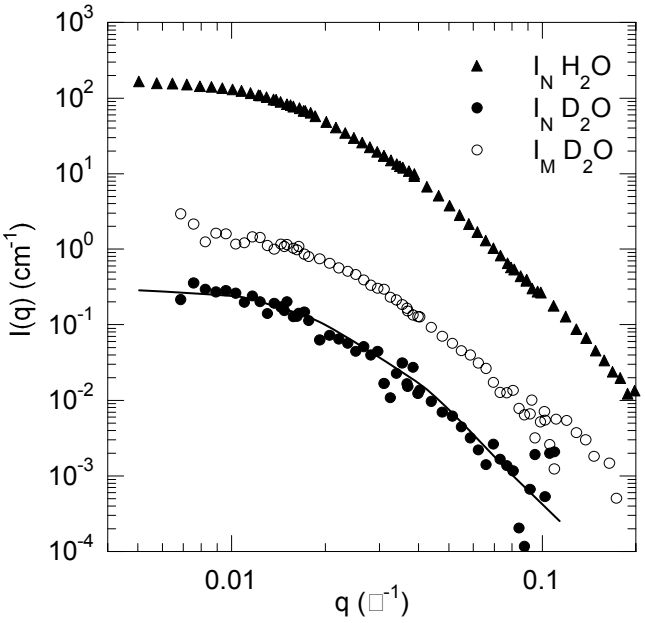


Figure 1: Nuclear scattered intensity in H_2O and D_2O, and magnetic scattering in D_2O obtained from measurements with dilute dispersions (Φ = 1 %).

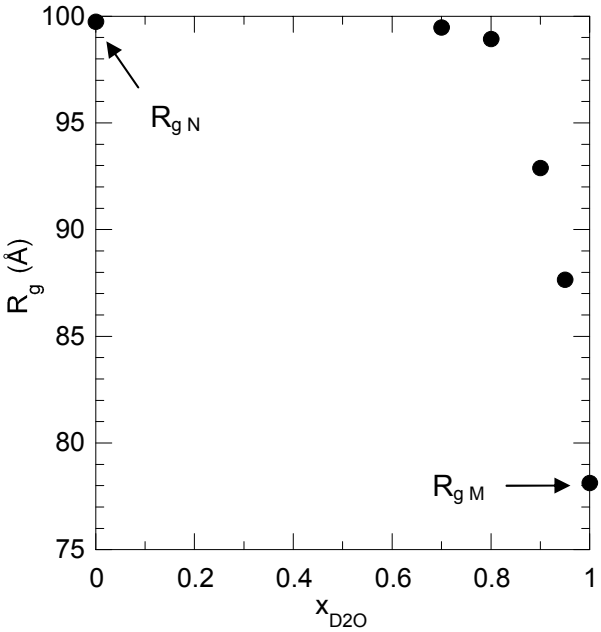


Figure 2: Mean radius of gyration R_g as a function of the fraction of D_2O for dispersions with Φ = 1 % (non-polarized neutrons).

Achievements and Main Results

We performed a very careful and precise analysis of the dilute samples of maghemite nanoparticles in water, which allowed determining the magnetic and the nuclear form factor, the intensity and shape of which could not be evaluated from calculation. The analysis of these form factors using the method described by Glatter [1] proves that the particles are roughly spherical and well dispersed in the liquid. The magnetic size is smaller than the nuclear one, which can be explained by the existence of a non-magnetic shell on the surface of the nanoparticles. Such a shell has also been evidenced by its strong influence on the magnetic properties of the nanoparticles, in particular their magnetic anisotropy energy [2,3]. The results also show that the magnetic signal can be neglected up to a fraction of D_2O around 75 %, which is very interesting for the study of many mixed systems, i.e. maghemite nanoparticles dispersed with polymers or surfactants for example. Indeed, while matching the polymer or surfactant, the scattering of the particles is nuclear and can be used to probe the structure of the systems.

References

[1] O. Glatter, J. Appl. Cryst. 13, 7 (1980)
[2] F. Gazeau et. al, EuroPhys. Lett. 40,575 (1997)
[3] F. Gazeau et. al, J. Magn. Magn. Mat. 186,175 (1998).

GKSS FORSCHUNGSZENTRUM in der HELMHOLTZ-GEMEINSCHAFT	**EXPERIMENTAL REPORT**	**GeNF SANS-1**

Study of the magnetic scattering in magnetic fluids and solids: concentrated samples

Proposer:	**Régine Perzynski,** [1]LI2C, UPMC, UMR 7612 CNRS-UPMC-ESPCI, case 51, 4 place Jussieu, 75005 Paris, France
Co-Proposers:	**Emmanuelle Dubois,** [1] **Vasyl Haramus,** [2]GKSS
Experimental Team:	**Guillaume Mériguet** [1]**, Elie Wandersman** [1]**,**
User Group Leader:	**Michael Avdeev** [3] Joint Institute for Nuclear Research, Frank Laboratory of Neutron Physics, 141980 Dubna, Moscow region, Russia
Date(s) of Experiment:	13–24 June 2005

Objectives

The intensity scattered by magnetic fluids, which are dispersions of magnetic nanoparticles in a liquid, is the sum of the magnetic scattering I_M and the nuclear scattering I_N. Our aim here is to determine the magnetic and nuclear structure factors S_M and S_N in concentrated samples, both without and with an applied magnetic field. Using high volume fractions of magnetic material allows maximizing the magnetic dipolar interactions between nanoparticles, while the global interactions can be varied from repulsive in average to attractive in average, keeping monophasic samples [1].

Experiment

Measurements have been performed on a biocompatible magnetic fluid, both on dilute and concentrated dispersions. They are constituted of maghemite (γ-Fe_2O_3) nanoparticles dispersed in water with a diameter around 10 nm in order to obtain stable solutions with high enough magnetic dipolar interaction for concentrated samples. Citrate molecules adsorbed on the surface of the particles ensure a negative charge at pH = 7, thus an electrostatic stabilization of the biocompatible colloidal solutions. This repulsive interaction can be tuned by the concentration of citrate molecules free in the solution, which controls the ionic strength.

The present report deals with the results on concentrated samples. In this system, the nuclear scattering I_N can be modified by changing the nature of the solvent, and the magnetic scattering I_M is constant. I_N is high in H_2O and low in D_2O. Four solid samples have been studied, with attractive or repulsive interactions, both in H_2O or D_2O in order to modify the ratio I_N/I_M (see Table 1). Measurements have been done with non-polarized neutrons (H=0) and polarized neutrons (H = 1 T).

Solvent	Volume fraction Φ	$[Citrate]_{free}$ (mol/L)	Potential
H_2O	0.22±0.013	0.01	repulsive
D_2O	0.24±0.013	0.01	repulsive
H_2O	0.29±0.017	0.5	attractive
D_2O	0.295±0.017	0.5	attractive

Table 1: characteristics of the samples measured.

Figure 1 shows the effective structure factors determined by dividing the intensity scattered by these samples by the intensity scattered by dilute samples, i.e. with negligible interactions, in the same solvent. As they are obtained with non-polarized neutrons, I_N and I_M are mixed. From measurements with polarized neutrons, thus with H = 1T, we can separate the different contributions and obtain: $I_N^{//}$, $I_N^{\perp}$ and $I_M^{\perp}$. Figure 2 shows, as an example, a repulsive solid in D_2O: this is the raw analysis, which reveals several difficulties of the treatment. Indeed, due to the method of preparation of these concentrated samples, several percent of

H_2O remain and, as the contrast of maghemite is very close to the contrast of D_2O, this induces a drastic variation of I_N compared to a sample in pure D_2O (like the dilute one). Moreover, the signal is low and the error bars are large. However, some qualitative and very interesting conclusions can be drawn yet.

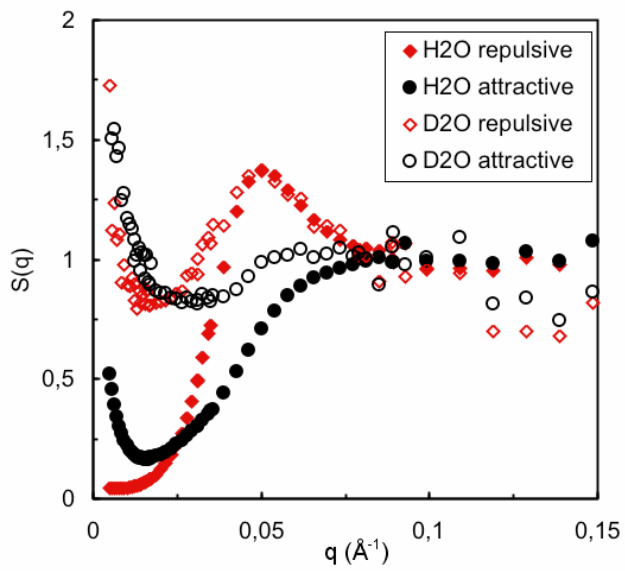


Figure 1: Effective structure factors for the 4 samples of Table 1. Non-polarized neutrons, H=0.

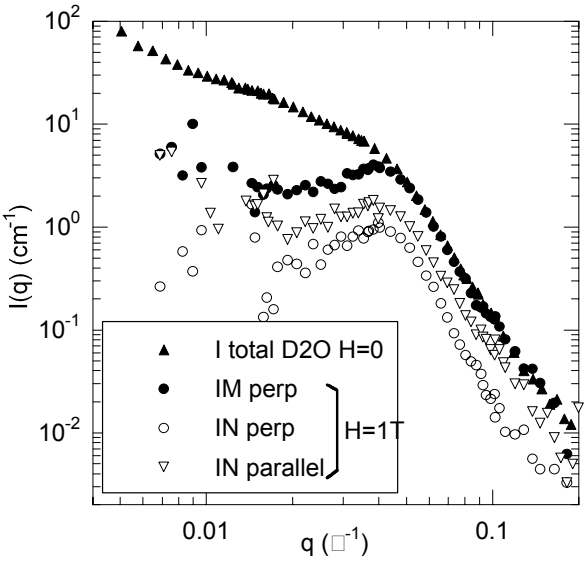


Figure 2: Scattering of the repulsive solid in D_2O. I total D_2O H=0 : non-polarized neutrons (H=0). Other curves: analysis of the data with polarized neutrons (H=1T).

Achievements and Main Results

The measurements with polarized neutrons allow concluding that the nuclear signal is dominant in H_2O, and that it is smaller than the magnetic signal in D_2O. Therefore, in H_2O, the effective structure factors (H=0, Figure 1) are close to the nuclear ones. For repulsive solids, there is a peak corresponding to the most probable distance of the first neighbouring particle (d ~ 125 Á here, in good agreement with the volume fraction) and a low compressibility. On the contrary, for attractive solids, this peak disappears and the compressibility is much higher. In D_2O, the magnetic signal is not negligible and strongly modifies the effective structure factor, especially at small q, indicating that $S_M(q)_{H=0} \neq S_N(q)_{H=0}$.

The comparison of the data without and with field is also very interesting. In Figure 2, the three components extracted using polarized neutrons signal are very different from the global intensity in D_2O and H=0. The equivalent sample in H_2O proves that this difference cannot be attributed to the modification of I_N, thus of the nuclear structure factor, under magnetic field. Consequently, this means that this difference comes from I_M and that $S_M(q)_{H=0} \neq S_M(q)_{H=1T}$.

These results constitute the first study of attractive and repulsive solids based on aqueous magnetic fluids with large magnetic dipolar interactions, both without and with magnetic field. Although the results remain rather qualitative here, we prove that $S_M(q)_{H=0} \neq S_M(q)_{H=1T}$ and that $S_M(q)_{H=0} \neq S_N(q)_{H=0}$. This can be the origin of the unexplained results that we observed in H_2O under field with neutrons in such samples. The treatment will be improved to reach quantitative results, however X-Rays measurements (no magnetic signal) are necessary in order to exploit them at the maximum (we applied for beamtime at ESRF, France).

Reference

[1] F. Cousin, E. Dubois, V. Cabuil, Phys. Rev. E 68, 021405-1 to 9 (2003)

GKSS FORSCHUNGSZENTRUM in der HELMHOLTZ-GEMEINSCHAFT	**EXPERIMENTAL REPORT**	**GeNF SANS-1**

Solution Conformation of comb copolymers containing different degree of graft PEO and its interaction with the anionic detergent (SDS)

Proposer:	**Per Claesson**[1], [1]Chemistry Department, KTH, Stockholm, Sweden
Co-Proposers:	
Experimental Team:	**Joseph Iruthayaraj[1], Luis Bastardo Zambrano[1]**
User Group Leader:	**Per Claesson**
Date(s) of Experiment:	3–9 July 2005

Objectives

Polymer-surfactant interactions play a key role in diverse applications ranging from many consumer products to drug release processes. Hence the study of their interactions has always been a subject of both academic and application interest. Association between PEO homopolymers and the anionic surfactant (SDS) is well characterised using range of techniques from tensiometry to sum frequency spectroscopy[1-3]. In this study the solution conformation of methacrylate based comb copolymers containing varying degree of PEO side chains (or equivalently varying degree of charged groups) and its interaction with the anionic surfactant (SDS) were elucidated using SANS. Results for four comb polymers, uncharged (100 % PEO side chains), and 25 % charged (75 % PEO side chains), 50 % charged (50 % PEO side chains) and 75 % charged (25 % PEO side chains) are summarized below. The main objectives of this work can be delineated as follows: i) to study the solution conformation adopted by the comb copolymers, containing different degrees of PEO side chains and positively charged groups (quarternized ammonium groups) along the back bone. ii) to study the interaction between the anionic surfactant, SDS, and the comb copolymers of varying PEO side chain density.

Experiment

The comb copolymer consists of two monomer types, one with long PEO (Mw 2000 g/mol) side chains attached to methacrylate backbone, the other with a positively charged quartnized ammonium group attached to methacrylate backbone. The structure of the polymer is shown in Figure 1. The ratio of PEO side chains to the charged groups were systematically varied during the synthesis providing a series of comb polymers containing different percentage of PEO side chains and charged groups.

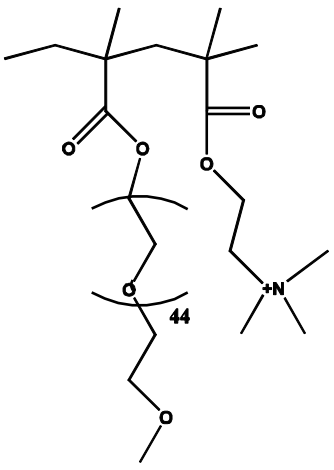


Figure 1: General chemical structure of the comb copolymers used in this study. Different copolymers vary in the percentage content of PEO and charged groups. The segment distribution is random.

SANS measurements were performed for comb copolymers of different PEO graft density (or charge densities) both in D_2O and in presence of 100mM $NaNO_3$. Association of SDS to the comb polymers were studied by performing the measurements under various contrasts using appropriate ratios of H_2O/ D_2O mixture and dSDS. All measurements were performed at 25 ^{0}C.

Achievements and Main Results

SANS scattering curves of comb polymers of varying PEO density (or equivalently varying charge density) is shown in Figure 2. The curves resemble each other up to 25 % charge density. Above 25 % charge density there appears a peak in the low q- range, corresponding to charge interaction between the polymer chains. The structure adopted by the low charge density comb polymers (<25 %) in solution is dictated by the repulsions of the PEO side chains where as for higher charge densities (>25 %) repulsion between the charged groups also make a significant contribution.

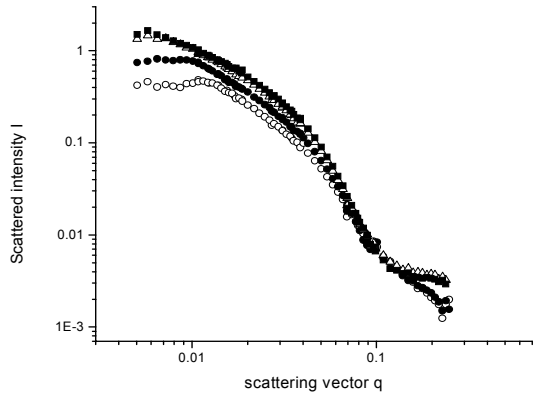


Figure 2: Effect of increasing the charge density (or equivalently decreasing PEO graft) of the comb polymer on solution conformation: un-charged (■); 25 % charged (Δ); 50 % charged (●); 75 % charged (○).

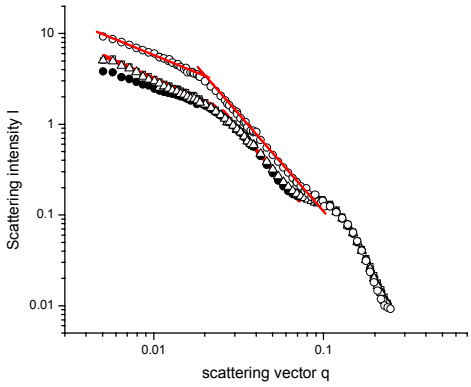


Figure 3: Scattering in presence of 18mM SDS in D_2O for comb copolymers of different charge density: uncharged (●), 10 % charged (□), 25 % charged (Δ) and 75 % charged (○).

SANS scattering curves of comb copolymers of varying PEO density (or equivalently varying charge density) in presence of 18mM SDS in D_2O is shown in figure 3. In this case both the polymer and the surfactant contribute to the total scattering. The slopes in the q-range 0.02–-0.06 are the same (-2.2) for uncharged to 25 % charged. For 75 % charged the scattering is linear over a broader q-range (0.018–0.1) with a slope of -2.03. A small hump seen at higher q-values can be interpreted as being due to surfactant micelles associated with the polymer.

References

(1) Schwuger, M. J. Journal of colloid and interface Science 1973, 43, 491.
(2) Cabane, B. The Journal of Physical Chemistry 1977, 81, 1639.
(3) Michael, T. L., Casford., Paul Davies. Langmuir 2003, 19, 7386.

GKSS FORSCHUNGSZENTRUM in der HELMHOLTZ-GEMEINSCHAFT	**EXPERIMENTAL REPORT**	**GeNF SANS-1**

Protonation-Induced Vesicle Formation in di-n-Decylmethylamine Oxide Surfactant

Proposer: **Co-Proposers:**	**Hideya Kawasaki**[1] Department of Chemistry, Faculty of Science, Kyushu University, Hakozaki Higashi-ku, Fukuoka 812-8581 JAPAN
Experimental Team:	**Vasyl Haramus**[2], [2]GKSS Research Centre
User Group Leader:	**Hideya Kawasaki**
Date(s) of Experiment:	1–14 August 2005

Objectives

We newly synthesized a double-tailed surfactant, di-n-decylmethylamine oxide (DDMAO) to examine the electrostatic effect on the spontaneous formation of unilamellar vesicles (ULV) in the aqueous media. The DDMAO surfactants exist as either a nonionic or cationic (protonated form) species depending on the pH of the aqueous solutions. In this study, we have performed the SANS measurements for the DDMAO solutions as a function of the degree of protonation (α) of DDMAO, and the surfactant concentration C (1 mM < C < 300 mM) to obtain the structural information on the DDMAO vesicles (e.g. vesicle size, bilayer thickness, and polydispersivity).

Experiment

Sample preparation: DDMAO surfactants were synthesized from di-n-decylmethylamine (Kanto Chemical Co.) through the oxidation in ethanol by hydrogen peroxide following, in most part, the similar procedure as for other alkyldimethylamine oxides [1], and they were purified by the extraction of the unreacted amine with hexane and recrystllized two times from hot acetone. The purity of DDMAO samples was confrimed by H^1-NMR(>98 % in purity). Samples of different degree of protonation (α) were prepared as follows: the prescribed amounts of DCl in D_2O(99.9% in purity) were added to the nonionic DDMAO solution in D_2O. Upon protonation of the DDMAO solution, the spontaneous formation of vesicles was took place in the α range ($0.05<\alpha<0.2$) at C = 10 mM.

Results: Figure 1 shows SANS profiles of DDMAO solutions (α = 0.2) at different concentrations. Samples with C > 100 mM exhibit Bragg maxima, which is typical of a lamellar phase (L_α). The lamellar repeat distance *d* varies linearly with the changes in C, from 176 Å to 727 Å with decreasing concentration from C = 300 mM to C = 100mM. In contrast, the scattering profiles for C < 75 mM do not exhibit sharp Brags peaks, with the scattering intensity decaying as q^{-2} over the q range from 0.02 to 0.1 $Å^{-1}$. This is consistent with the form factor of locally flat, sheet-like objects such as bilayers of ULV. The weak oscillatory behaviour in the scattering patters indicates that the ULV are polydisperse. The bilayer thickness δ is almost independent of C, which is estimated to be 21 ± 1 Å with the analysis by IFT for the vesicle phase (plane approximation). At a low concentration of C = 1 mM, the scattering profile do not show the q^{-2} dependence and the scattering intensity remarkably decreases, indicating a large change in the morphology of the DDMAO self-assembly. It is likely that micelle–to-vesicle transition occurs around C = 1 mM.

The fact that these scattering profiles are almost no change in the whole concentration range from 2 mM to 75 mM except for low q rage indicates that the ULV are highly stable over the wide concentration range. These results are contrast to another charged double-tailed surfactant systems such as di-n-decyldimethylammonium bromide (DDAB), where the dominant structures of DDAB vesicles are mutilamellar, and the ULV are stable only in the very low surfactant concentration less than 1 mM [2,3,4]. Preliminary our results indicated that the size of DDMAO vesicles(C =10 mM, α = 0.2) was no change for periods of weeks and months by a dynamic light scattering (DLS), suggesting the high stability of DDMAO vesicles for a long time. In addition, it was also found that the ULV are stable in the temperature change between 25 °C and 50 °C.

Salt concentration and the α values both dramatically changed the stability of the ULV (C=10 mM). In the a range ($0.05 < \alpha < 0.3$), the scattering profiles show the q^{-2} dependence characteristic for the ULV. In the α more than 0.4, however, the phase separation occurs. The addition of NaCl salt (5 mM) also induced the phase separation for the DDMAO solution at α = 0.2. These observations suggest that the high stability of the ULV is attributed to the electrostatic effect in the weakly charged membrane. Actually, some theoretical studies indicated that ionized membranes can form vesicles spontaneously when the Gaussian modulus of the membranes becomes negative for a symmetrically charged membranes, which depends on the charge density and the Debye length [5, 6].

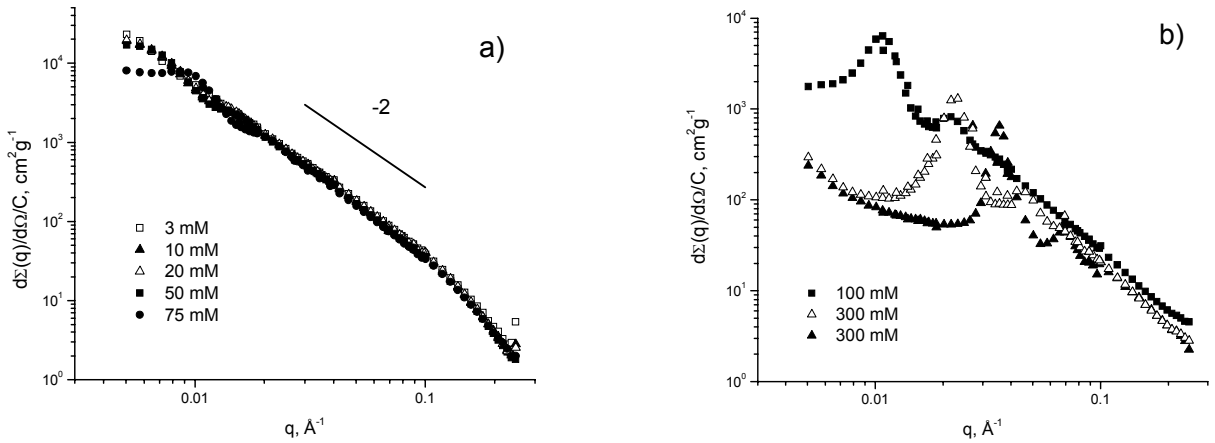


Figure 1: SANS profiles of DDMAO (α= 0.2)samples at 25 °C. (a) C = 5, 10, 20, 50 and 75 mM. (b) C = 100, 200, and 300 mM. Scattering intensities are normalized to the surfactant concentration C.

Achievements and Main Results

Spontaneously formed unilamellar vesicles (ULV) composed of a double-tailed surfactant of di-n-decylmethylamine oxide (DDMAO) were studied with small-angle neutron scattering. The size of ULV was almost independent of both *C* and T, respectively. The SANS data showed that the ULV are highly stable in the wide concentration range (2 mM < C < 75 mM) and in the temperature range T (25 °C < T < 50 °C). The electrostatic effect was found to be important factors in the stability of the weakly charged ULV.

References

[1] H. Kawasaki, M. Souda, S. Tanaka, N. Nemoto, G. Karlsson, M. Almgren, and H. Maeda, *J. Phys. Chem B,* 106, 1524 (2002).

[2] E. F. Marques, O. Regev, A. Khan, B. Lindman, *Adv. Colloid Interface Sci.,* 100-102, 83, (2003)

[3] E. F. Marques, O. Regev, A. Khan, M.D.G. Miguel, B. Lindman, *J. Phys. Chem B,* 103, 8353 (1999).

[4] Y. Ono, H. Kawasaki, M. Annaka, H. Maeda, *J. Colloid. Interface Sci.,* 287, 685(2005).

[5] W. Z. Helfrich, *Naturforsch*. 28C, 693(1973).

[6] V. Kumaran, *Phys. Rev. E*, 64, 051922(2001).

GKSS FORSCHUNGSZENTRUM in der HELMHOLTZ-GEMEINSCHAFT	**EXPERIMENTAL REPORT**	**GeNF SANS-1**

Variable contrast study of coexisting fluorocarbon-rich and hydrocarbon-rich micelles

Proposer:	**Mats Almgren,** Uppsala University, Uppsala, Sweden
Co-Proposers:	
Experimental Team:	**Vasyl Haramus,** GKSS Research Centre
User Group Leader:	**Mats Almgren**
Date(s) of Experiment:	17–25 August 2005

Objectives

Mixtures of fluorocarbon and hydrocarbon surfactants in aqueous solution either assemble to form mixed micelles, or to form coexisting populations of hydrocarbon-rich and fluorocarbon-rich micelles. In earler experiments (May 2004) we have shown that contrast variation SANS results give strong support for the demixing of micelles into hydrocarbon-rich and fluorocarbon-rich populations in solutions containing a fluorinated and a normal cationic surfactant. This is the first time such a demixing have been verified by SANS studies [1]. In present experiments the objective was to determine the width of the composition distribution of micelles in water solutions containing a mixture of a normal cationic surfactant, CPC, and a partially fluorinated surfactant, HFDePC, with the same headgroup.

Experiment

In SANS fluorinated surfactants and hydrogenated surfactants have quite different scattering length densities, and would seem to be ideally suited for contrast variation experiments in H_2O/D_2O mixtures. In earlier studies using mixtures of the cationic fluorocarbon surfactant HFDe-d-PC (N-(1,1,2,2-tetrahydroperfluorodecanyl)pyridinium chloride), with a deuterated headgroup, and a hydrocarbon surfactant with a different headgroup, cetyltrimethyl-ammonium chloride (CTAC), we have shown that a substantial residual scattering is retained at the solvent composition where the average scattering length density of mixed micelles would match that of the solvent [1, 2]. We also showed that for micelles of similar size the residual scattering is related to the width, σ, of the composition distribution.[2]

In this follow up study we have repeated the measurements using a pair of surfactants with the same headgroup, so that the non-ideallity is only affected by the differences in the hydrophobic region of the surfactants. We plan to expand the investigations in future measurements by varying the surfactant tail lengths. The (partially) fluorinated surfactant was the same as in the previous studies, and the hydrocarbon surfactant hexadecylpyridinium chloride (CPC, Merck, analytical grade). 20 mM of each surfactant was used, and to reduce the electrostatic interactions the solutions contained 63.5 mM NaCl. The contrast was varied using seven solvent mixtures with fractions of D_2O varying between 0.1 and 1.0.

Data analysis by Indirect Fourier Transformation (IFT) was performed at q>0.02 Å^{-1} where the effects of intermicellar interactions are negligible. This yields the scattering at zero angle ($d\Sigma(0)/d\Omega$) and the radius of gyration (R_g) without any presumptions regarding particle size and shape.
Figure 1 shows the scattering curves for solutions with salt in D_2O and at “match point” of mixture (38 % D_2O).

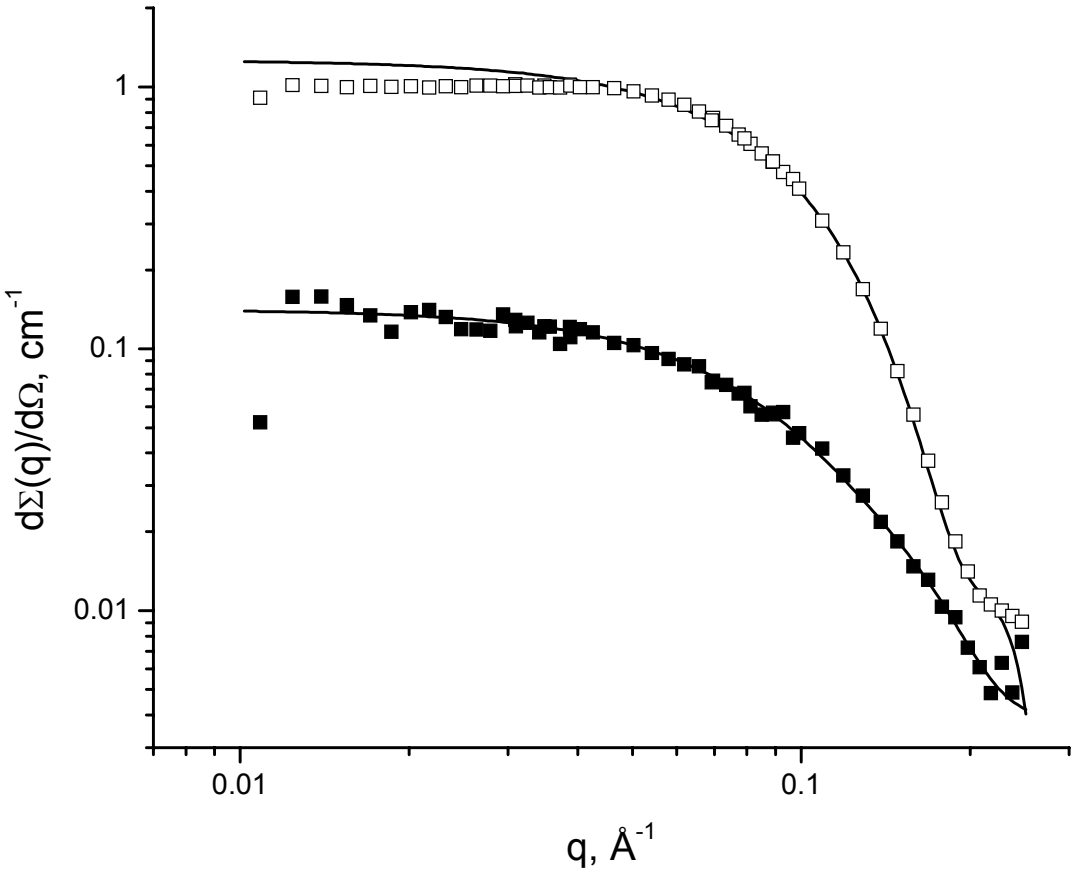


Figure 1. Scattering intensity as a function of scattering vector for samples with the same amounts of the surfactants (33 mM surfactant *in toto*). Empty symbols are solution 0.1 M NaCl in D_2O and filled symbols is solution at match point, solid lines are the fit by IFT.

Achievements and Main Results

The results from this study are in line with the previous results for a very similar system, and give little new physical insights. They will be much more interesting together with results from the planned extension to measurements on a system with shorter tail length of the hydrocarbon surfactant, dodecylpyridinium chloride instead of the hexadexyl analogue, and on a system with higher salt concentration. In the first case we expect mixed micelles that do not demix appreciably, and it is of interest to determine to what extent the milder non-ideality broadens the composition distribution. In the second case, longer micelles are expected. We shall try to find a salt concentration region where the elongation is limited (can be tested in cryoTEM investigations).

References

[1] Kadi, M.; Hansson, P.; Almgren, M.; Bergström, M.; Garamus, V. M. *Langmuir* 2004, *20*, 3933–3939

[2] Almgren M, Garamus V.M. *J. Phys. Chem. B* 2005, 109, 1138–11353.

GKSS FORSCHUNGSZENTRUM in der HELMHOLTZ-GEMEINSCHAFT	**EXPERIMENTAL REPORT**	**GeNF SANS-1**

The study of the orbital part of the magnetic scattering amplitude in the heavy-fermion compound $CeRu_2Si_2$ by means of SAPNS

Proposer:	**S.V. Grigoriev[1],** [1] Petersburg Nuclear Physics Institute
Co-Proposers:	**G.P. Kopitsa[1]**
Experimental Team:	**G.P. Kopitsa[1],V.M. Haramus[2]**, [2] GKSS Research Centre
User Group Leader:	**S.V. Grigoriev[1]**
Date(s) of Experiment:	31 August – 16 Septermber 2005

Objectives

The proposal was aimed to continue of the investigation of the neutron-carrier scattering in single crystal $CeRu_2Si_2$ at low temperatures (≈1 K) and magnetic fields H = 0 ÷ 2.5 T by means of small angle polarized neutron scattering (SAPNS) [1].

Experiment

1. Theoretical background. The theoretical studies [2–4] have shown that the orbital part of the magnetic scattering amplitude contains the term, which is singular at $q \to 0$ and gives rise the small-angle neutron scattering on the conduction electrons in metals:

$$F_{\sin g} = -i \cdot r \frac{\boldsymbol{\sigma}[\boldsymbol{q} \times \boldsymbol{p}]}{q^2} \quad , \tag{1}$$

where $r = |\gamma| e^2/mc^2 = 5.4 \cdot 10^{-13}$ cm and $\gamma = -1.91$ is the neutron g-factor; $\boldsymbol{q}$ is the momentum transfer and $\boldsymbol{p}$ is the electron momentum. It was also shown [2–4] that in metals the scattering cross section is proportional to $(m/M)^2$, where m is the effective mass of the electrons (carriers) and M is the mass of the neutron. For ordinary metals this factor is of order 10^{-5}–10^{-6} and the neutron-electron scattering is negligibly small. However for some heavy-fermion substances $m \sim 100\, m_e$ [5] and $(m/M)^2 \sim 10^{-2}$. In such cases the neutron-carrier scattering could be observed if one takes into account that the static cross section $d\Sigma(\vartheta)/d\Omega$ is proportional to ϑ^{-1} for $2E\vartheta >> T$ and $T/(\vartheta^2 E)$ for $T >> 2E\vartheta$, where $\vartheta << 1$ is the scattering angle and E is the neutron energy. The crossover from one regime to another is observed at $q_c = k \cdot \sin(T/2E)$.

Our previous experiment [1] showed presence of the additional small angle neutron scattering at low temperatures of order of 1 K. This scattering was observed at $q \le 0.04$ Å and may be attributed to the contribution of the neutron-carrier scattering to the orbital part of the magnetic scattering amplitude in this heavy-fermion system, as predicted theoretically in [4]. Moreover, it was found that the applied magnetic field results in both the increase of the scattering at $q \le 0.04$ Å and the appearance of the additional scattering at $q > 0.04$ Å. At small q the field-induced scattering is mostly anisotropic with respect to the magnetic field H while at large q scattering is isotropic and the crossover point is well described by $q_c = k \cdot \sin(T/2E)$.

2. Sample. The intermetallic system $CeRu_2Si_2$, which crystallizes in a body-centered tetragonal structure (the $ThCr_2Si_2$ structure) with lattice parameters $a = b = 4.197$ Å and $c = 9.797$ Å [6], is an archetypal heavy-fermion compound with a large value of the linear coefficient of the specific heat $\gamma = C/T \approx 350$ mJ/K^2 mol below $T \approx 1$ K [7,8]. According to data of the dHvA experiments [9,10], in this compound the effective mass of quasi-particles foot up to $\approx 200 m_e$. The large single crystal ($V \cong 0.4$ cm^3) was grown in a three-arc furnace using the Czochralski method [6].

3. Experimental Technique. In the present experiments the initial polarization $P_0 \approx 0.95$ and the wavelength $\lambda = 8.1$ Å were used. The range of momentum transfer $7 \cdot 10^{-3} < q < 2 \cdot 10^{-1}$ Å^{-1} was obtained using four sample-to-detector distances (0.7–9.7 m).
At first, the single crystal was so mounted in a criostat that the direction of crystallographic axis *c* (001) was vertical and parallel to the plane of the detector (position 1). In second position 2 of the sample the axis *c* was perpendicular to the plane of the detector and anti-parallel to direction of axis *c* in [1] (position 3). The measurements for each position of the sample were carried out at two different temperatures $T \approx 1.1$ K and $T = 290$ K. The external magnetic field *H*, produced by the magnet, was vertical directed and changed from 0 to 2.5 T.

4. Data presentation. In present experiment we found the presence of the additional small angle neutron scattering at low temperatures of order of 1 K. This scattering is weak but statistically resolved and observed at $q \leq 0.04$ Å as in [1].
The two-dimensional representations of the cross section $d\Sigma(q)/d\Omega$ of magnetic small-angle neutron scattering in magnetic field $H = 1$ T at $T = 0.9 \div 1.1$ K for various crystallographic orientations of single crystal $CeRu_2Si_2$ are presented in Fig.1.

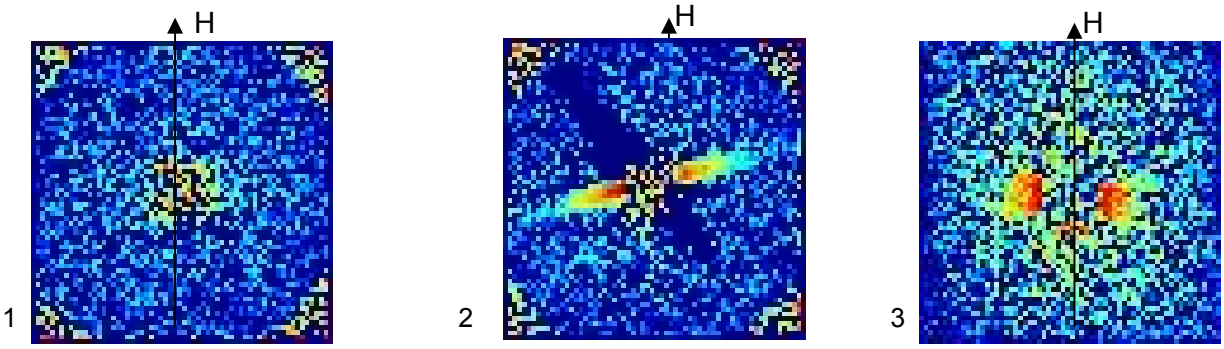


Figure 1: The two-dimensional representations of $d\Sigma(q)/d\Omega$ of SANS in magnetic field $H = 1$ T at $T = 0.9 \div 1.1$ K for various crystallographic orientations of single crystal $CeRu_2Si_2$ (see text above).

It is seen from this figure that the field induced scattering occurs if and only if the axis *c* (001) is perpendicular to the direction of the magnetic field and the plane of the detector (sample positions 2 and 3). Then axis *c* is parallel to the magnetic field *H* (position 1) this scattering is particularly absent.

5. Results. In the course of SAPNS experiment on the single crystal $CeRu_2Si_2$ at $T \approx 1.1$ K we corroborated, firstly, our results which were obtained in [1]. Secondly, it was found that the applied magnetic field results in both the increase of the scattering at $q \leq 0.04$ Å and the appearance of the additional scattering at $q > 0.04$ Å. Moreover, it was found that this scattering is depend on the crystallographic orientation of the single crystal.

References

[1] G.P. Kopitsa, S.V. Grigoriev, V.M. Garamus, V.V. Runov, S.V. Maleyev, A.D. Yashenkin, JETP Letters, Vol. 81, No. 11, 2005, pp. 556–560.
[2] R.J.Elliott, Proc.Roy.Soc. 235 A, 298 (1956).
[3] S.L.Ginzburg, S.V. Maleyev, Fiz.Tv.Tela 7, 3065(1965); Sov.Phys. Phys.Solids. 8, 2320 (1966).
[4] S.V. Maleyev, Usp. Fiz. Nauk, 172, 617 (2002).
[5] G.R. Stewart, Rev. Mod. Phys. 56, 755 (1984).
[6] L. P. Regnault, W.A. Erkelens, J. Rossat-Mignod, P. Lejay and J. Flouquet, Phys. Rev B 38, 4481 (1988).
[7] M.J. Besnus et al., Solid State Commun 55, 779 (1985).
[8] R.A. Fisher, C. Marcenat, N.E. Phillips, P. Haen et al., J. Low Temp. Phys. 84, 49 (1991).
[9] H. Aoki, S. Ujii et al., Phys. Rev. Lett 71, 2110 (1993).
[10] S.R. Julian, F.S. Tautz et al., Physica B 199–200, 63 (1994).

GKSS FORSCHUNGSZENTRUM in der HELMHOLTZ-GEMEINSCHAFT	**EXPERIMENTAL REPORT**	**GeNF SANS-1**

SANSPOL study of organic non-polar ferrofluids stabilized by mixed surfactants

Proposer: **Co-Proposers:**	**L. Vékás**[1,3], [1]Laboratory of Magnetic Fluids, CFATR, Romanian Academy, Timisoara Division, Timisoara, Romania, [3]National Center for Engineering of Systems with Complex Fluids, Univ. Politehnica, Timisoara, Romania
Experimental Team: **User Group Leader:**	**Doina Bica[1] , Oana Marinica[3] , M.V. Avdeev[2] , M.Balasoiu[4], Vasyl Haramus[5]** [2]Frank Laboratory of Neutron Physics, Joint Institute for Nuclear Research, Dubna, Russia, [4]Institute of Space Sciences, Bucharest, Romania, [5]GKSS Research Centre
Date(s) of Experiment:	27 September – 14 October 2005

Objectives

Long-term colloidal stability of magnetic nanofluids (ferrofluids), especially at high volume fraction of magnetic nanoparticles, is a complex issue connected to the synthesis procedure followed, including the nature of surfactant(s) and carrier liquids used [1]. The dimensionless coupling parameter λ, which is half the ratio of the dipolar energy of two aligned dipoles at close contact to the thermal energy, should be kept below 1 to ensure highly stable magnetic fluids. During preparation repulsive forces due to coating of magnetic cores are introduced to prevent irreversible aggregation of particles produced by attractive van der Waals and dipolar interactions. When the dipolar interactions are much stronger than the thermal energies, particle chains start growing and forming more complex structures, depending on the particle volume fraction, size distribution, temperature and magnetic field applied. An interesting feature of magnetic nanofluid synthesis is that the relative strengths and ranges of various interaction potentials can be controlled by the diameter of magnetic cores and the thickness of the surfactant layer.

Experiment

In the given experiments on the small-angle scattering of polarized neutrons (SANSPOL), non-polar organic liquid based magnetic nanofluids (MNFs) were studied, having magnetite nanoparticles coated with various chain length surfactants, such as myristic acid (MA), $C_{14}H_{28}O_2$, and oleic acid (OA), $C_{18}H_{34}O_2$, as well as their mixtures. Our previous studies revealed [2] that these fatty acids show different efficiency in dispersing different size-fractions of nanometric magnetite particles. While oleic acid is proved to be highly efficient surfactant to stabilize nanomagnetite over the wide size interval of 2–20 nm [3, 4], shorter fatty acids stabilize partially this interval dispersing in the carrier only a fraction of smaller particles. Nevertheless, it should be pointed out that the resulting nanofluids with the MA stabilization are as highly stable in strong magnetic field (up to 2.5 T in the current experiments) as the samples stabilized by OA. Taking into account that the considered surfactants are well miscible in bulk liquids, one could expect that a similar property takes place at the interface with magnetite particles. Thus, the synthesis of magnetic fluids with regulation of particle size distribution can be realized with the help of mixtures of fatty acids.

Achievements and Main Results

As the main result, our structural investigations of magnetic fluids prepared with mixtures of different fatty acids confirm this expactation and point out the fact that the characteristic size of the magnetite particles can be changed during the synthesis in the range of about 4–10 nm. The effect of tailoring the stabilizant layer thickness is illustrated in Fig.1, where the

nuclear scatettering contribution obtained from the polarization analysis under magnetic field [4] is shown for three ratios MA/OA in ferrofluids based on deuterated benzene. The volume fraction of magnetic particles in the studied systems was about 1 % to avoid effects of the interparticle interaction on the scattering. The magnetic particle size distribution function was determined from fits of the core-shell model of non-interacting particles [4].
The size regulation effect is also confirmed in complementary studies by magnetometry for wider class of fatty acids including lauric acid (LA), $C_{12}H_{24}O_2$ (Fig. 2). These findings are in agreement also with magneto-rheological investigations. All the samples show Newtonian behaviour in magnetic field, while the field induced viscosity change is rather small (up to a few percent), especially in the cases of MA and LA stabilized samples.
All these open new prospects towards the size regulation synthesis of organic non-polar ferrofluids. Taking into account that preparation of organic ferrofluids is often the first stage for producing ferrfolfuids on polar madia, current studies are of a great importance for the synthsis of polar ferroflsuids as well. We connect further developments of the SANS application in diagnostics and research of the new class of ferrfluids with the use of deuterated surfactants in the contrast variation techniqie. The aim is to realize how the surfactant are mixed at the interface with magnetite particles. For the moment, we cannot conclude about this, since all of the usual fatty acids are very close in their scatteing lenght densities.

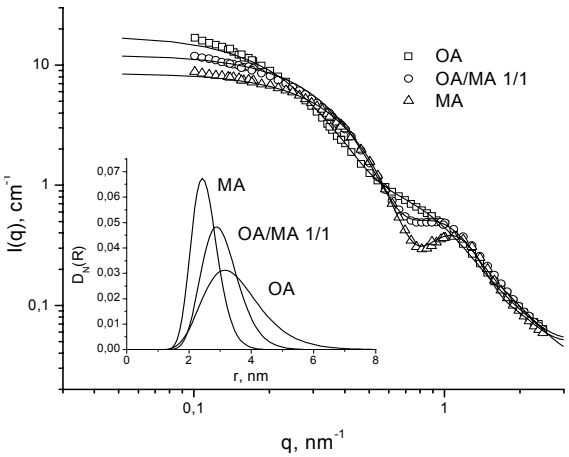


Figure 1. Nuclear scattering contributions obtained by SANSPOL analysis for 1 % d-benzene based ferrofluids stabilzied by different mixtures of fatty acids. In the inset, detemined particles size distribution function of magnetite are shown.

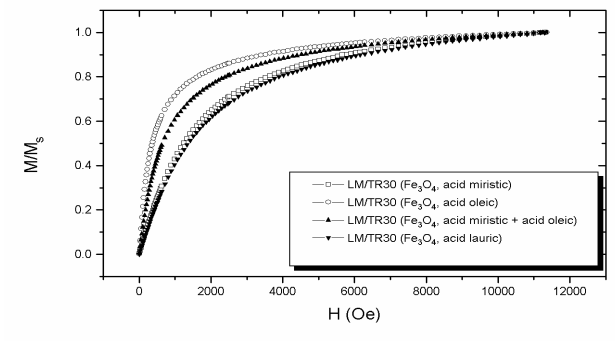


Figure 2. Relative full magnetization curves for samples of transformer oil based magnetic fluid stabilized with different chain length surfactants, LA, MA and OA.
Mixing of surfactants of different chain lengths, MA: OA = 1:1, conducted to a relative magnetization curve situated between those corresponding to samples with MA (LA) and OA monolayer, which indicate the different magnetite sizes stabilized in the fluids.

References

[1] Doina Bica, Romanian Rep. Phys., 47, No. 3-5, 265–272 (1995)
[2] L. Vekas, D. Bica, M.V. Avdeev, M. Balasoiu, V.M. Garamus, in: GeNF Experimental Report 2004, GKSS 2005/7
[3] L.Vékás, Romanian J. Phys. vol. 49, Nos. 9-10, 707–721 (2004)
[4] M.V. Avdeev, M. Balasoiu, V.L. Aksenov, V.M. Garamus, J. Kohlbrecher, D. Bica, L. Vekas, J. Mag. Mag. Mater. 270 (2004) 371–379

GKSS FORSCHUNGSZENTRUM in der HELMHOLTZ-GEMEINSCHAFT	EXPERIMENTAL REPORT	GeNF SANS-1

Conformation investigation of hen egg white lysozyme conjugated with poly(ethylene glycol)

Proposer:	**L. He[1],** [1]Centre for Biomolecular Engineering,University of Queensland, St. Lucia 4072, Australia
Co-Proposers:	**A. Middelberg[1]**
Experimental Team:	**L. He[1],**
	Vasyl Haramus[2], [2]GKSS Research Centre
User Group Leader:	**A. Middelberg**

Date(s) of Experiment:	31 October 2005 – 4 November 2005

Objectives

The aim of the proposed project is to investigate the conformation of lysozyme conjugated with poly(ethylene glycol) and comparing it with native lysozyme. PEGylated proteins have been receiving increasing attentions because of their extensive pharmaceutical and biomedical application (Tao et al., 2004). Using lysozyme as a model protein, we will study how PEGlyation changes conformations of proteins and consequently predict the related physical properties and functions.

Experiment

Hen egg white lysozyme was conjugated with PEG using mPEG-NHS (mono-methoxy-PEG-N-Hydroxy-Succinimide) reagent ME-050-CS Sunbright, and the tetra-PEGylated lysozyme (4-PEG-lysozyme) was purified from the reaction product by gel filtration chromatography column. The quartz cuvettes (2 mm path length) containing the sample solutions were placed in a thermostatted sample holder. The raw data were corrected for background contribution from the solvent and sample cell by conventional procedures. 20 mM sodium phosphate buffer prepared from D_2O and/or H_2O was used as solvent for all experiments.

Achievements and Main Results

The production method of lysozyme PEGylation has a significant effect on its behaviour in solution. The SANS data show that there was a significant amount of aggregates in the PEG-lysozyme solution prepared from its lyophilized powder (Figure 1), suggesting that a lyophilisation step can induce aggregation of PEG-lysozyme. Interestingly, a freshly prepared PEG-lysozyme without a lyophilisation step shows a typical scattering spectra of monodisperse particles. The mechanism of this interesting aggregation behaviour will be further investigated in the future study.

As mentioned in the objective section, our main purpose is to investigate the conformation of PEG-lysozyme. We have thus performed H_2O/D_2O contrast experiment, aiming to highlight the PEG part and the protein part separately. Our theoretical calculation using the literature data (Jacrot and Zaccai, 1981) has shown that a matching point of lysozyme is around 40 % D_2O. Indeed, our measurement on pure lysozyme using 40 % D_2O phosphate buffer has shown that its spectra is almost identical to that of the same buffer (data not shown). This preliminary experiment gave us confidence to perform further contrast variation experiment to elucidate the structure of this interesting molecules in future experiments. The experiments are planed to be performed in 2006 once a new beam line time is proofed.

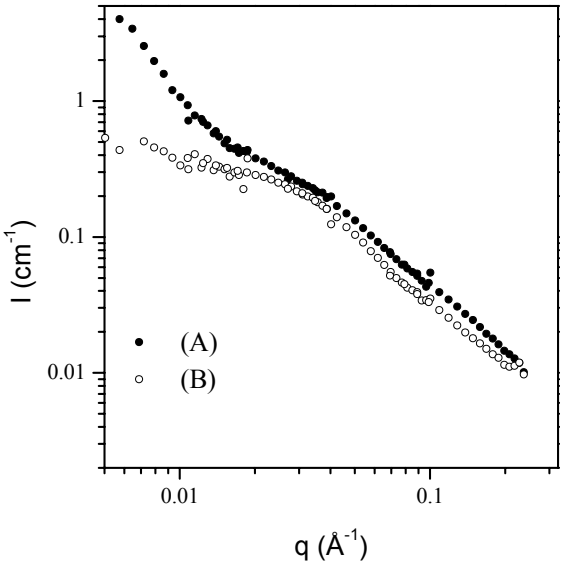


Figure 1. Comparison of scattering spectra of PEG-lysozyme prepared from lyophilized powder (A) and the freshly prepared solution without a lyophilisation step (B).

References

Tao et al. 2004. alpha-aldehyde terminally functional methacrylic polymers from living radical polymerization: application in protein conjugation “pegylation”. *JACS*, 126, 13220–13221.

Jacrot B, and G. Zaccai 1981. Determination of molecular weight by neutron scattering. *Biopolymers*, 20, 2413–2426

GKSS FORSCHUNGSZENTRUM in der HELMHOLTZ-GEMEINSCHAFT	**EXPERIMENTAL REPORT**	**GeNF SANS-1**

Comparison of conformation of new growth/adhesion-regulating effector galectin-3 and its carbohydrate-recognition domains

Proposer: **Co-Proposers:**	**L. He[1],** [1] Centre for Biomolecular Engineering,University of Queensland, St. Lucia 4072, Australia **A. Middelberg[1]** **H.-J. Gabius[2],** [2] Institute for Physiological Chemistry, Ludwig-Maximilians-University Munich, Germany
Experimental Team: **User Group Leader:**	**L. He[1],** **Vasyl Haramus[3],** [3]GKSS Research Centre **A. Middelberg**

Date(s) of Experiment:	5–12 November 2005

Objectives

The aim of the proposed project is to investigate conformation difference of full length galectin-3 and its carbohydrate-recognition domains (CRDs). We have previously shown that the purity of our preparation passes most rigorous quality control and that analysis by ultracentrifugation is not sufficently sensitive to reach our aim (Kopitz et al., 2003; Morris et al., 2004). Galectin-3 is distinct from any other, because it is composed of three domains, with only one being the lectin domain (Gabius et al., 2004). Together with SANS data of other lectins which we have already obtained (He et al., 2003), scientific outcome of this work will likely harbour relevance beyond the galectin family.

Experiment

The range of scattering vectors from 0.007 to 0.25 $Å^{-1}$ was used. In all experiments, the neutron wavelength λ was 8.1 Å with a wavelength resolution $\Delta\lambda/\lambda$, of 10 %. The quartz cuvettes (2 mm path length) containing the sample solutions were placed in a thermostated sample holder. The raw data was corrected for background contribution from the solvent and sample cell by conventional procedures. 20 mM sodium phosphate buffer prepared from D_2O was used as solvent for all experiments.

Achievements and Main Results

Most current studies on the galectin-family have focused on galectin-1 and galectin-3, which have emerged as promising molecular targets for cancer therapy (Liu and Rabinovich, 2005). Indeed, NH_2-terminally truncated form of galectin-3 (CRDs) is efficacious for reduction in tumor growth and inhibits metastasis in an orthotopic nude mouse model of human breast cancer (John et al., 2003). In this work, we first investigated the CRD of human galectin-3, which was produced from the full length galectin-3 by removing the collagenase-sensitive tandem repeat part at its N-terminal. The pair distance distribution function (*p(r)* function) of truncated galectin-3 resulted from its scattering spectra is compared with that of the full length human galectin-3 (Figure 1). The truncated galectin-3 shows a typical *p(r)* function of a spherical particle. The *p(r)* function of the full length one shows a shape feature of a spherical particle connecting with a rod, suggesting that the tandem repeat part of the galectin-3 may have a rode like shape.

Encouraged by this finding, we further measured the scattering spectra of mouse galectin-3 in the presence and absence of its ligand. No significant change of scattering induced by the ligand has been observed, which is similar to the behaviour of human galectin-3. Compared to human galectin-1 that we studied before, they differ in the extent of the ligand effect on their conformation. We have also studied the spectra of phosphorylated gal-3 which is reported to loose its carbohydrate-binding activity, although the phosphorylation site in the N-terminus is far from the C-terminal CRD in sequence. However, due to the extreme difficulty to obtain a large amount of phosphorylated gal-3, the spectra measured at a low concentration of the protein do not give us a clear information on its shape.

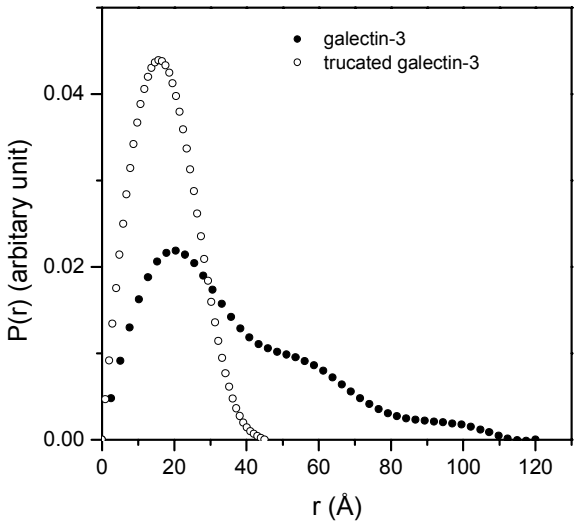


Figure 1.
Comparison of p (r) function of full length and truncated galectin-3.

References

Gabius HJ, Siebert HC, Andre S, Jimenez-Barbero J, Rudiger H. 2004. Chemical biology of the sugar code. Chembiochem 5(6):741–764

He LZ, Andre S, Siebert HC, Helmholz H, Niemeyer B, Gabius HJ. 2003. Detection of ligand- and solvent-induced shape alterations of cell-growth-regulatory human lectin galectin-1 in solution by small angle neutron and x-ray scattering. Biophysical Journal 85(1):511–524

John CM, Leffler H, Kahl-Knutsson B, Svensson I, Jarvis GA. 2003. Truncated Galectin-3 Inhibits Tumor Growth and Metastasis in Orthotopic Nude Mouse Model of Human Breast Cancer. Clin Cancer Res 9(6):2374–2383

Liu FT, Rabinovich GA. 2005. Galectins as modulators of tumour progression. Nature Reviews Cancer 5(1):29–41

GKSS FORSCHUNGSZENTRUM in der HELMHOLTZ-GEMEINSCHAFT	EXPERIMENTAL REPORT	GeNF SANS-2
Small-angle scattering instrument SANS-2		

SHORT INSTRUMENT DESCRIPTION:

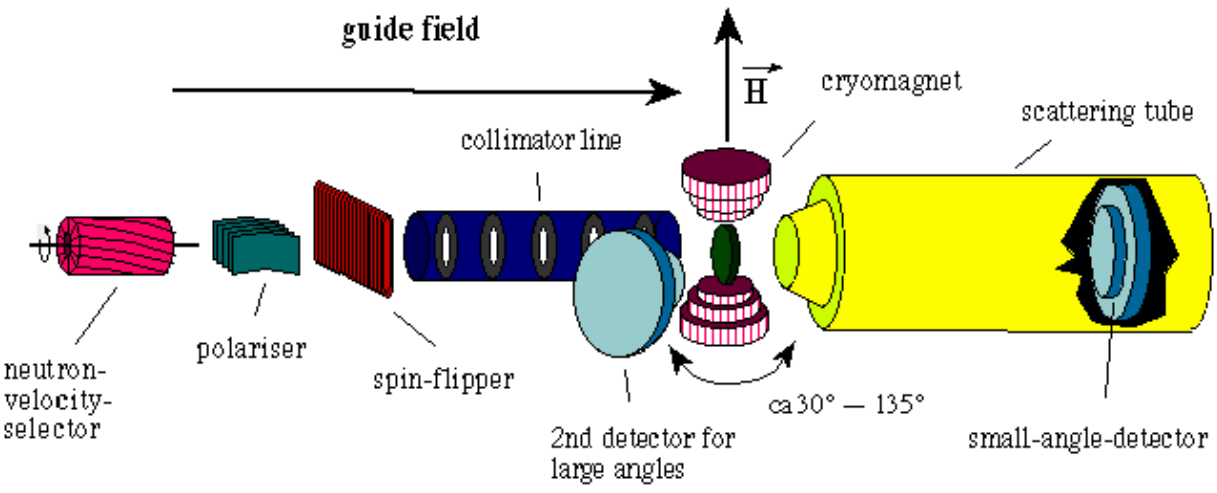
Small angle neutron scattering using cold non-polarised/polarised neutrons is a powerful tool for investigating the structure of matter in the range between 1 and 100 nm. It is a non destructive method for a wide range of application in:
– Metal physics (precipitates, clusters, interfaces, grain boundaries,...)
– Materials science (defects, porosity,....)
– Nanocrystalline materials (grain size, magnetic structures,...)
– Polymers and polymer systems (blends, mixtures, structure and morphology,...)
– Biology (viruses, proteins,...)
– Complex liquids (microemulsions, colloids, liquid crystals,...)

Local Contact:

HELMUT ECKERLEBE
Phone/Fax : +49 (0)4152 87 – 1202 / +49 (0)4152 87 – 1338
e-mail: helmut.eckerlebe@gkss.de

Dr. P. Klaus Pranzas
Phone/Fax : +49 (0)4152 87 – 1326 / +49 (0)4152 87 – 1338
e-mail: pranzas@gkss.de

SCHEMATIC VIEW OF SANS-2:



INSTRUMENT DETAILS:

Beamline:	beamline 8 – cold neutron guide NG-2, radius of curvature R = 900 m, cross section 3 x 4 cm^2
Monochromator:	helical slot velocity selector (Dornier)
Wavelength range at sample position:	0.3 to 2.0 nm
Wavelength resolution:	$\Delta\lambda/\lambda$ = 0.1 (2 additional velocity selectors with $\Delta\lambda/\lambda$ = 0.05 and 0.2 available)
Length of collimation:	max. 16 m (2 m elements)
Flux at sample position:	$\Phi_{max} = 2 \cdot 10^7$ cm^{-2} s^{-1} (1 m collimation, λ = 0.5 nm)
Range of momentum transfer:	$0.01 \leq q \leq 3$ nm^{-1} (small-angle scattering) $q \leq 25$ nm^{-1} (wide-angle scattering with 2. detector)
Distance sample to detector:	1.0 m ≤ d ≤ 22 m optional 2. detector for wide angles: d = 1 m
Detector: active area: resolution: background:	2-dim position-sensitive ^{3}He-counter 50 x 50 cm^2 0.25 x 0.25 cm^2 < 0.5 cps
Supplementary equipment:	– several electro-magnets up to 2.0 T (horizontal and vertical fields) – superconducting magnet up to 5.0 T – cryostats (8–300 K) – furnace (-30 °C to +400 °C, atmospheric condition, inert gas and vacuum) – linear translation, rotary, tilting and lift tables (freely programmable sample position) – "HOLONS": holographic combined with SANS setup (see table A)
Special features:	– Sample environment space is variable from a few mm up to 2500 mm – User-friendly software for data reduction and evaluation running on PC (SANDRA a. o.)

GKSS FORSCHUNGSZENTRUM in der HELMHOLTZ-GEMEINSCHAFT	**EXPERIMENTAL REPORT**	**GeNF SANS-2**

The precipitation sequences of a novel steel during varied heat treatments

Proposer:	**Michael Bischof [1], Helmut Clemens [1]**
Co-Proposers:	[1]Montanuniversität Leoben, Department of Physical Metallurgy and Materials Testing, Leoben, Austria **P. Staron [2],** [2] GKSS Research Centre
Experimental Team:	**P. Klaus Pranzas[2], Helmut Eckerlebe[2], Gerhard Kozik[2]**
User Group Leader:	**Michael Bischof [1]**
Date(s) of Experiment:	April and September 2005

Objetives

SANS measurements along with transmission electron microscopy (TEM) and atom probe field ion microscopy (APFIM) were successfully used to study the precipitation sequence of a novel tool steel which is age hardening by secondary hardening carbides and intermetallic NiAl precipitates [1]. However, additional measurements had to be made in order to fully characterize the precipitation behaviour. Furthermore, measurements have been performed to characterize scattering effects which are possibly caused by the magnetic microstructure of the material.

Experiment

In order to fully characterize the precipitation behaviour of the steel described in [1], two different kinds of heat treatment have been performed.

One set of samples was annealed isothermally at a temperature of 610°C for times ranging from 0 min to 10000 min. Thereby, an annealing time of 0 min means that the sample was heated up rapidly to the target temperature and immediately quenched to room temperature. The quenching rate λ was chosen as 0.3 for all samples, what means that the theoretical cooling time from 800 to 500 would have been 30 sec.

A second set of samples was annealed isochronally to target temperatures between 450°C and 750 °C. The heating rate was chosen as 20 K/min and λ for the subsequent cooling process was again 0.3.

Prior to annealing all samples were austenitised at 990 °C for 30 min and subsequently quenched with λ 0.3. All heat treatments were performed on a quenching dilatometer which enables setting very reproducible time-temperature sequences.

Additionally, two samples of the steel described in [2] have been prepared to study the influence of retained austenite and possible scattering due to a inhomogenous magnetisation of the martensitic matrix, e.g. due to dislocations. Both samples were quenched from an austenitising temperature of 1060 °C to room temperature and one of the samples was additionally annealed at 300 °C for 3 x 1 h. SANS measurements were performed on both samples, whereas the quenched-only sample was subsequently cooled in liquid nitrogen and measured again.

Specimens for SANS-measurements were prepared by cutting discs of 1 mm and 0.3 mm from the heat treated rods. All measurements were carried out at the SANS-2 facility at GKSS. Scattered neutrons were detected by a position-sensitive detector with a resolution of

256x256 pixels. Four detector distances (1 m, 3 m, 9 m and 21 m) were used with appropriate apertures and collimators to cover scattering vectors Q from 0.025 nm^{-1} to 2.5 nm^{-1}. The measurements were performed using neutrons at a wavelength of λ=5.8 nm and a wavelength spread of $\Delta\lambda/\lambda$=10 %. The neutron beam impinging on the samples had a diameter of 3 mm. The samples were magnetized to saturation in a field of 2 T. Measured intensities were corrected for sample transmission, background and detector efficiency. The nuclear cross sections were measured at azimuthal detector angels of α=0° and 180°, while the sum of nuclear and magnetic cross section was measured at angels of α=90° and 270°, where α is the angle between the scattering vector and the magnetization. The scattered intensity was averaged over sectors of 20° around the given mean angles. Absolute cross sections were calculated by comparison with the incoherent scattering of vanadium.

Achievements and Main Results

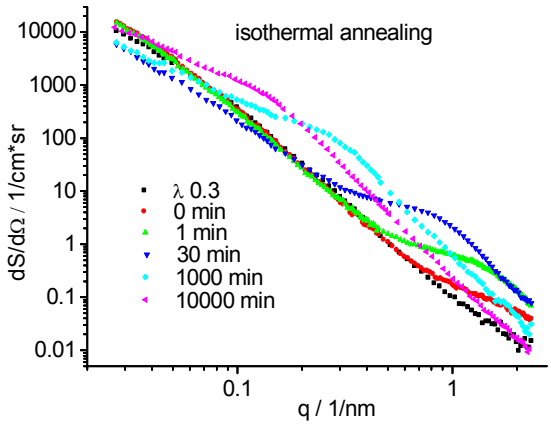


Figure 1: Scattering curves of steel samples isothermally annealed at 610 °C.

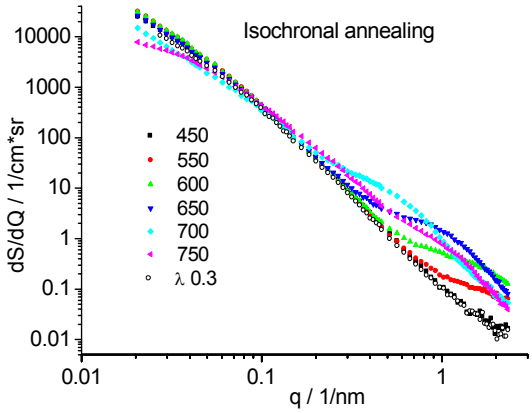


Figure 2: Scattering curves of isochronally annealed steel samples.

Fig. 1 shows the resulting scattering curves obtained for samples isothermally annealed at 610 °C, as partially published in [1]. It is clearly visible that a large volume fraction of particles is forming after very short annealing times. In order to distinguish between carbides and the preceding intermetallic phase, TEM and APFIM measurements have been performed, showing good agreement with the SANS data. However, especially the size distributions of M_2C carbides and the intermetallic NiAl phase tend to overlap and therefore it is difficult to determine the corresponding volume fractions independently.
Fig. 2 represents the results obtained for isochronally annealed samples. Additionally, as in Fig. 1, the scattering curve of an as-quenched sample is shown as a reference. At 450 °C only a little fraction of very small carbides or clusters has formed. The formation of the intermetallic phase can be ruled out due to thermodynamic reasons. Between 550 °C and 700 °C a significant fraction of particles has formed and proceeds coarsening, depending on the corresponding target temperature. However, at 750 °C a reversal process occurs which can be correlated to the partial dissolution of the intermetallic NiAl phase. On the other hand, the M2C carbides are still thermodynamically stable and proceed coarsening. Consequently, the size distributions of this carbide and the NiAl phase are no longer interfering each other and, therefore, its volume fraction can now be determined.
While the evolution of the scattering curves with changing annealing conditions is well understood at scattering vectors q > about 0.2 1/nm, the behaviour is somewhat unexplained for

smaller values. Scattering in this q-region occurs from large inhomogeneities within the material which might be primary carbides. However, according to the SANS measurements, these particles tend to dissolve, what is in strong contradiction to results from thermodynamic calculations as well as TEM studies [1]. The same observation could be reproduced for different kinds of steels, e.g. the one analysed in [2]. Therefore, in order to investigate the reason for the changing scattering behaviour in this q-region, additional measurements have been made as explained in the experimental part of this report. However, data processing of these measurements, which have been performed not earlier than in September this year, is still under progress and their result will be presented elsewhere.

References

[1] M. Bischof et al., Zeitschrift für Metallkunde 96 (2005) 9, pp. 1074–1080.
[2] H. Leitner et al., Materials Science and Engineering A 398 (2005) 1-2, pp. 323–331.

GKSS FORSCHUNGSZENTRUM in der HELMHOLTZ-GEMEINSCHAFT	**EXPERIMENTAL REPORT**	**GeNF SANS-2**

Characterization of precipitates in a high-strength low-alloy steel

Proposer:	**H. Leitner**, [1]Montanuniversität Leoben, Leoben, Austria
Co-Proposers:	**H. Clemens,** [1] **P. Staron,** [2]GKSS Research Centre
Experimental Team:	**M. Bischof[1], P. Staron[2], P.K. Pranzas[2]**
User Group Leader:	**H. Clemens[1]**
Date(s) of Experiment:	April 2005

Objectives

Precipitates in the size range from nanometres to microns are affecting the mechanical and thermo-physical properties of steel. In the present study a high-strength low-alloy (HSLA) steel containing Ti, Nb, and V is investigated in the as-rolled and different annealed conditions. The combination of modern transmission electron microscopy (TEM) and small-angle neutron scattering (SANS) enables the analysis of precipitates in the nanometre region, which are relevant for the strength of the steel.

Experiment

For several years there has been the demand for hot-rolled strip steel with yield stresses above 700 MPa. The driving force for this development is the aim to reduce component-weight, especially in mobile applications, while the requirements for easy processing, i.e. cold-forming and weldability, have to be preserved. Due to the small size of involved strengthening precipitates the traditional metallographic techniques are of limited use.

SANS was used for the study of changes in particle size distributions as a function of the annealing condition. As the matrix of the investigated steel is ferromagnetic, it was magnetized to saturation by a magnetic field of 2 T. Then the nuclear cross sections can be measured parallel to the applied magnetic field, while the sum of nuclear and magnetic cross section can be measured perpendicular to the field. As the precipitates are nonmagnetic, the ratio of magnetic and nuclear scattering cross section can be analysed additionally.

A total of 6 samples of a HSLA steel with 95.6 % Fe and 0.17 %C were measured in the as-rolled state and after annealing treatments for 35 min at temperatures between 300 °C and 700 °C. After hot-rolling the material under investigation exhibits a martensitic microstructure resulting in a hardness of about HV2=508. Subsequent annealing treatments at temperatures between 250 °C and 500 °C lead to a considerable decrease in strength (HV2=476 at 250 °C and HV2<400 at 500 °C), which is attributed to tempering of martensite. Annealing at temperatures of about 600 °C leads to a plateau or peak in hardness (HV2=400), followed by a sharp drop (HV2<330) when the material is annealed above 650 °C. The task is to correlate these changes in the mechanical properties with changes in the particle size distribution.

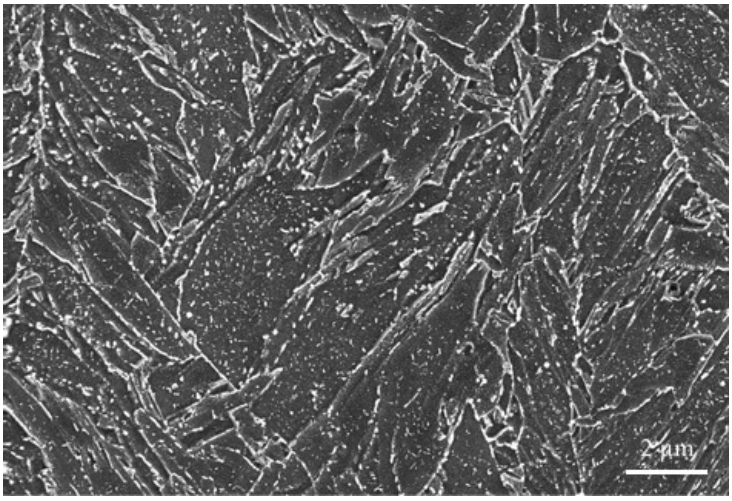


Figure 1: SEM image of a sample annealed for 35 min at 610 °C.

Achievements and Main Results

There are significant changes in the SANS cross sections with the annealing state (Fig. 2). Especially, there is a large drop at the rather low annealing temperature of 300 °C; its origin is not yet fully clear. Most likely the drop is due to annealing effects and the sample tempered at 300 °C can serve as a reference sample. Then, possibly by chance, the particle size distribution shows only small changes from the as-rolled state to annealed states at 570 °C or 590 °C (Fig. 2). There is a bimodal size distribution of particles with sizes of 1 nm and 20–40 nm with a total volume fraction of approximately 1 %. At 700 °C the particles grow larger with a reduced number density (coarsening), which seems to correspond to the above mentioned drop in hardness. A careful analysis of the SANS data in combination with electron microscopy results and mechanical data will contribute to a more detailed picture of the strengthening mechanism in the investigated HSLA steel.

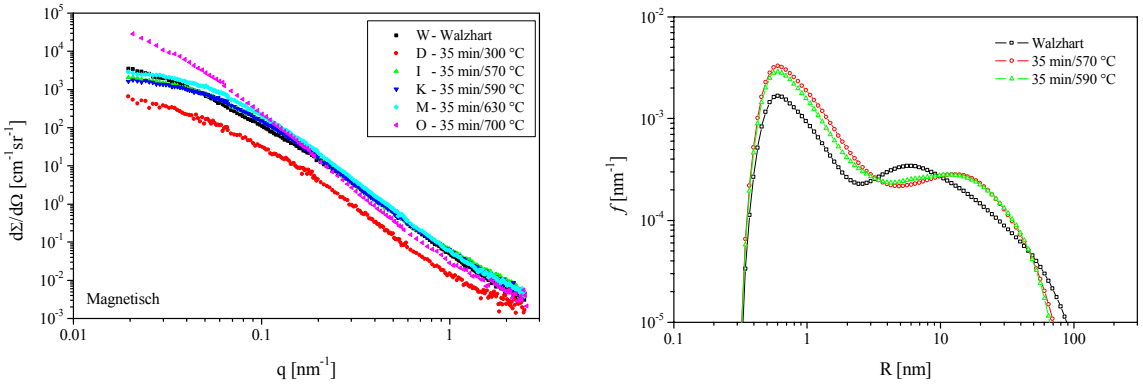


Figure 2: Measured magnetic scattering cross section (left) and corresponding particle size distributions.

GKSS FORSCHUNGSZENTRUM in der HELMHOLTZ-GEMEINSCHAFT	EXPERIMENTAL REPORT	GeNF SANS-2

Polarised SANS measurements of the FLL of Niobium

Proposer:	**Sebastian Mühlbauer[1],** [1]Physik Department E21, TU-München, James Franck Str.1, 85747 Garching
Co-Proposers:	
Experimental Team:	**Sebastian Mühlbauer[1],** **Daniel Lamago[2],**
User Group Leader:	**Sebastian Mühlbauer[1]**
	[2]ZWE FRM-II, TU-München, Lichtenbergstr.1, 85747 Garching

Date(s) of Experiment:	11–17 April 2005

Objectives

Recent polarised SANS measurements by various groups [1, 2] of the flux line lattice (FLL) of superconducting niobium showed clear polarisation dependent scattering that cannot be explained by means of the ideal model of the FLL. In isotropic superconductors no spin dependent scattering occurs, because the flux lines are orientated parallel to the applied magnetic field *B* as well as the polarization of the neutrons is parallel to *B* [3]. Spin dependent scattering only occurs either i) assuming a non zero nuclear scattering length distribution with the same periodicity as the FLL (interference term) or ii) assuming a bending of the FLL, ruling out the geometrical constraint. In order to examine, whether the observed polarisation dependece is an intrinsic property of pure niobium or is caused by sample impurities, polarised SANS experiments on a single crystal niobium sample were performed at the SANS-2.

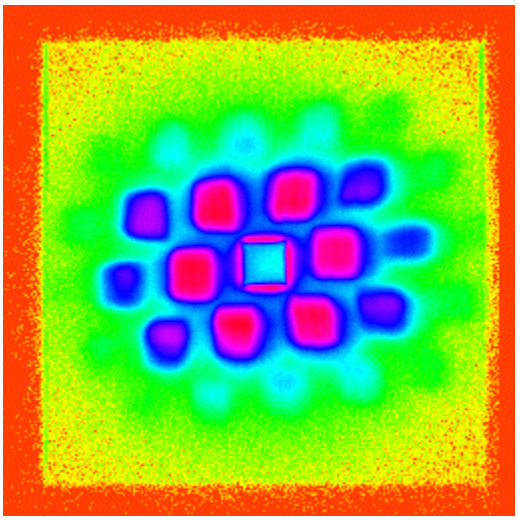
Experiment

A cylindric shaped single crystal niobium sample (19 mm diameter, 3 mm width) was placed inside a closed cycle cryostat perpendicular to the incident neutron beam. A magnetic field of 0-2000 G was also applied parallel to the incident neutron beam by means of a set of water cooled Helmholtz coils. Both the magnetic field and the sample could be rotated independently inside the scattering plane, in order to adjust the scattering geometry. By placing a bender in front of the collimation tube of the SANS-2, a polarised neutron beam was generated. The polarisation direction was chosen parallel to the incident neutron beam to avoid depolarisation at the sample environment, and could be reversed using a flipper-coil. Several scans through the phase diagram were performed: Constant-T scans, varying the magnetic field from 0–2000 G and constant-B scans, varying the temperature from 9–4 K. Each scan was performed for both polarisation directions as well as zero field cooled and non zero field cooled.

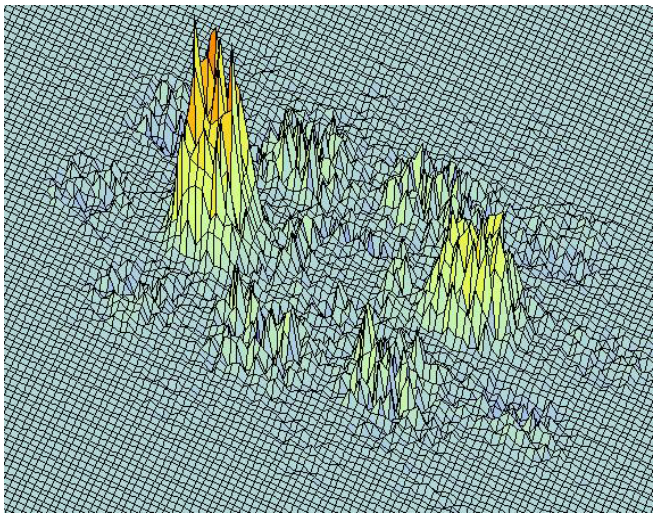
Achievements and Main Results

Analysing the achieved data by subtracting both polarisation directions, the results of [1,2] could be reproduced: A clear polarisation dependent signal was observed, which was clearly connected to the Shubnikov phase of the sample. Above T_c, the differential signal was zero, contrarily to the Meisser phase, where polarised SANS measurements are impossible due to the meissner screening of the sample. Further measurements with samples of a different

residual resistivity ratio, and therefore different pinning properties will show if a local bending of the FLL is the origin of the polarised signal or wether a difference in the local scattering length, related to the pinning centres originates this behaviour.



The Six-fold scattering pattern of the flux line lattice of niobium recorded at 4.5 K and 1200 G.



The polarised signal, obtained by substracting the two incoming polarisation directions, up and down.

References

[1] K. Neumann, et al, Eur. Phys. J. B 1, 5–9, (1998)
[2] Experimental Report ILL 5-51-229
[3] E. M. Forgan, et al., Physica B 267-268, 115 (1999)

GKSS FORSCHUNGSZENTRUM in der HELMHOLTZ-GEMEINSCHAFT	**EXPERIMENTAL REPORT**	**GeNF SANS-2**

SANS study of the early stages of crystallization in the Fe-Zr-B-Cu nanocrystalline alloys

Proposer:	**Ivan Skorvánek**[1]
Co-Proposers:	**Jozef Marcin**[1]
	[1]Institute of Experimental Physics SAS, Košice, Slovakia
Experimental Team:	**Jozef Marcin**[1]**,**
	Helmut Eckerlebe[2]**,** [2] GKSS Research Centre
User Group Leader:	**Ivan Skorvánek**[1]

Date(s) of Experiment:	April 24 – May 3, 2005

Objectives

Fe-Zr-B-Cu nanocrystalline alloys belong to important group of soft magnetic materials, called also NANOPERM. The previous investigations performed by HRTEM [1] and APFIM-technique [2] have provided some insight into the early stages of nanocrystallization in these alloys, revealing the significant role of the microscopic inhomogeneities (such as Cu-rich precipitates) and/or tiny medium range order (MRO) clusters, which are present in the thermally treated amorphous precursor alloy. However, the knowledge about the nature of such inhomogeneities in different pre-crystallization structural stages is still rather poor. In order to get more information in this respect, we have performed the SANS experiments on NANOPERM-type samples characterised by different microstructure.

Experiment

Amorphous ribbons of $Fe_{86}Zr_7B_6Cu_1$ alloy were prepared by the method of planar flow casting. Pieces of these ribbons were annealed for 1 hour under high vacuum (better than 10^{-6} mbar) at temperatures 400, 440 and 480°C to prepare the series of samples characterized by different microstructure. The crystallization behavior and the changes of microstructure upon annealing were studied by DSC calorimetry, X-ray diffraction and VSM-magnetometry. The results of these experiments have revealed that the sample annealed at 480°C for 1 hour exhibits already a clear presence of the ferromagnetic bcc-Fe nanograins, while the samples annealed at 400 and 440°C correspond to different pre-crystallization structural stages of thermally relaxed parent amorphous material.

Small angle neutron scattering experiments were carried out at the SANS-2 facility of the FRG-1 reactor at GeNF. In order to cover a wider range of scattering vectors, the measurements performed at 3 detector distances (1 m, 3 m and 9 m) were supplemented by using the wide-angle 2-dimensional side detector. A neutron beam with a wavelenght of λ= 0.58 nm was used. The magnetic field of 1 T was applied perpendicular to the neutron beam direction in order to saturate the ferromagnetic samples. All measurements were performed with polarization of the primary neutron beam parallel and antiparallel to the sample magnetization. After usual corrections for background, transmission and efficiency, two-dimensional anisotropic SANS patterns were analysed according to

$$I(Q,\varphi) = A(Q) + B(Q)\sin^2\varphi$$

where φ angle between the scaterring vector ***Q*** and the external magnetic field ***B***. For complete alignement of the moments along ***B***, $A(Q)$ corresponds to nuclear scattering and $B(Q)$ to magnetic scattering, which is proportional to the Fourier transform of the magnetization density $M(r)$.

Achievements and Main Results

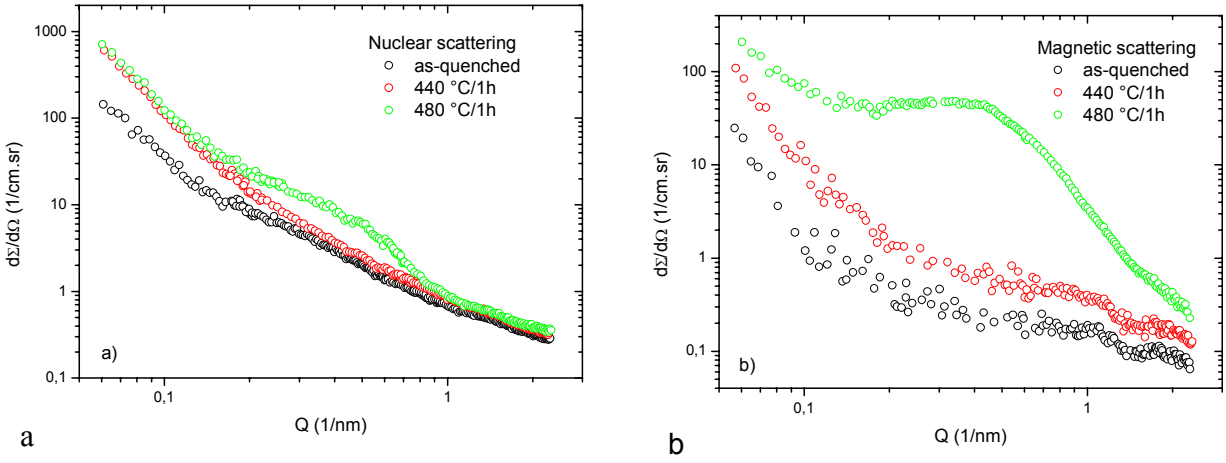


Figure 1: Nuclear a) and magnetic b) scattering curves at room temperature.

Figures 1(a) and (b) show the nuclear and magnetic SANS components for the investigated samples obtained at 300 K. A marked difference between the nuclear and magnetic SANS components for the sample annealed at 480°C for 1 hour in comparison to other samples is clearly connected with the presence of magnetic inhomogeneities of bigger dimensions after this heat treatment, which are associated with the ferromagnetic bcc-Fe nanocrystalline grains (10-20 nm) embedded in a weak magnetic amorphous residual phase. Additional shoulder in the corresponding magnetic scattering curve observed for this sample at large scattering vectors (from 1.4 to 2.2 nm^{-1}) seems to be associated with a presence of much smaller scattering centers, which could correspond to that of Cu-rich clusters (1–2 nm) observed for the alloy of similar composition by using APFIM [2,3]. A similar shoulder at the largest scatterings vector range is visible also for samples annealed at lower temperatures. However, rather poor statistics of data, which seems to be a consequence of the considerably lower volume fraction of corresponding scattering centers in these thermally relaxed amorphous alloys do not allow us to conclude in more details about the nature of these nanoscale inhomegeneities. Further interpretation of data is in progress.

Acknowledgement

This research project has been supported by the European Commission under the 6th Framework Programme through the Key Action: Strengthening the European Research Area, Research Infrastructures; Contract n°: RII3-CT-2003-505925.

References

[1] M. Nakamura et al., Mater. Sci. Eng. A, 179/180, 1994, 487
[2] T. Okubo et al., Scripta Mater. 44 (2001) 971
[3] Y. Zhang et al. , Acta Mater. 44 (1996) 1497

GKSS FORSCHUNGSZENTRUM in der HELMHOLTZ-GEMEINSCHAFT	**EXPERIMENTAL REPORT**	**GeNF SANS-2**

SANS study of amorphous and annealed $Ni_{36.5}Pd_{36.5}P_{27}$ glass

Proposer:	**S. Gruner,** TU Chemnitz, Inst. f. Physik, D-09107 Chemnitz
Co-Proposers:	**I. Kaban, W. Hoyer,** TU Chemnitz, Inst. f. Physik, D-09107 Chemnitz
Experimental Team:	**S. Gruner, I. Kaban,** TU Chemnitz, Inst. f. Physik, D-09107 Chemnitz **H. Eckerlebe,** GKSS Research Centre

Date(s) of Experiment:	13th – 19th June 2005

Objetives

Metallic glasses are characterized by unique physical properties and offer exciting possibilities for many technological applications. However, many problems concerning glass formation abilities, the glass transition phenomenon, temperature and mechanical stability of glasses and glass structure are still not solved. The general aim of our study is to investigate the physical properties and atomic structure of $Ni_{36.5}Pd_{36.5}P_{27}$ metallic glass below and above the glass transition temperature ($\vartheta_g \approx 315$ °C).
Small-angle neutron scattering (SANS) is applied for investigation of the annealing process and evolution of nanocrystalline structures during heat treatment in the $Ni_{36.5}Pd_{36.5}P_{27}$ glass.

Experiment

Amorphous ribbons of $Ni_{36.5}Pd_{36.5}P_{27}$ alloy were prepared by a melt spinning technique. Pieces of the ribbons were annealed 15 min under high vacuum (better than 10^{-4} mbar) at various temperatures. Changes in the microstructure upon annealing have been studied using the SANS-2 instrument at the FRG-1 reactor at GeNF.
The scattered neutrons were detected by a two-dimensional position-sensitive ^{3}He detector. The measurements were performed with the neutron wavelength λ = 5.8 Å ($\Delta\lambda/\lambda$ = 0.1) at four sample-detector distances (1 m, 3 m, 9 m and 21.720 m). The magnitude of the diffraction vector $Q = 4\pi \sin\theta/\lambda$, where 2θ is the scattering angle, ranged from ~0.02 nm^{-1} to ~3.0 nm^{-1}.
The experimental data were treated with the SANDRA programme [1]. The measured intensity was corrected for absorption, background scattering, detector efficiency and geometry. The scattering data were averaged over azimutal scattering angle and absolute cross sections were calculated by comparison with the incoherent scattering of vanadium.

Achievements and Main Result

Figure 1 shows the plots of the coherently scattered intensity for the as-prepared and four annealed ribbons of $Ni_{36.5}Pd_{36.5}P_{27}$ metallic glass. The SANS intensity evolution after heat treatment indicates the formation of nano-sized structural inhomogeneities. It is seen that noticeable small-angle scattering signal is already observed for $Ni_{36.5}Pd_{36.5}P_{27}$ glass annealed at 315 °C, i.e near the glass transition temperature, well below the crystallization temperature. With increasing of the annealing temperature the SANS intensity increases which is obviously connected to the growth of nanocrystalline particles during annealing of the $Ni_{36.5}Pd_{36.5}P_{27}$ glass.

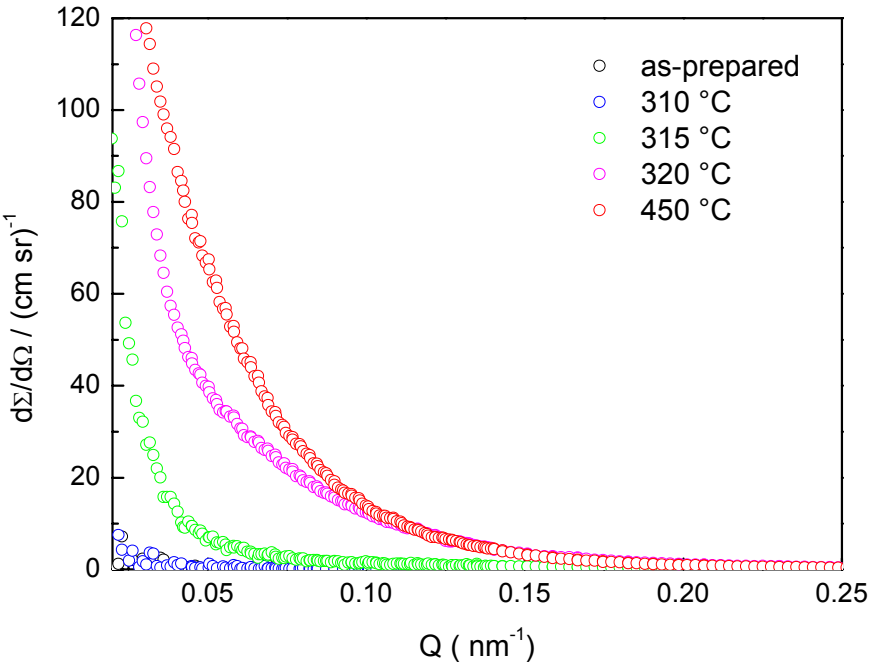


Figure 1: Experimental SANS spectra for $Ni_{36.5}Pd_{36.5}P_{27}$ metallic glass.

Acknowledgements

We (S. Gruner and I. Kaban) acknowledge GKSS Research Centre for hospitality and financial support.

References

[1] P. Biemann, M. Haese-Sailler, P.Staron, SANDRA (SANS Data Reduction and Analysis); http://www.gkss.de/pages.php?page=w_abt_genesys_sandra.html&language=d&version=g

[2] Hermann, Rainer-Harbach, Steeb, Z. Naturforsch. 35a (1980) 938–945

[3] Guinier, Fournet, *Small-Angle Scattering of X-rays*, J. Wiley & Sons Inc., New York 1955

GKSS FORSCHUNGSZENTRUM in der HELMHOLTZ-GEMEINSCHAFT	EXPERIMENTAL REPORT	GeNF SANS-2

SANS investigation of Cu alloys for applications to technology for the restoration of ancient organs

Proposer:	**Adrian Manescu[1],** [1]Università Politecnica delle Marche, Via Brecce Bianche, Ancona, 60100, Italy
Co-Proposers:	**Alessandra Giuliani[1]**
	Fabrizio Fiori[1]
Experimental Team:	**Mauro Moglianetti[1],**
	Paolo Ferraris[1],
User Group Leader:	**Franco Rustichelli[1]**

Date(s) of Experiment:	3–7.July 2005

Objetives

The important aim of our research was the analysis of the microstructure of thin Cu-based alloy reed tongues, taken form historic organs. The tongues microstructure influences the sound that the reed pipe gives. The phase morphology in different regions of the reed tongues can give us important information needed both for the restoring of historical organs and for the building of new ones with the same acoustic features of baroque and medieval ones.

An essential problem was the fact that many of the reed tongue samples which are given us for analysis are taken from organs and must be put back without destroying them in any way; so only non-destructive testing can be performed. This implies that the microtructure analysis can not be performed by destructive or partially destructive techniques, like SEM or TEM for example.

Experiment

All the measurements were performed using a wavelength of 5.8Å. The maximum collimation length was 16m. On five of eight samples the measurements were performed in two points, the vibrating and fixed part of reeds pipe tongue. For the last three samples, because of their geometrical shape, the measurement was performed in only one point, in the middle of the sample. The dimension of the circular slits in front the samples was 8*mm* in diameter. Measurements using Vanadium and Teflon standard samples were performed in order to do the normalizations.

Achievements and Main Results

A first result that we obtained was that there are no small precipitates – in the higher part of the analysed Q range there is no evident scattering effect. From the macroscopic cross section vs Q curves we obtained the information that there are some larger precipitates – futher U-SANS measurements are needed for a better understanding of the shape/concentration of these precipitates.

GKSS FORSCHUNGSZENTRUM in der HELMHOLTZ-GEMEINSCHAFT	EXPERIMENTAL REPORT	GeNF SANS-2/DCD

Fingerprinting Marbles of Archeological Interest

Proposer:	**Roberto Triolo[1],** [1]Università degli Studi di Palermo 90128 Palermo, Italy
Co-Proposers:	**Fabrizio Lo Celso**[1]
	Irene Ruffo[2], [2]Ist. Istr. Sup. "Ugo Mursia",90044 Carini (PA, Italy)
Experimental Team:	**Fabrizio Lo Celso[1], P. Klaus Pranzas[3]**, [3]GKSS Research Centre
User Group Leader:	**Fabrizio Lo Celso**[1]
Date(s) of Experiment:	27th June – 1st July 2005

Objectives

Among the natural composites, there is a wide variety of stones, such as marbles, used in buildings, monuments, statues and other objects of archaeological or cultural heritage interest. Marbles may look very different as far as texture, color, mechanical and physical properties are concerned, mainly as consequence of their "formation history". Combined Ultra Small and Small Angle Neutron Scattering may be a suitable investigation technique for collecting useful information for the “fingerprinting” (structural parameters and texture) of white and polychromic marbles.

Experiment

The marble formation is usually the consequence of an isochemical metamorphic evolution of a sedimentary carbonate rock (a protolith mostly composed by calcite and dolomite) or a previous marble. Metamorphic transformations usually refer to solid-state processes that take place in the presence of a fluid or melt phase. During metamorphism changes in temperature, pressure or chemical composition determine the change in the equilibrium condition, (i.e. mineralogies of the system). The system re-equilibration, concerning marbles, usually occurs trough a recrystallisation process that follows the destruction of the original calcite-dolomite matrix. In principle a metamorphic process involving such recrystallisation, in a quite narrow range of temperatures, requires the progressive rebuilding of the material at different length scales going from the elementary cell (Å) trough intermediate aggregates (µm) to crystals (mm). However, it has been observed that while the size of the elementary cell is mainly determined by the chemical composition of the protolith and/or of the interacting fluids, the temperature effect, characterizing the metamorphic process, determines the size, texture and kind of the crystals at macroscopical level. At the mesoscale level (going from few Å to the limit of µm) there is not much information known about the metamorphic degree. Such events are possibly indicative of power law scaling, typical of fractal structures. Neutron scattering is a most appropriate technique for measuring volume fractal properties because of a unique advantageous feature of the neutron-matter interaction, the high penetrability of neutrons. Sample volumes covering the length scale of fractal behaviour can be studied. Sampling of the object volume is determined by the beam cross-section (order of mm) and is insensitive to local variations in microstructure. Complex natural composite materials like rocks are seen by neutrons as two-phase systems with a density contrast characteristic of an overall, average texture "signature".

A quite large number of samples (34) coming from Greece and Italy, including white and polychromic marbles, have been measured at the SANS-2 instrument. Variable sample to detector distance has been used, 1m to 21.7m with λ=0.57 nm and 21.7m with λ=1.14 nm giving approximately a momentum transfer range $8x10^{-3} < q < 2.4\ nm^{-1}$.
A selection of previous samples, including both white and polychromic marbles, were also measured at the DCD instrument (λ=0.44 nm and approx. $10^{-5} < q < 3x10^{-2}\ nm^{-1}$). USANS measured cross section are reported in figure 2 for 6 samples. The analysis of USANS desmeared data will be performed together with the SANS measurements.

Achievements and Main Results

Typical SANS measured cross section is reported in figure 1. Although a hierarchical structure model[1] should be taken into account for the analysis of combined USANS-SANS measurements, we consider in a first step only the SANS region which is easy to spot. The power law exponent (3.65) obtained for this region indicates a surface fractal ($q > 0.05\ nm^{-1}$). All samples measured at the SANS-2 instrument have shown such behaviour, although it is reasonable to apply the above mentioned model which implies the knowledge of the USANS region. The hierarchical structure model indeed takes into account the existence of a network (mass fractal) of fractal aggregates (which have a rough "surface" and therefore are fractals themselves) formed by monodispersed solid primary particles.

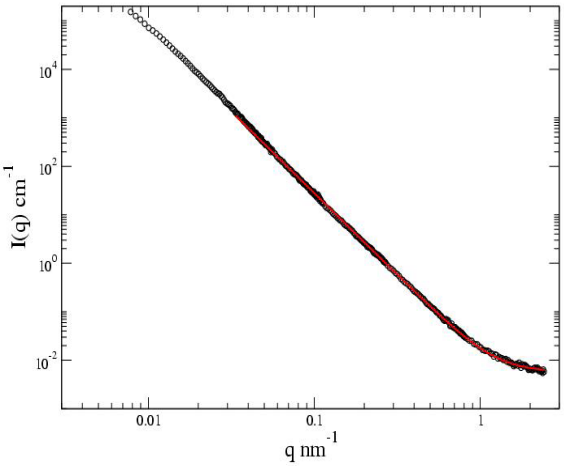


Figure 1: SANS curve of a white italian marble. Solid line represents best fit to the experimental data using a simple power law plus a cutoff limit.

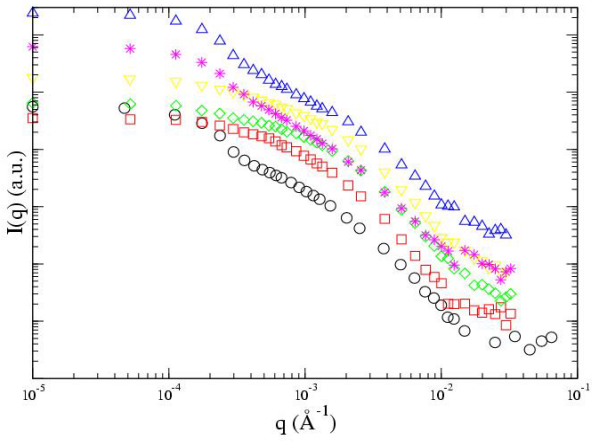


Figure 2: USANS smeared curves of selected white and polychromic marbles. Data are vertically shifted for clarity.

The majority of the samples show a two dimensional isotropic SANS patterns from which one dimensional scattering curves with power law behaviour were calculated. Such behaviour is typical for fractal structures, in particular for surface fractals. If a more complete analysis is considered using the combined USANS and SANS curves, these surface fractals are parts of more extended structures of a network of aggregate mass fractals. The correlation of the structural parameters with the provenance and type of marbles will be considered, along with results from other techniques, to obtain a detailed fingerprinting of the materials.

References

[1] A. Emmerling, R. Petricevic, P. Wang, H. Scheller, A. Beck, and J. Fricke, J. Non-Cryst. Sol. 185, 240 (1994).

GKSS FORSCHUNGSZENTRUM in der HELMHOLTZ-GEMEINSCHAFT	EXPERIMENTAL REPORT	GeNF SANS-2

Light-induced phase separation in polymer dispersed liquid crystals (PDLC)

Principal Proposer:	**Martin Fally[1], Irena Drevenšek-Olenik[2]** [1]Faculty of Physics, University of Vienna, Austria [2]J. Stefan Institute & University of Ljubljana, Slovenia
Experimental Team:	**Martin Fally[1], Irena Drevenšek-Olenik[2], P. Klaus Pranzas[3], Jürgen Vollbrandt[3]** [3]GKSS Research Centre

Date(s) of Experiment:	04–07July 2005

Scientific Objectives

This experiment was the first one of a series, which is targeting on the clarification of the photopolymerization induced phase separation process in (holographic) polymer dispersed liquid crystals (H-PDLC). The initial stage of H-PDLCs is a homogeneous solution, that is a mixture of mesogenic (liquid crystal (LC) forming) molecules and photosensitive monomers. Upon holographic exposure, a photopolymerization reaction takes place more rapidly in the bright regions of the optical interference pattern and consequently the monomers diffuse to these regions while the liquid crystalline molecules congregate in the dark regions [1]. Besides this, when a specific level of photopoymerization is reached locally, de-mixing of the compounds starts to take place, resulting in formation of LC droplets embedded in a polymer matrix. This complex process produces optical holograms with a very high spatial modulation of refractive index. In addition, due to the strong electrooptic response of the LC domains, optical diffraction from these holograms is electrically switchable with low amplitude external voltages.

There is very little known on the details of the H-PDLC formation, especially in the stages before and close to the miscibility breakdown. The ultimate goal is to explore the associated phase separation process, which determines the final size and the shape of the LC droplets and consequently the electro-optical properties of the H-PDLCs. Therefore, we intend to investigate the process *in-situ*, during creation of the grating, by **neutron diffraction** employing the device **HOLONS** at SANS-2 [2,3]. To tackle this complex problem we took the first of several steps in this experiment: To demonstrate that the achievable contrast, i.e., the scattering length densities, between the LC and the polymer is large enough to observe neutron scattering (PDLC) or diffraction (H-PDLC).

Experimental Technique

Small-angle neutron diffraction experiments were performed at SANS-2. The neutron wavelength was λ=11.6 Å or 19.6 Å with a FWHM $\Delta\lambda/\lambda$=10 %. Full collimator length (16 m) with diaphragms – entrance: [10x40] mm^2 and exit Ø=5 mm – and maximum detector distance (21 m) were used, so that the angular spread was <1 mrad.

A series of PDLC [4] and H-PDLC samples was fabricated from an UV curable mixture prepared from commercially available constituents: an UV curable prepolymer (PN393, Nematel), nematic liquid crystal (TL203, Merck) and 1,1,1,3,3,3,3-Hexafluoroisopropyl acry-

late (Sigma-Aldrich). The ratio of different constituents was selected following the formulations previously reported in literature. A drop of the mixture was placed between two glass plates separated by 50 µm mylar spacers. Homogenous illumination or a holographic two-wave mixing set-up, i.e., a sinusoidal intensity distribution, with different exposures or intensities of UV-laserlight (λ_L=351 nm) were employed to prepare PDLC and H-PDLC, respectively.
In the case of high contrast between illuminated and dark regions, the H-PDLCs could act as gratings not only for light but also for neutrons [5]. However, note that the thickness of the samples is about two orders of magnitude smaller than for photo-neutronrefractive materials reported in literature [2]. To prove that H-PDLC is a **new photo-neutronrefractive medium**, **diffraction** from that grating was demonstrated using the SANS-2 facility.
For PDLCs the homogeneous illumination results in formation of LC droplets or clusters (phase separation) that are homogeneously dispersed in a polymer matrix. The size of the clusters is very sensitive to the recording conditions. By performing SANS experiments we intended to reveal the mean size of these LC-clusters as a function of exposure.

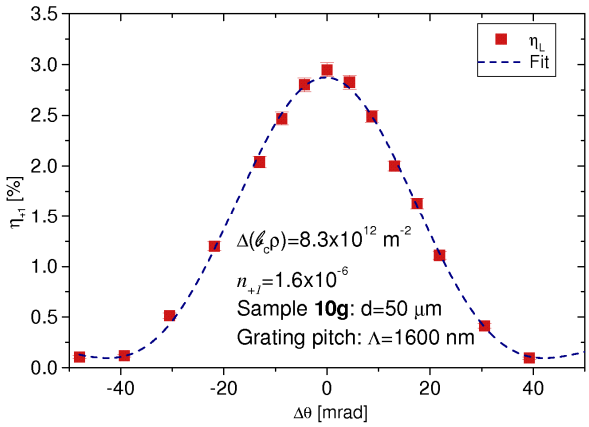
Results
The diffraction experiments on the H-PDLC were performed under highly unfavourable conditions:
(1) The samples had been prepared for light-optical measurements, so that the two embracing glass plates with a thickness of 1 mm each were supposed to give a tremendous background on the scattering signal from the sample with a thickness of only 50 µm.
(2) The sample itself contains a big amount of hydrogen that contributes to incoherent scattering, and
(3) the suppliers keep the exact chemical formula of the compounds secret, so that estimations of the expected contrast are difficult.

Despite these facts we **succeeded to detect the grating and could even conduct complete rocking-curves,** i.e., the angular dependence of the diffraction efficiency η in the vicinity of the Bragg angle. Fig. 1 shows $\eta_{+1}=I_{+1}/I_T$ for the +first diffraction order of an H-PDLC sample with a thickness of d = 50 m. Here, $I_{+1,T}$ denote the number of neutrons diffracted to the +first order and the total number of neutrons reaching the detector, respectively. Note that the diffraction efficiency is proportional to the square of the thickness. As the FWHM of the rocking curve is 30 mrad and thus much larger than the angular spread (~0.5 mrad), it can be fitted by using the two-beam coupling theory [6] (dashed line in Fig. 1). This allows us to evaluate the light-induced neutron refractive-index change n_{+1} and hence the **light-induced coherent scattering-length density modulation** $\Delta b_c\rho$)[2]. This modulation is more than **one order of magnitude larger** as compared to that of any material probed up to now. At present H-PDLC therefore is the most efficient medium for light-induced neutron-refractive index-changes. The diffraction efficiency can be even increased by simply enlarging the thickness or the wavelength as $\eta(\Delta\theta = 0) = \left[1/2\lambda d\Delta\left(b_c\rho\right)\right]^2$, where $\Delta\theta$ denotes the deviation from Bragg angle. This is demonstrated in Fig. 1(b) for diffraction using a wavelength of 19.6 Å. Here, even **second order** diffraction can be observed.

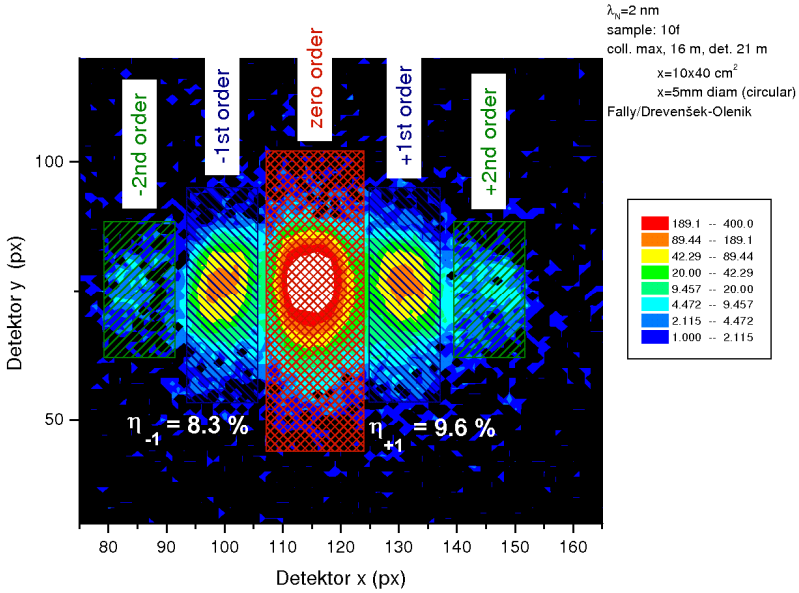
The scattering experiments on the PDLC did not yet yield valuable information. Reasons might be, that the models of droplet formation discussed in literature are wrong, in particular for UV-cured samples like ours, or that the contrast was not good enough to resolve those droplets. Further investigations are required to decide about this question.

Figure 1:

(a) angular dependence of the diffraction efficiency η_{+1} for an H-PDLC sample (thickness 50 µm).



(b) SANS pattern at Bragg angle ($\Delta\theta$=0) for λ=19.6 Å: 0th, 1st and 2nd diffraction orders are visible.



Relevance to other Applications or to other Techniques

H-PDLC could be used as a new material for fabricating neutron-optical devices for cold neutrons, such as beamsplitters, mirrors, interferometers, lenses etc.

This research project has been supported by the European Commission under the 6th Framework Programme through the Key Action: Strengthening the European Research Area, Research Infrastructures. Contract n°: RII3-CT-2003-505925. We further acknowledge support by FWF P-15642 and ÖAD-WTZ SI-A7/0405.

References

[1] C. C. Bowley and G. P. Crawford: Appl. Phys. Lett. 76, 2235 (2000)
[2] M. Fally: Appl. Phys. B 75, 405–426 (2002)
[3] F. Havermeyer, R. A. Rupp, D.W. Schubert, E. Krätzig: Physica B 276-278, 330 (2000)
[4] M. A. Ellabban, M. Fally, H. Uršič, I. Drevenšek-Olenik: Appl. Phys. Lett. 87, 151101 (2005)
[5] R. A. Rupp, J. Hehmann, R. Matull, K. Ibel: Phys. Rev. Lett. 64, 301(1990)
[6] H. Kogelnik: AT&T Tech. J. 48 (9), 2909 (1969)

GKSS FORSCHUNGSZENTRUM in der HELMHOLTZ-GEMEINSCHAFT	**EXPERIMENTAL REPORT**	**GeNF SANS-2 / DCD**

Investigation of structural changes of nanocrystalline MgH_2/Cr_2O_3 for reversible storage of hydrogen

Proposer:	**Martin Dornheim, P. Klaus Pranzas,** GKSS Research Centre
Co-Proposers:	**Thomas Klassen, Andreas Schreyer,** GKSS Research Centre
Experimental Team:	**P. Klaus Pranzas**
User Group Leader:	**P. Klaus Pranzas**
Date(s) of Experiment:	July 2005

Objectives

Magnesium hydride offers a safe alternative to the storage of hydrogen in compressed or liquid form. It has a high storage capacity of up to 7.6 wt.%. Nanocrystalline MgH_2 has high absorption and desorption rates of hydrogen as well as very good thermal and cycling stability. The sorption properties are distinctly enhanced by the addition of metal-oxide catalysts. However, the influences of microstructure, e.g. grain and particle sizes, and distribution of different additives on kinetic properties as well as structural changes due to hydrogen sorption and desorption have hardly been investigated up to now. The aim of this work is to characterize structural changes of high energy ball-milled MgH_2 during absorption and desorption of hydrogen with and without additives using varying milling parameters.

Experiment

The MgH_2 samples were milled in a FritschP5 planetary ball mill using hardened Cr-steel or ceramic milling tools (Yttrium stabilized ZrO_2 balls and Al_2O_3 vials) and an initial ball-to-powder weight ratio of 10:1. The Cr_2O_3 additive had an initial particle sizes of 50 µm and 75 nm (µ- and nano- Cr_2O_3) respectively. The MgH_2 powder was milled together with 10 wt.% of Cr_2O_3 for up to 200 hours. All handling of the samples was carried out under Ar atmosphere. Samples containing Cr_2O_3 as well as samples which were prepared using different milling times, vial and ball materials (ceramic or steel) were measured at the instruments SANS-2 and DCD at room temperature in quartz cuvettes with a thickness of 1 mm.
At SANS-2 distances between sample and detector of 1, 3, 9 m (λ = 0.58 nm) and 21 m (λ = 0.58 nm and 1.16 nm, $\Delta\lambda/\lambda$ = 0.1) were used to cover the range of scattering vector q from 0.009 nm^{-1} to 2.4 nm^{-1}. Scattering data were corrected for sample transmission and detector response and normalized by monitor counts. The differential scattering cross section was obtained by calibration with a Vanadium reference sample with a thickness of 1.28 mm.

With ultra small-angle neutron scattering (USANS), particle sizes up to 24 µm are detectable. The measurements were carried out at the double-crystal diffractometer DCD using a wavelength of 0.443 nm resulting in an accessible range of scattering vector q from 10^{-5} to 10^{-2} nm^{-1}.

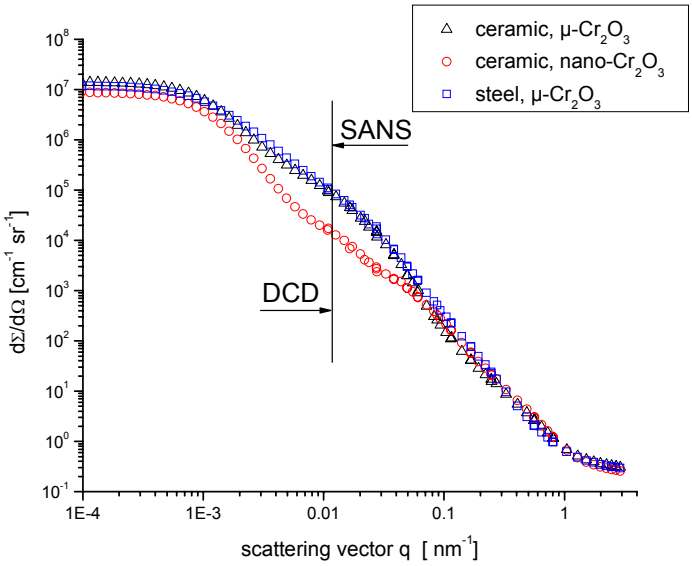


Figure 1: *SANS/USANS curves of MgH_2 samples with μ- and nano- Cr_2O_3 additives after 200 h of milling.*

Achievements and Main Results

Figure 1 shows three examples of combined SANS/USANS curves of MgH_2 after addition of normal chromium oxide powder (μ-Cr_2O_3) and commercially available nanoparticles (nano-Cr_2O_3) after 200 h of milling using steel or ceramic vials and balls. The obtained scattering curve of the sample using nano-additives shows a sharp shoulder at a scattering vector q of about 0.08 nm^{-1}, corresponding to a diameter of 78 nm. This value is in agreement with the initial particle size of the nano-Cr_2O_3 particles of 75 nm. At a q-value of about 0.02 nm^{-1} the curves of the samples milled with μ-Cr_2O_3 show a higher cross section than the sample with nano-additives as well as the samples without additives (see figure 2). This signal corresponds to the presence of Cr_2O_3 particles with diameters of 300 nm.

In figure 2 SANS/USANS curves of 3 samples are shown which were prepared by varying the milling time from 20 h to 200 hours, using steel and ceramic vials and balls. The curves of the samples prepared with different vial materials show a distinct deviation at a q-value of 0.1 nm^{-1} which corresponds to a radius of about 30 nm. In the curves of the samples for which different milling times were used only small structural changes appear. The scattering curves of the samples with Cr_2O_3 additives in figure 1 bend down at a q-value of $1 \cdot 10^{-3}$ nm^{-1}, whereas the curves of the samples without additives shown in figure 2 bend already down at $4 \cdot 10^{-4}$ nm^{-1}. This indicates that the presence of Cr_2O_3 additives leads to smaller MgH_2 particle sizes. The results show the potential of the combination of SANS and USANS to characterize structural changes in nano-crystalline metal hydrides over a large size range.

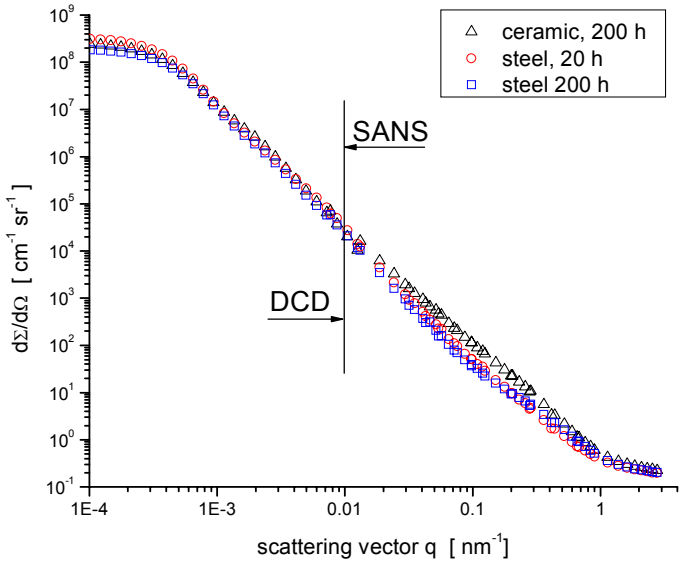


Figure 2: *SANS/USANS curves of MgH_2 samples using different milling times and vial and ball materials.*

GKSS FORSCHUNGSZENTRUM in der HELMHOLTZ-GEMEINSCHAFT	EXPERIMENTAL REPORT	GeNF SANS-2

Characterisation of coherent precipitates in a hard coating

Proposer:	**Paul Mayrhofer,** [1]Materials Chemistry, RWTH Aachen
Co-Proposers:	**Helmut Clemens,** [2]Physical Metallurgy and Materials Testing, Montanuniversität Leoben
	Peter Staron, [3]GKSS Research Centre
Experimental Team:	**Paul Mayrhofer[1],**
	Helmut Eckerlebe[3]
User Group Leader:	**Helmut Eckerlebe[3]**
Date(s) of Experiment:	3–11.August 2005

Objetives

TiAlN is one of the major industrial coatings used for the protection of tools. In the as-deposited state, the TiAlN coatings show a homogeneous solid solution with NaCl structure (fcc). This phase is, however, metastable and tends to decompose into their stable constituents fcc TiN and hcp AlN. It has been shown that due to the decomposition process of fcc-TiAlN during thermal exposure nm-sized precipitates form. Consequently the hardness of this kind of coating increases as additional obstacles are provided for the dislocation movement (Mayrhofer et al. 2003). The main objective of the investigation of TiAlN hard coatings by SANS was to clarify the size distribution and development of their precipitates as a function of annealing temperature.

Experiment

1. Samples

TiAlN coatings, 1.6 µm in thickness, have bee deposited onto Sapphire substrates (12x14x0.6 mm) by arc evaporation using a Metaplus industrial system. The samples are investigated in their as-deposited condition as well as after annealing in Ar atmosphere for 1.5 h at 500, 600, 700, 750, 800, 850, 900, 950, 1000, and 1050 °C.

2. Small-angle neutron scattering

Small-angle neutron scattering (SANS) measurements were carried out with the instrument SANS-2 at the Geesthacht Neutron Facility (GeNF). Selector-monochromated neutrons with a mean wavelength of λ = 0.58 nm and a wavelength spread of $\Delta\lambda/\lambda$ = 10 % were used. Detector distances up to 13 m were used with appropriate collimations to cover scattering vectors q from 0.03 nm^{-1} to 2.5 nm^{-1} ($q = 4\pi\sin(\theta)/\lambda$ where 2θ is the scattering angle). In this case, an additional lateral area detector was used, which can be rotated around the sample to cover larger scattering vectors. Measured intensities are corrected for sample transmission, background intensity, and detector response; macroscopic differential scattering cross sections are obtained by calibration against the incoherent scattering of Vanadium. In this case, however, the sample volume of the annealed samples 850 to 1050 °C were unknown and, therefore, the cross sections of these samples were matched with the sample as-deposited at q > 2 nm^{-1}.

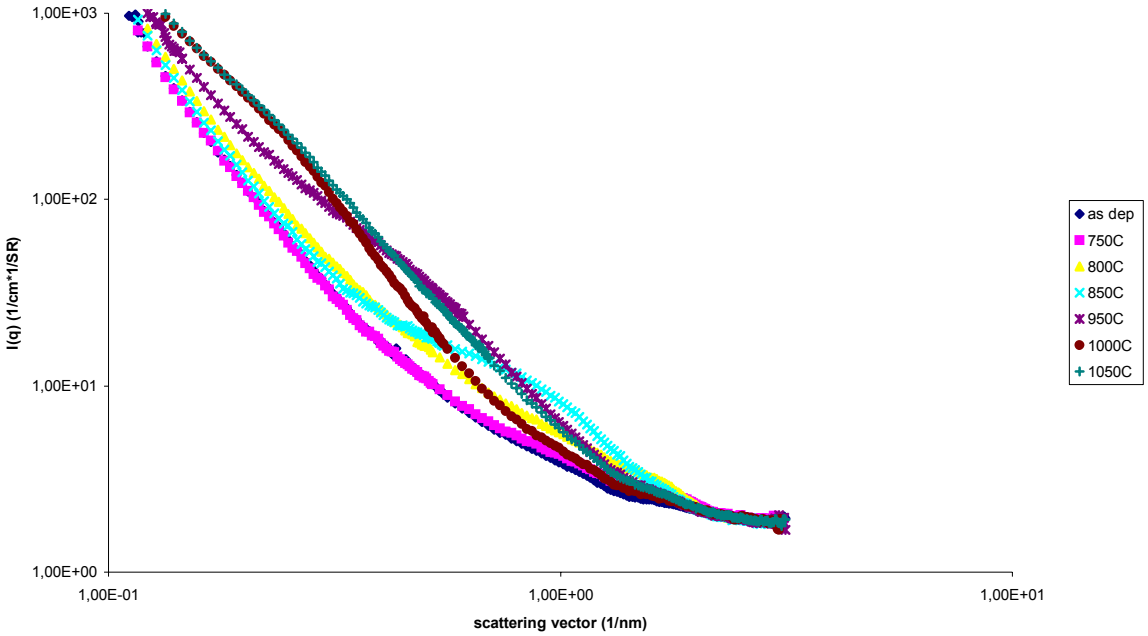


Figure 1.

Achievements and Main Results

During the investigations by SANS it appeared that two different particle families develop at different annealing temperatures. Furthermore it could be obtained that in the very early stage of the decomposition process of TiAlN the formed particles are not sharply separated from the parent phase, indicating that phase separation is due to spinodal decomposition (Mayrhofer et al., 2005) and not due to nucleation and growth. This result and the obtained size distribution and development of the particles as a function of annealing temperature would not have been possible to obtain by x-ray diffraction or transmission electron microscopy. The obtained results allow developing a simple kinetic model for the decom-position process of TiAlN coatings. Furthermore, the effectiveness of additional alloying elements in influencing this decomposition process can now be investigated.

References

Mayrhofer, P.H. et al. (2003). Appl Phys. Lett. 174, 2049–2051.
Glatter, O. (1977). J. Appl. Cryst. 10, 415–421.
Glatter, O. (1980). J. Appl. Cryst. 13, 7–11.
Guinier, A., Fournet, G. (1955). *Small-Angle Scattering of X-Rays*. John Wiley&Sons, Chapman & Hall.
Kinning D.J., Thomas E.L. (1984). Macromolecules 17, 1712–1718.
Kostorz, G. (1979). In: *Treatise on Materials Science and Technology, Vol. 15: Neutron Scattering*, edited by G. Kostorz, H. Herman, pp. 226-288. New York: Academic Press.
Pedersen J.S. (1994). J. Appl. Cryst. 27, 595–608.
Mayrhofer, P.H., Music, D., Schneider, J.M. (2005). Appl. Phys. Lett., submitted.

GKSS FORSCHUNGSZENTRUM in der HELMHOLTZ-GEMEINSCHAFT	**EXPERIMENTAL REPORT**	**GeNF SANS-2**

The effect of heat treatment on the precipitation of Al-Si alloys

Proposers:	**Hans Peter Degischer**[1], **Anke Pyzalla**[1] [1]Vienna University of Technology
Experimental Team:	**Rodrigo Coelho**[1], **Guillermo Requena**[1],**Fernando Lasagni**[1], **Klaus Pranzas**[2], **Helmut Eckerlebe**[2] [2]GKSS Research Centre
User Group Leader:	**Anke Pyzalla**[1]
Date(s) of Experiment:	17th–25th August 2005

Objetives

Thermal stability of Al-Si alloys is an important property for their application in engine components. During solution treatment, Si dissolves substitutionally in a fcc cell. During precipitation, Si changes to a diamond structure with higher atomic volume than Al-Si fcc [1]. Therefore, the precipitation of Si causes an expansion of the alloys [2,3]. By TEM observation, it was found that the morphology of Si precipitates depend strongly with the "aging" temperature and previous thermal history of the material. The objective of this work is to determine the size and shape of Si precipitates of an Al-Si alloy after different heat thermal treatments.

Experiment

Description of Materials

An AlSi1.7 alloy was produced using a squeeze casting process by LKR Ranshofen, Austria. The Al-Si binary system presents a simple phase diagram, with an eutectic point close to 12.2 wt.% Si, between an aluminium solid solution of only 1.6 wt.% silicon at the eutectic temperature (~ 577 °C) and pure-Si as the second phase. The composition of the alloy is depicted in Table 1.

Table 1: Composition of the AlSi1.7 alloy [wt.%], rest Al.

Alloy	Si	Fe	Cu	Ni
AlSi1.7	1.74	0.0655	0.0024	0.0049

Different thermal treatments were carried out as shown in Table 2. The T4 solution treatment was carried out in a Linn High Therm furnace model 70.26 followed by water quenching. T6* and T6 thermal treatments were performed after T4 in TMA (Thermomechanical Analyser) 2940 CE dilatometer. T4a and T7* thermal treatments were totally performed in the dilatometer.

Table 2: Designation of the thermal treatments.

T1: as-cast						
T4: T1 +540°C/4h + H_2O						
T4a: T1 +540°C/4h →20K/min→RT						
Temperature [°C]	175	200	250	300	370	420
T4:RT to T+H_2O	**T6*a**	**T6*b**	**T6*c**	**T6*d**	**T6*e**	**T6*f**
T4:RT to T/1h+H_2O		**T6a**		**T6b**		
T4:RT to T/10h+H_2O		**T6c**				
T4a:RT to T+H_2O		**T7*b**	**T7*c**	**T7*d**	**T7*e**	**T7*f**

Theory:

DSC runs of water quenched AlSi1.7 samples show an exothermic peak between 200–300°C (Figure 1 a)-A) due to the formation of Si precipitates, which agrees with previous investigations [4,5]. During solution treatment Si dissolves substitutionally in an fcc cell which has an atomic volume of $6.60 \times 10^{-23} cm^3$/at. During precipitation, Si changes to a diamond structure with an atomic volume 23% higher ($8.01 \times 10^{-23} cm^3$/at) than in Al-Si fcc. Therefore, Si precipitation causes an expansion of the alloys, which could reach 0.27vol% if all 1.2 % Si dissolved at 540 °C could be quenched. The exothermic peak for T4 condition observed by DSC coincides with the CTE peak calculated from Δl vs T-curves (about 56 $ppmK^{-1}$). The precipitation peak is followed by an endothermic reversion up to the end of the measured temperature interval (Figure 1 a)-B). This peak B at 510 °C is due to the dissolution of Si causing a reduction in the atomic volume to that of Al-fcc again confirmed by the reduction of the CTE.

Figure 1-b) depicts the coefficient of thermal expansion and heat flow vs. temperature of AlSi1.7 samples after slow cooling at 1 (T4b) and 20K/min (T4a) from solution treatment temperature. T4a condition presents an exothermic peak at 420 °C (Figure 3b-A) of about 0.006W/g, whereas in T4b no exothermic formation of Si precipitates was observed. This temperature range A agrees with the CTE peak for T4a, which amounts to $35 ppmK^{-1}$. In the DSC curve for T4a condition, an endothermic peak (B) at about 510°C was observed after the exothermic precipitation of Si (A). AlSi1.7 in T4b presents also an endothermic effect starting at lower temperatures (~360 °C). Both endothermic effects are related to the dissolution of Si causing a reduction in the measured CTE at same temperature range, like in the T4 condition.

It is important to note that both the exothermic (A) and endothermic (B) peak shift considerably from lower to higher temperatures from the T4 condition to T4a.

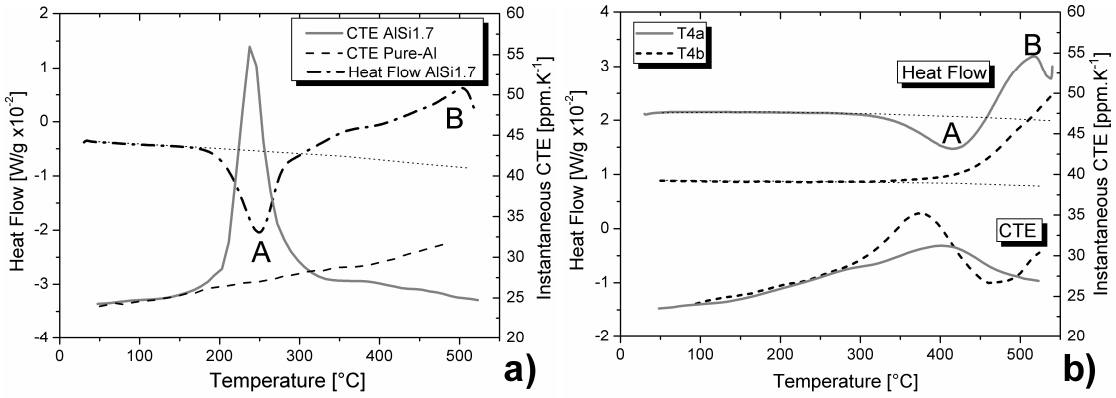


Figure 1: Instantaneous CTE and DSC heat flow vs. temperature of AlSi1.7 in comparision with Pure-Al after a) 4 hours of ST at 540 °C + water quenching (T4) b) 540°C/4h + slow cooling at 1 (T4b) and 20K/min (T4a) to RT.

The SANS experiments were carried out at RT for 20x20x4 mm³ samples heat treated as described in Table 1. The measurements were performed at distances of 1, 9 and 21 m between the detector and the sample with measurement times of 1 h per position.

Achievements and Main Results

The scattering curves of AlSi1.7 in the T4 condition shows roughly similar results to that on the T4a condition with a detachment of both curves at intermediate cross sections values of the curve. Supersaturation of Si is expected in T4 whereas incoherent Si platelets were observed in T4 by TEM observation [2]. Cross section vs. q vector of samples in the T6* conditions show all similar results, although formation of Si precipitates was expected for the T6*c,d conditions. Figure 3 a) depicts the evolution of Si precipitation after T4a. The scattering curves of AlSi1.7 in T7*d and T7*e shows a marked difference compared to the T7*b,c curves (where the presence of small Si platelets was expected). As in DSC runs, the forma-

tion of Si precipitates is observed at higher values of q. After that, the scattering curve decrease in the T7*e condition to that of T7*b,c due to the dissolution of Si. Although TEM observation reveals the formation of Si incoherent precipitates in the T6b and T6c conditiond, the cross section shows similar for all T6 conditions. The detection of Si precipitates by this technique is still being studied since the contrast between Al and Si, results in SLDD of about $5.2x10^7$ which is up to three orders of magnitude smaller than for Al-Fe, Al-Mg and Al-Cu systems.

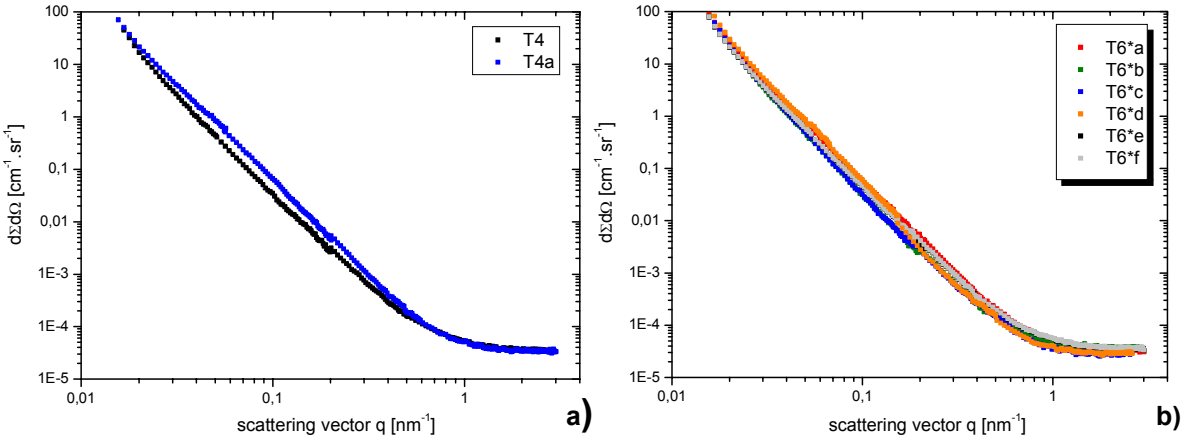


Figure 2: Cross section vs. scattering vector of AlSi1.7 a) T4 and T4a condition, and b) T6* conditions.

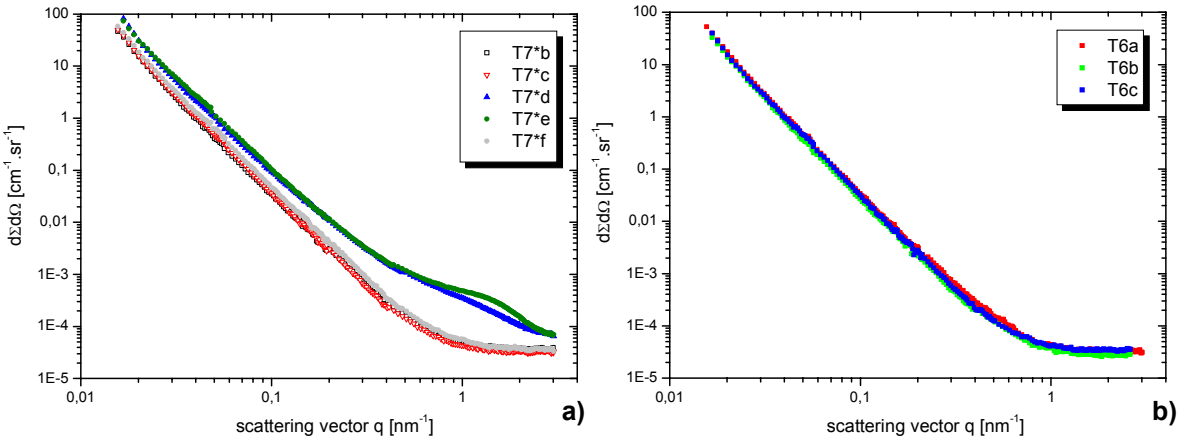


***Figure 3*:** Cross section vs. scattering vector of AlSi1.7 a) T7* conditions, and b) T6 conditions.

References

[1] Van Mourik P., de Keijser Th.H., Mittemeijer E.J.; Scripta Metallurgica, Vol. 21 (1987), 381–385.

[2] Lasagni F., Requena G., Degischer H.P., Mingler B., PapakyriacouM.: In: Proceedings Metallographie Tagung. Eds.: Pohl M., Petzow G, Bochum, Werkstoff-Informationsgesellschaft GmbH, Vol. 36, 2004, p. 443–448.

[3] Lasagni, F.; Degischer, H.P.; Papakyriacou, M.: accepted for publication. Journal of Metallic Materials (2005).

[4] Hälldahl L.: Thermochimica Acta, 214, 1993, p. 33.

[5] Starink M.J., Zahra A.-M., Philosophical Magazine A, Vol.77 No.1 (1998) 187–199.

GKSS FORSCHUNGSZENTRUM in der HELMHOLTZ-GEMEINSCHAFT	**EXPERIMENTAL REPORT**	**GeNF SANS-2**

Investigation of magnetic and structural properties of nanosystems with cobalt embedded into mesoporous silica and alumo-silicate matrices

Proposer:	**Sergey V. Grigoriev**, [1] PNPI, Gatchina, St-Petersburg, 188300, Russia
Co-Proposers:	**Natalia A. Grigoryeva,** [2]SPSU, St-Petersburg, 198504, Russia
Experimental Team:	**Natalia A. Grigoryeva[2], P. Klaus Pranzas[3], Helmut Eckerlebe[3],** [3]GKSS Research Centre
User Group Leader:	**Sergey V. Grigoriev[1]**
Date(s) of Experiment:	October 2005

Objectives

The proposal was aimed to investigate magnetic and structural features of a new class of nanocomposites based on silica and alumo-silicate matrices with embedded cobalt nanoparticles. Mesoporous silica and alumo-silicate are the promising potential matrices for the preparation of nanocomposites. One could expect that the size and the shape of nanoparticles incorporated into the matrices would be consistent with the dimensions of the porous framework. A hydrophobic metal complex $Co_2(CO)_8$ was introduced into the hydrophobic part of the as-prepared meso-SiO_2/surfactant or meso-Al/SiO_2 composite. Decomposition of $Co_2(CO)_8$ was carried out by UV-irradiation in vacuum for 10 hours. To provide better crystallinity of cobalt nanowires we performed additional annealing in hydrogen flow at temperatures of 300, 350 and 400 °C for 3 hours for silica matrix and 300, 400 and 500 °C for 3 hours for alumo-silicate matrix. The samples obtained were denoted as Co-SiO_2-300, Co-SiO_2-350, Co-SiO_2-400, Co-MAS-300, Co-MAS-400 and Co-MAS-500, respectively. The magnetic nanocomposites have been studied by Small Angle Polarized Neutron Scattering (SAPNS) in order to reveal the effect of annealing on their properties.

.

Experiment

The SAPNS experiments were carried out at the SANS-2 scattering facility of FRG-1 research reactor in Geesthacht. A polarized beam of neutrons with an initial polarization of P_0=0.94, the neutron wavelength λ=5.8 Å ($\Delta\lambda/\lambda$=0.1) and a divergence of 1.5 mrad was used. The temperature and magnetic field were changed in the range of temperatures 10K – 300 K and magnetic fields 0 – 300 mT, respectively.

Achievements and Main Results

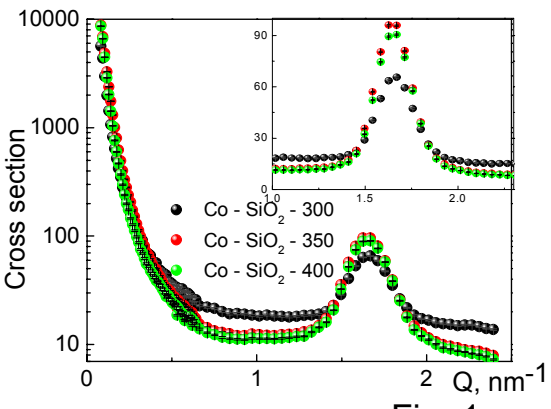


Fig. 1.

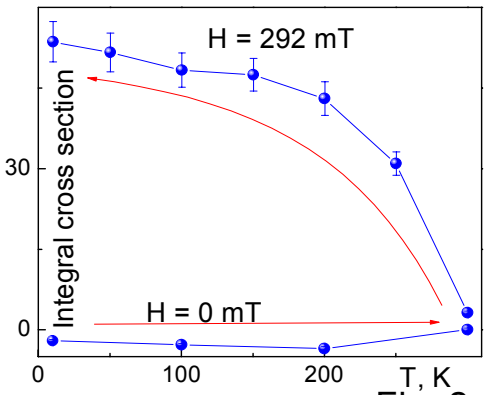


Fig. 2.

Q-dependence of the neutron scattering cross-section is presented in Fig.1 for the samples Co-SiO_2-300, Co-SiO_2-350, Co-SiO_2-400 and in Fig.3 for the samples Co-MAS-300, Co-MAS-400 and Co-MAS-500, respectively. The diffraction peak corresponds to the scattering on the regular two-dimensional structure of nanotubes in randomly oriented single particles. The Bragg reflection is imposed on the background consisting of two contributions: (i) small angle scattering on the individual channels and nanowires and incoherent q-independent scattering. The incoherent contribution is different for the samples, which were annealed at different temperature, the higher annealing temperature, the less incoherent background. This is related to amount of hydrogen inside pores. The coherent part of the small angle scattering is much larger for the samples of alumo-silicate matrices, what is attributed to imperfectness of the hexagonal structure in case of Al to Si substitution.

The field-dependent and temperature-dependent scattering intensity was extracted as I_H (q) = I(q,H) - I(q,0) and I_T (q) = I(q,T) - I(q, 300K). The samples Co-SiO_2-300 and Co-MAS-300 have shown the largest field-dependent part of the scattering in the series. We summarized the scattering intensity I_T(q) and I_H(q) over the Bragg peak. The temperature dependent part of the integral cross section is shown in fig.2 for Co-SiO_2-300 and in Fig.4 for Co-MAS-300. The samples were, first, heated up in Zero Field and, second, cooled down in the field of H = 292 mT. The figures demonstrate no temperature dependence in Zero Field regime and an increase of the cross-section with saturation for Field Cooling regime.

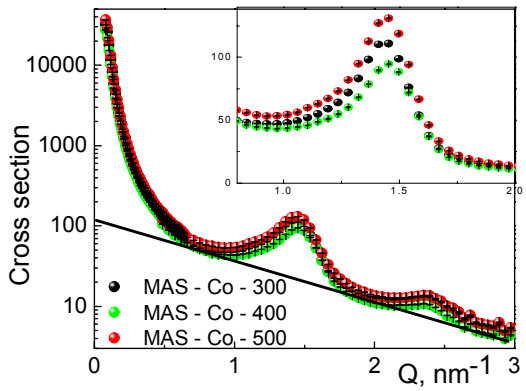


Fig. 3.

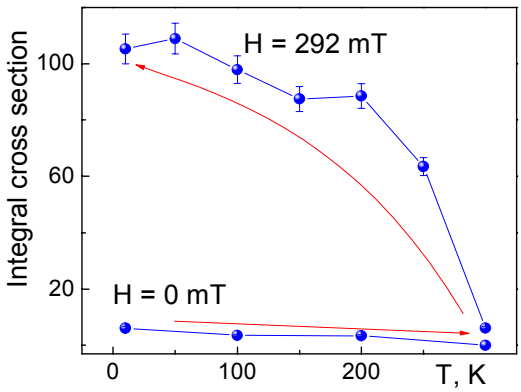


Fig. 4.

The field-dependent part of the integral cross section was measured in the field range from -292 mT to +292 mT for Co-SiO_2-300 at T=10 K and T=300 K in fig.5 and Fig.6, respectively. The measurements reveal a large hysteresis in field dependent part of the cross-section I_H(q) different for two different temperatures. As a conclusion, the temperature and magnetic field behaviour of the magnetic contribution into diffraction peak shows existence of the hexagonal structure of the magnetic nanowires in the sample. Further treatment and interpretation of the data are in progress.

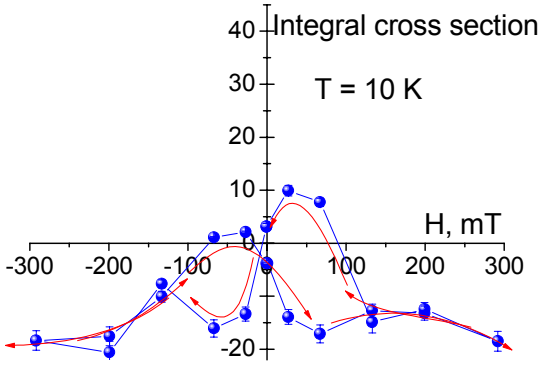


Fig. 5.

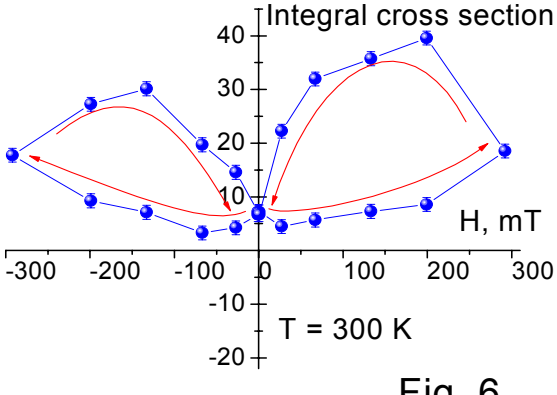


Fig. 6.

GKSS FORSCHUNGSZENTRUM in der HELMHOLTZ-GEMEINSCHAFT	EXPERIMENTAL REPORT	GeNF SANS-2

Low temperature properties of the helix structure in MnSi under applied field

Proposer:	**Sergey V. Grigoriev,** [1]PNPI, Gatchina, St-Petersburg, Russia
Co-Proposers:	**Alexey Okorokov,** [1]PNPI, Gatchina, St-Petersburg, Russia
Experimental Team:	**Sergey V. Grigoriev,** **Helmut Eckerlebe[2],** [2]GKSS Research Centre
User Group Leader:	**Sergey Grigoriev**

Date(s) of Experiment:	25–30 September 2005

Objectives

The weak itinerant ferromagnet MnSi with the space group $P2_13$ and the lattice constant a=0.4558 nm has ordered below T_c= 29 K in a left-handed ferromagnetic spiral along the ⟨1 1 1⟩ directions with a propagation vector **k** = (2π/a) (ξ, ξ, ξ), where ξ= 0.017 [1,2]. The helicity is realized by an antisymmetric Dzyaloshinski-Moriya (DM) exchange interaction caused by the lack of a center of symmetry in Mn atomic arrangement [3,4]. This DM interaction is isotropic itself but another weak anisotropic exchange (AE) interaction fixes a direction of the magnetic spiral along one of the cube diagonals. The magnetic behaviour of MnSi under applied magnetic field is puzzling. It is believed that at $T << T_c$ the magnetic spiral domains transform into a single domain in a weak magnetic field H_{C1} of order of 50 mT and a conical phase appears. The cone angle decreases as the field increases and the induced ferromagnetic state appears at H_{C2} = 600 mT. As was also shown in [1], when the direction of the applied magnetic field **H** is not collinear to one of the ⟨1 1 1⟩, the direction of the helix wavevector **k** follows the direction of the magnetic field. The period of the helix does not depend on the direction of the field. The **k**-rotation effect was recently interpreted by Maleyev on the basis of evaluation of the ground state energy and spin wave spectrum for MnSi [5]. The presence of a gap in spin wave spectrum was predicted, which must influence strongly the helix structure in presence of the field. The SANS experiments were aimed to study the spin structure of MnSi under applied field at low temperature and thus to examine this new theory.

Experiment

1. Sample

The single crystal MnSi was chosen for the study. The sample was a disc with a thickness of 1.5 mm and a diameter of 15 mm. The crystallographic mosaic and orientation of the sample was tested on the X-ray diffractometer at GKSS (Germany). The average value of the FWHM over all measured reflections is 0.25°.

2. Small-angle neutron scattering

Small-angle neutron scattering (SANS) measurements were carried out with the instrument SANS-2 at the Geesthacht Neutron Facility (GeNF). Neutrons with a mean wavelength of λ = 0.58 nm and a wavelength spread of Δλ/λ = 10 % were used. Sample - Detector distance of 4 m was used with appropriate collimations to cover scattering vectors *q* from 0.06 nm^{-1} to 0.6 nm^{-1} ($q = (4\pi/\lambda)\sin(\theta/2)$ where 2θ is the scattering angle). The field ranged from 0 to 800 mT was directed along [1 1 1] axis. The magnetic structure of MnSi has a complicated irreversible behavior at H≠0. Therefore, it is important that the scattering intensity is meas-

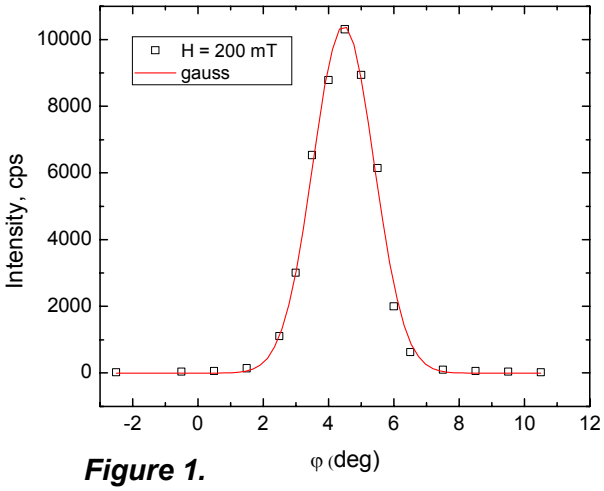


Figure 1.

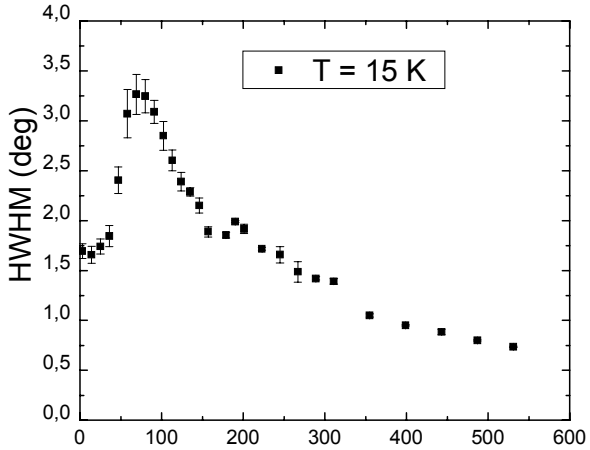


Figure 2.

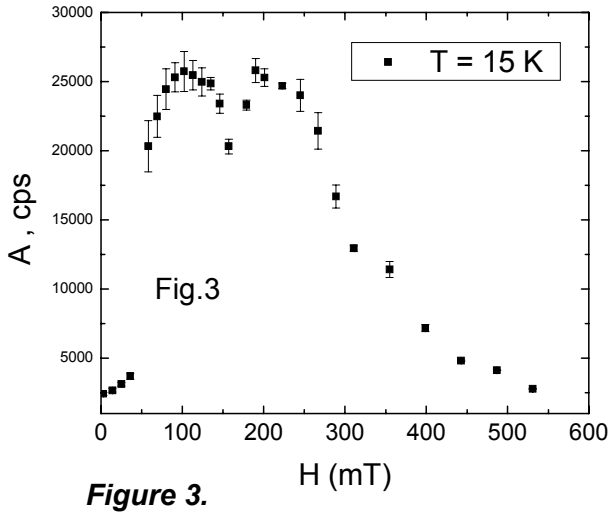


Figure 3.

ured in the following way: (i) zero field cooling from the paramagnetic state to the temperature of the interest; (ii) uprising field from H = 0 to the field value of the interest; and (iii) the magnetic field direction is fixed with respect to the sample in the rocking scan experiment .Using this principles the rocking curves of the Bragg peak (111) were taken at different values of the field at T = 15 K.

Achievements and Main Results

The typical example of the rocking curve is shown in Fig.1 for H = 80 mT. The curve is well fitted by the Gauss function: $I(\varphi) = I_{BG} + (2/\pi)^{1/2}(A/\Delta_M)\exp(-2(\varphi-\varphi_c)^2/\Delta_M^2)$, where I_{BG} is a small value. The integral intensity A, the center of the Gaussian φ_c, and its HWHM, or mosaic of the helix structure, were obtained from the fit. First, the magnetic mosaic Δ_M = 2 HWHM ~ 3.2° is much larger than the mosaic of the crystallographic structure Δ_{CR} = 0.25°. The value of Δ_M does not change significantly with temperature from 10 K to T_C. Figure 2 shows Δ_M as a function of the field. It increases up to the maximum at H = 70 mT and then decreases exponentially to the resolution level of order of 0.75°. The field dependence of the integral intensity A is shown in Fig.3. It is small at low H, then it increases sharply at H = 60 mT, and decreases again diminishing to zero at H_{C2} = 570 mT. It has a well-pronounced minimum at H_{ins} = 160 mT. Thus, we observe the magnetic structural instabitity at H_{ins} at low temperature T = 15 K similar to that in the critical range.

References

[1] Y. Ishikawa, K Tajima, D. Bloch and M.Roth, Soild State Commmun. **19** (1976) 525
[2] Y. Ishikawa, G. Shirane, J.A. Tarvin, M. Kohgi, Phys.Rev.B **16** (1977) 4956
[3] I.E. Dzyaloshinskii, Zh. Exp. Teor. Fiz. **46** 1420 (1964) [Sov. Phys. JETP **19**, 960 (1964)
[4] P.Bak, M.H.Jensen, J.Phys.**C13**, L881 (1980)
[5] S.V.Maleyev, Phys.Rev.B, in press (2005)

GKSS FORSCHUNGSZENTRUM in der HELMHOLTZ-GEMEINSCHAFT	**EXPERIMENTAL REPORT**	**GeNF SANS-2**

Investigation of the structural instability of the spin helix in MnSi under applied field near T_c.

Proposer:	**Sergey V. Grigoriev,** [1]PNPI, Gatchina, St-Petersburg, Russia
Co-Proposers:	**Alexey Okorokov,** [1]PNPI, Gatchina, St-Petersburg, Russia
Experimental Team:	**Sergey V. Grigoriev,** **Helmut Eckerlebe[2],** [2]GKSS Research Centre
User Group Leader:	**Sergey Grigoriev**

Date(s) of Experiment:	1–7 October 2005

Objectives

The weak itinerant ferromagnet MnSi with the space group $P2_13$ and the lattice constant a=0.4558 nm has ordered below T_c= 29 K in a left-handed ferromagnetic spiral along the ⟨1 1 1⟩ directions with a propagation vector **k** = (2π/a) (ξ, ξ, ξ), where ξ= 0.017 [1,2]. The helicity is realized by an antisymmetric Dzyaloshinski-Moriya (DM) exchange interaction caused by the lack of a center of symmetry in Mn atomic arrangement [3,4]. This DM interaction is isotropic itself but another weak anisotropic exchange (AE) interaction fixes a direction of the magnetic spiral along one of the cube diagonals. The magnetic behaviour of MnSi under applied magnetic field is puzzling. It is believed that at $T << T_c$ the magnetic spiral domains transform into a single domain in a weak magnetic field H_{C1} of order of 50 mT and a conical phase appears. The cone angle decreases as the field increases and the induced ferromagnetic state appears at H_{C2} = 600 mT. The situation becomes even more complicated near T_C. In presence of the magnetic field a new, so-called, A-phase was found at H_A ~ 160 mT and slightly below T_C by measuring the magnetization and magnetoresistance [5]. The AC susceptibility measurements had confirmed the presence of the A-phase [6]. The SANS experiments were aimed to study the spin structure of MnSi near T_C under applied field and thus to clarify the nature of the A-phase.

Experiment

1. Sample

The single crystal MnSi was chosen for the study. The sample was a disc with a thickness of 1.5 mm and a diameter of 15 mm. The crystallographic mosaic and orientation of the sample was tested on the X-ray diffractometer at GKSS (Germany). The average value of the FWHM over all measured reflections is 0.25°.

2. Small-angle neutron scattering

Small-angle neutron scattering (SANS) measurements were carried out with the instrument SANS-2 at the Geesthacht Neutron Facility (GeNF). Neutrons with a mean wavelength of λ = 0.58 nm and a wavelength spread of $\Delta\lambda/\lambda$ = 10 % were used. Sample – Detector distance of 4 m was used with appropriate collimations to cover scattering vectors *q* from 0.06 nm^{-1} to 0.6 nm^{-1} ($q = (4\pi/\lambda)\sin(\theta/2)$ where 2θ is the scattering angle). The incident beam was directed along the crystallographic axis [1 1

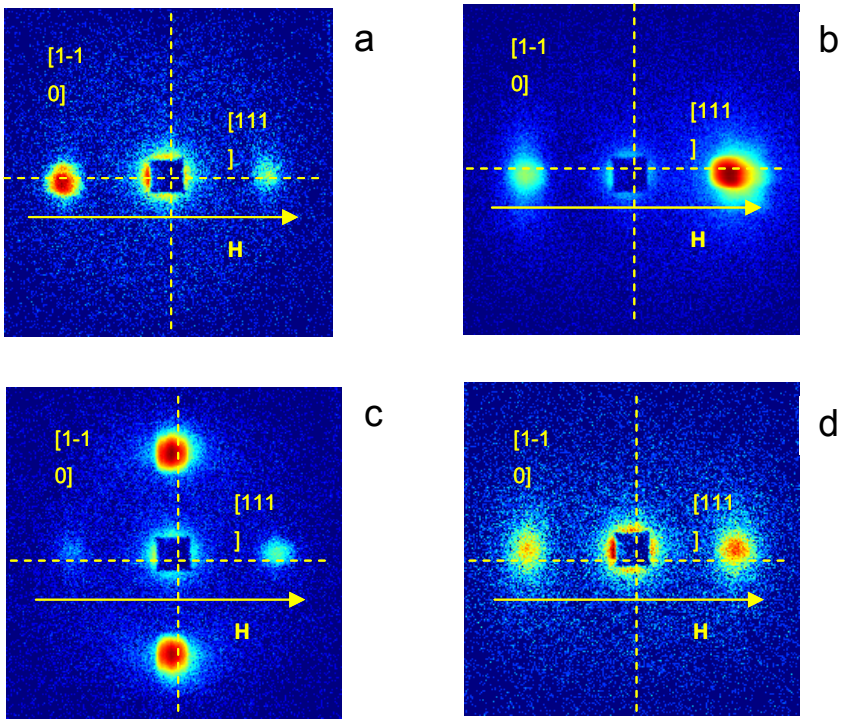
-2]. This configuration allows vectors parallel to [1 1 1] and [1 -1 0] be in the scattering plane and perpendicular to the beam. The field ranged from 0 to 800 mT was directed along [1 1 1] axis. The polarization followed the direction of the magnetic field. The scattering intensity was measured in the temperature range from T = 10 K to T = 50 K with accuracy better than 0.02 K.

Achievements and Main Results

Maps of the SANS intensities at T=28.5 K are shown in Fig.1 for four values of the magnetic field. At H = 0 (a) two reflections from the domains oriented along [111] are observed. When the magnetic field H > H_{C1} is applied along the [111] axis, it produces a magnetically uni-domain sample with the spin helix along the chosen axis. It is well seen that the field makes the scattering along [111] more intense (b). The magnetic field H ~ 150 mT leads to a collapse of the spiral structure along [111] and appearance of the reflections along [1 -1 0] (c). With further increase of the field above 180 mT the helix structure along [111] restores, while it vanishes along [1 -1 0]. At H = H_{C2} ~ 340 mT the helix transforms into the induced ferromagnet and Bragg reflections dissolve. The similar picture is observed for the critical scattering above T_c Thus, we observe the 90°-reorientation of the spin helix from the [111] axis to [1 -1 0] axis under magnetic field H ~ 150 mT applied along [111] in the close vicinity to T_c. The detailed analysis of the data is in progress.

References

[1] Y. Ishikawa, K Tajima, D. Bloch and M.Roth, Soild State Commmun. 19 (1976) 525.
[2] Y. Ishikawa, G. Shirane, J.A. Tarvin, M. Kohgi, Phys.Rev.B 16 (1977) 4956.
[3] I.E. Dzyaloshinskii, Zh. Exp. Teor. Fiz. 46 1420 (1964) [Sov. Phys. JETP 19, 960 (1964)].}
[4] P.Bak, M.H.Jensen, J.Phys.C13, L881 (1980).
[5] K.Kadowaki, K. Okuda, M. Date, J.Phys.Soc.Jpn. 51 (1982) 2433.
[6] C. Thessieu, C.Pfleiderer, A.N. Stepanov, J. Flouquet, J. Phys.Condens.Matter 9, 6677 (1997).



GKSS FORSCHUNGSZENTRUM in der HELMHOLTZ-GEMEINSCHAFT	**EXPERIMENTAL REPORT**	**GeNF SANS-2**

SAPNS study of system of nickel nanoparticles embedded into Al_2O_3

Proposer:	**Sergey V. Grigoriev**, [1] PNPI, Gatchina, St-Petersburg, 188300, Russia
Co-Proposers:	**Natalia A. Grigoryeva,** [2]SPSU, St-Petersburg, 198504, Russia
Experimental Team:	**Natalia A. Grigoryeva[2], P. Klaus Pranzas[3], Helmut Eckerlebe[3],** [3]GKSS Research Centre
User Group Leader:	**Sergey V. Grigoriev[1]**
Date(s) of Experiment:	November 2005

Objectives

The experiments were aimed to investigate the magnetic properties of the nickel nanoparticles embedded into the Al_2O_3 matrix by means of small angle polarized neutron scattering (SAPNS). This kind of information is important because magnetic nanomaterials are considered to be the most promising candidates for data storage devices [1]. However, the use of purely nanocrystalline systems is limited because of their low stability and tendency to form aggregates. One of the well-known solutions of the problem is encapsulation of the nanoparticles in a chemically inert matrix. Such an approach enables one to avoid aggregation of nanoparticles and protect them from the effect of external factors and therefore, makes it possible to take advantage of the specific properties of nanomaterials [2]. The aluminum oxide is a promising potential matrix for the preparation of magnetic nanocomposites. An aluminium plate is oxidized and the layer of Al_2O_3 is then exploited for preparation of the matrix. The channels/pores are burnt in this layer to produce hexagonal structure of these pores. These pores are treated by $C_2H_2O_4$ during 10-100 hours for different samples in order to increase a diameter of the pores. The nickel is electro-chemically introduced in these pores. In the TEM experiment a regular hexagonal structure of nanopores and nickel nanoparticles with periodicity a ≈ 100 nm is observed.

Experiment

1. Sample For this study we have prepared four matrices with different diameters of the pores Al_2O_3–100, Al_2O_3–100-0-5, Al_2O_3–150-0-5. One of the matrices was filled with Ni nanoparticles: Al_2O_3–100-Ni.

2. Small-angle neutron scattering SAPNS measurements were carried out with the instrument SANS-2 at the Geesthacht Neutron Facility (GeNF). Neutrons with a mean wavelength of λ = 0.58 nm and a wavelength spread of $\Delta\lambda/\lambda$ = 10% were used. Detector distances up to 16 m were used with appropriate collimations to cover scattering vectors q from 0.03 nm^{-1} to 0.18 nm^{-1}. An external magnetic field (0 and 733 mT) was applied in the horizontal plane and perpendicularly to the incident beam. We determine the total (nuclear and magnetic) scattering ($I(q) = I^+(q) + I^-(q)$) and the polarization dependent part of the scattering ($\Delta I(q) = I^+(q) - I^-(q)$) where $I^+(q)$ and $I^-(q)$ are the intensities for neutrons polarized parallel (+) and anti-parallel (-) to the magnetic field.

Achievements and Main Results

The spectra for matrices with different chemical treatment are presented in Fig. 1. The Bragg peaks correspond to the scattering on the regular structure of nanotubes. The period of the structure d is obtained from the Bragg law $\lambda = 2d\sin(\theta/2)$, or, $d = 2\pi/q_c \cong$ 92 nm, 97 nm, 98 nm for Al_2O_3–100, Al_2O_3–100-0-5 and Al_2O_3–150-0-5, respectively. The widths of the Bragg peaks are equal to 0.030 nm^{-1}, 0.026 nm^{-1} and 0.027 nm^{-1} for Al_2O_3–100, Al_2O_3–100-0-5

and Al_2O_3–150-0-5, respectively. Figures 2 shows that intercalation of nickel into the matrix does not shift the position of the Bragg peak what makes clear that the matrix was not destroyed by intercalation. The small angle scattering is significantly increased in the samples with Ni. This scattering at small q ($q< 0.04$ nm^{-1}) is caused by presence of individual nanowires. or formation of clusters. The field-dependent scattering intensity was extracted as $I_H(q) = I(q,H) - I(q,0)$ and is presented in Fig.3.

The polarization-dependent term of the scattering was extracted. It is well known that this term is determined by the nuclear–magnetic interference in the neutron cross-section. It can be written as: $\sigma_{Int}(\mathbf{q},\mathbf{P}_0) = 2 \langle \mathbf{P}_0 \mathbf{m}_{\perp q} \rangle A_n A_m \mathrm{Re}(F_{nm}(\mathbf{q}))$, where A_n, A_m are the nuclear and magnetic contrasts, $\mathbf{m}_\perp = \mathbf{m} - (\mathbf{me})\mathbf{e}$, $\mathbf{m}$ is the magnetization and $\mathbf{e} = \mathbf{q}/q$. The interference term shows the correlations existing in system between nuclear and magnetic objects and it is proportional to the average magnetization of the system. The positive nuclear-magnetic interference $\Delta I(q)$ is observed over the whole q-range under study but no or negative interference is visible at the Bragg peak (Fig.4). Further interpretation of the data is in progress.

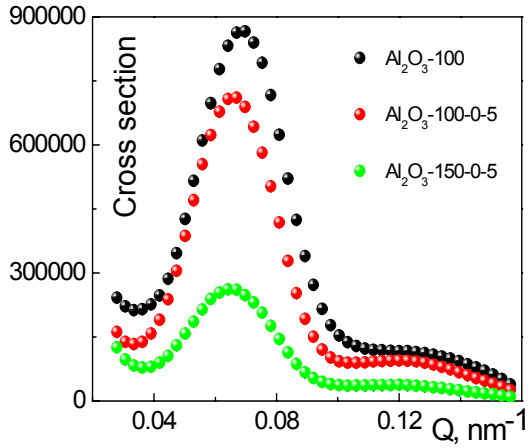


Fig. 1.

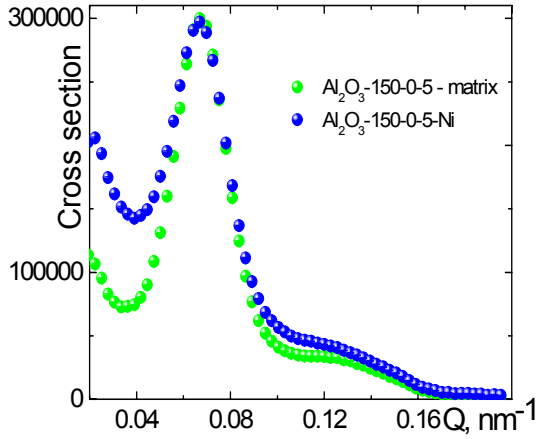


Fig. 2.

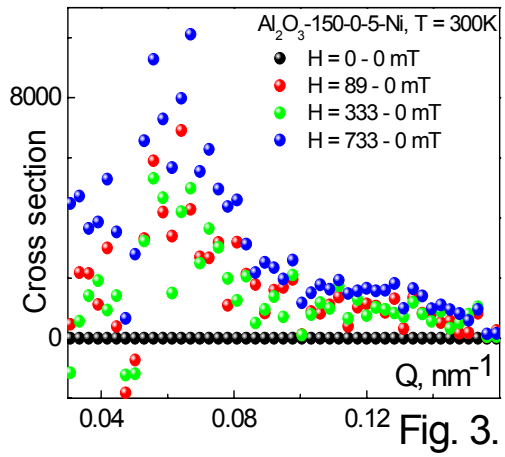


Fig. 3.

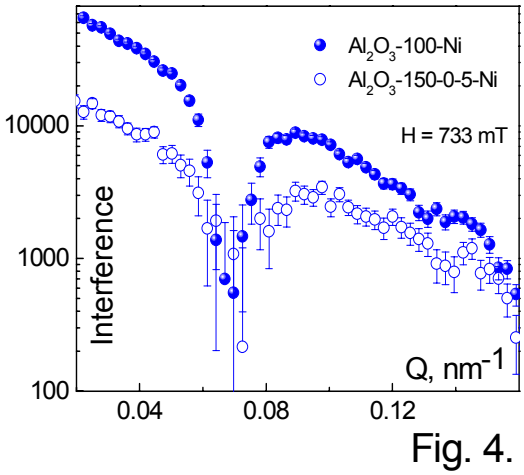


Fig. 4.

References

[1] L. Thomas, F. Lionti, R. Ballou, D. Gatteschi, R. Sessoli, B. Barbara, Nature **383** (1996) 145.

[2] K.J. Kirk, Contemp. Phys. **41** (2000) 61.

GKSS FORSCHUNGSZENTRUM in der HELMHOLTZ-GEMEINSCHAFT	EXPERIMENTAL REPORT	GeNF SANS-2

Temperature induced spin conversionin a molecular complex as seen by SANS

Proposer:	**Dmitry Chernyshov,** [1]
Co-Proposers:	**Sergey V. Grigoriev[2],**
	Karl WilhelmTörnroos[3],
	Brita Vangdal[3],
	[1]Swiss-Norwegian Beam Lines at the European Synchrotron Radiation Facility, Grenoble, France
	[2]Petersburg Nuclear Physics Institute, St.-Petersburg, Russia
	[3] Dept. of Chemistry, University of Bergen, Bergen, Norway
Experimental Team:	**D. Chernyshov [1],**
	S. V. . Grigoriev[2]
	H. Eckerlebe[4]
	P. K. Pranzas[4]
	[4]GKSS Research Centre
User Group Leader:	**K. W. Törnroos[3]**

Date(s) of Experiment:	25–30 October 2005

Objectives

Some octahedral iron(II) complexes assume two spin states – low spin (LS, S=0 singlet $t_{2g}^6e_g^0$) and high spin (HS, S=2, quintet $t_{2g}^4e_g^2$)) with an energy difference ~k_BT, and are therefore considered as bi-stable. The two distinct molecular states differ in volume, colour and magnetic state, implying a potential application as a memory unit or molecular switch [1]. The transition between two states is characterized by a transition curve relating space and time average of the spin states and temperature. This project aimed at following the spin conversion as a function of temperature for the molecular Fe(II) complex ($[Fe^{II}(2\text{-pic})_3]Cl_2$ 2-propanol solvate, pic=picolylamine**)** using SANS in order to probe the potential nuclear and magnetic response at the mesoscopic length scale (tens of nanometres).

Experiment

The crystal structure, thermodynamics and magnetic properties of the substance are known for several solvates of the $Fe^{II}(2\text{-pic})_3]Cl_2$ complex [2]. The small-angle scattering was studied with the SANS-2 instrument at the FRG-1 research reactor at Geesthacht. A beam polarized in the horizontal plane with a wavelength of 0.58 nm was used. Small-angle scattering from the polycrystalline sample was recorded with help of a 256x256 position-sensitive detector constructed at GKSS. The temperature on the sample position was varied between 40 and 230 K.

The nuclear scattering signal detected in the small-angle range was found to consist of a homogeneous and temperature-independent background, presumably due to the incoherent scattering from the structural hydrogen, and a θ-dependent small-angle scattering ~Q^{-4}. The homogeneity and absence of any temperature dependence of the background signal has been proven by measurements at the shortest possible sample-to-detector distance (~1 m) at various temperatures. The refined scattering exponent slightly fluctuates around a value of 3.8 and no deviations of scattering at low $Q^{-3.8}$ has been found for the small-angle scattering

even at the longest possible sample-to-detector distance (~17 m), for the temperatures probed. These observations indicate the presence of rather large static and temperature independent correlations with a radius of order of ~100 nm.
It is natural to assume that this scattering comes from the mosaic blocks of the crystalline material. Contrary to the scattering exponent and to the correlation length, the intensity of the small angle scattering is found to be temperature dependent and proportional to the fraction of molecules in the most dense low-spin state (Fig.1).
No magnetic scattering was observed in the small angle range.

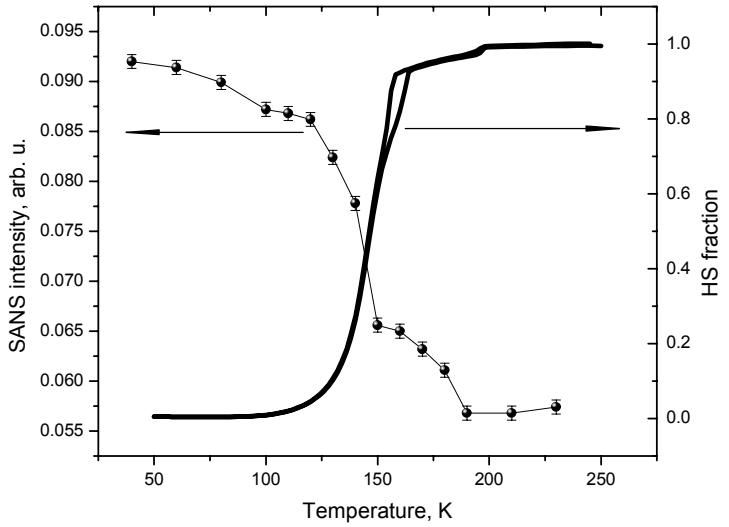


Figure 1: The intensity of the SANS scattering fitted from the data measured upon heating, and the fraction of HS molecules deduced from the SQUID measurement, as a function of temperature.

Achievements and Main Results

As far as we are aware of, this is the first application of the SANS technique for studying spin crossover in a molecular solid. The intensity of small-angle scattering is found to follow the transition curve deduced from macroscopic and structural properties thus showing the sensitivity of the SANS signal to the spin conversion process in molecular crystals.
X-ray diffraction has shown the presence of long-range correlations but also the absence of short-range correlations between molecules in the HS and LS states [3].
Our preliminary results of the SANS measurements indicate the lack of correlations at the mesoscopic scale as well. These observations strongly support a mean-field scenario of the spin crossover [4,5].

References

[1] *O. Kahn, C. J. Martinez, Science 279 ,1998, 44*
[2] *M. Hostettler, K. W. Törnroos, D. Chernyshov, B. Vangdal & H. B. Bürgi, Angew. Chem. Int. Ed. 43, 2004, 4589*
[3]. *D. Chernyshov, M. Hostettler, K. W. Törnroos and H.-B. Bürgi, Angew. Chem. Int. Ed. 42, 2003, 3825*
[4]. *D. Chernyshov, H.-B. Bürgi, M. Hostettler & K. W. Törnroos, Phys. Rev. B70, 2004, 094116*
[5]. *K. Boukheddaden, I. Shteto, B. Hôo, and F. Varret, Phys. Rev. B62, 2000, 14796.*

GKSS FORSCHUNGSZENTRUM in der HELMHOLTZ-GEMEINSCHAFT	EXPERIMENTAL REPORT	GeNF SANS-2

SANS study of the magnetic structure of $Tb_xY_{1-x}Mn_6Sn_6$ compounds

Proposer:	**Sergey V. Grigoriev**[1]
	[1]PNPI, Gatchina, St-Petersburg, 188300, Russia
Co-Proposers:	**Yury Chetverikov**[1]**, Aleksey Okorokov**[1]
Experimental Team:	**Yury Chetverikov**[1]**,**
	Helmut Eckerlebe[2]**,** [2]GKSS Research Centre
User Group Leader:	**Aleksey Okorokov**[1]

Date(s) of Experiment:	6– 20 November 2005

Objectives

The proposal was aimed to investigate the magnetic structure in the intermetallic compounds $Tb_xY_{1-x}Mn_6Sn_6$ ($0 \le x \le 0.25$) by means of small angle neutron scattering (SANS). In such intermetallic materials the competition between different exchange interactions results in a variety of the magnetic structures. Thus, giant magnetoresistance was recently found in this type of materials.

The YMn_6Sn_6 is a compound crystallized in hexagonal $HfFe_6Ge_6$-type structure (space group P6/mmm) [1]. The lattice has an intrinsically layered structure, where Mn atoms are organized in a so-called “kagome“ lattice within the ab planes, which are stacked along the c axis with Y and Sn_3 atomic planes between them. The Mn-Mn interplane distance through Sn_3 atomic plane is slightly larger than that through Y atomic plane. Below the Neel temperature T_N=333K the YMn_6Sn_6 compound has an incommensurate periodic structure [2]. It is believed that spins are ordered in the helix along the c axis similar to a simple planar helimagnet [3].

To make clear a role of different exchange interactions we studied samples where Y is partially substituted by Tb. The substitution of magnetic Tb for Y in the $Tb_xY_{1-x}Mn_6Sn_6$ compounds changes the magnetic ordering type from incommensurate antiferromagnetic to ferrimagnetic at the concentration $x \approx 0.2$. The ferrimagnets at $x > 0.2$ show a change of the magnetocrystalline anisotropy with increase of temperature from an easy-axis type to an easy-plane type through a conical phase [4].

Experiment

1. Samples. Samples of $Tb_xY_{1-x}Mn_6Sn_6$ were prepared as powders with x = 0; x = 0.175; x = 0.2; x = 0.225; x = 0.25 and with the particle size less than 0.1 mm^3. Compounds were made by melting the high purity metals in an induction furnace in argon atmosphere following by the homogenization annealing in argon at 800 C for 48 hours.

2. Small-angle neutron scattering. The use of SANS allows one to observe large-scale magnetic ordering modes such as long periodical structures, domain walls or critical spin fluctuations. The experiments were carried out at the SANS-2 scattering facility of FRG-1 research reactor in Geesthacht (Germany). Neutron beam with the neutron wavelength λ = 5.7 Å ($\Delta\lambda/\lambda$ = 0.1) and a divergence of 2.5 mrad was used. The scattered neutrons were detected by a position sensitive detector with (256 × 256) pixels. The scattering intensity was measured in the temperature range from T = 25 to 370 K.

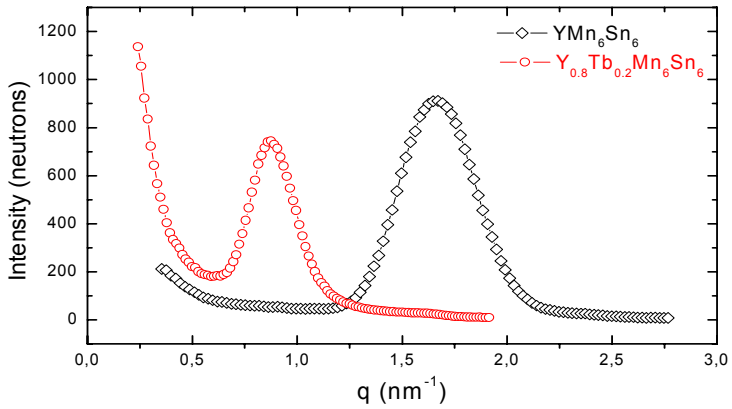


Figure 1: *q*-dependence of scattering intensity for different samples, at T = 175 K.

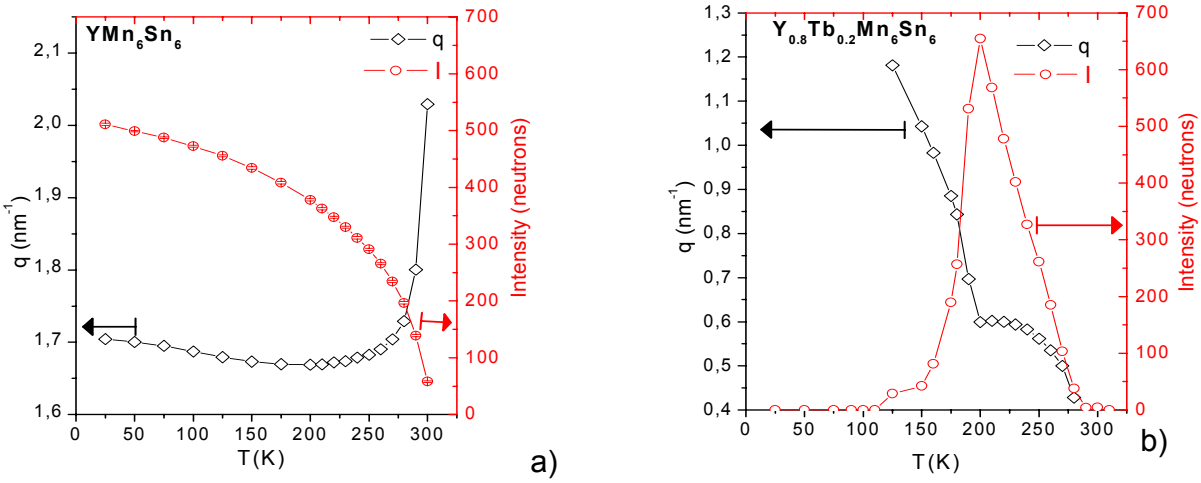


Figure 2. Temperature dependences of the peak's position and peak's intensities for YMn_6Sn_6 (a) and $Y_{0.8}Tb_{0.2}Mn_6Sn_6$ (b) samples.

3. Achievements and Main Results. The q-dependence of the neutron intensity for YMn_6Sn_6 and $Tb_{0.2}Y_{0.8}Mn_6Sn_6$ are presented in Fig. 1 (T = 175 K). Two contributions in both curves are well seen. The first one is a diffraction peak, which originates from the scattering on the magnetic long periodic structure. The second one is a small angle scattering attributed to the magnetic inhomogeneities such as domains or critical spin fluctuations.

The period of the magnetic structure calculated from diffraction peak position is d_{TB0} = 3.76 nm for YMn_6Sn_6 and is $d_{TB.2}$ = 7.06 nm for $Tb_{0.2}Y_{0.8}Mn_6Sn_6$. Coherent lengths of magnetic periodicity are w_{TB0} = 17 nm and $w_{TB.2}$ = 28 nm.

The total intensity of $Tb_{0.2}Y_{0.8}Mn_6Sn_6$ peak is smaller than that for YMn_6Sn_6 while small angle scattering for $Tb_{0.2}Y_{0.8}Mn_6Sn_6$ is much stronger. This may be caused by closeness of the $Tb_{0.2}Y_{0.8}Mn_6Sn_6$ magnetic structure to the ferrimagnet phase transition on the c-T phase diagram [4].

The position q_C and total intensity I of the YMn_6Sn_6 peak are shown in Fig.2 a as a function of temperature. Intensity of the peak decreases with the temperature and diminishes at $T=T_N$. The value of q_C has hardly remarkable decrease from 25 K to 200 K and increases sharply as temperature approaches to T_N = 333 K. It is supposed that the structure has a tendency to the commensurate antiferromagnet as $T \rightarrow T_N$. This temperature behavior is completely different from one for simple planar helimagnet [3].

Temperature behavior of $Tb_{0.2}Y_{0.8}Mn_6Sn_6$ peak is even more complex (Fig.2b). Below T = 125 K the incommensurate structural peak is suppressed. We believe that the structure

is purely ferrimagnetic in this temperature range. In the range 125 K < T < 200 K the diffraction peak appears and its intensity increases with increase of T while q_C decreases. This may be explained by appearance of the spin cone structure with the cone angle α, which increases with temperature. The T- behavior changes at T = 200 K. The intensity decreases to zero at $T \rightarrow T_N$ and the position of the peak is constant for $T \in$[200 K–240 K] and then it decreases down to zero at 300 K. The last observation may correspond to the formation of the ferrimagnet with the easy-plane anisotropy. The interpretation of the obtained results is in progress.

References

[1] R.R. Olenich, L.G. Akselrud, Y.P. Yarmoliuk, Dopov. Akad. Nauk Ukr. RSR Ser. A 2, 84 (1981).

[2] G. Venturini, D. Fruchart, B. Malaman, J. Alloys Comp. 236,102 (1996)

[3] P. de V. Du Plessis, A.M. Venter, G.H.F. Brits, J.Phys.: Condens.Matter 7, 9863 (1995).

[4] N.K. Zajkov, N.V. Mushnikov, E.G. Gerasimov, V.S. Gaviko , M.I. Bartashevich, T. Goto, V.I. Khrabrov, J. Alloys Comp. 363, 40 (2004)

GKSS FORSCHUNGSZENTRUM in der HELMHOLTZ-GEMEINSCHAFT	EXPERIMENTAL REPORT	GeNF SANS-2

Investigation of the magnetic structure of the ferromagnet $ZrZn_2$.

Proposer:	**Stephanie Pouget**[1], [1]6 rue Jules Horowitz 38043 Grenoble Cedex France
Co-Proposers:	**Sergey V. Grigoriev**[2], [2]PNPI, Gatchina, St-Petersburg, 188300, Russia **Niels van Dijk**[3], [3]Delft University of Technology, Mekelweg 15, 2629 JB Delft, The Netherlands
Experimental Team:	**Niels van Dijk**[3], **Sergey Grigoriev**[2], **Helmut Eckerlebe**[4], [4]GKSS Research Centre
User Group Leader:	**Sergey V. Grigoriev**[2]
Date(s) of Experiment:	1–7 November 2005

Objectives

In 1958, Matthias and Bozorth [1] discovered that despite being made from non magnetic elements, $ZrZn_2$ becomes ferromagnetic at low temperature. This compound crystallizes in the C15 cubic Laves structure, and the 4d orbitals of the Zr atoms (which form a diamond structure lattice) are responsible for the magnetic behaviour. This behaviour is characterized by a rather low Curie temperature T_C= 28.5 K, compared to other ferromagnetic metals, and a weak saturation moment of 0.17 μ_B. Some 40 years later, superconductivity at ambient pressure was observed at T ~ 0.3 K in the ferromagnetically ordered phase of $ZrZn_2$ [2]. This came after the discovery of superconductivity in UGe_2, below 1 K, and within a limited pressure range [3], which had provided an unanticipated example of coexistence of superconductivity and ferromagnetism. The electronic pairing mechanism needed for superconductivity is believed to be magnetic in origin for both materials.
Muon spin rotation measurements have recently been performed on a $ZrZn_2$ sample, which again gave unexpected results [4,5]. The measured coherent muon signal at helium temperature cannot be explained by a normal ferromagnetic structure, but it could be explained by the presence of a long-range magnetic modulation. We propose to check this hypothesis by looking for low Q magnetic satellites and investigating their temperature dependence.

Experiment

1. Sample

The polycrystalline sample $ZrZn_2$, a tablet of 1.2 mm in thickness and 8 mm in diameter, has been studied. The sample is the same as used for investigations [4,5].

2. Small-angle neutron scattering

Small-angle neutron scattering (SANS) measurements were carried out with the instrument SANS-2 at the Geesthacht Neutron Facility (GeNF). Neutrons with a mean wavelength of λ = 0.58 nm and a wavelength spread of $\Delta\lambda/\lambda$ = 10 % were used. Detector distances up to 10 m were used with appropriate collimations to cover scattering vectors q from 0.03 nm^{-1} to 2.5 nm^{-1} ($q = 4\pi\sin(\theta)/\lambda$ where 2θ is the scattering angle). The scattering intensity was measured in the temperature range from T = 10 K The magnetic contribution to the scattering was extracted as $I_m(q) = I(q,T) – I(q,T$ = 60 to T = 60 K. The external magnetic field **H** from

1 to 900 mT was applied. K). The polarization-dependent cross-section was measured also in so-called, "inclined" geometry, when the magnetic field is inclined at the angle $\varphi = 45^{o}$ with respect to the incident beam **k**. This geometry allows one to observe the left-right asymmetry in SAPNS pattern that originate from the interaction of the neutron spin with the chiral dynamical excitations, i.e. with the spin waves. It is separated from other contributions as the asymmetric part of the polarization dependent scattering: $\Delta I(\theta) = [I_{+}(\theta)+I_{-}(-\theta)-I_{+}(-\theta)-I_{-}(\theta)]$, where $I_{+}(\theta)$ and $I_{-}(\theta)$ are intensities with the polarization directed along and opposite to the field.

Achievements and Main Results

Q-dependence of SANS intensity is presented in Fig.1 for two different temperatures T = 10 K and T = 25 K. We calculated the integral scattering intensity over the whole q-range: $I_{int} = 2\pi\int I(q)qdq$. The temperature dependence of I_{int} is shown in Fig.2. The magnetic field suppresses this scattering (Fig.3). This scattering is attributed to inelastic scattering, i.e. to spin waves. The polarization-dependent cross-section was measured in the inclined geometry and integrated over q ($\Delta I_{int} = 2\pi\int\Delta I(q)qdq$) is plotted in fig.4 as a function of the magnetic field at T = 25 K. The scattering is observed in the range of fields 0 < H < 100 mT. The interpretation of the results obtained is in progress.

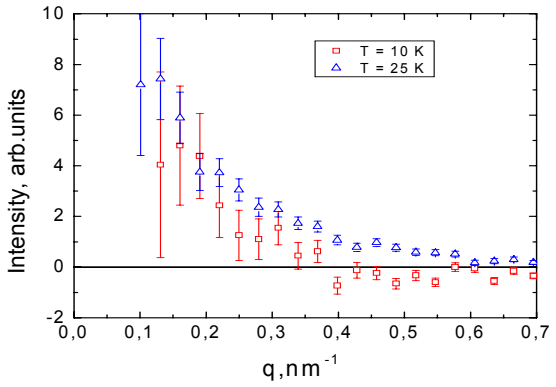


Figure 1: *Scattering Pattern at 10 and 25 K.*

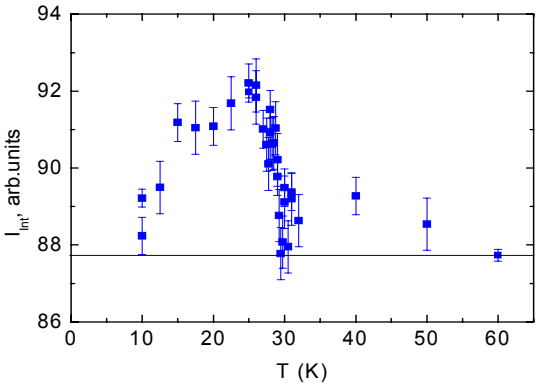


Figure 2: Temperature dependence of I_{int}.

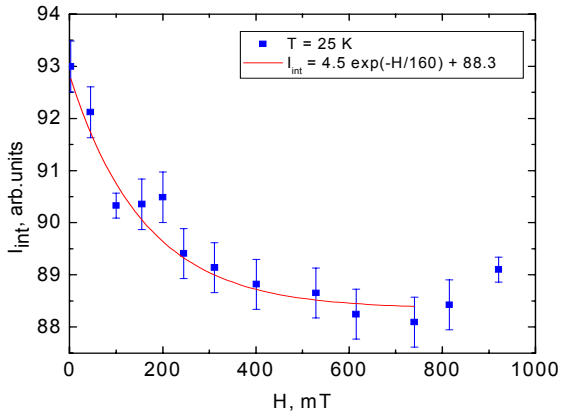


Figure 3: *Magnetic field dependence of I_{int}.*

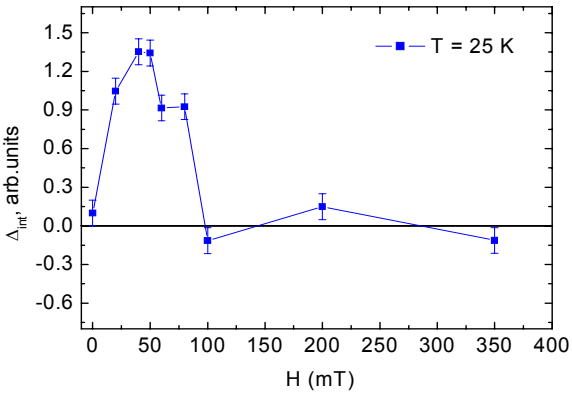


Figure 4: *Magnetic field dependence of the polarization-dependent cross-section.*

GKSS FORSCHUNGSZENTRUM in der HELMHOLTZ-GEMEINSCHAFT	EXPERIMENTAL REPORT	GeNF SANS-2

SANS study of new magnetic nanocomposites based on mesoporous silica with embedded Fe-particles.

Proposer:	**Sergey V. Grigoriev**, [1] PNPI, Gatchina, St-Petersburg, 188300, Russia
Co-Proposers:	**Natalia A. Grigoryeva,** [2]SPSU, St-Petersburg, 198504, Russia
Experimental Team:	**Natalia A. Grigoryeva[2], P. Klaus Pranzas[3], Helmut Eckerlebe[3],** [3]GKSS Research Centre
User Group Leader:	**Sergey V. Grigoriev[1]**
Date(s) of Experiment:	September 2005

Objectives

Modern information technologies require development of novel high-density data storage devices due to colossal growth of digital information volume. The materials used as a recording media should meet numerous requirements: 1) the size of the magnetic particles should be much less than the size of magnetic domain in bulk material (usually 500–1000 nm), 2) magnetic particles should possess large magnetic moment, large remanence and large coercive force, which are necessary both for steady reading the information, and it's time stability. The special role in creation of the components for such devices belongs to high-quality nanostructure and nanocomposites with detached and strongly anisotropic magnetic nanoparticles. This proposal aimed to investigate magnetic properties of a new class of nanocomposites (Fe-SiO_2) based on silica matrix with hexagonal arrangement of cylindrical pores ($a_0 \approx 4$ nm) and embedded iron nanoparticles (2 x 100 nm^2), which is promising material for a novel high-density data storage devices.

Experiment

Small-angle neutron scattering (SANS) measurements were carried out with the instrument SANS-2 at the Geesthacht Neutron Facility (GeNF). A polarized beam of neutrons with an initial polarization of $P_0 = 0.94$, the neutron wavelength $\lambda = 5.8$ Å ($\Delta\lambda/\lambda = 0.1$) and a divergence of 1.5 mrad was used. An external magnetic field (0 ÷ 292T) was applied in the horizontal plane and perpendicularly to the incident beam. Temperature was changed from 10 K to 300 K. We determine the total (nuclear and magnetic) scattering ($I(q) = I^+(q) + I^-(q)$) and the polarization dependent part of the scattering ($\Delta I(q) = I^+(q) - I^-(q)$) where $I^+(q)$ and $I^-(q)$ are the intensities for neutrons polarized parallel (+) and anti-parallel (-) to the magnetic field.

Achievements and Main Results

Q-dependence of the neutron scattering for mesoporous silica is typically presented as a diffraction peak, which corresponds to the scattering on the regular two-dimensional structure of nanotubes in randomly oriented single particles. The period of the structure d is obtained from the Bragg law $\lambda = 2d \sin(\theta/2)$, or, $d = 2\pi/q_c \cong 3.8$ nm. The small angle scattering is observed also and attributed to scattering on the individual channels and nanowires. The field-dependent and temperature-dependent scattering intensity was extracted as $I_H(q) = I(q,H) - I(q,0)$ (Fig.1) and $I_T(q) = I(q,T) - I(q, 300K)$ (Fig. 4), respectively. We summarized the scattering intensity over the Bragg peak and plotted the integral cross section as a function of the

field in the range from -292m T to + 292 mT at T = 300 K (Fig.2). The measurements reveal a large hysteresis in field dependent part of the cross-section $I_H(q)$. The nuclear-magnetic interference $\Delta I(q)$ is observed in the small q-range only but no interference is visible at the Bragg peak. The interference term shows the correlations existing in system between nuclear and magnetic objects and it is proportional to the average magnetization of the system. The field dependence of the integral interference cross-section for small q is presented in Fig. 3. It gives an additional information complementary to that shown in Fig.2. Further interpretation of the data is in progress.

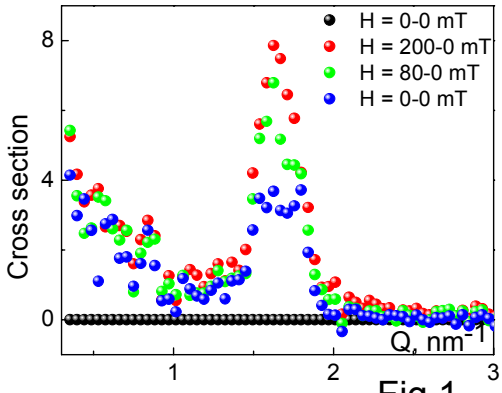


Fig.1.

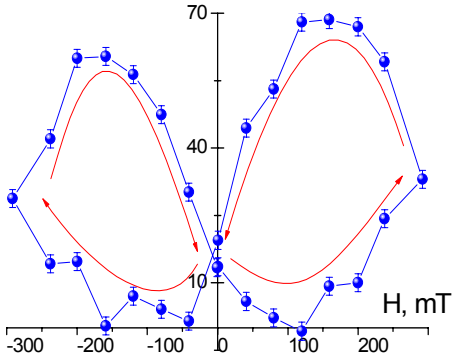


Fig.2.

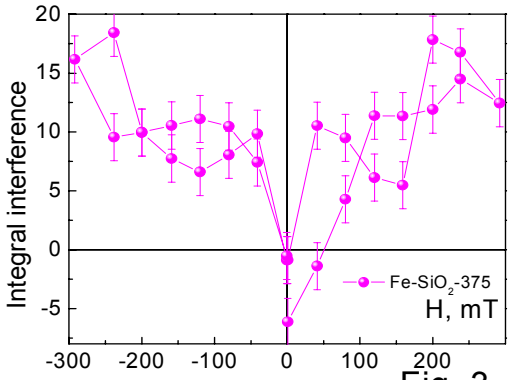


Fig. 3.

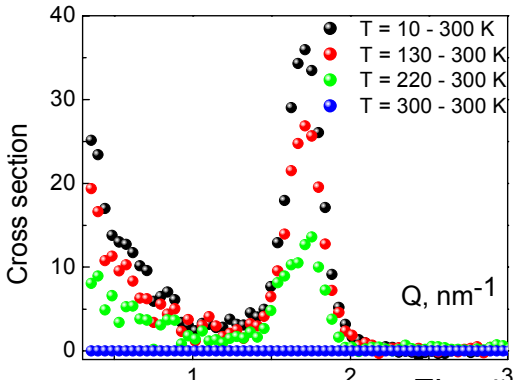


Fig. 4

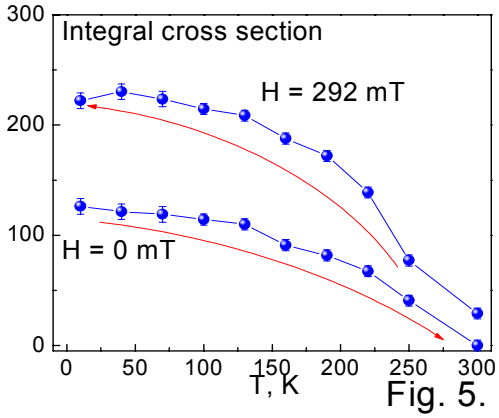


Fig. 5.

The temperature dependent part of the integral cross section is shown in Figure 5 for Zero Field Heating and for Field Cooling at H = 292 mT.

The temperature and magnetic field behavior of the magnetic contribution into diffraction peak shows existence of the hexagonal structure of the magnetic nanowires in the sample. We believe that the system is ruled by the competition of the magnetic field, dipole-dipole and thermal interactions.

GKSS FORSCHUNGSZENTRUM in der HELMHOLTZ-GEMEINSCHAFT	EXPERIMENTAL REPORT	GeNF SANS-2

Bulk Properties and Neutron Diffraction of the Phase Diagram of MnSi	
Proposer:	**D. Lamago[1],** [1]Technische Universität München
Co-Proposers:	**C. Pfleiderer[1], P. Böni[1]**
Experimental Team:	**D. Lamago[1], H. Eckerlebe[2], P. K. Pranzas[2],** [2]GKSS
User Group Leader:	**D. Lamago[1]**
Date(s) of Experiment:	December 2005

Scientific Objective

We reported on magnetization, specific heat and SANS measurements on the intermetallic compound MnSi. In the recent years the properties of MnSi have attracted great scientific interest because of its intriguing behavior in the vicinity of the Curie temperature (T_C = 29 K). The lack of a center of symmetry in the crystal structure of MnSi gives rise to a single-handed helical spin structure and to a chirality in the magnetic fluctuations, that has been even observed well above T_C. The magnetic ground state appears to switch abruptly from a weakly spin polarized Fermi-liquid to an extended non-Fermi liquid (NFL) phase at a pressure of 14.6 kbar. Recent neutron scattering experiment show that large magnetic moments survive far into the NFL-phase, where the scattering intensity observed everywhere on the surface of a small sphere suggests partial order analogous to liquid crystals.
Despite theoretical and experimental investigations the critical behavior of MnSi, i.e. The observation of a diffuse ring around T_C is still a puzzle. Motivated by theoretical predictions [1, 2] of the new chiral universality class of helimagnets, we reinvestigate the magnetic critical properties of MnSi by comparing bulk measurements with small angle neutron scattering data.

Experimental Technique

The specific heat measurements of a single crystal of MnSi have been measured on a 9 T Physical Property Measurement System from Quantum Design. Neutron scattering experiments were carried out on the SANS-2 instrument at the FRG1 neutron source at the GKSS research center in Geesthacht (Germany). The incident neutrons with a wavelength = 5.8 Å have an initial polarization P_0 = 0.95. The scattered neutrons were detected by a position sensitive detector with (128 x 128) pixels. The high quality single crystal was oriented in such a way that two axes [111] were set in a plane perpendicular to the incident beam.

Results

Fig. 1 displays the intensity distribution of the magnetic peaks just below the transition temperature. Diffuse scattering characteristic of critical scattering is observed around the Bragg peaks. The anisotropic spin interactions decreases or vanish leading to strong fluctuations in the orientation of the wave vector of the helix leading to a distribution of the neutron intensity everywhere on the surface of a small sphere as reported in numerous studies before. By fitting our SANS data with a Lorentzian using T_C = 28.7 K, the analysis of the diffuse scattering, as shown in Fig. 2, allows the determination of the staggered susceptibility (proportional to the area of peak intensity for $T > T_C$), the magnetization (proportional to the area of the peak intensity for $T < T_C$) and the correlation length (proportional to the width of the peak for $T > T_C$) and thus the critical exponents.

Fig. 2a shows the temperature dependence of the magnetic contribution to the specific heat at zero field. The pronounced peak of the specific heat at T = 28.51 K is taken as the phase transition from the paramagnetic phase into the helical phase. As the temperature increases the specific heat is dominated by a broad shoulder at T = 28.80 K suggesting the presence of an additional transition in the crystal. This result is most likely connected with our small angle neutron scattering results where a kink is observed in the staggered susceptibility (Fig. 2c). We conclude that the peak in the specific heat is not entirely due to the transition from the paramagnetic phase to the helical order, but may correspond to an additional transition in MnSi. The temperature dependence of the magnetic specific heat as well as the neutron scattering results suggest that an interpretation of the diffuse scattering in terms of a second order phase transition can only be considered as a first approximation [3]. Forthcoming analysis is planned to explain the origin of this unusual behavior.

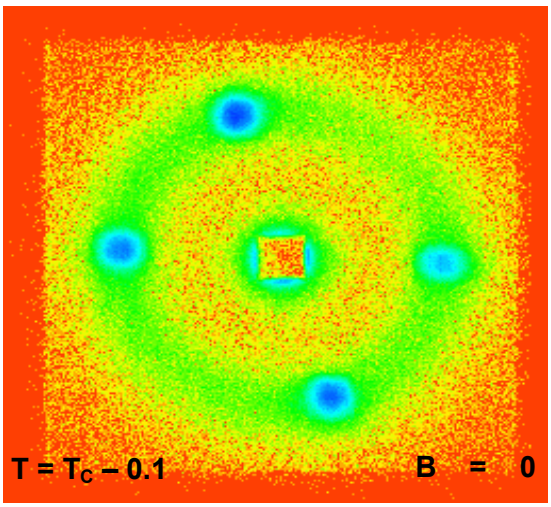


Figure 1: Distribution of Scattering intensity in MnSi at T = 28.9 K. Magnetic diffuse scattering is observed around the Bragg peaks at zero field.

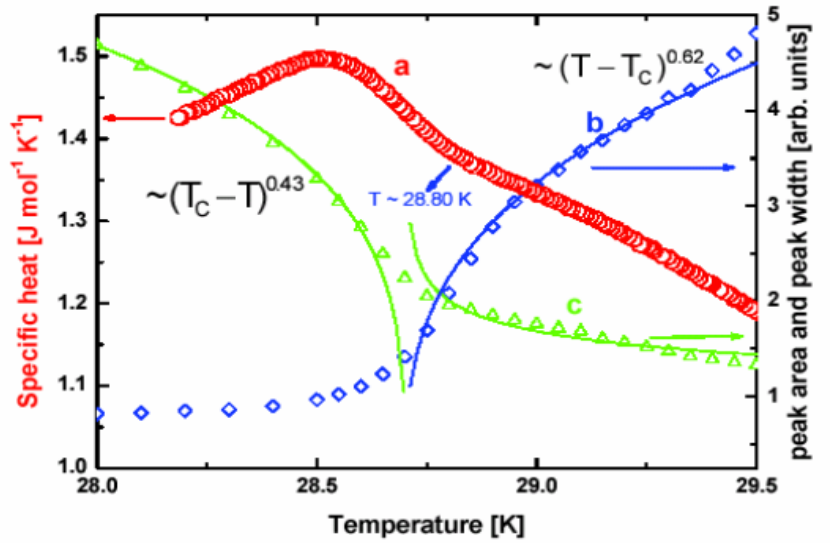


Figure 2: Temperature dependence of: (a) magnetic specific heat, (b) the peak width and (c) the peak area at zero magnetic field. The error bars are smaller than the symbol size.

References

[1] H. Kawamura, J. Appl. Phys. 63, 3086 (1988).
[2] P. Azaria, B. Delamotte, T. Jolicoeur, J. Appl. Phys. 69, 8 (1991).
[3] S. Grigoriev, S.V. Maleyev and A.I. Okorokov, Yu.O. Chetverikov, R. Georgii, P. Böni, D. Lamago, H. Eckerlebe and K. Pranzas, Phys. Rev. B 72, 134420 (2005).

GKSS FORSCHUNGSZENTRUM in der HELMHOLTZ-GEMEINSCHAFT	**EXPERIMENTAL REPORT**	**GeNF SANS-2**

SANS investigation of neutron-irradiated RPV steels with special emphasis on Ni effect

Proposer:	**A. Ulbricht,** Forschungszentrum Rossendorf
Co-Proposers:	**F. Bergner,** Forschungszentrum Rossendorf
Experimental Team:	**A. Ulbricht, F. Bergner**
	P. K. Pranzas, GKSS Research Centre
User Group Leader:	**F. Bergner**
Date(s) of Experiment:	12–15 December 2005

Objectives

The SANS experiment is aimed at studying the influence of neutron fluence and Ni content on irradiation-induced changes of the microstructure of WWER 1000-type reactor pressure vessel (RPV) steel. A feature of this material is a high Ni content (> 1 wt.-%) in comparison with other RPV steels. We assume that the increased radiation susceptibility of the WWER 1000 steel is due to increased Ni. Significant progress is expected from the SANS measurements performed for one and the same WWER 1000 steel in different irradiation conditions and for model alloys with systematically varied Ni content.

Experiment

The WWER 1000 steel (0.03% Cu, 1.27 % Ni) was irradiated at a temperature of 290°C and a neutron flux of 3 x 10^{13} cm^{-2} s^{-1}. The unirradiated and two irradiated conditions have been investigated. Specimen dimensions are about 10 mm x 10 mm x 1 mm. Additionally, pure Fe and a Fe-3%Ni alloy were available (unirradiated condition and one neutron fluence) as slices of 5 mm diameter. The SANS measurements were carried out at a wavelength of 0.58 nm with sample - detector distances of 1 and 4 m. The samples were placed in a saturation magnetic field. Scattering data were normalized by monitor counts and corrected for sample transmission and detector response. Because of the small dimensions and the weak scattering expected relatively long measuring times were preselected for the Fe and Fe-Ni specimens. Data analysis was performed using software routines provided by GKSS.

Achievements and Main Results

Total, nuclear and magnetic scattering intensities are shown in Fig. 1 for the WWER 1000 steel. The large-*Q* results for the unirradiated condition (D0) are presented in Fig. 2 as Porod plot. The coherent magnetic scattering cross section is depicted in Fig. 3. A clear irradiation effect can be deduced in the *Q*-range greater than 0.8 nm^{-1} for the neutron irradiated condition D1 and more pronounced for condition D2. This effect is caused by the formation of irradiation-induced defect or solute clusters. Under the assumption of spherical non-magnetic scatterers the size distribution function was calculated by Fourier transformation using a procedure according to Glatter (Fig. 4). The calculated total volume fraction of irradiation induced clusters is shown in Fig. 5. A monomodal distribution of irradiation induced clusters with peak radius of about 0.9 nm is observed (Fig. 4). The total volume fraction of clusters increases about linearly with neutron exposure. This is the typical behaviour of defect clusters in contrast to Cu rich precipitates for which a fast saturation should occur.

As expected, Fe and Fe-3%Ni exhibit a weaker scattering effect combined with a unfavourable signal to noise ratio. A more detailed data analysis is therefore needed.

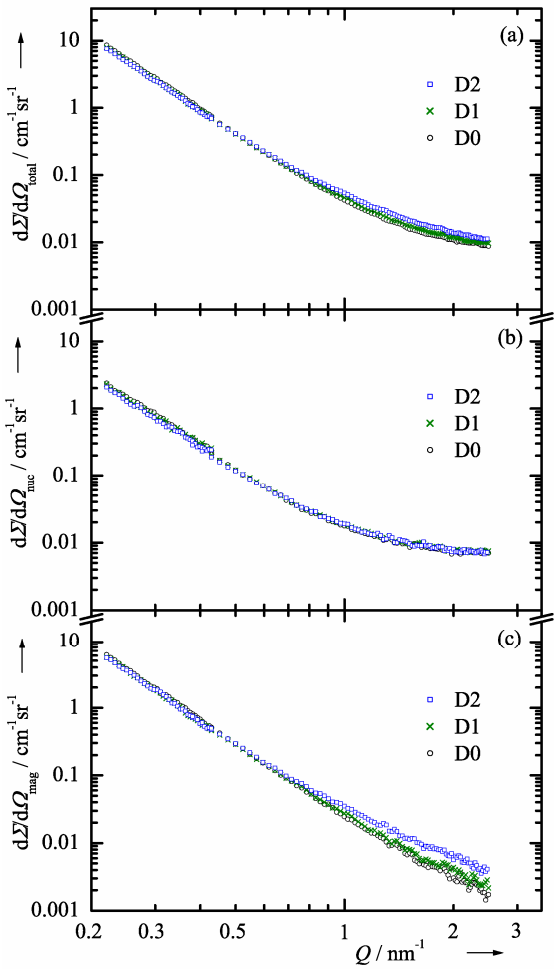


Figure 1: Total (a), nuclear (b) and magnetic (c) SANS intensities for irradiated (D1, D2) and unirradiated (D0) conditions of WWER 1000 steel.

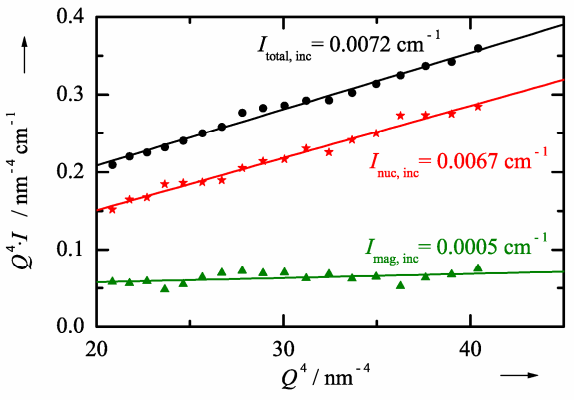


Figure 2: Porod plot for the unirradiated condition of the WWER 1000 steel.

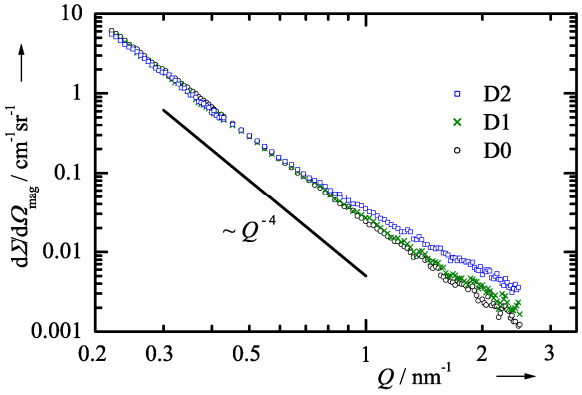


Figure 3: Coherent magnetic scattering cross sections for WWER 1000 steel.

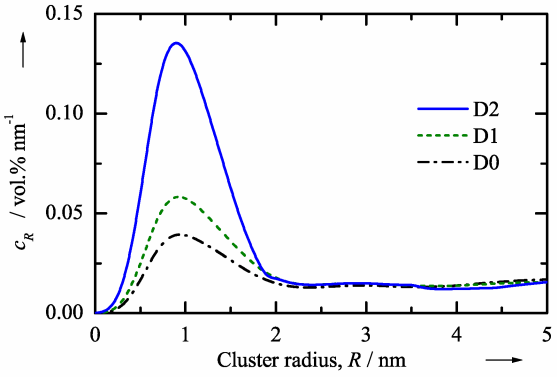


Figure 4: Volume distribution of scatterers for WWER 1000 steel.

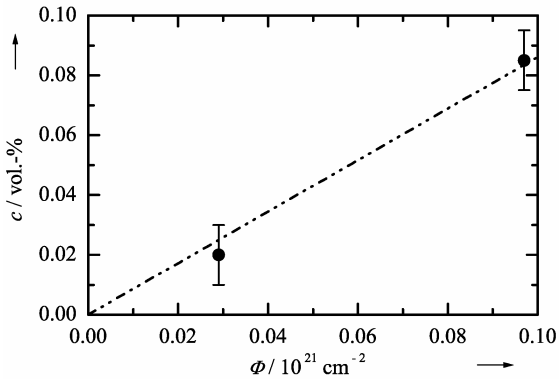


Figure 5: Total volume fraction of irradiation induced clusters vs. neutron fluence.

GKSS FORSCHUNGSZENTRUM in der HELMHOLTZ-GEMEINSCHAFT	EXPERIMENTAL REPORT	GeNF DCD
Double crystal diffractometer DCD		

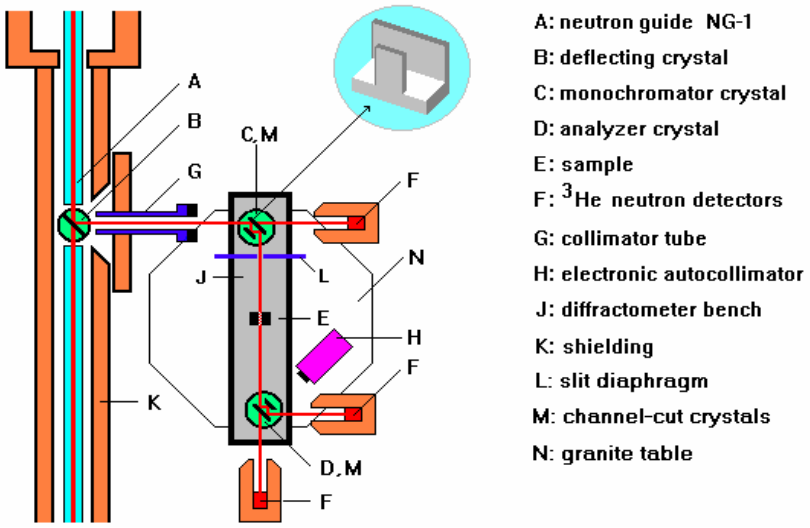
Short Instrument Description:

The double crystal diffractometer for ultra small angle neutron scattering (USANS) uses non-polarised cold neutrons to characterise in materials large creep pores, fatigue and sintering cavities, precipitates, voids, bubbles, etc. with particle sizes in the range with about 100 nm to 40 μm in diameter.

Local Contact:

Dr. P. Klaus Pranzas
Phone/Fax : +49 (0)4152 87 – 1326 / +49 (0)4152 87 – 1338
e-mail: pranzas@gkss.de

Schematic View of DCD:



Instrument Details:

Beamline:	beamline 8 – cold neutron guide NG-1, max. beam cross section 30 x 40 mm^2
Deflecting crystal:	Si(111), Si(311), mosaic spread 0.1 mrad
Monochromator / analyser:	channel-cut perfect Si crystals
Wavelength resolution	$\Delta\lambda/\lambda = 1 \cdot 10^{-5}$ (λ = 0.443 nm)
Max. flux at deflecting crystal	$\Phi = 2.3 \times 10^{8}$ cm^{-2} s^{-1}
Flux at sample position:	$\Phi \approx 500$ cm^{-2} s^{-1} (Si(111), λ = 0.443 nm) $\Phi \approx 180$ cm^{-2} s^{-1} (Si(311), λ = 0.232 nm)
Range of momentum transfer:	$1 \cdot 10^{-5}$ $nm^{-1} \leq Q \leq 5 \cdot 10^{-2}$ nm^{-1}
Detectors:	three ^{3}He-detectors
Control of crystal alignment:	electronic autocollimator, angular resolution < 0.05 μrad

GKSS FORSCHUNGSZENTRUM in der HELMHOLTZ-GEMEINSCHAFT	**EXPERIMENTAL REPORT**	**GeNF DCD**

USANS investigations of organized nanostructures of diblock copolymers in immiscible solvents

Proposer:	**Ryukhtin, Vasyl**[1], [1] Nuclear Physics Institute, Academy of Sciences of the Czech Republic, 25068 Řež near Prague, Czech Republic
Co-Proposers:	**Stepanek, Petr**[2], [2] Institute of Macromolecular Chemistry, Heyrovský Sq. 2, 16206 Prague 6, Czech Republic
Experimental Team:	**Ryukhtin, Vasyl**[1], **Pranzas, Klaus**[3], [3] GKSS Research Centre
User Group Leader:	**Ryukhtin, Vasyl**[1]
Date(s) of Experiment:	4th April–25th April 2005

Objectives

Block and graft copolymers in applicable solvents can form various microstructures and thus influence properties of the whole studied system, *e.g.*, they can stabilize particles of colloidal dimensions or "compatibilize" immiscible homopolymers. Such systems found numerous applications in many sectors of industrial technology.

Long-range-ordered nanostructures have been found in solutions of diblock copolymers in two partially miscible solvents. Such self-ordered nanostructures are formed by periodically arranged domains of solvents, stabilized by the block copolymer (see Fig.1). Recent performed investigations of such systems by small-angle neutron scattering (SANS) have shown that the ordered structure has either a hexagonal or cubic symmetry with a period of 60–110 nm. The long range periodic structure is limited in extend, typically it consists of grains that have an expected size of about several μm, as was estimated by birefringence measurements on similar systems. The grains (of typical size of several μm) can neither be observed by dynamic light scattering (relaxation time of the grains is too large) nor be detected by birefringence measurements as described for polymer melts, because in this case the two used solvents are isorefractive and the resulting structure is not birefringent.

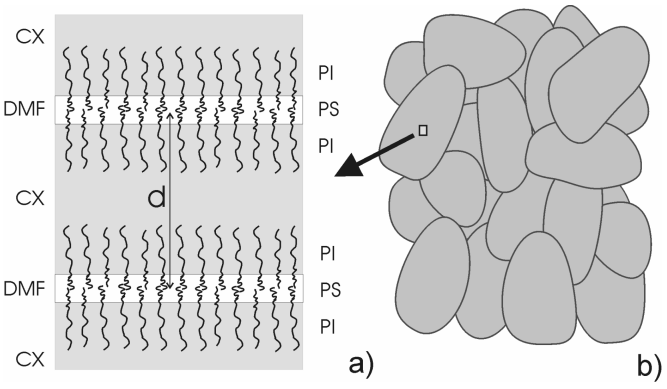


Figure 1: Schematic structure of microphase separated solutions (a) forming the grain structure (b).

Experimental

We used the DCD instrument to characterize the structure of the long-range ordered grains and their kinetics formed in microscopically ordered solutions of poly[styrene-b-(ethylene-co-propylene)] in a mixture of deuterated cyclohexan (d-CX) and dimethylformamide (DMF). The 4 samples CP-1, CP-4, CP-6 and CP-7 with different content of diblock copolymer and DMF were investigated at DCD at a wavelength of 4.43 Å. In order to investigate the dependence of the temperature on the grain size, the samples were measured at several temperatures: 16.4 ^{0}C,

28 ^{0}C, 37 ^{0}C and 46 ^{0}C. The specimens were slowly heated up to 46 ^{0}C and then measured after 8 hours after getting equilibrium conditions. Subsequently, the temperature was slowly decreased step by step to required values with 7–8 hours waiting for equilibrium before the measurement was started.

Results

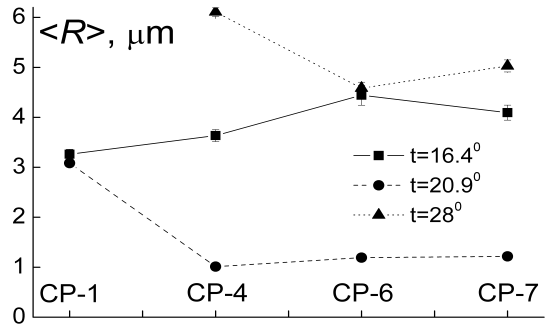


Figure 2: Mean sizes of the grains determined by DCD.

USANS data were fitted by means of SASProfit program based on indirect Fourier Transformation method. A log-normal distribution of incoherent spheres was chosen as model system. The results of data fitting are shown in Fig. 2. In the samples quenched down to room temperature the biggest grains were detected in the mixture with minimum concentration of DFM (CP1, 12.0 %). The substantial difference of the values derived from DCD curves measured at the ambient temperature and those measured at temperatures of 28 ^{0}C and 16.4 ^{0}C can be explained by different cooling regimes. In the first case the samples were heated up to 50–60 ^{0}C and afterwards rapidly cooled down, in the other case – temperature was changing very slowly. Actually, one can notice that the slow cooling facilitates the formation of larger grains in the studied solutions.

In order to estimate the kinetics of the nucleation of the grains in the initial phase the samples were measured *in-situ* after quick cooling in the region near Q=0 with very short exposition time per experimental point (see Fig. 3). Lack of statistics does not allow to perform a data treatment, nevertheless these rough results demonstrate qualitatively the difference in dynamics of creation of the grains for different solutions. One can see that the process of creation of the long-ranged structure takes a rather long time (more than 3.5 hours) for the most of the samples with the exception of the sample CP-1, which has minimum DMF concentration. In this solution the grains were formed already just after the quick cooling and the following formation was very weak.

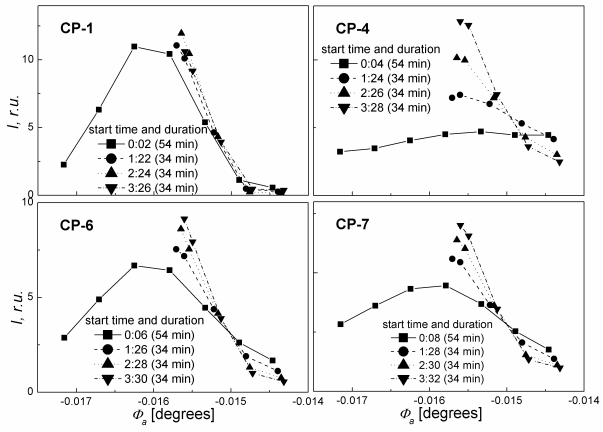


Figure 3: Parts of the analyser rocking curves in dependence of the analyser rotational angle Φ_a measured in-situ with the samples quenched down to room temperature.

Conclusions

The formation of diblock copolymer grains in the partially miscible solvents was studied by USANS. It was shown that the mean size of the grains is strongly dependent on the cooling regime, *i.e.* slowly cooled solutions contained much larger grains than those cooled rapidly. USANS data measured *in-situ* qualitatively demonstrated the different kinetics of initial stage of grain nucleation after quick cooling. The estimated relaxation time is larger than 3.5 hours for most of the samples. Furthermore, a significant difference in the size of the grains was observed for solutions in dependence on the DMF content. The grain structure was not observed in the whole set of samples at 37 ^{0}C and 46 ^{0}C and in sample CP-1 with minimum concentration of DMF at 28 ^{0}C.

GKSS FORSCHUNGSZENTRUM in der HELMHOLTZ-GEMEINSCHAFT	EXPERIMENTAL REPORT	GeNF PNR
Reflectometer for polarised neutrons PNR		

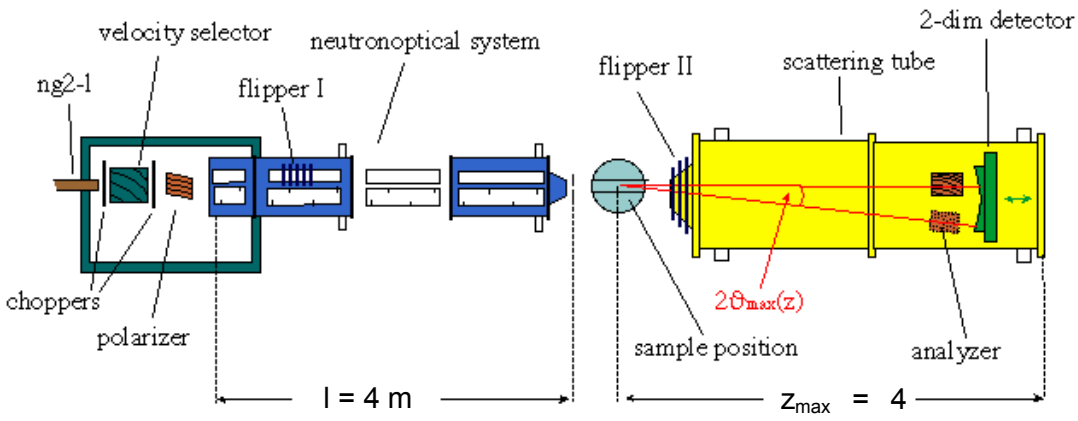
Short Instrument Description

The polarised neutron reflectometer is used to study magnetic and other surfaces, layers, thin films and membranes applying cold non-polarised/polarised neutrons at high fluxes.

Local Contact:

Dr. Danica Solina
Phone/Fax : +49 (0)4152 87-1373 / +49 (0)4152 87-1338
e-mail: danica.solina@gkss.de

Schematic View of PNR:



Instrument Details:

Beamline:	beamline 8 (NG-2l), cross section 30 x 40 mm^2
Monochromator:	helical slot selector
Wavelength:	$\lambda \geq 0.635$ nm
Wavelength resolution:	$\Delta\lambda/\lambda = 0.05$
TOF equipment:	2 choppers, to be used if a resolution better than 0.05 is required
Polariser and analyser:	set of bent supermirrors
Spin flipper:	hf-flipper or Mezei-coil-flipper
Collimation lengths:	4 m
Flux at sample position: (beamsize: 0.5 x 40 mm^2)	$\Phi_{nonpol} = 1 \cdot 10^5$ cm^{-2} s^{-1}(unpolarised) $\Phi_{pol} = 3 \cdot 10^4$ cm^{-2} s^{-1} (polarised neutrons)
distance sample-detector:	3 m to 4 m
angular range:	0° ≤ □ ≤ 4°
Detector:	2-dim position-sensitive ^{3}He-counter
Ancillary equipment:	– refrigerator cryostat – temp.-range: 12–475 K – electro magnet up to 0.9 T – superconducting magnet up to 5 T

GKSS FORSCHUNGSZENTRUM in der HELMHOLTZ-GEMEINSCHAFT	EXPERIMENTAL REPORT	GeNF PNR

Polarized neutron reflectivity studies on $CoPt_3/FePt_3$ multilayers

Principal Proposer:	**F. Klose[1], D. Lott[2], P. Mani[3]** [1]SNS, Oak Ridge National Laboratory, Oak Ridge, TN, USA [2]GeNF, GKSS Research Centre [3]MINT Center, University of Alabama, Tuscaloosa, AL, USA
Experimental Team:	**F. Klose[1], D. Lott[2], U. Tietze[2]**
Date(s) of Experiment:	November 28 – December 8, 2005

Introduction

Lattice-matched antiferromagnetic/ferromagnetic films offer an ideal layered system to study exchange bias. Epitaxial films of $FePt_3$ exhibit an antiferromagnetic ordering with a spin wave vector Q_A = (½ ½ 0) and a Néel temperature of T_N = 160 K [1]. The low T_N of the antiferromagnetic phase allows to perform field cooling through T_N of an antiferromagnetic/ferromagnetic system. $CoPt_3$ is chosen as the ferromagnet since it has the same $L1_2$ crystal structure as $FePt_3$, nearly the same lattice constant, and it can be grown with an in-plane easy axis. X-ray diffraction shows that the Bragg peak widths of the rocking curves for $FePt_3$ films grown on Al_2O_3(11$\underline{2}$0) and MgO are very different indicating that the samples grown on Al_2O_3(11$\underline{2}$0) have larger grains and a smaller mosaic spread. On the other side, results from vibration sample magnetometry reveal that only the sample grown on MgO shows a significant exchange bias effect, suggesting that antiferromagnetic films with fewer defects and strain-free interfaces yield a lower exchange bias. Here at GKSS, polarized neutron reflectivity was carried on a $CoPt_3/FePt_3$ multilayer grown on MgO to elucidate the magnetic switching behavior for different temperatures and magnetic fields. Owing to the significant difference in the neutron scattering length density between Fe and Co the technique allows to probe the layer-specific magnetizations of the system.

Results and discussion

The sample consists of five bilayers of $CoPt_3$(10nm)/$FePt_3$(20nm) deposited on a MgO substrate with a Fe(1nm)/$CrPt_3$(2nm) buffer layer and capped with Pt(1.5 nm). The system was first magnetized at a maximum field of 0.9 Tesla with the field direction in the sample plane. Afterwards the system was field cooled to T = 18 K. For the first measurement shown in Fig. 1, the magnetic field at the sample position was reversed and set to a small value of 6mT close to the remanence field. A small splitting of the non-spin-flip channel is observed at the first Bragg peak at about 0.78 degrees in theta indicating a ferromagnetic contribution of the layered system. With increasing magnetic field the splitting at the first Bragg peak of the multilayer structure reverses and increases strongly as it shown in figure 2 for a magnetic field strength of H = 320 mT confirming the observation obtained by SQUID measurements [2]. However, at the second structural peak only very weak splitting is observed indicating that there is a much weaker ferromagnetic contribution. One of the objectives of the experiments was to examine the switching behavior of the ferromagnet. If it would be governed by coherent rotation intensity should be observed in the spin-flip channels which collect the contribution of the scattering due to the magnetic moments of the sample perpendicular to the field direction. Since no significant spin-flip intensity was observed during the reversal process,

the switching due coherent rotation can be excluded indicating that the process is probably due to domain formation.
The same sets of scans were also carried out at higher temperature. Figure 3 shows as an example a measurement at room temperature and at a magnetic field of H = 320 mT. The splitting behavior of the non spin flip channel changed. Now also at the second peak the splitting between the two non-spin flip channels can be clearly observed indicating that the $FePt_3$ has softened and contributes now to the ferromagnetism of the system. By reversal of the magnetization of the sample no significant intensity in the spin flip channels is detected suggesting that the principle switching mechanism has not changed at increased temperature. For more exact structural interpretation of the measured reflectivity curves simulation is under way.

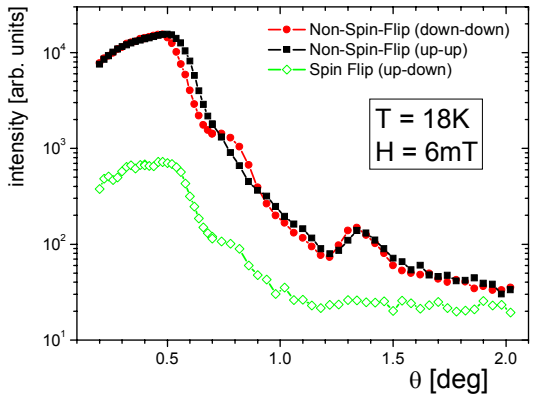


Figure 1: Polarized neutron reflectivity data taken at T = 18 K at H = 6 mT.

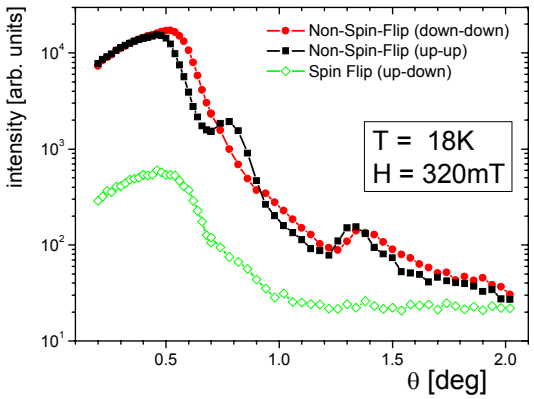


Figure 2: Polarized neutron reflectivity data taken at T = 18 K at H = 320 mT.

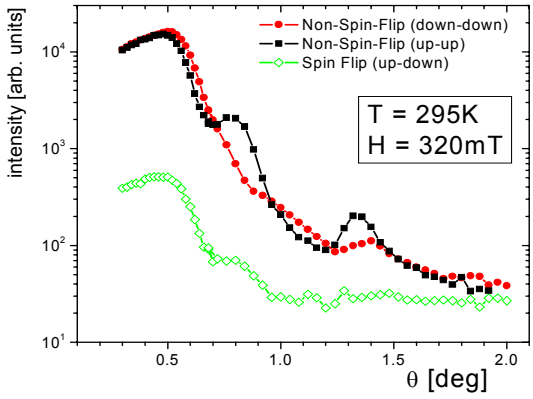


Figure 3: Polarized neutron reflectivity data taken at T = 295 K at H = 320 mT.

References

[1] S. Maat et al., Phys. Rev. B 63, 134426 (2001)
[2] P. Mani, F. Klose, G. J. Mankey private communication

GKSS FORSCHUNGSZENTRUM in der HELMHOLTZ-GEMEINSCHAFT	EXPERIMENTAL REPORT	GeNF PNR

Polarized neutron reflectivity studies on Fe/Cr/Sn/Cr multilayer

Principal Proposer:	**D. Lott[1], M. Almokhtar[2], A. Schreyer[1]** [1]GeNF, GKSS Research Centre [2]Physics Department, Assiut University, Assiut, Egypt
Experimental Team:	**D. Lott[1], U. Tietze[1]**
Date(s) of Experiment:	September 5 – September 20, 2005

Introduction

In Fe/Cr multilayer systems, the magnetic coupling of the Fe layers is mediated through the Cr layers. The Cr layers themselves are antiferromagnetically ordered, showing commensurate (CSDW) and incommensurate spin density waves (ISDW) depending on temperature and the thickness of the separating Cr layers [1].
Recently, Fe/Cr/Sn/Cr multilayers were studied by Moessbauer spectroscopy [2]. The monolayer (ML) of Sn inserted into the Cr layers serves as a Moessbauer probe permitting the study of the magnetic local environment around Sn providing details about of the magnetic stucture of Cr. This allows to infer the common features of Cr in Fe/Cr and Fe/Cr/Sn/Cr superlattices.
In recent experiments, complimentary neutron diffraction studies were carried out on a set of Fe/Cr(t) and Fe/Cr(t/2)/Sn(2Å)/Cr(t/2) multilayers with t = 80 Å and t = 160 Å [3]. The magnetic order of the Cr layers was examined, systematically comparing the systems with and without Sn inserted in the Cr layers. Both systems without Sn show similar behavior, with an ISDW at low temperatures (T) transforming into a CSDW phase at higher temperatures consistent with previous work [1]. In contrast to these, the multilayers with Sn show drastic changes with additional asymmetric modulations in the diffraction spectra along (00L) and (0H0). Surprisingly, the periodicity of the modulation corresponds to a doubling of the structural period for the samples with Sn insertion. One possible interpretation of this finding could be the formation of a spiral structure of the Cr spins leading to an antiferromagnetic ordering of the Fe layers and consequently to a doubling of the magnetic periodicity [1]. Here, polarized neutron reflectivity studies were carried out to examine the magnetic alignment of the Fe layers in the multilayer systems with Sn.

Results and discussion

For the experiment the samples were prepared under the same conditions as for the diffraction scans mentioned above. First they were magnetized in a magnetic field of 0.9 Tesla along the sample plane which was sufficient to saturate the samples. For the polarized neutron reflectivity measurements the magnetic field was then reduced again to about 5 mT. Figure 1 shows the spin-flip and non-spin-flip channels collected at a temperature of T = 17 K for the sample with t = 80 Å. A large splitting of the non-spin-flip channels can be observed at the first peak of the superlattice structure while the spin flip
channels show no significant signal. In case of an antiferromagnetic alignment of the Fe layers an additional peak should appear in the reflectivity scans at about half the angular position of the superlattice peak. Since this is clearly not the case for neither the spin-flip nor the non-spin-flip channels, it can be concluded that the Fe layers are totally collinearly aligned along the applied magnetic field showing no antiferromagntic ordering. Therefore, the spiral

configuration of the Cr spins in the above suggested form can be excluded as a reason for the doubling of the modulation features in the diffraction pattern. The experiment was carried out for several temperatures up to room temperature. Figure 2 shows the different polarization channels for the sample with t = 80 Å at room temperature. No significant changes are found, e.g. no additional peak at the half angular position of the superlattice structure. For both samples with t = 80 Å and t = 160 Å (not shown here) no antiferromagnetic coupling between the Fe layers could be observed. The additional modulation seen in the high angle data [3] could be recently interpreted by theoretical calculations based on other effects [4].

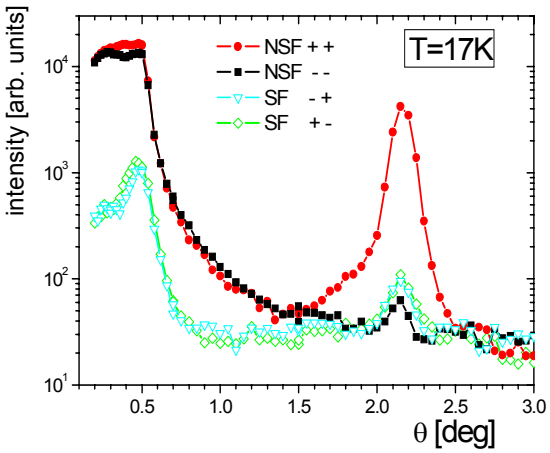


Figure 1: Polarized neutron reflectivity on Fe(10Å)/Cr(40Å)/Sn(2Å)/Cr(40Å) multilayer with polarization analysis at T = 17 K. Channels are not corrected for background and flipping ratios.

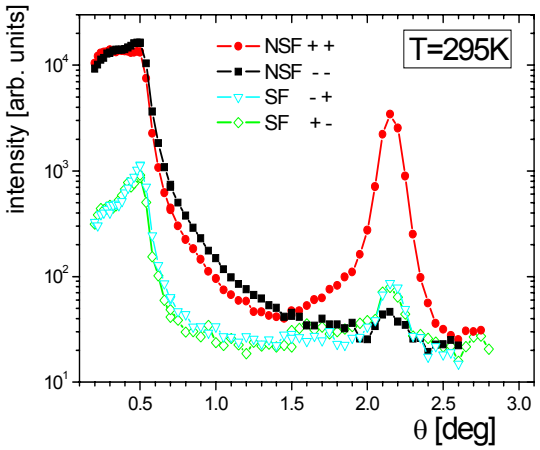


Figure 2: Polarized neutron reflectivity on Fe(10Å)/Cr(40Å)/Sn(2Å)/Cr(40Å) multilayer with polarization analysis at T = 295 K. Channels are not corrected for background and flipping ratios.

References

[1] A. Schreyer et al., Phys. Rev. Lett., 79, 4914 (1997)
[2] M. Almokhtar et al., Phys. Rev. B 66, 134401 (2002)
[3] D. Lott et al., Physica B 350, 245 (2004)
[4] A. Gruenwald, Diplomarbeit, University of Hamburg (2005)

GKSS FORSCHUNGSZENTRUM in der HELMHOLTZ-GEMEINSCHAFT	EXPERIMENTAL REPORT	GeNF NeRo
New neutron reflectometer NeRo		

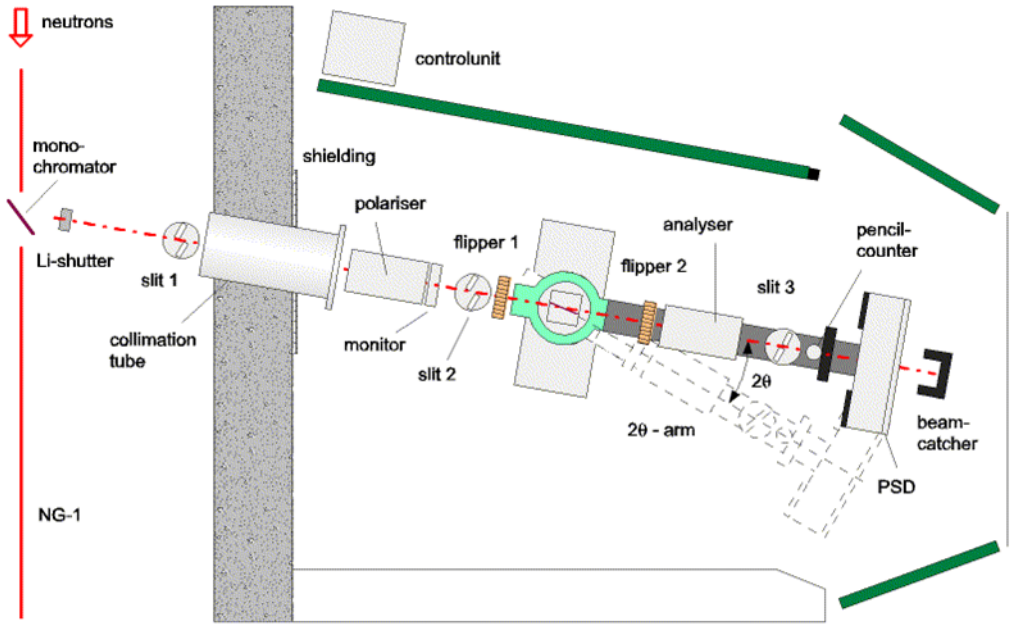
Short Instrument Description

The new Neutron Reflectometer NeRo has been built at the former location of TOREMA 2. The instrument is designed for measurements of thin film systems including polymer and magnetic systems using cold non-polarised/polarised neutrons with high resolution.

Local Contact:

Dr. Dieter Lott
Phone/Fax : +49 (0)4152 87 – 1372 / +49 (0)4152 87 – 1338
e-mail: dieter.lott@gkss.de

Schematic View of NeRo:



Instrument Details:

Beamline:	beamline 8 (NG-1)
Wavelength:	λ = 0.435 nm;
Wavelength resolution	$\Delta\lambda/\lambda$ = 0.02
Angular range	$0 \leq \theta \leq 10°$
Flux at sample position:	$\Phi = 5 \cdot 10^4$ cm^{-2} s^{-1} (unpolarised, standard collimation)
Detectors:	2-dim position-sensitive ^{3}He-counter ^{3}He pencil counter
Ancillary equipment:	refrigerator cryostat − temp.-range: 12–475 K electro magnet with field up to 0.9 T

GKSS FORSCHUNGSZENTRUM in der HELMHOLTZ-GEMEINSCHAFT	EXPERIMENTAL REPORT	GeNF NeRo

The New Neutron Reflectometer – NeRo

Authors: **D.Solina, D. Lott, U. Tietze, O. Frank, V.Leiner, A. Schreyer**
GKSS Research Centre

Introduction

Specular neutron reflectometry is an established technique for the study of magnetic thin films [1, 2] and soft matter materials [3]. Recent years have seen a diversity in samples studied which include laterally structured magnetic films in the micron to nanometre scale [4, 5]. In this case polarized diffuse scattering can play a strong role in understanding the magnetic behaviour of these structures. With the continuing strides made in the field of thin films and structured magnetic materials there is an ever increasing need for instrumentation that can accommodate the needs for the study of these films.
This paper will give a short description of the new Neutron Reflectometer, NeRo (fig. 1), that came online early this year at Geesthacht Neutron Facility (GeNF).

Description of NeRo

NeRo replaces TOREMA, a standard reflectometer at GeNF which was limited in scan range of about 5° in 2 θ. In comparison NeRo covers the range of -20° ≤ 2 θ ≤ 100° allowing it to operate as both a reflectometer and diffractometer. It is situated on a cold neutron guide at GeNF's research reactor FRG-1. A pyrolitic graphite monochromator has been used to give a 0.433 nm monochromatized beam of neutrons with wavelength resolution of better than 2 %.
NeRo can be used in both polarized and unpolarized modes. The polarizer and analyzer can be inserted automatically by the user via software commands. The polarizer and analyzer are both transmission type supermirrors.
The slit system on NERO is also automated allowing for remote control of beam width and acceptance angle during measurements.
NERO has a horizontal scattering geometry, thus it requires samples to be oriented vertically. Silicon cells can be used for studying liquid interfaces. The sample stage is adaptable and can accommodate heavy sample environments such as a cryo-furnace and various kinds of magnets. Available upon request are a 0.9T magnet and cryostats over a temperature range of about 3–475 K.
NeRo has been equipped with both a pencil detector for fast specular measurements and a 2-D position sensitive detector allowing for the collection of specular and diffuse data. The 2-D detector has an efficiency of approx 60 % with a sensitive area of 250 mm × 250 mm and resolution of 3 mm. The readout is by charge division. A super-mirror stack will be available in 2006 for time efficient measurements of magnetic diffuse reflectivity.
All components (excluding flippers) are controlled via LABVIEW. The user interface has been designed to allow simple programming of alignment, scan modes and measurement. Data can be viewed and manipulated as data is collected. All collected data and manipulated data is saved in an easy to view ascii format.
Reflectivities over nearly 6 orders of magnitude can be measured quite easily with room for further improvement (see. Fig. 2)

Summary

NeRo is characterized by its versatility in that it can operate in both reflection and diffraction modes. It can operate in both polarized and un-polarized modes. It also allows for the study of diffuse scattering over a wide range of angles with a sample environment that can accommodate heavy equipment such as magnets and cryostats.

Access to NeRo

NeRo is open to national and international users from universities and other research institutes at no cost. Industrial applications are welcome at a negotiable cost. Proposals are accepted throughout the year and forms can be obtained online at http://genf.gkss.de.

Acknowledgements

The authors would like to give special thanks to M. Pauls for making the detector and T. Krist for the polarizers.

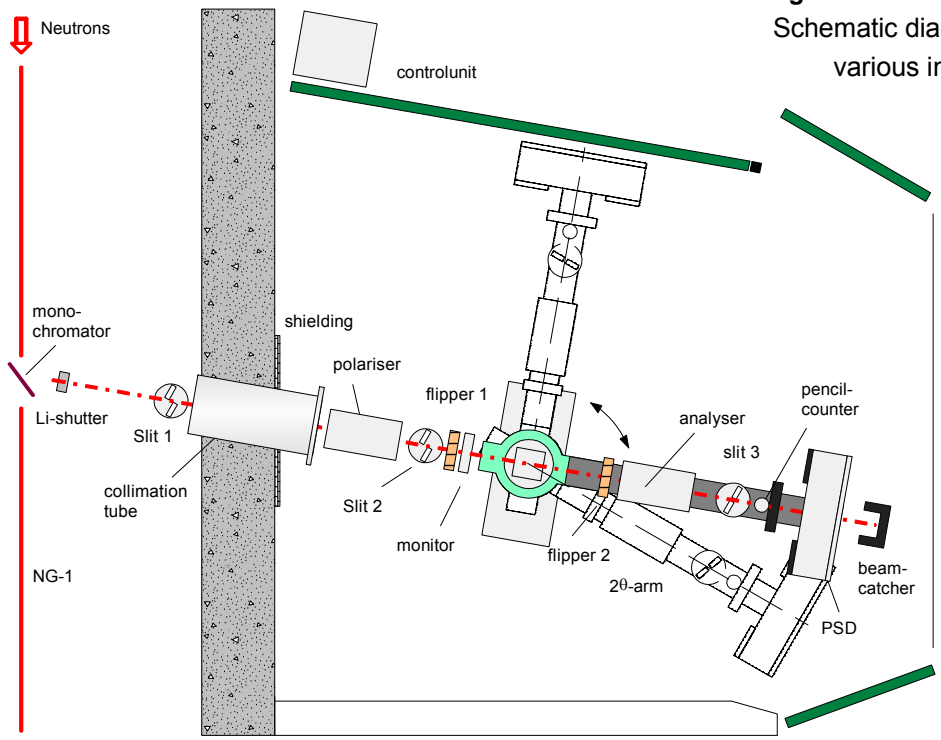


Figure 1:
Schematic diagram of NeRo showing various instrument components.

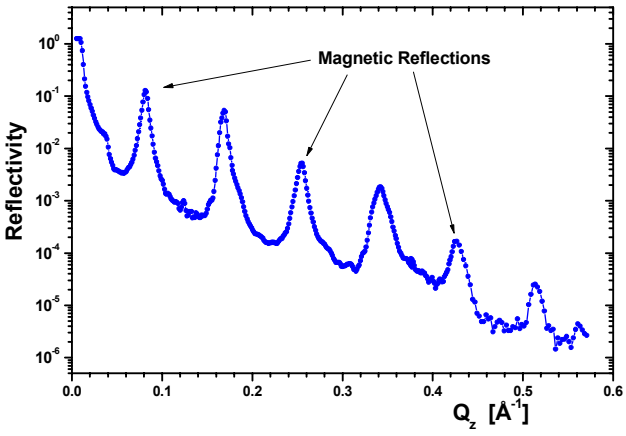


Figure 2:
Specular neutron reflectivity pattern obtained for a Fe[10Å]/Cr[28Å] multilayer of 60 periods. The magnetic Peaks due to the antiferromagnetic ordering in the Fe layers are indicated in the graph.

References

[1] M. R. Fitzsimmons, S. D. Baden, J. A. Borcher, G. P. Felcher, J. K. Furdyn, A. Hoffman, J. B. Kortright, I. K. Schuller, T. C. Schulthess, S. K. Sinha, M. F. Toney, D. Weller, S. Wolf, J. Magn. Magn. Mater. 271 (2004) 103.

[2] A. Schreyer, T. Schmitte, R. Siebrecht, P. Bödeker, H. Zabel, S. H. Lee, R. W. Erwin, C. F. Majkrzak J. Kwo, M. Hong, J. Appl. Phys. 87 (2000) 5443.

[3] Webster J, Langridge S, Curr. Opin. Colloid Interface Sci. 4 (1999) 186.

[4] K. Theis-Bröhl, T. Schmitte, V. Leiner, H. Zabel, K. Rott, H. Brückl, J. McCord, Phys. Rev. B 67 (2003) 184415.

[5] M. Pannetier, F. Ott, C. Fermon, Y. Samson, Physica B 335 (2003) 54.

GKSS FORSCHUNGSZENTRUM in der HELMHOLTZ-GEMEINSCHAFT	**EXPERIMENTAL REPORT**	**GeNF NeRo**

Neutron diffraction and reflectivity studies on Gd/Y

Principal Proposer:	**A. Grünwald[1,2], A. Wildes[2], W. Schmidt[3], H. Tartakowskaya[4], A. Schreyer[1]** [1] GKSS Research Centre, Institut for Material Science [2] Institut Laue-Langevin, Grenoble/FRANCE [3] Forschungszentrum Jülich, GERMANY [4] Institut for Magnetism, UKRAINE
Experimental Team:	**D. Lott[1], U. Tietze[1], A. Grünwald[1,2]**
Date(s) of Experiment:	November 2005

Introduction

The aim of the experiment was to characterize a Gd/Y superlattice sample for an upcoming experiment of inelastic measurements at the triple axis neutron diffractometer PANDA, located at the new research reactor FRM2 in Munich.

Magnetic fluctuations and spin dynamics in superlattices are of great interest due to the reduced dimensionality of the magnetic structure and the great flexibility in the choice of sample composition. Rare earth superlattices are prime candidates for a study of magnetic excitations with inelastic neutron scattering. They exhibit the largest magnetic moments of all elements, leading to a very large magnetic scattering length for neutrons. Recently it has been shown that it is possible to extract information on spin-wave excitations in exchange coupled Dy/Y superlattices by inelastic neutron scattering [1]. Since then significant effort has been spent on the theoretical analysis suggesting the occurrence of periodic oscillations of discrete spin wave eigenvalues caused by a folding of the Brillouin zone and resulting from the finite thickness of the Dy layers in the superlattice. However, these measurements are difficult as the inelastic signal is very weak due to the small amount of sample material. For the following experiment in Munich measurements on a $[Gd/Y]_{x100}/Al_2O_3$(substrate) superlattice are planed, investigating for the first time a system containing a ferromagnet. Based on previous successful measurements on the Dy/Y sample, scans around the Gd/Y (0002) peak and in the small angle regime are proposed. Therefore it is essential to have exact knowledge of the peak structure in both regimes, e.i. to ensure that the weak inelastic signal is not superimposed by any intense structural peak.

Experiment

For the determination of the superlattice period and the peak structure in the small angle regime and around the Gd/Y (0002) peak conventional small angle reflectivity and high angle diffraction were carried out. All measurements were performed at room temperature using the standard setup of NeRo – cold neutrons with a wavelength of 0.433 nm diffracted from a graphite monochromator crystal – without any additional sample environment. A 2-D position sensitive He^3 detector was used for detection. In order to access the Bragg reflections at higher Q-values the $\lambda/2$ contribution in the wavelength spectrum of NeRo was used.

Results

The high angle diffraction scan (Fig. 1) clearly shows the Gd/Y (0002) peak at $Q = 2.20\,\text{Å}^{-1}$ and the Al_2O_3 substrate peak at $Q = 2.66\,\text{Å}^{-1}$. No additional peaks are observed within this range, thus parasitic effects due to elastic structural peaks could be excluded for the upcoming inelastic scattering measurement at PANDA.

The reflectivity scan (Fig. 2) provides the first and second superlattice reflection at $Q = 0.149\,\text{Å}^{-1}$ and $Q = 0.295\ \text{Å}^{-1}$, corresponding to a superlattice period of $\Lambda_{SL} = 43$ Å.

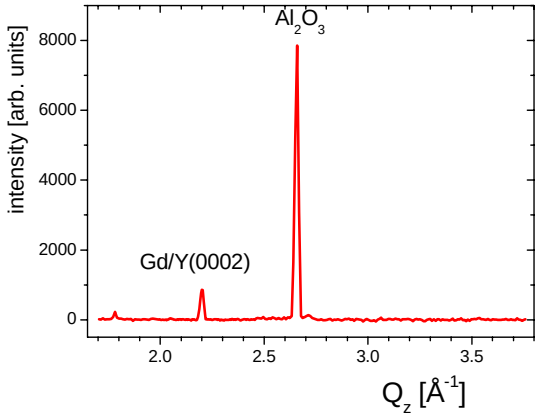


Figure 1: Neutron diffraction scan of a Gd/Y multilayer measured at T = 295 K > T_C.

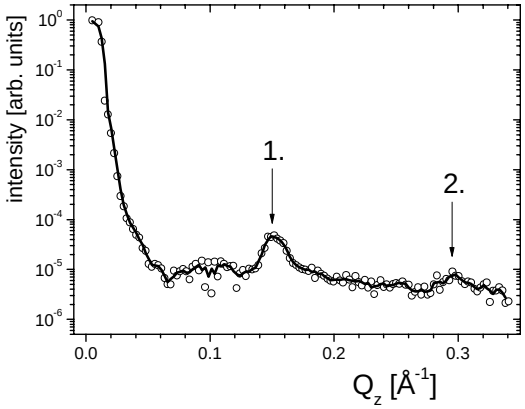


Figure 2: Neutron reflectivity scan of a Gd/Y multilayer measured at T = 295 K > T_C.

Reference

[1] A. Schreyer et al., J. Appl. Phys. 87 (2000) 5443

GKSS FORSCHUNGSZENTRUM in der HELMHOLTZ-GEMEINSCHAFT	EXPERIMENTAL REPORT	GeNF ARES

Diffractometer for the analysis of residual stresses ARES

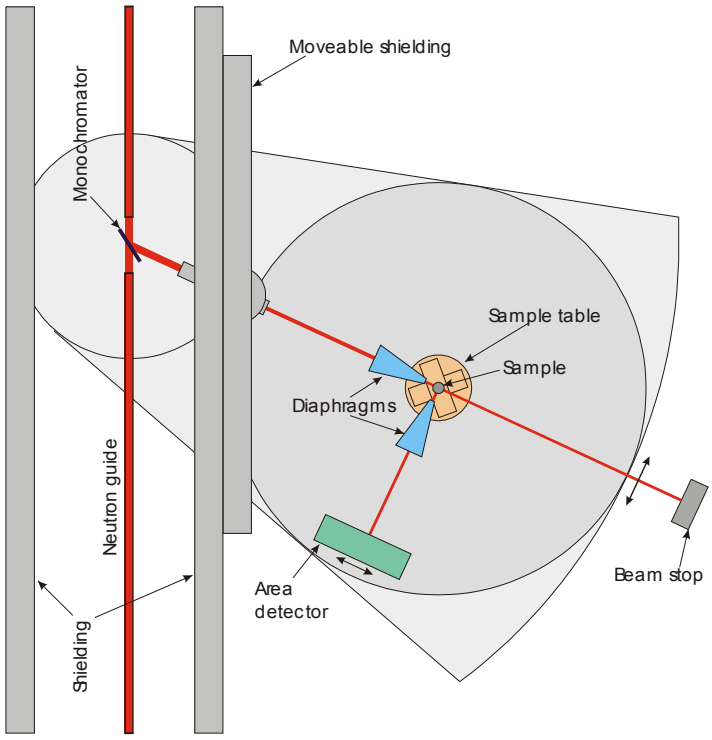
Short Instrument Description:

The diffractometer ARES is designed for the analysis of residual stresses ('strain scanner') in specimens with technical sizes (up to approx. 100 kg) using thermal neutrons.

Local Contact:

Dr. Peter Staron
Phone/Fax : +49 (0)4152 87–1208 / +49 (0)4152 87–1356
e-mail: peter.staron@gkss.de

Schematic View of ARES:



Instrument Details:

Location at FRG-1:	beamline 7; thermal neutron guide, cross section 42 × 90 mm^2, (supermirrors on top and bottom wall)
Monochromator:	elastically bent perfect Si monochromator, Si (311), Si (220), double focussing
Take-off angle:	57° to 120°, continuously selectable
Wavelength:	λ = 0.16−0.23 nm (with Si 311)
Flux at sample position:	$\Phi \approx 5 \cdot 10^5$ cm^{-2} s^{-1}
Sample displacements:	x, y (range 200 mm), z (range 150 mm), Ω
Detector:	2-dim. position-sensitive ^{3}He-counter
Distance sample-detector:	100−150 cm
Sample environment:	load frame for in-situ tests planned

GKSS FORSCHUNGSZENTRUM in der HELMHOLTZ-GEMEINSCHAFT	**EXPERIMENTAL REPORT**	**GeNF ARES**

Residual stresses in a water-quenched IN 718 plate

Proposer:	**U. Cihak** [1]University of Leoben, Austria
Co-Proposers:	**P. Staron** [2]GKSS Research Centre
Experimental Team:	**P. Staron[2]**
User Group Leader:	**H. Clemens[1]**
Date(s) of Experiment:	18.04.–03.05.2005

Objectives

The residual stress state in a small water-quenched plate made of the nickel-based superalloy IN 718 shall be determined for comparison with predictions of a finite element (FE) model. This test is part of the investigation of residual stress states in water-quenched IN 718 turbine discs for aero engines. The thin plate serves two purposes: first, an influence of the specimen geometry on the FE results can be checked and, second, the use of a thin plate of the same material saves beam time.

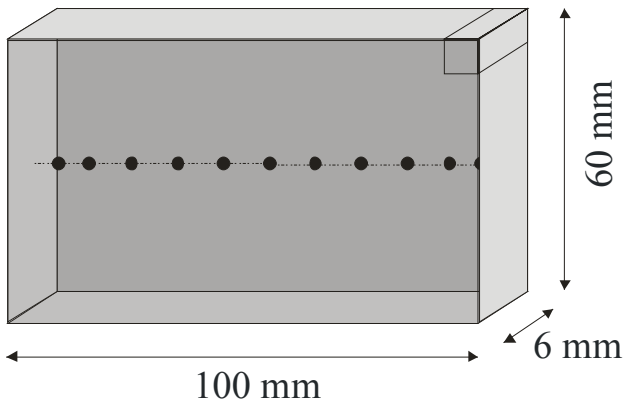
Experiment

Sample

The investigated sample was a 100 mm long, 60 mm wide, and 6 mm thick plate of the nickel-based superalloy IN 718. The plate was given the same heat treatment and water-quenching that are used in the production of investigated turbine discs.

Measurements

The nominal size of the used gauge volume was 3×3×3 mm^3 for the measurement of strains in three orthogonal directions. Due to the small grain size of the material, a large number of diffracting grains are contained within this gauge volume. The water-quenched material con-taines mainly the γ-phase. Three different diffraction peaks of the γ-phase (200, 220, and 311) were recorded with an area detector at angles of about 55°, 82°, and 100° at a wavelength of 1.647 Å.

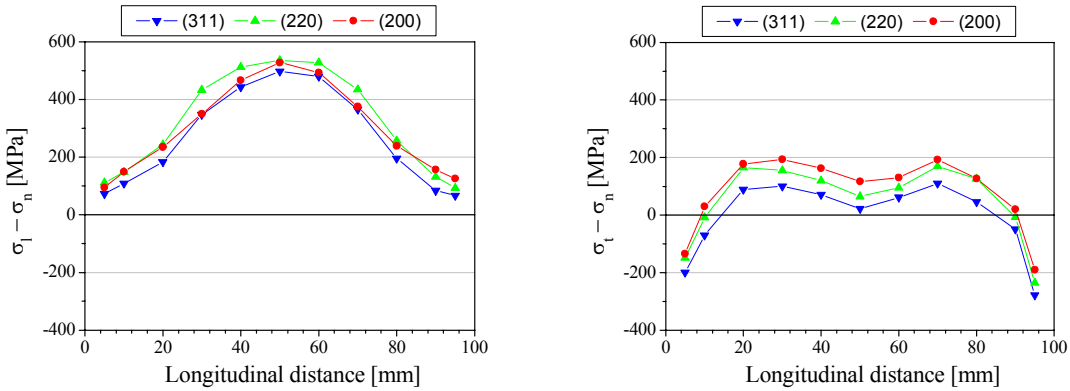


Experimental results

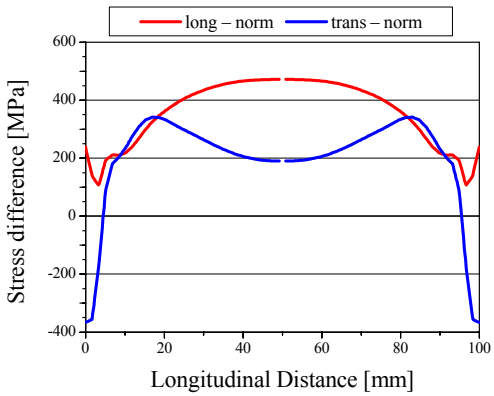
The figure shows the differences in the longitudinal and transverse stresses obtained from the measurements (the longitudinal direction is parallel to the long edge of the plate). As there should be a plane stress state in the thin disc, the differences should actually give the stresses in the two directions. Different reflections have been used to study the influence of microstresses on the result. It can be seen that the stress results of the three reflections are close together; the maximum deviation of around 100 MPa exists between 311 and 200 in

the transverse direction. This deviation can be attributed to microstresses in the material. According to literature, 311 should give the best representation of macrostresses.

Comparing the measured stresses with results of the FE simulation (see lower figure) shows that the simulation gives qualitatively similar results, although still significant differences exist. This result has confirmed that temperature-dependent heat transfer coefficients have to be used in the simulation. They have to be derived from costly temperature measurements, however, with a constant coefficient the simulation results differ much more from the measured results. Both results are not directly compared because the simulation results are not yet integrated over a volume element similar to the gauge volume used in the measurement.



Residual stresses obtained from the measurement
a) $\sigma_{long} - \sigma_{norm}$,
b) $\sigma_{trans} - \sigma_{norm}$.



Result of the FE simulation.

Achievements and Main Results

The residual stresses in an IN 718 plate have been determined from the measurements. This is an important addition to the investigation of the residual stress state IN 718 turbine discs for aero engines. The results for the studied plate have shown that temperature-dependent heat transfer coefficients have to be used in the simulation. With a constant coefficient the simulation results differ much more from the measured results and it seems that even a qualitative agreement can not be achieved.

GKSS FORSCHUNGSZENTRUM in der HELMHOLTZ-GEMEINSCHAFT	**EXPERIMENTAL REPORT**	**GeNF ARES**

Residual Strain Measurements within forged engineering components and model parts

Proposer:	**U. Cihak,** [1]Mining University Leoben, Leoben, Austria
Co-Proposers:	**M. Stockinger,** [2]Böhler Schmiedetechnik, Kapfenberg, Austria
Experimental Team:	**U. Cihak,** [1]
	P. Staron, [3]GKSS Research Centre
User Group Leader:	**H. Clemens**[1]
Date(s) of Experiment:	21.06.2005–01.07.2005

Objectives

A new heat-treatment route for the nickel-based alloy IN718, called direct-ageing, involves water-quenching, which results in high residual stresses [1]. The present investigation is part of a study optimizing the prediction of these stresses in forged turbine disc pre-forms by adopting Finite Element Simulations (FEM) to neutron diffraction results. Forged components made of the same material can have very different grain sizes depending on their thickness and thus the realizable plastic deformation [2]. Therefore, model plates with different grain sizes made of IN718 have been investigated by neutron diffraction.

Experiment

Sample

Rectangular samples (100x60x6 mm³) were cut by electro discharge machining from a turbine disc pre-form (Plate A) and form a larger, forged aeroengine component (Plate B). These IN718 plates were then reheated to the forging temperature and subsequently quenched in water. Figures 1a,b show the resulting microstructures, consisting of a γ-matrix and low amounts (3–4 vol.%) of embedded delta phase particles.

Measurements

Figure 2 indicates the three main orthogonal directions of the strain measurements, which have all been performed with a nominal gauge volume of 3x3x3 mm³ and a neutron wavelength of 1.647 Å. The measurement time was chosen to be 5000–6000 s for each point in both plates. Additionally, to the (311) reflection three more diffraction peaks of the γ-matrix (220), (200), (111) were recorded to study possible influences of microstrains. In each direction the respective reference lattice parameters d_0 were determined on cubes (4x4.1x4.2 mm³) cut from the plates after the measurements.

Experimental Results

As previous studies have shown that a temperature dependent heat-transfer coefficient has to be employed in the FEM calculations to model the quenching process realistically, Figure 3 shows FEM results based on variable thermal boundary conditions. In order to be able to compare the measured results directly to the FEM calculation, the elastic strains are depicted in Figure 3 and not the stresses derived from these strains.

The measured strains in the three main directions determined with the different reflections are very close together in Plate A. They are also very close to the simulated elastic strains, except for the transversal direction, which can most likely be attributed to a not yet perfectly optimized FEM model. However, all measured strain components follow the trend of the simulated strains along the centre line of the plate. Basically the longitudinal strains exhibit a maximum in the middle region, which is balanced by a minimum of the transversal strains. As there are no big differences between the four reflections the influence of microstrains is regarded as minor.
In plate B there is a larger scatter of the data and thus no clear trend can be observed. Only the (311) reflection seems to follow the trend of the simulated strains reasonably well. These large deviations in plate B are attributed to the large grain size, which is depicted in Figure 1b. The sample has to be tilted during the measurement in order to get more grains to fulfil the reflection condition. However, the grain size is so large that even additional sample tilting and an elongated gauge volume are not likely to give representative macrostrain values.

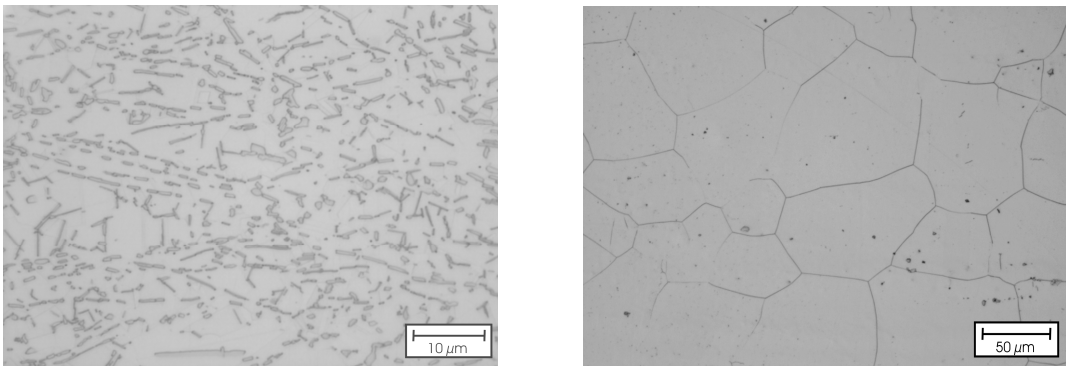


Figure 1: Microstructure of water-quenched In718. a) Plate A taken from the forged turbine disc. b) Plate B taken from a larger forged aeroengine component.

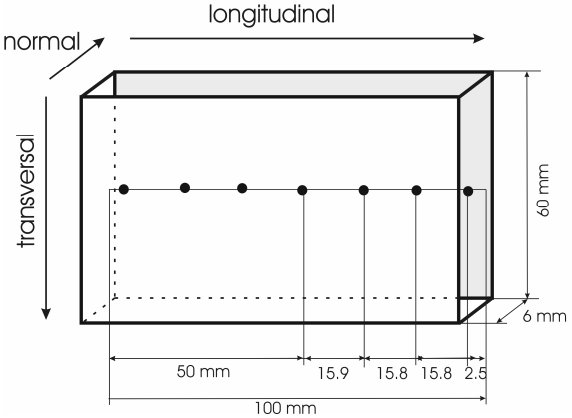
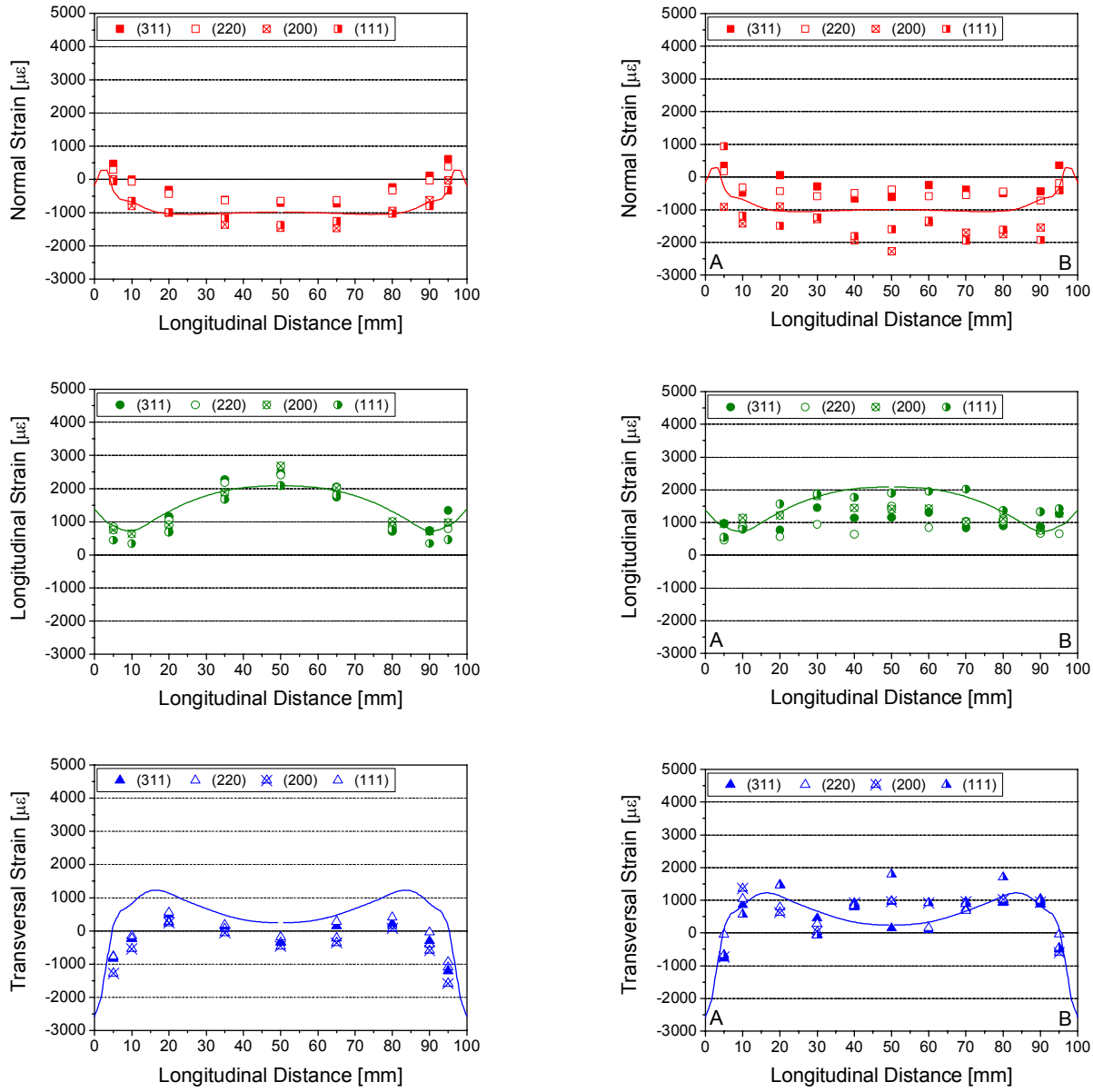


Figure 2: Dimensions of the investigated plates (A and B), the measurement locations and the directions of the three main strain components: normal, longitudinal and transversal.

Achievements and Main Results

Residual strains within two water-quenched IN718 plates with different grain sizes were measured by neutron diffraction. This investigation was important to evaluate the influence of grain size on the residual stresses state, because the FEM models usually contain no grain size information. For a comparison between FEM results and measurements a minimum spatial resolution is required, and therefore the gauge volume cannot randomly be extended. Consequently, the grain size shown in Figure 1b can be regarded as out of bounds for neutron measurements with a spatial resolution of 3x3 mm².



a) ***b)***

Figure 3: (a) Residual Strains in Plate A (a) and Plate B (b) obtained from the four reflections of the γ-matrix: (311), (220), (200), and (111) compared to the simulated elastic strains based on a temperature dependant heat-transfer coefficient.

References

[1] D.D. Krueger, Superalloy 718 – Metallurgy and Applications; Superalloy 718 – Metallurgy and Application, ed. Loria, The Minerals, Metals & Materials Society (1989) pp. 279–296.

[2] M. Stockinger: PhD Theisis, Technische Universität Graz, Austria (2003).

GKSS FORSCHUNGSZENTRUM in der HELMHOLTZ-GEMEINSCHAFT	**EXPERIMENTAL REPORT**	**GeNF ARES**

Evolution of internal stresses during isothermal creep of an Al-Si piston alloy

Proposer:	**Hans Peter Degischer**[1], **Anke Pyzalla**[1] [1]Vienna University of Technology
Experimental Team:	**Guillermo Requena**[1], **Rodrigo Coelho**[1], **Peter Staron**[2] [2]GKSS Research Centre
User Group Leader:	**Anke Pyzalla**[1]

Date(s) of Experiment:	17th–25th August 2005

Objectives

Subject of the experiments are short fibre reinforced metals (SFRM) that show prospects for applications in combustion engines. Main requirements for these applications include a low mass, high thermal conductivity, sufficient strength and ductility, a low overall thermal expansion coefficient and a high isothermal and thermal cycling creep resistance up to 300 °C. The aim of the experiments is a systematic investigation and comparison of the evolution of load partitioning between the metal matrix and the reinforcement [i] as well as the development of 2nd order microstresses in the SFRM after exposure to isothermal creep conditions.

Experiment

The investigated SFRMs were produced by squeeze casting. An AlSi12CuMgNi [ii] was used as the matrix, while pre-forms of random planar oriented Saffil® short fibres were used as reinforcement. The composites were produced using reinforcement volume fraction of 10 and 15 %.

When Al-Si alloys are used, Si segregates along the fibers during homogenisation and the Si forms bridges between the fibers resulting in a hybrid Si-Al_2O_3 three dimensional network [iii]. The creep properties of the SFRMs were tested at 300 °C with loads applied in a direction within the plane of predominant fiber orientation [iv]. The creep tests revealed that the fibers increase the creep resistance considerably compared to the pure matrix alloy and particle reinforced alloys [v]. Surprisingly the creep rate at different loads held constant for prolonged periods (more than 100 h) was found to depend on the sequence of the load changes: starting with a certain external stress produced a stationary creep rate significantly higher than that at the same stress after the sample had experienced a period at a somewhat higher load. Our hypothesis is that this effect is due to a redistribution of the internal stresses and/or more pronounced reorientation of the reinforcing structure during the period of higher loads increasing the load carrying capacity of the reinforcement architecture.

To study the evolution of internal stresses during the creep tests, cylindrical samples of 20 mm length and 6 mm diameter were cut from the gauge length of creep specimens of both SFRMs subjected to different exposure times. In order to analyse and quantify the residual stresses in the Al, Si and Al_2O_3 phases arising from the creep exposure, the samples were subjected to neutron diffraction measurements at room temperature. Al_2O_3 and Si powders were used as reference materials. The tests were carried out using three 2θ steps with a range of approximately 16° and centres in 46, 66.5 and 90°. An unreinforced matrix sample was also tested at 2θ=46° using rotation steps of 15° in order to evaluate the effects of grain size on the diffraction patterns.

Achievements and Main Results

Fig. 1 shows a set of spectra with centre at 46° obtained for an unreinforced matrix sample for five rotation angles. A very strong dependence of the diffraction intensity on the rotation angle is observed for the Al reflexes. The large grains present in this material are responsible for this effect. For this reason, only the Si and Al_2O_3 reflexes will be used to calculate the residual stresses during these first experiments.

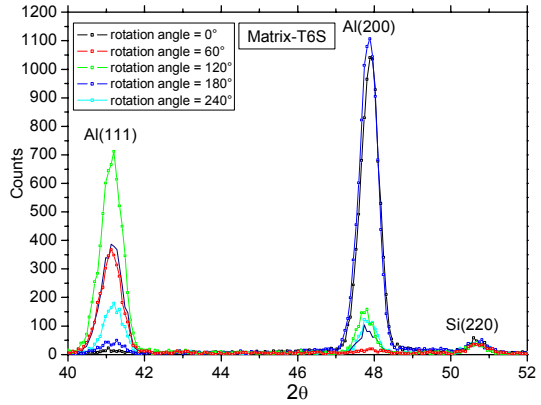


Figure 1:
Spectra obtained for the matrix alloy for different rotation angles.

Fig. 2 shows the spectra obtained during the diffractometry measurements with centre at 46° for all the SFRM samples and the Al_2O_3 and Si powders. The effect of the grain size is also observed here for the Al reflexes. The Si(220) reflex observed in Fig.2 is one of the Si reflexes that have been chosen for processing since it shows a "clean" pattern without contamination by any of its neighbour reflexes. The evaluation of the diffraction patterns is still being carried out and will be complemented with new measurements in GKSS. The final results will be subject of a future report.

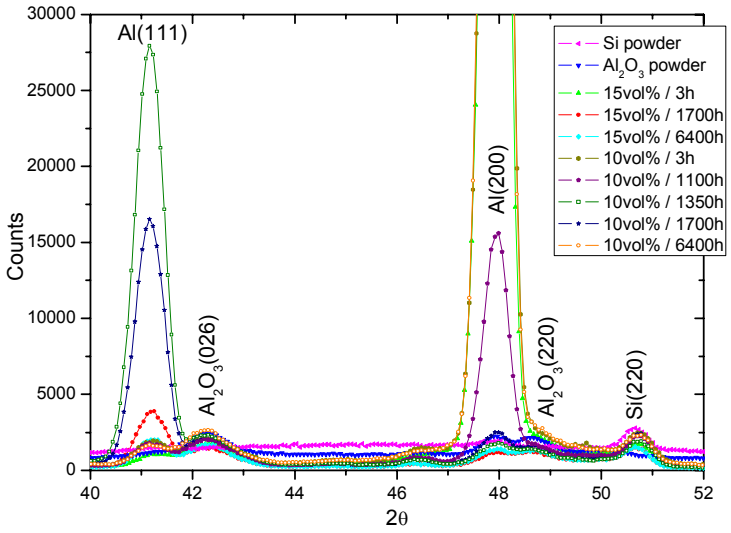


***Figure 2*:**
Diffraction patterns obtained for the 10 and 15 vol.% SFRM and Al2O3 and Si powders.

References

[1] A. Dlouhy, G. Eggeler, N. Merk, *Acta Mater.*, 43, *1995*, 535–550.

[2] Y. D. Huang, N. Hort, H. Dieringa, K. U. Kainer, Composites Science and Technology 65 (2005) 137–147.

[3] F. Lasagni, G. Requena, H.P. Degischer, M. Papakyriacou; Verbundwerkstoffe und Werkstoffverbunde", Ed. by M. Schlimmer, April 2005, Frankfurt, MatInfo..

[4] G. Requena, PhD Thesis: *Creep behaviour of discontinously reinforced Al-alloys;* Vienna Univ. of Technology, 2004.

[5] G. Requena, H.P. Degischer, "Effects of particle reinforcement on creep behaviour of AlSi1MgCu", Z. Metallkd., 96, 2005, 805–8011

GKSS FORSCHUNGSZENTRUM in der HELMHOLTZ-GEMEINSCHAFT	**EXPERIMENTAL REPORT**	**GeNF ARES**

Residual stresses in an austenitic steel plate with a weld

Proposer:	**H. Wohlfahrt,** [1]TU Braunschweig, Institut für Füge- und Schweiss-technik
Co-Proposers:	**P. Staron,** [2]GKSS Research Centre
Experimental Team:	**P. Staron**[2]
Date(s) of Experiment:	29.08.–04.09.2005

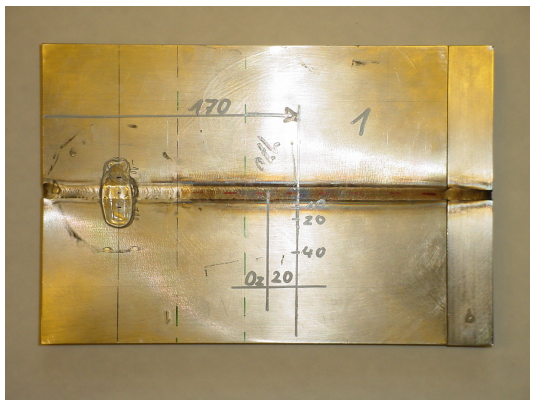
Objectives

The residual stress state in an austenitic steel plate shall be determined by different European laboratories using different experimental methods. This round robin test is initiated by the International Institute of Welding (IIW). The used experimental methods, besides neutron diffraction, are X-ray diffraction, the hole drilling method, and possibly other methods. The special purpose of neutron diffraction is to obtain in-depth stress profiles.

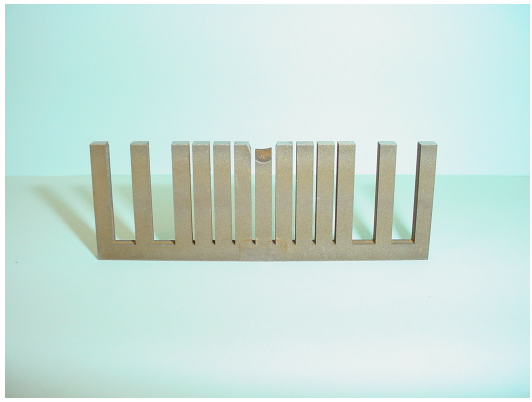
Experiment

Samples

The investigated sample was a 300 mm long, 200 mm wide, and 30 mm thick austenitic steel plate (316 LNSPH, carbon content 0.024 %) with a two-pass TIG weld on the top side (see figure). The used filler material was 316 L.



A reference sample was cut from one end of the plate by electro discharge machining (EDM). The macro-stresses within the reference material cut in this way relax largely; therefore it can serve as a stress-free reference from which d_0 can be determined. The reference sample has a comb-like shape, the teeth have a cross section of 4 mm × 4 mm (see figure).



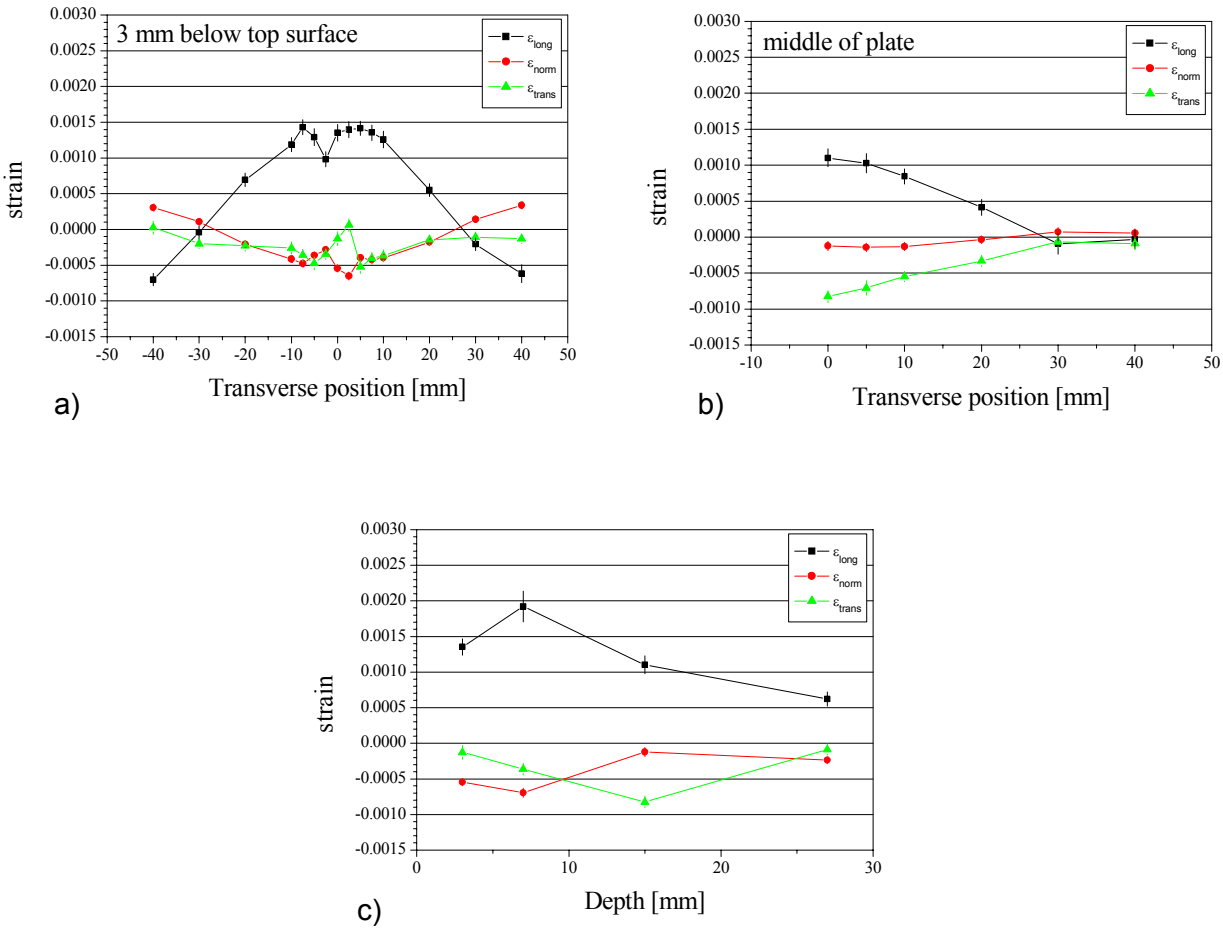
Measurements

The nominal size of the used gauge volume was 3×3×30 mm^3 for the measurement of transverse and normal strains. The long edge of the gauge volume was parallel to the longitudinal direction, assuming that the stresses do not change significantly over this distance. This gauge volume was used to increase intensity and thus reduce required beam time; in addition the grain statistics is improved (i.e. the number of diffracting grains is increased). The gauge volume for the measurement of longitudinal strains was 3×3×3 mm^3 because stress gradients are present in the transverse direction. To cover the same total volume element as in the measurements for

the transverse and normal directions, the small gauge volume was moved 6 mm and 12 mm in both directions along *x*, giving a total of five measurements for each point that are summed up. The γ-Fe (311) diffraction peak was recorded with an area detector at an angle of about 98.4°.

Experimental results

Strains in three orthogonal directions were measured at a total of 23 points along three different scan lines (a) 3 mm below the top surface, b) in the middle of the plate, and c) through the thickness of the plate below the weld). It was not possible to obtain information about d_0 in the weld from the used reference sample. A comparison of other d_0 values from the reference sample and those calculated from the plate measurements using the plane stress assumption showed that the latter assumption seems realistic. Therefore, strains have been calculated using the plane stress assumption.



Residual strains **a)** across the weld, 3 mm below top surface; **b)** across the weld in the middle of the plate; **c)** in the plate depth below the weld.

Achievements and Main Results

The residual stresses in different depths inside the 30 mm thick steel plate can be determined from the current experimental results. This is an important completion to the other experimental results that are mostly confined to the near-surface regions. An assessment of the results will take place when the results of all participating laboratories will be available. These results give also the chance for a comparison with predictions of finite element models.

GKSS FORSCHUNGSZENTRUM in der HELMHOLTZ-GEMEINSCHAFT	EXPERIMENTAL REPORT	GeNF ARES

Residual stresses in laser beam welded T-joint Al sheets

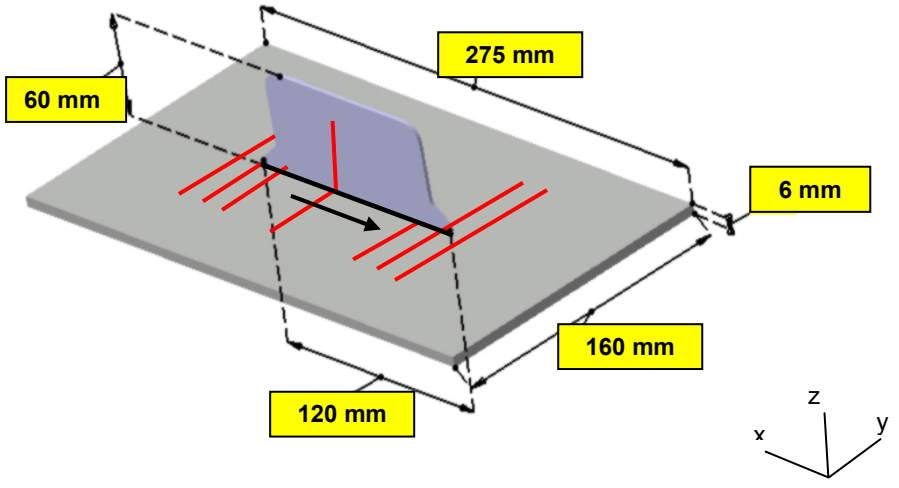
Principal Proposer:	**M. Koçak, F. Bayraktar** GKSS Research Centre
Experimental Team:	**Funda Seniz Bayraktar, P. Staron** GKSS Research Centre
Date(s) of Experiment:	01.08.–19.8, 05.09–10.10, 17.10–07.11, 11.11–15.11, 19.11–21.11.2005

Introduction

Residual stresses are an inescapable consequence of manufacturing and fabrication processes such as quenching, welding, forging and machining operations. They can also be introduced into components as a result of deformation and creep during use or due to the different response of particles and matrix in a multiphase material. The magnitudes of weld residual stresses can often be a high proportion of the yield or proof strength. High residual stresses in regions near the weld may promote brittle fracture, fatigue, or stress corrosion cracking. Welding of aluminum alloys is considered an essential long-term alternative to riveted structures for high-strength aerospace alloys because of their high strength/weight ratio. Thus, the retention of good post-weld microstructures and properties, and the control of residual stress and distortion are essential. Among the fusion welding methods, laser technology (LBW) appears to be the most promising solution for structural 6XXX aerospace alloys due to its high level of specific power and the limited area involved [1].

Experimental

The investigated specimens was laser beam welded T-joint configurations with a 6 mm thick Al alloy grade 6056 base plate (skin) and 2 mm thick Al alloy grade 6013 T part (clip). The dimensions of the specimens are shown in Fig. 1.



Specimen D

Figure 1: Schematic illustration of the specimen.

Internal strain measurements have been performed at 15 points along a 56 mm long scan lines (red lines in Fig. 1) in the middle of a plate using neutron diffraction. The measurements on the clip have been at 8 points performed through the middle scan line.

Neutrons of 0.16427 nm wavelength from an elastically bent perfect Silicon (311) monochromator were used. Strain measurements in three perpendicular directions are required to determine the stresses in these directions. The three directions are chosen as the principal sample axes x, y, and z. The gauge volumes in which the strains are measured are defined by Cd diaphragms. For run-ins, run-outs and middle positions (Fig. 2a and 2b) on the base plate of both specimens a matchstick-like gauge volume of nominal size 2*2*10 mm^3 was used for measurements of y and z strains for improving the intensity [2]. A cubic gauge volume size 2*2*2 mm^3 was used for measurements of x strains, because large stress gradients are expected in the y direction. In order to increase the number of diffracting grains for the small gauge volume, the gauge volume was shifted by 2.5 mm in x direction during the measurement. Therefore, approximately the same volume as in the two other directions is analysed. By this way, the grain size of the material proved to be small enough to ensure a good grain statistics even with the small gauge volume of approx. 8 mm^3. However, for the measurements in the clip (Fig. 2c) matchstick-like gauge volume of nominal size 1*1*30 mm^3 was used for measurements of y and z strains and a gauge volume size 1*1*2 mm^3 was used for measurements of x strains; the gauge volume was shifted by 3 mm in x direction during the measurement. In order to compare the results obtained from clip with the results from middle position of the base plate, the measurement in the base plate (Fig. 2d) is repeated with the same gauge volume provided for the measurement in the clip. The Al (311) diffraction peak was recorded with an area detector at an angle of about 84° [2]. This peak is recommended because the influence of micro-stresses on the stress results should be small, i.e. the (311) peak gives a good measure for the macro-stresses [4]. In general, diffractometric elastic constants have to be used here for E and ν, which depend on the hkl of the reflection that is used for the strain measurement [5]. However, the elastic anisotropy of Al is small and the macroscopic values E=70 GPa and ν=0.33 were used for the Al (311) reflection [5].

For the determination of a triaxial stress state, the knowledge of the unstrained lattice parameter d_0 (or the peak position θ_0) at each measured point inside the sample is required (cf. equation 1). As the lattice parameter can change e.g. with the solute content (Vegard's law [6]), or, more generally, with the chemical composition of the material, d_0 can depend on the heat input the material has experienced during welding. Therefore, proper reference material is required for the determination of the stress-free lattice parameter d_0. For this purpose a reference sample could be cut out of the specimens, in which macroscopic stresses can relax. Here, this problem was overcome by assuming a plane stress state in the material [7]. From the condition $\sigma_z = 0$, d_0 can be calculated for each point.

Results

The results showed that;

a) there is a maximum of longitudinal tensile stress in the heat affected zone of the clip reaching up to about 200 Mpa;
b) at the middle position significantly higher tensile longitudinal stresses appear in comparison to run-ins and run-outs;
c) the tensile stresses at run-ins of the base plate are higher compared to the stresses at the run-outs.

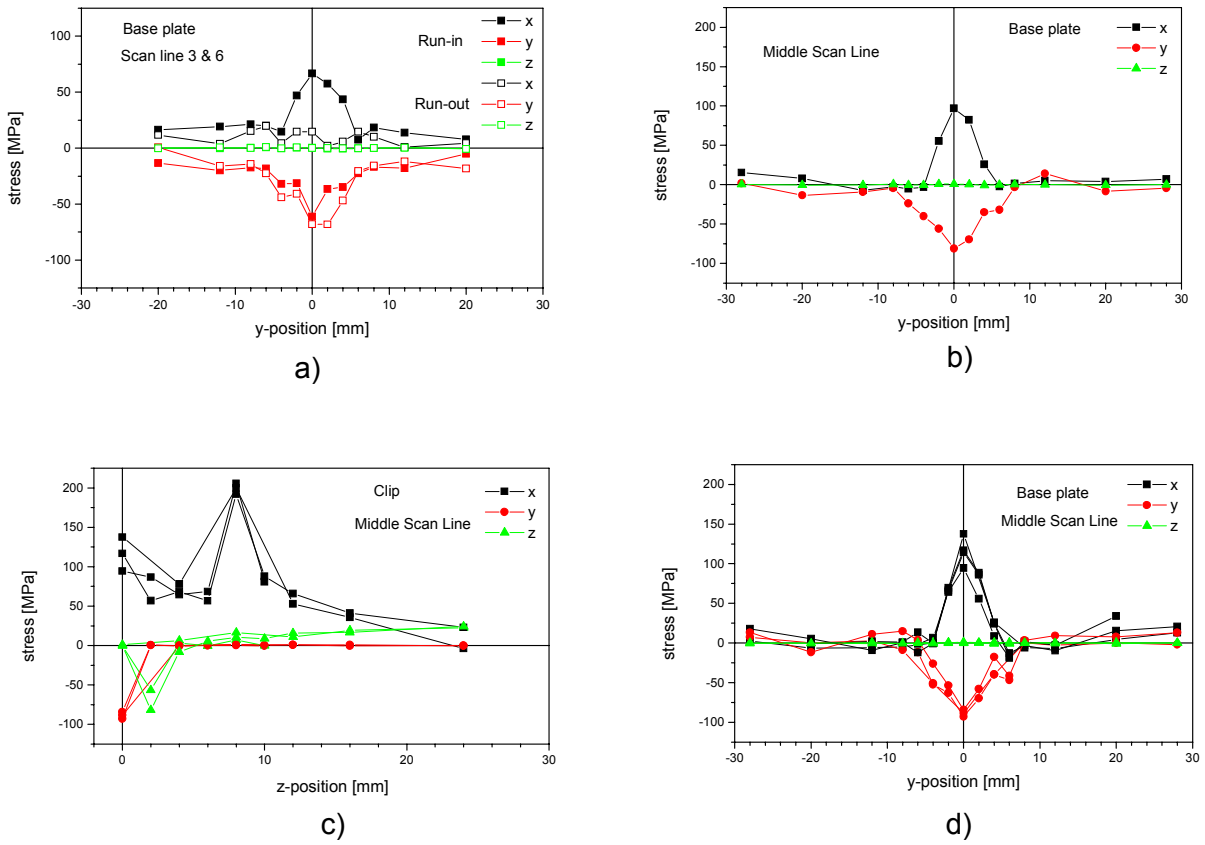


Figure 2: Residual stress results.

References

[1] M.N. James, D.J. Hughes, Z. Chen, D.G. Hattingh, P.J. Webster, “Residual stresses and fatigue performance”, 11th International Conference on Fracture (ICF), Turin (Italy), March 20–25, 2005.

[2] L. Pintschovius, V. Jung, E. Macherauch, O. Vöhringer, Materials Science Engineering 61 (1983) 43–50.

[3] B. Clausen, T. Lorentzen, T. Leffers, Acta Materialia 46 (1998) 3087–3098.

[4] ISO Technology Trends Assessment (TTA) 3:2001 „Polycrystalline materials-Determination of residual stresses by neutron diffraction“.

[5] V. Hauk, “Structural and Residual Stress Analysis by Nondestructive Methods”, Amsterdam, Elsevier (1997).

[6] H.G. Priesmeyer, in “Measurement of residual and applied stress using neutron diffraction”, (eds. M.T. Hutchings and A.D. Krawitz), NATO ASI series E 216 (1992) 277–284.

[7] A.J. Allen, M.T. Hutchings, C.G. Windsor, C. Andreani, Advances in Physics 34 (1985) 445–473.

GKSS FORSCHUNGSZENTRUM in der HELMHOLTZ-GEMEINSCHAFT	EXPERIMENTAL REPORT	GeNF FSS
Neutron time-of-flight spectrometer FSS		

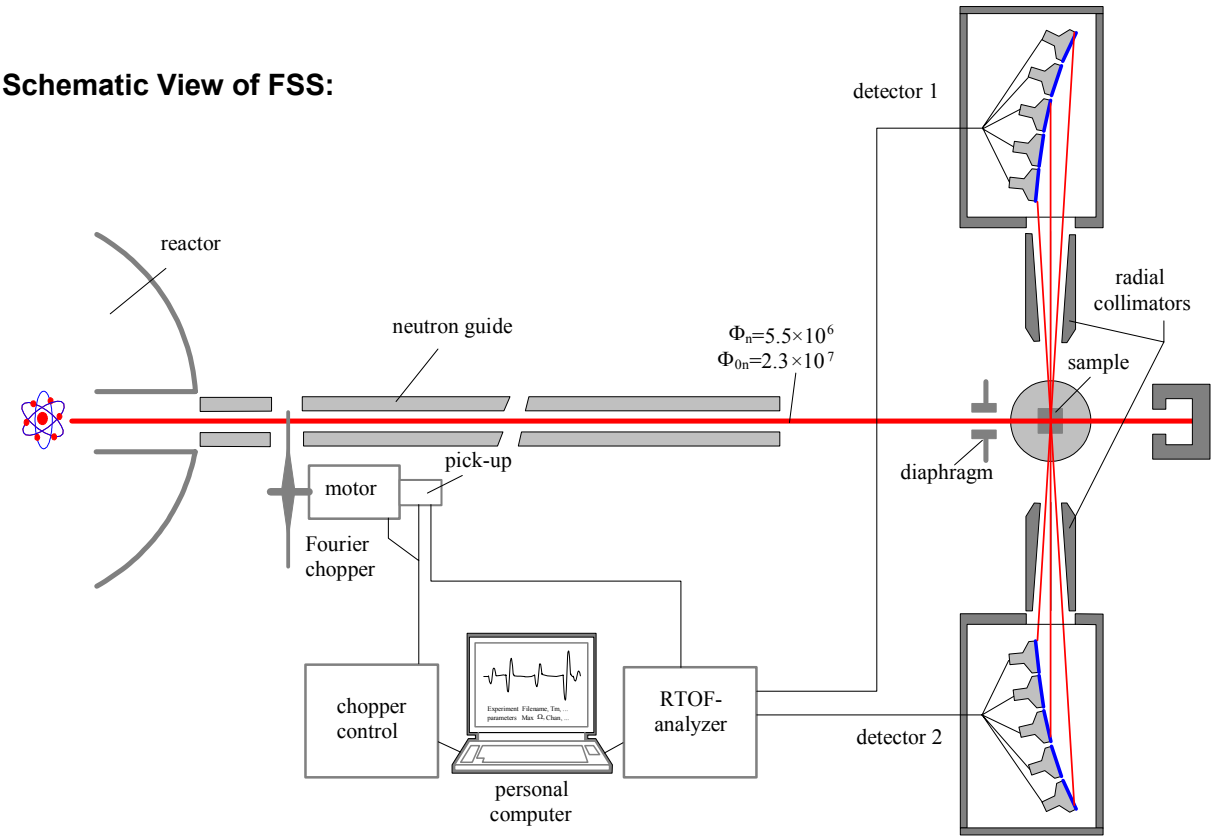
Short Instrument Description:

The spectrometer FSS is a Fourier reverse time-of-flight spectrometer (system Hiismäki) to investigate residual stresses in polycrystalline material specimens with technical sizes using thermal neutrons. Details can be found in P. Hiismäki, Modulation Spectrometry of Neutrons with Diffraction Applications, World Scientific, 1997.

Local Contact:

Prof. Dr. Hans Georg Priesmeyer
Phone/Fax : +49 (0)4152 87–1315 / +49 (0)4152 87–1338
e-mail: priesmeyer@gkss.de

Schematic View of FSS:



Instrument Details:

Location at FRG-1:	beam line 9, thermal neutrons
Flight path:	21.15 m Ni-coated curved neutron guide, radius of curvature: 3000 m characteristic wavelength: λ_{char} = 0.183 nm beam size: 2 x 20 mm^{-2} to 15 x 108 mm^{-2}
Fourier chopper:	1024 slits, 1760 rpm max. operating speed
Flux at sample position:	Φ = 5.5·10^6 cm^{-2} s^{-1}
Wavelength range:	λ = 0.1 nm to 0.4 nm

GKSS FORSCHUNGSZENTRUM in der HELMHOLTZ-GEMEINSCHAFT	EXPERIMENTAL REPORT	GeNF FSS

Simultaneous Positron Annihilation and Neutron TOF – diffraction Investigation of fcc – Iron under Compression

Principal Proposer:	**Hans G. Priesmeyer** Institut für Experimentelle und Angewandte Physik, Universität Kiel
Experimental Team:	**Hans G. Priesmeyer** Institut für Experimentelle und Angewandte Physik, Universität Kiel
Date(s) of Experiment:	April 2005

In the context of the project „In-Situ Untersuchung plastischer Verformungszustände mit Hilfe neutronen-induzierter Positronenvernichtungsstrahlung und hochauflösender Neutronendiffraktometrie“, funded through DFG Pr267/13-1, a uniaxial compressive experiment has been performed at the FSS TOF-diffractometer. Neutron capture, which is always a competing process to neutron scattering, leads to the emission of isotope – specific high-energy prompt gamma radiation, which in turn produces positrons within the bulk of the specimen. The subsequent decay of the positrons results in annihilation radiation which is influenced by crystalline defects, such as dis-locations created by plastic deformation. Plastic deformation on the other hand leads to an increase in the mosaic spread of the Bragg reflections for elastically scattered neutrons. By suitable collimation of both the neutron and gamma beams it was assured that the meas-urements were made within the same gauge region.
While the line shape was observed using a HPGe detector looking from above, an NaJ scintillation detector was used for background reduction and better gauge volume definition (see Fig.1)



Figure 1: Experimental setup showing the specimen in the stress rig together with the lead-shielded HPGe detector and its dewar.

The analysis of the annihilation line shape was done in the usual way by calculating and comparing the shape parameter S and the wing parameter W. Neutron reflections were analysed by single-peak fitting, which allows to determine both positions and widths for up to seven independent reflections simultaneously.

GKSS FORSCHUNGSZENTRUM in der HELMHOLTZ-GEMEINSCHAFT	**EXPERIMENTAL REPORT**	**GeNF FSS**

On the correlation between the linear coefficient of thermal expansion and the diffraction – elastic constants for polycrystalline copper

Principal Proposer:	**Hans G. Priesmeyer** Institut für Experimentelle und Angewandte Physik, Universität Kiel
Experimental Team:	**Hans G. Priesmeyer** Institut für Experimentelle und Angewandte Physik, Universität Kiel
Date(s) of Experiment:	June 2005

Both the linear coefficient of thermal expansion (LCE) and the diffraction-elastic constants E_{hkl} can be determined by neutron time-of-flight diffraction using the FSS spectrometer. Since both material properties depend on the inter-atomic coupling potential within the material, correlation between them can be expected. Tabular values for the macroscopic Young's modulus and LCE's show a slight anti – correlation (cf. Fig 1).

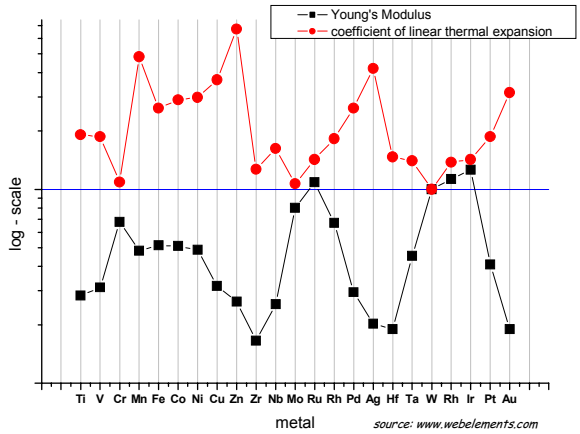


Figure 1:

Anti-correlation between the macroscopic Young's modulus and the LCE's of several metals, normalized to isotropic tungsten (log scale for higher resolution of details). Data were taken from www.webelements.com .

These findings are strongly supported by the fact, that materials with high macroscopic elastic modules have high melting point temperatures (Fig.2), while these in turn can be shown to be inversely proportional to the corresponding LCE's.

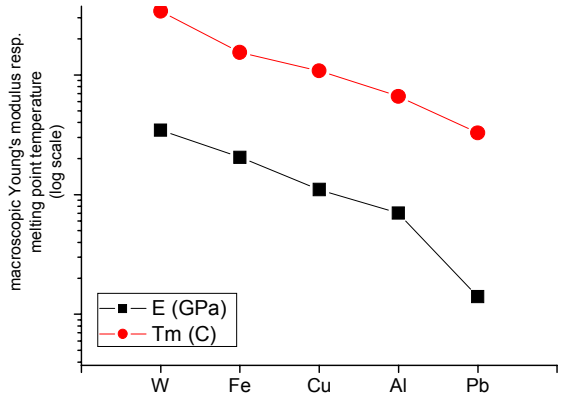


Figure 2:

Interrelation between macroscopic elastic constants and melting temperatures of several metals
(data taken from L.H. Van Vlack, Materials for Engineering).

Measurements carried out at FSS have shown for the first time, that the anti-correlation observed in the comparison between the macroscopic elastic properties and the LCE's also holds on the microscopic atomic scale. fcc - copper has been chosen as a model material, because of its high elastic anisotropy $E_{111}/E_{200} = 2.7$.

Results are shown in Figure 3:

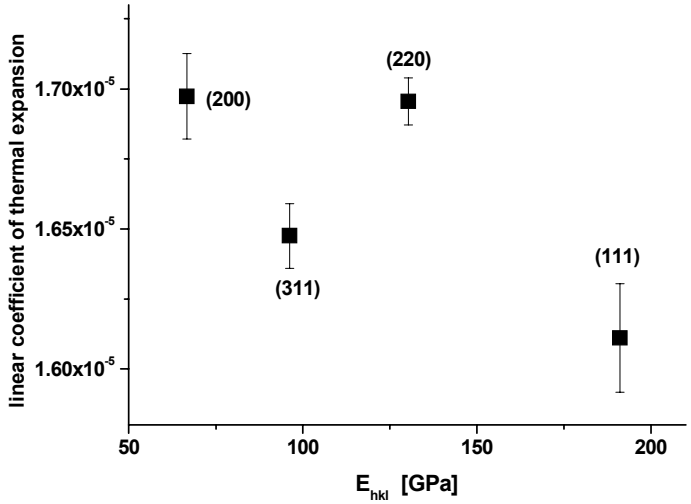


Figure 3:
LEC_{hkl} vs. E_{hkl} for polycrystalline copper.

The general tendency of increasing elastic constants with decreasing linear coefficients of thermal expansion is met for the (200), (311) and (111)-reflections and can be qualitatively explained by different shapes of the inter-atomic potential: while the LCE is related to the first derivative of the potential, Young's modulus is related to its second derivative. Thus a narrower potential valley will cause less shift of the centre-of-gravity of the oscillating atom, but have a higher slope. A theoretical interpretation of these experimental data on the basis of quantum mechanical calculations by K. Fuchs[1] is ongoing. It should also explain the deviation of the (220)-reflection from the trend of the other reflections.
According to most textbooks on materials the LEC's for cubic crystal systems should be isotropic. The results of this experiment suggest a revision of this statement for elastically anisotropic materials

[1] K. Fuchs, A Quantum Mechanical Investigation of the Cohesive Forces of Metallic Copper. Proceedings of the Royal Society (London), 151 (1935), 585–602

GKSS FORSCHUNGSZENTRUM in der HELMHOLTZ-GEMEINSCHAFT	**EXPERIMENTAL REPORT**	**GeNF FSS**

Residual stresses in a rolled sheet of magnesium alloy AZ31

Principal Proposer:	**J. Bohlen** GKSS, Institut für Werkstoffforschung Zentrum für Magnesiumtechnologie
Experimental Team:	**Hans G. Priesmeyer** Institut für Experimentelle und Angewandte Physik, Universität Kiel

Date(s) of Experiment:	August / September 2005

A rolled sheet of 1.6 mm thickness, made of magnesium alloy AZ 31, H24 tempered/Spectralite, has been scanned in the rolling, the transverse, and the normal direction in order to determine local three dimensional stress states. The reference lattice spacings needed to calculate strains were measured using Mg powder as well as a metal block, which was considered to be almost strain-free. As can be seen from typical neutron time-of-flight diffraction spectra taken with FSS, the material has a high degree of texture (cf. Fig. 1)

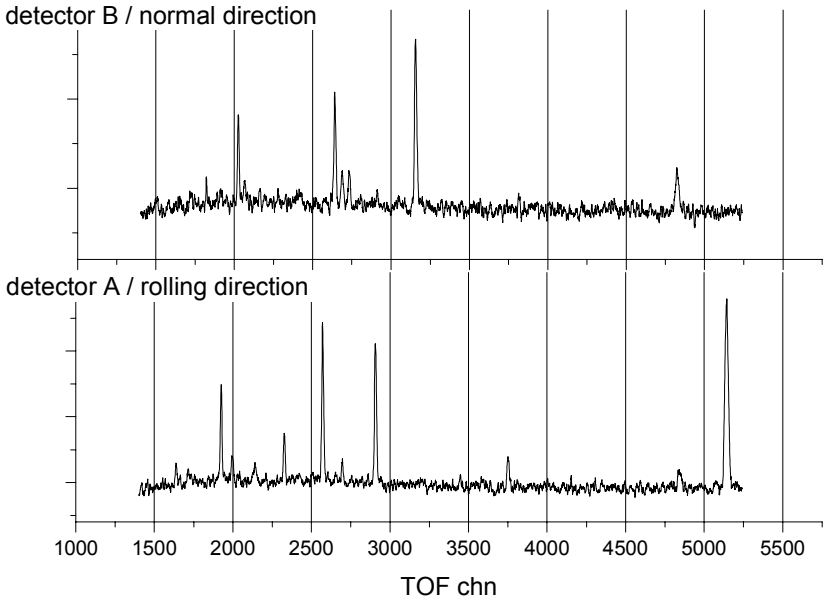


Figure 1: Neutron time-of-flight spectra of rolled AZ31, taken with FSS.

The following figure shows the experimental setup, which allows to measure two strain directions (rolling and normal resp. transverse and normal) at the same time, since the spectrometer is equipped with two opposite 90°-detectors.

The analysis of the collected data is in progress. The orientation distribution function of the textured specimen should be determined next, since a detailed description of the stress states is aggravated by the fact, that their calculation must take the ODF of the rolled sheet into account.

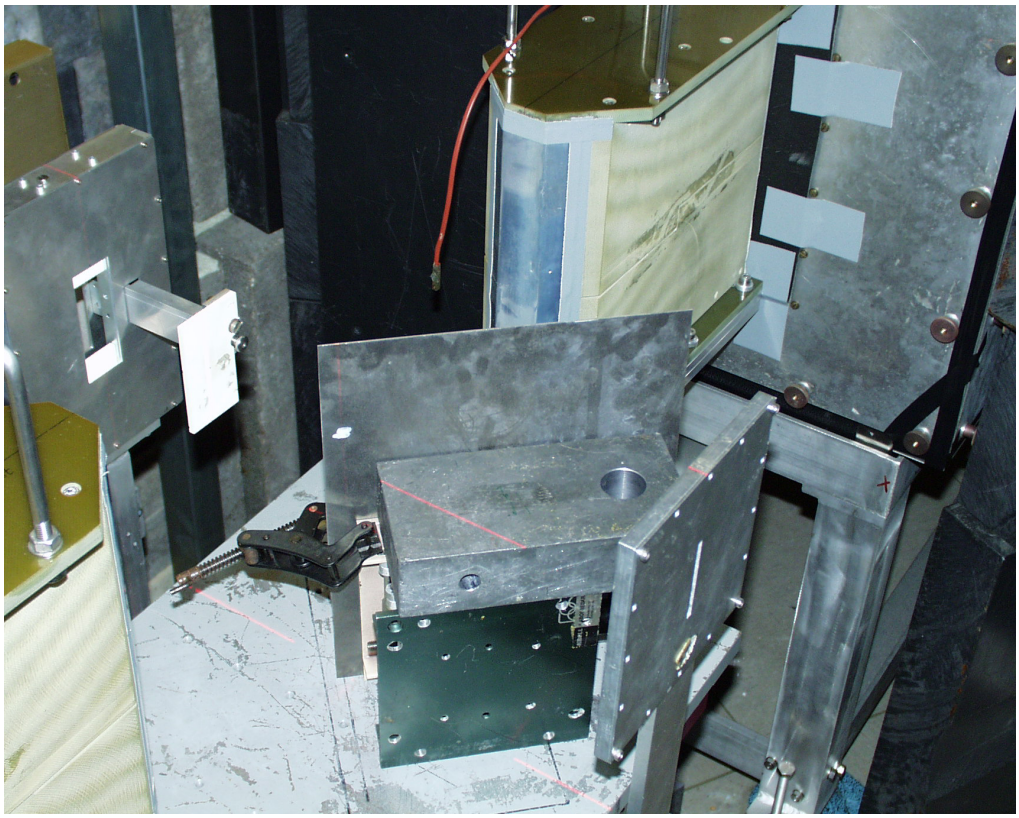


Figure 2: AZ 31 sheet in measuring position between the two radial collimators at FSS.

GKSS FORSCHUNGSZENTRUM in der HELMHOLTZ-GEMEINSCHAFT	**EXPERIMENTAL REPORT**	**GeNF FSS**

Positron annihilation and neutron diffraction experiments on aluminium alloys

Principal Proposer:	**Hans G. Priesmeyer** Institut für Experimentelle und Angewandte Physik, Universität Kiel
Experimental Team:	**Hans G. Priesmeyer** Institut für Experimentelle und Angewandte Physik, Universität Kiel
Date(s) of Experiment:	September 2005

Positron annihilation experiments on low-Z materials like aluminium, performed as outlined in project proposal DFG Pr 267/13-1, can be expected to need increased measuring time, since the cross section for pair production in a material depends on its atomic number and the energy of the incident gamma ray according to the cross section relation for pair-production

$$\sigma_{e+} \approx Z^2 \cdot \ln E_\gamma$$

Aluminium alloys are widely used structural materials, which often contain copper as an alloy constituent and the element itself produces a rather high-energy prompt gamma radiation upon thermal neutron capture. Copper captures neutrons and the isotope ^{63}Cu transforms into the isotope ^{64}Cu, which is radioactive and emits either electrons or positrons. Therefore the positron annihilation method can suitably be applied to most Al alloys. Experiments were made at FSS to determine the experimental parameters to perform simultaneous annihilation and diffraction investigations with adequate statistical accuracy for Aluminium alloys with copper contents between zero and 4.5 wt.-%.

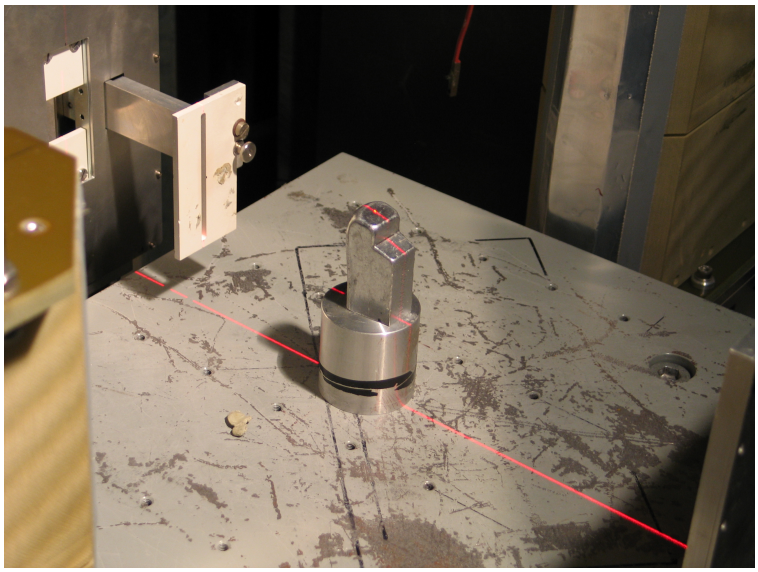


Figure 1: Cast aluminium alloy (Deutsche Aluminium Werke, Bonn) in measuring position at FSS.

GKSS FORSCHUNGSZENTRUM in der HELMHOLTZ-GEMEINSCHAFT	**EXPERIMENTAL REPORT**	**GeNF FSS**

Combined positron annihilation and neutron diffraction investigation on welds

Principal Proposer:	**Hans G. Priesmeyer** Institut für Experimentelle und Angewandte Physik, Universität Kiel
Experimental Team:	**Hans G. Priesmeyer** Institut für Experimentelle und Angewandte Physik, Universität Kiel
Date(s) of Experiment:	November/December 2004

As neutron absorption competes with neutron scattering, during strain measurements by neutron diffraction additional information is available through simultaneous gamma-ray spectroscopy. Isotope-specific high-energy prompt gamma radiation can produce positrons within the bulk of the specimen. Their subsequent decay results in annihilation radiation, which is influenced by material properties like crystalline defects near or within welds. It is common practise to analyse the annihilation line shape using the shape parameter S and the wing parameter W, defined in the following figure:

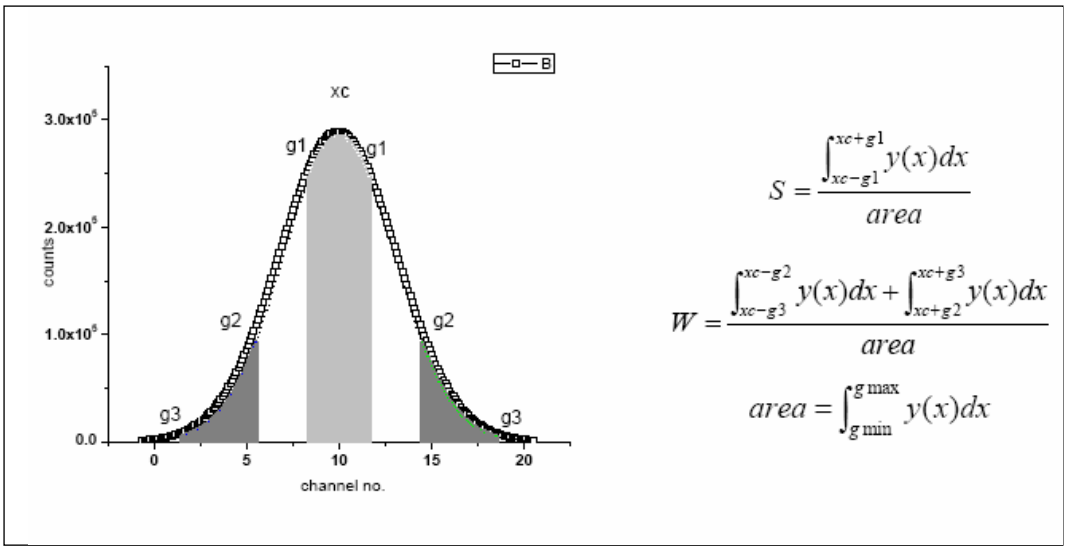


Figure 1: Definition of the parameters S and W , used to interpret annihilation line shapes.

Often an increase in the mosaic spread of the Bragg reflections for elastically scattered neutrons can be observed, too. Suitable collimation has assured that the information from both neutron diffraction and positron annihilation comes from the same gauge region within the specimens.
The gamma-spectrometer used in these experiments had an improved instrumental energy resolution and the NaJ (Tl) coincidence detector was replaced by a fast Bariumgermanate (BGO) detector of smaller size and higher efficiency.

Simultaneous neutron diffraction and gamma ray scans across weldments have been made (cf. Fig.2) for friction stir welded Al2024 (**A**), a carbon steel T-butt weld (**B**), a friction welded

aluminium-steel liner of the type used for the cold source at FRG-1 (**C**), and low-carbon steel x-weld (**D**).

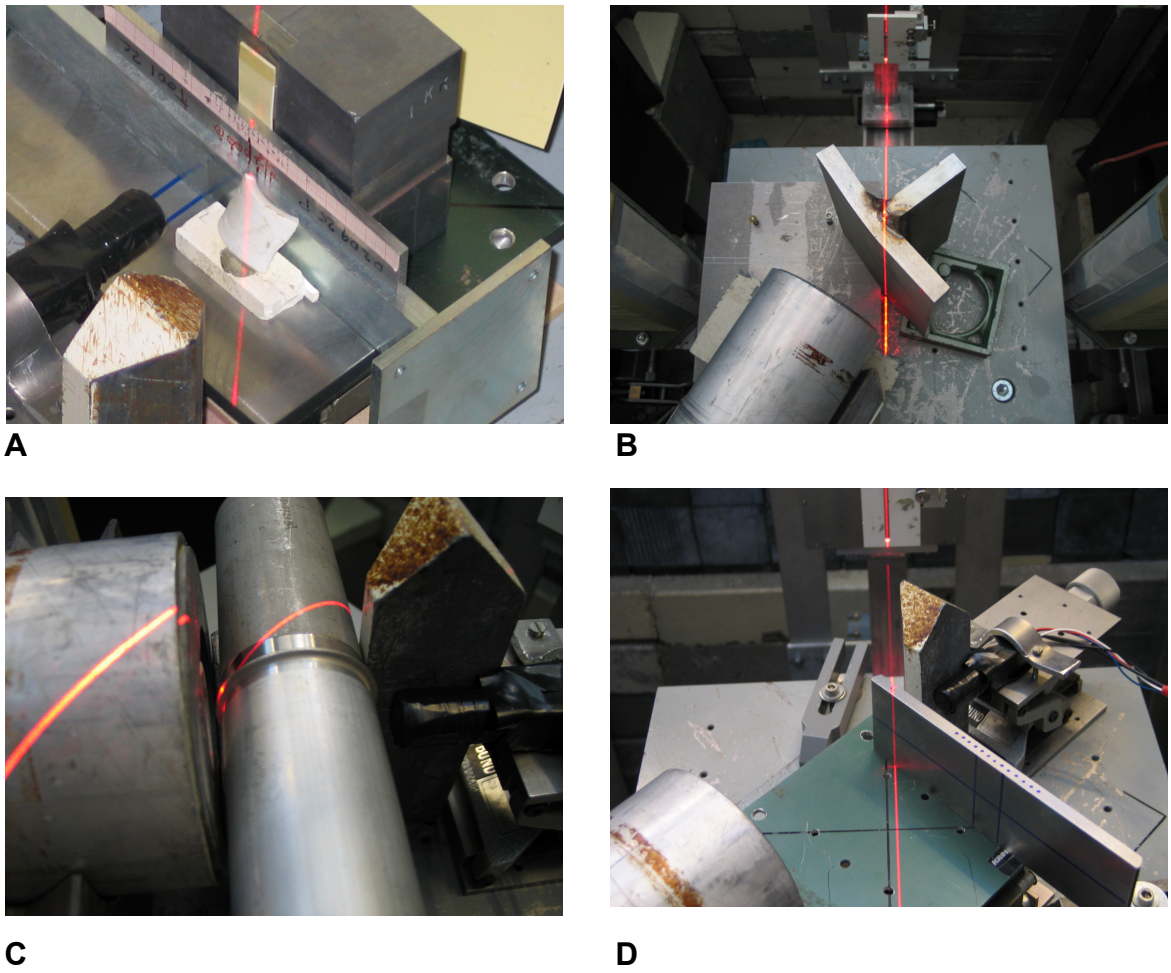


Figure 2: Different welded structures in the measuring position at FSS.

Analysis of the data is in progress, but a first result may be reported for the friction stir welded specimen:
Al2024 is an aluminium alloy with a copper content of ~ 3.5 %, which finds its application in aerospace industry. It was found, that the S-parameter correlates with the independently measured Vickers hardness gradient near the welding seam.

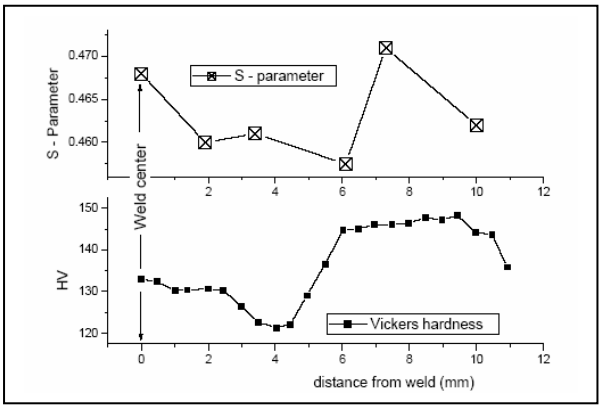


Figure 3:
Correlation between S-parameter and Vickers hardness near friction stir weld.

GKSS FORSCHUNGSZENTRUM in der HELMHOLTZ-GEMEINSCHAFT	EXPERIMENTAL REPORT	GeNF FSS

Positron annihilation investigation of a quenched steel cylinder

Principal Proposer:	**Hans G. Priesmeyer** Institut für Experimentelle und Angewandte Physik, Universität Kiel
Experimental Team:	**Hans G. Priesmeyer** Institut für Experimentelle und Angewandte Physik, Universität Kiel
Date(s) of Experiment:	December 2005

A quenched non- transforming steel cylinder has be re-investigated by simultaneous positron annihilation and neutron diffraction. The stress field which had developed upon water quenching had been measured earlier; it compared well to finite-element calculations made by Hougardy and Wildau, MPI für Eisenforschung, Düsseldorf, who also prepared the specimen.

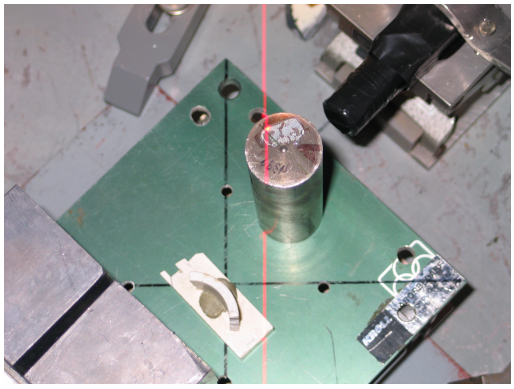


Figure 1:
Steel cylinder in measurement position. Neutron beam direction and gauge positon are marked by laser beams. The BGO scintillation detector (covered in black) – used to measure annihilation radiation in coincidence – is a new development. The crystal size is 8 mm ∅ x 12 mm.

After subtracting the background of annihilation radiation prevailing near the experimental setups, peaks from the rim and the centre of the cylinder show considerable differences, as can be seen from Fig. 2.
The interpretation of these findings is underway.

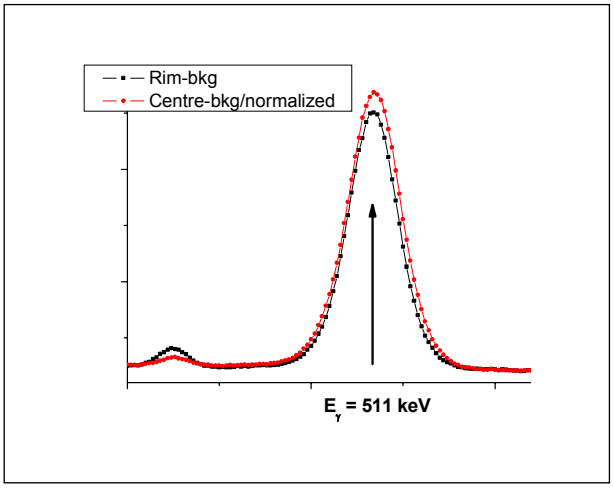


Figure 2:
Annihilation radiation from different gauge volumes in quenched steel cylinder.

GKSS FORSCHUNGSZENTRUM in der HELMHOLTZ-GEMEINSCHAFT	EXPERIMENTAL REPORT	GeNF TEX-2
Neutron texture diffractometer TEX-2		

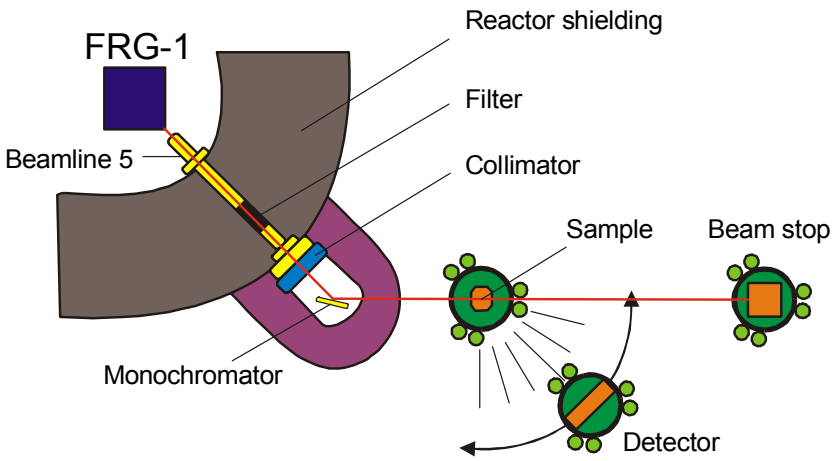
Short Instrument Description:

The four circle neutron texture diffractometer is used to characterise textures in metallic, ceramic and geologic materials applying thermal, non-polarised neutrons.

Local Contact:

Prof. Dr. Heinz-Günter Brokmeier
Phone/Fax: +49 (0)4152 87–1207 / +49 (0)4152 87–1338
e-mail: brokmeier@gkss.de

Schematic View of TEX-2:



Instrument Details:

Location at FRG-1:	beamline 5, thermal neutrons maximum beam cross section: 45 x 45 mm^2
Primary collimation:	30', 42', 51'
Monochromator:	Cu (111), Cu (200), PG (002), Ge (311)
Take-off angle:	17.2°, 27.2°, 37.2°, 47.2°, 57.2°
Wavelength range:	λ = 0.0–0.27 nm (in steps)
Flux at sample position:	$\Phi = 0.3–2 \cdot 10^6$ cm^{-2} s^{-1}
Angular range	Φ: -360° to +360° X: -360° to +360° Ω: -46° to + 46° 2Φ: -75° to +120°
Detector:	^{3}He- single detector 38° JULIOS-PSD 2-D-pos. sensitive detector (active area 30 x 30 cm^2)

Instrument Details (continued)**:**

Sample geometries (standard):	cube 10 mm edge, sphere 15–20 mm ∅ cylinder 10–15 mm ∅, 10–15 mm high
(various):	e.g. wires, tubes, tensile samples
Distances: sample–^{3}He detector	40–200 cm
sample–JULIOS	70–100 cm
Sample environment:	mirror furnace up to 2000 K loading device: tension up to 15 kN, compression up to 20 kN sophisticated set of sample holders

GKSS FORSCHUNGSZENTRUM in der HELMHOLTZ-GEMEINSCHAFT	**EXPERIMENTAL REPORT**	**GeNF TEX-2**

Global textures of ECAP deformed nickel

Proposer:	**Werner Skrotzki[1],** [1]Institute of Structural Physics, Division of Metal Physics, Dresden University of Technology,
Co-Proposer:	**Burghardt Klöden[1]**
Experimental Team:	**Heinz-Günter Brokmeier[2],** [2]Institut für Werkstoffkunde und Werkstofftechnik, TU Clausthal
User Group Leader:	**Werner Skrotzki[1]**

Date(s) of Experiment:	2005

Objetives

ECAP is at present one of the most promising techniques to produce bulk nanostructured or ultrafine-grained materials (grain size in the range of 100–1000nm) for structural applications. The process has received considerable attention in the last few years due to the advent of nano-technology, and it continues to receive attention of the scientific community due to its future industrial potential [1, 2]. In ECAP a billet is deformed in a narrow deformation zone at the plane of intersection of two die channels of equal area cross-section and the strain mode approximates closely to simple shear (Fig. 1).

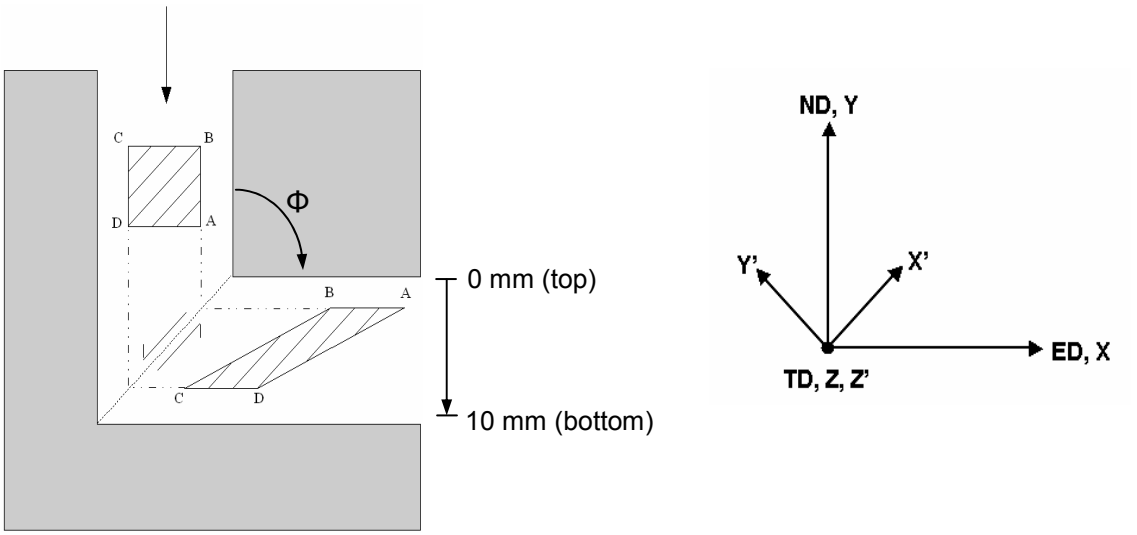


Figure 1: Idealized simple shear model of ECAP showing the shape change of a material element with shear by $\gamma = 2$. (ND = normal direction, TD = transverse direction, ED = extrusion direction, X, Y, Z = ECAP reference system; X' ,Y', Z' = simple shear reference system).

As the overall billet geometry remains nearly constant during ECAP, multiple passes through the die are possible without any reduction in cross-sectional area. This allows materials to be deformed to very high plastic strains that cannot be readily obtained in more conventional processes, such as rolling. Large plastic deformation results in the development of texture, which will be demonstrated here for nickel. The study belongs to a project on the dependence of ECAP textures of fcc metals on stacking fault energy.

Experiment

The material used was extruded 3N nickel. Specimens with 9.9 mm x 9.9 mm square cross section and 100 mm length were cut by spark erosion. To get a homogeneous, strain-free starting microstructure the billets were annealed 1 hour at 600 °C. ECAP was carried out at a crosshead speed of 1 mms^{-1} at 400 °C using a Zwick 200 kN screw driven machine and a die set with rectangular intersection of the channels without any rounding of the corner region. The number of ECAP passes was limited to 3. Between individual passes the specimen was introduced in the same sense (Route A, that is no rotation around the specimen long axis between intermediate passes).

Neutron texture measurements were done on a cube of 9.9 mm x 9.9 mm x 9.9 mm taken from the middle part of both the starting and the ECAP billets. The results are presented in the form of an inverse pole figure (starting sample) and ODF sections calculated with the software developed by Dahms and Eschner [3] (ECAP samples).

Achievements and Main Results

The starting texture is a <100>+<111> double fibre texture in pressing direction (Fig. 2).

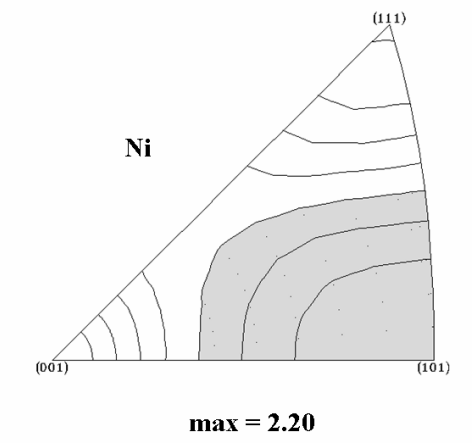


Figure 2:
Starting texture of Ni displayed as inverse pole figure of the pressing direction. Isolines: 0.5, 0.75, 1.0, 1.25, 1.5, 1.75, 2.0 mrd (multiples of a random distribution), grey area is below one.

During ECAP the texture changes to components typical for simple shear in the transition plane of the two die channels (Fig. 3). It is represented by φ_2 = 0° and φ_2 = 45° ODF sections, which for fcc metals contain all major ECAP texture components. The preferred orientations after ECAP are compared with the ideal components of simple shear in the intersection plane of the die channel. The transformation to the ECAP reference system has been given by Tóth et al [4] and is presented in the upper part of Fig. 3. The transformed components are distinguished by subscript E. Moreover, the cube component being a rotated Goss component in the shearing system is indicated. A detailed analysis and discussion of the texture components with respect to intensity and deviation from ideal simple shear positions will be given elsewhere.

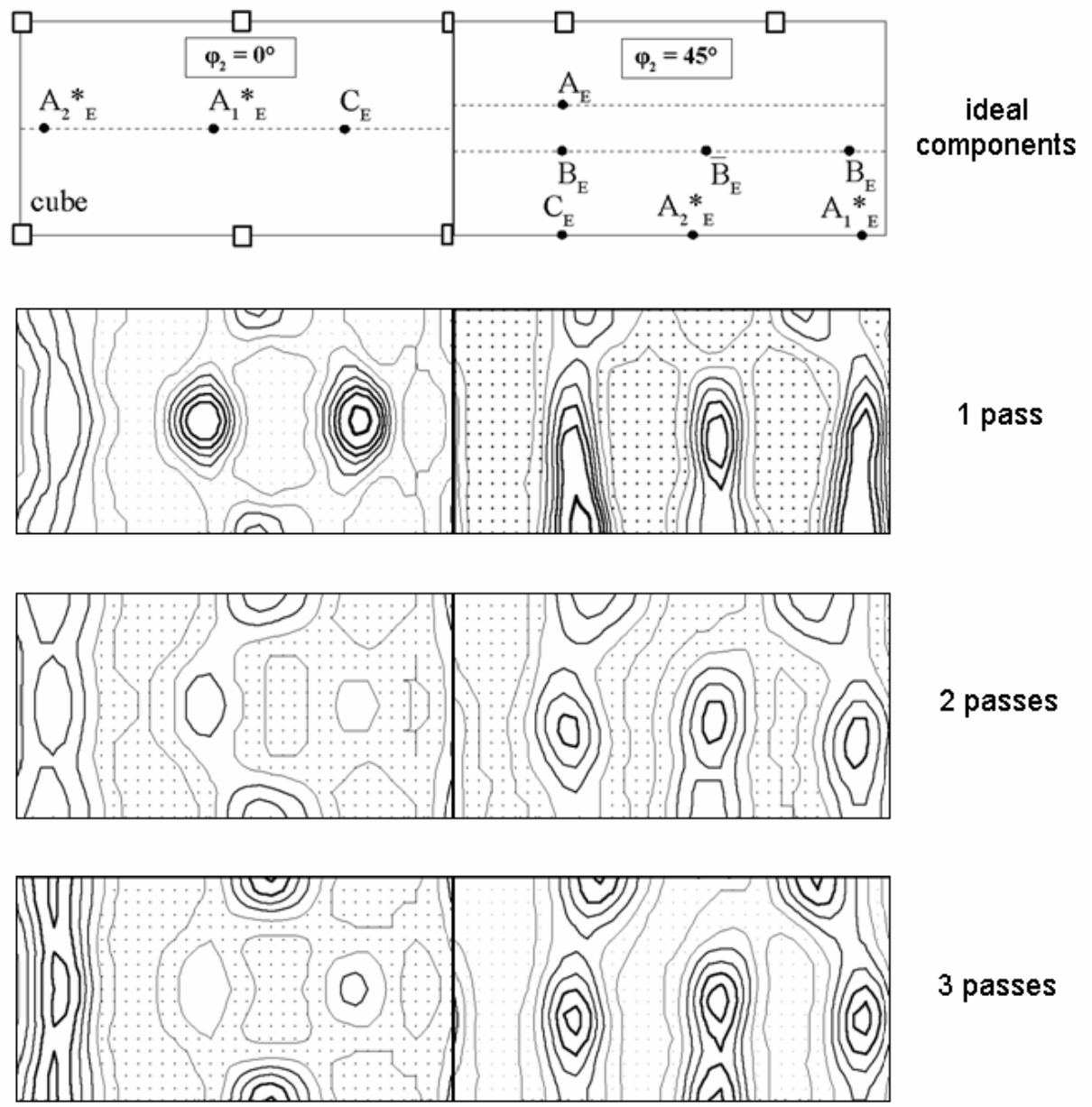


Figure 3: Textures of ECAP deformed Ni (Route A; isolines: 0.5, 1.0, 1.5, 2.0, 2.5, 3.0, 4.0 mrd). Top figure is the key figure of the ideal compnents.

References

[1] V.M. Segal, Mater. Sci. Eng. A 97 (1995), 157.
[2] R.Z. Valiev, Mater. Sci. Eng. A 234 (1997), 59.
[3] M. Dahms and T. Eschner, Software manual (1996).
[4] L.S. Tóth, R. Arruffat Massion, L. Germain, S.C. Baik and S. Suwas. Acta Mater. 52 (2004) 1885.

GKSS FORSCHUNGSZENTRUM in der HELMHOLTZ-GEMEINSCHAFT	**EXPERIMENTAL REPORT**	**GeNF TEX-2**

Texture development in Mg-Zn-Y alloy under different deformation processes

Proposer:	**M. Y. Zheng[1], W. M. Gan [1], S. W. Xu[1], K. Wu[1]**,[1] School of Materials Science and Engineering, Harbin Institute of Technology, Harbin 150001, China
Co-Proposers:	**H.-G. Brokmeier[2]**, [2]Institut für Werkstoffkunde und Werkstofftechnik, TU Clausthal, Germany
Experimental Team:	**W. H. Ye[3], S. B. Yi[2], H.-G. Brokmeier[2]** [3] GKSS Research Centre
User Group Leader:	**H.-G. Brokmeier[2]**
Date of Experiment:	May 2005

Objectives

High performance magnesium alloys have great potential in aerospace and other high technological applications. In order to improve their properties, these magnesium alloys are usually subjected to thermomechanical processing. As a result, both grain-refinement due to recrystallization and high intensity of texture are attained in the materials. Therefore, it is crucial to understand the correlation among deformation mechanisms, texture and properties in the deformed magnesium alloys [1]. In this research, to understand the deformation mechanisms during normal extrusion and ECAP (equal channel angular pressing) of Mg-Zn-Y alloy [2,3], the texture developed in normal-extruded and ECAP processed Mg-Zn-Y alloy were measured.

Experiment

The material used in this investigation was a Mg-Zn-Y alloy having a composition of Mg-11wt.%Zn-0.9wt.%Y (ASTM designation: ZW1101). The alloy was initially produced by conventional ingot casting under a dynamic SF_6 and CO_2 mixed gas atmosphere, and cast into an air-cooled metal mould. The ingot was then hot extruded at 380 ^oC at a rate of 0.2 m/min to give rectangular bars with 15 mm in thickness and 15 mm in width corresponding to a reduction ratio of 9:1. The extrusion rods were cut into 10×10×60 mm^3 rectangular billets for ECAP (designated as EX-ECAP[4]). The ECAP processing was conducted on the billets by the die with a channel angle of 90^o and a curvature angle of 37° through the die using processing route B_C, in which the specimen rotated by 90^o in the same direction between each pass. The specimen was ECAP processed at 250 ^oC for the first pass, 200 ^oC for the second to the eighth pass at a pressing speed of 40 mm/min.

Texture measurements were carried out using neutron diffractometer TEX-2. Four completed pole figures, i.e. (0002), $(10\bar{1}0)$, $(11\bar{2}0)$, $(10\bar{1}1)$, were measured for the as-cast, as-extruded and EX-ECAPed Mg-Zn-Y alloy.

Achievements and Main Results

The pole figures of the as-cast and as-extruded ZW1101 alloy are shown in Figure 1. The as-cast Mg-Zn-Y alloy shows a random texture, as shown in Figure 1 (a) and (b), while as-extruded alloy exhibits a strong ED // $<10\bar{1}0>$ fiber texture, as shown in Figure 1 (c) and (d). After the extruded alloy was subjected to ECAP, the basal planes tend to be inclined about

45 $_{o}$C to the extrusion direction, as shown in Figure 2. And the texture sharpness increases with increasing ECAP passes.

The tensile stress-strain curves of the Mg-Zn-Y alloy under different conditions are shown in Figure 3. The high ultimate tensile stress and high elongation obtained in the as-extruded alloy are considered to be resulted from the fine grain size due to recrystallization during hot extrusion, the unidirectional distribution of I-phase particles as strengthen phases along the extrusion direction, and the $<10\bar{1}0>$ fiber texture formed in the matrix alloy after extrusion. After the extruded alloy was subjected to ECAP processing, the yield strength of the alloy was increased slightly. Basal slip is generally considered as the main deformation mechanism of magnesium alloys at ambient temperature. High schmid factor obtained when basal planes incline about 45^{o} to the extrusion direction will lead to lower yield strength. However, in the present case, yield strength was not decreased after ECAP processing. The decrease of yield strength due to texture modification is may be balanced by increase of yield strength due to the significant grain refinement after ECAP processing.

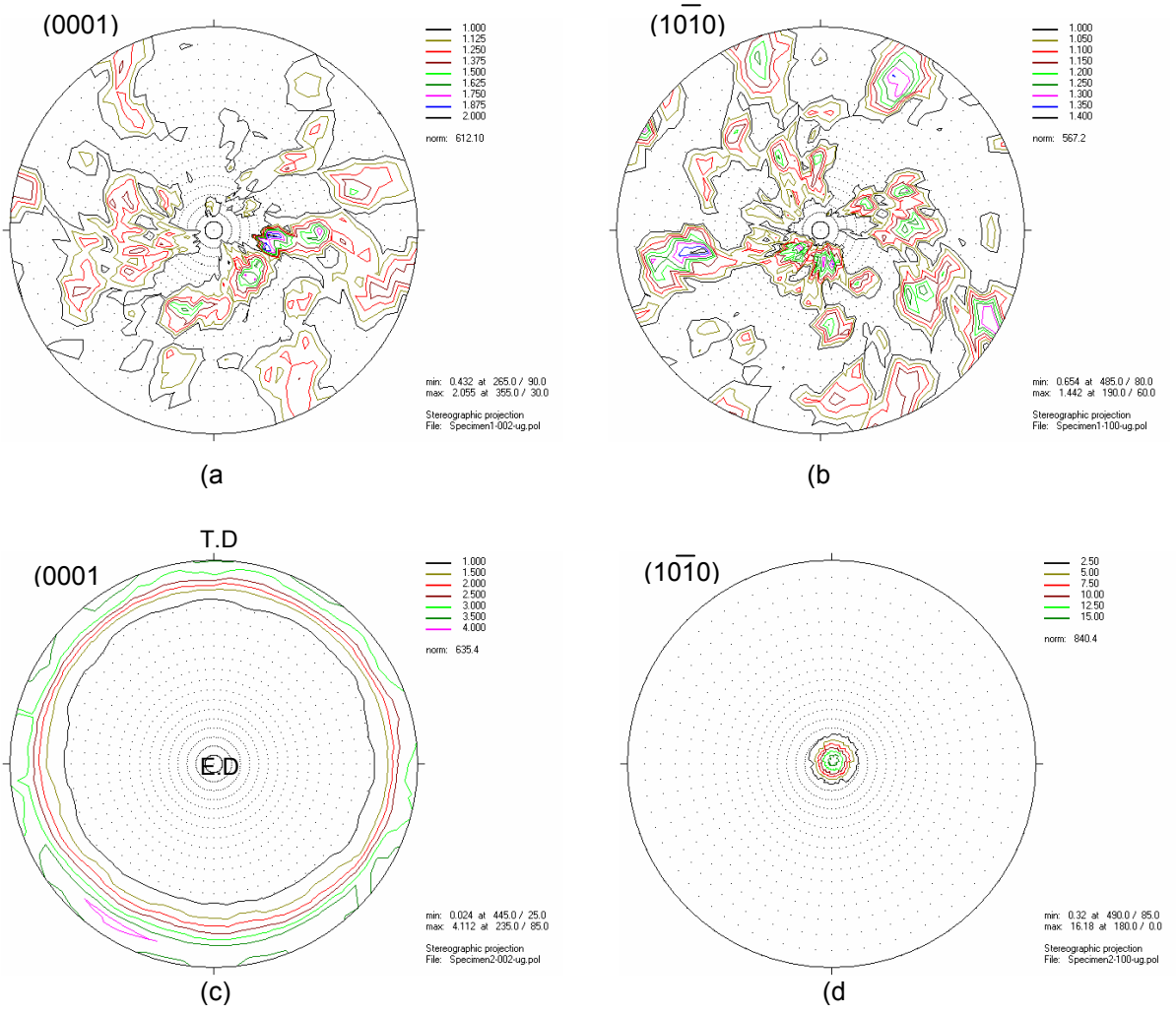


Figure 1: Pole figures of the (a), (b) as- cast and (c), (d) as- extruded Mg-Zn-Y alloy.

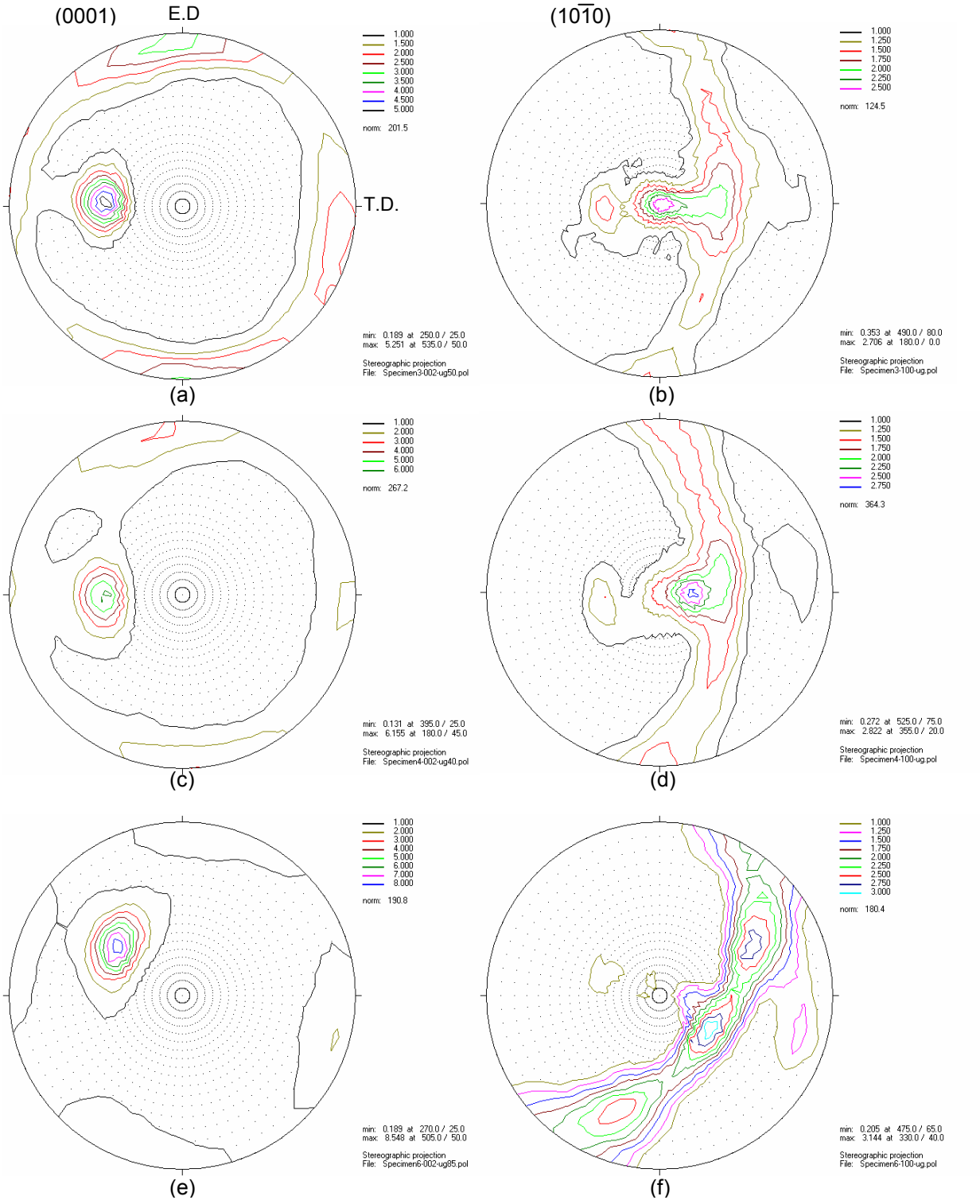


Figure 2: Pole figures of (a), (b) EX-1P ECAPed, (c), (d) EX-4P ECAPed and (e), (f) EX-8P ECAPed ZW1101 alloy.

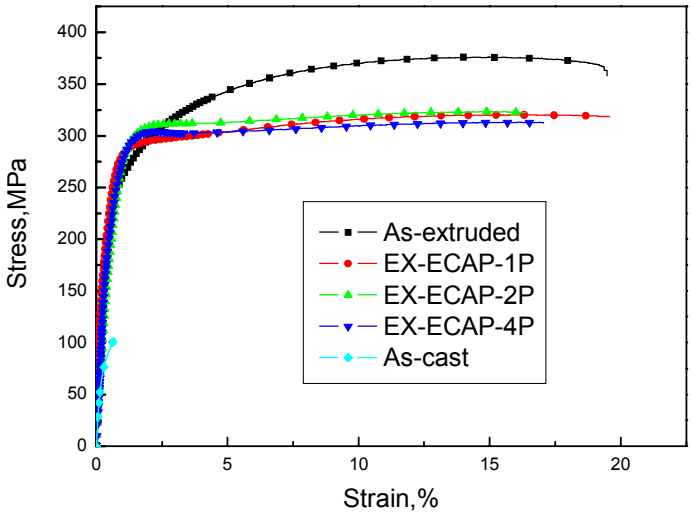


***Figure 3*:**

Tensile stress-strain curves of ZW1101 magnesium alloy under different conditions.

References

[1] S. R. Agnew, M. H. Yoo, C. N. Tomé. Acta mater. 2001, 49(20): 4277–4289

[2] M. Y. Zheng, X. G. Qiao, S. W. Xu, K. Wu, S. Kamado, Y. Kojima. Mater. Sci. Forum. 2005, 488-489: 589–592

[3] M. Y. Zheng, X. G. Qiao, S. W. Xu, W. M. Gan, K. Wu, S. Kamado, Y. Kojima, H. G. Brokmeier. Trans. Nonferrous Metals Soc. China. 2005, 15(4): 715–721

[4] K. Matusbara, Y. Miyahara, Z. Horita, T.G. Langdon. Acta Mater. 2003, 51: 3073–3084

GKSS FORSCHUNGSZENTRUM in der HELMHOLTZ-GEMEINSCHAFT	**EXPERIMENTAL REPORT**	**GeNF TEX-2**

Influence of temperature and aluminium content on the texture formation of extruded Mg-alloys

Proposers:	**Jan Bohlen[1], Dietmar Letzig[1]** [1]Institute for Materials Research, GKSS Research Centre
Experimental Team:	**Bernd Schwebke[2], Heinz-Günter Brokmeier[2]** [2]Institut für Werkstoffkunde und Werkstofftechnik, TU Clausthal
User Group Leader:	**Heinz-Günter Brokmeier[2]**
Date(s) of Experiment:	March 2005

Motivation

Recent activities in Magnesium research are focused on the development of suitable magnesium wrought alloys for the production of semi-finished products such as extruded profiles. The deformation and recrystallization behaviour as it appears during thermo-mechanical treatment like extrusion determines the properties of the material by changing its microstructure. More in particular, the texture of the wrought component has a significant influence on the activation of deformation modes and therefore is an important issue for an alloy development with the aim to improve mechanical properties.

Objectives

The objective of these measurements is to understand the influence of both the alloy composition and the extrusion parameters on the micro-structural development. In particular this is the concentration of solute aluminium in alloys from the magnesium AZ-series and the extrusion temperature during hydrostatic extrusion.

Experiment

Magnesium billets from alloys AZ31, AZ61 and AZ80 were extruded into round bars by using the hydrostatic extrusion process. The extrusion temperature was 100 °C and 300 °C, respectively. Directly behind the die exit the bars were water-cooled. Therefore a study of dynamic processes that became active during extrusion became possible. Fig. 1 shows micrographs from bars extruded at 100 °C. Fig. 2 shows inverse pole figures in extrusion direction from the same bars whereas Fig. 3 shows the inverse pole figures for bars extruded at 300 °C.

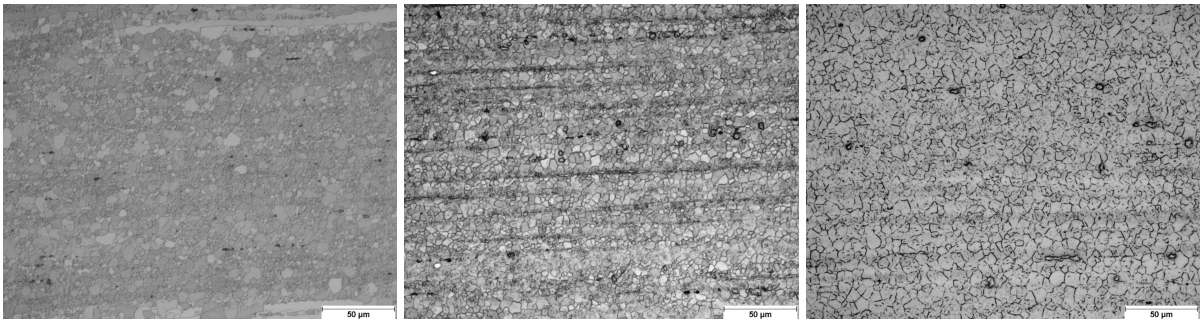


Figure 1: Microstructure of a round bar after hydrostatic extrusion at 100 °C. (extrusion direction →), from left to right: AZ31, AZ61, AZ80.

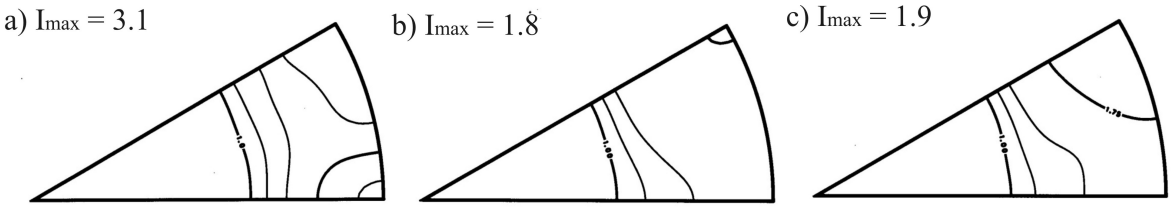


Figure 2: Inverse pole figures of extruded bars at 100°C, I_{max} are max. intensities: a) AZ31 (lev.: 1,0, 1,5, 2,0, …), b) AZ61 (lev.: 1,0, 1,25, 1,5, …), c) AZ80 at 110°C (lev.: 1,0, 1,25, 1,5, …).

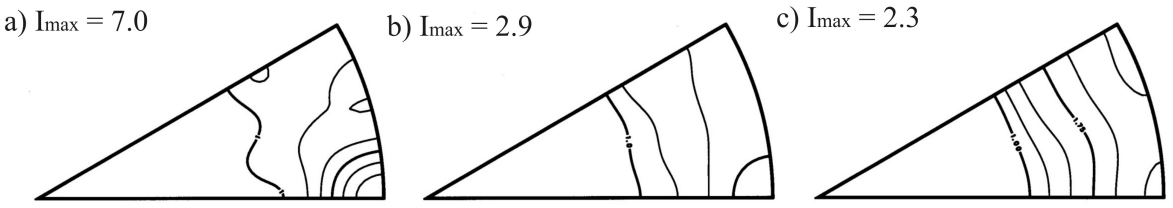


Figure 3: Inverse pole figures of extruded bars at 300 °C, I_{max} are the max. intensities: a) AZ31 (lev.: 1, 2, 3, …), b) AZ61 (lev.: 1,0, 1,5, 2,0, …), c) AZ80 (lev.: 1,0, 1,25, 1,5, …)

Achievements and Main Results

A significant result of the extrusion trials is the fact that also after extrusion at 100°C a recrystallized microstructure is found [1]. Thus, new grains have formed dynamically during extrusion and grown throughout the trial. A typical <10.0>-fibre texture is found like it is often observed for round bars from hexagonal structured metals after uniaxial deformation. The intensity of this <10.0> pole is significantly lower for AZ61 compared to AZ31. In AZ80 on one hand an even lower <10.0> pole intensity is found than for AZ61, but also a second fibre component is visible around the <11.0> pole. Thus, a double fibre results with two prismatic-type poles.

The inverse pole figures from bars extruded at 100/110 °C also show a double fibre texture where the <10.0> pole is less pronounced than in the trial at 300°C. On the other hand the <11.0> pole is more pronounced. In AZ61 with a higher content of aluminium the same is found, however, the intensity of the <11.0> pole is slightly higher compared to the <10.0> pole. The intensities are lower than in AZ31. In AZ80 the <11.0> pole is even more pronounced compared to AZ61. If the results are compared with a view to the lower temperature, the main differences are lower pole intensities in general, but also a higher significance of the <11.0> pole in all three alloys.

These achievements allow a study of the influence of texture on mechanical properties of magnesium extruded bars. Especially the yield asymmetry between tensile and compression tests is affected by the maximum intensities [2].

References

[1] J. Swiostek, D. Letzig, K. U. Kainer, Proceedings of the First Russian International Conference and Exhibition of Magnesium – Broad Horizons, Nov 29th–Dec 01st 2005, accepted

[2] J. Bohlen, J. Swiostek, H.-G. Brokmeier, D. Letzig, K.U. Kainer: Low temperature hydrostatic extrusion of magnesium alloys, In: N. R. Neelameggham et al. Ed., „Magnesium Technology 2006“, TMS Annual Meeting San Antonio (2006), submitted for publication

GKSS FORSCHUNGSZENTRUM in der HELMHOLTZ-GEMEINSCHAFT	**EXPERIMENTAL REPORT**	**GeNF TEX-2**

Influence of cooling conditions on microstructure and texture during extrusion of magnesium alloys

Proposers:	**Jan Bohlen[1], Dietmar Letzig[1]** [1]Institute for Materials Research, GKSS Research Centre
Experimental Team:	**Bernd Schwebke[1], Heinz-Günter Brokmeier[2]** [2]Institut für Werkstoffkunde und Werkstofftechnik, TU Clausthal
User Group Leader:	**Heinz-Günter Brokmeier[2]**
Date(s) of Experiment:	May – June 2005

Motivation

Semi-finished products from magnesium wrought alloys like extruded profiles are in the focus of present studies in order to improve the mechanical properties of final structural parts. The parameter settings during extrusion play an important role for the development of the microstructure and texture and influence the resulting mechanical properties of the extruded component. Furthermore an additional heat treatment at elevated temperature changes microstructure and texture.

Objectives

The objective of these measurements is to understand the influence of the cooling condition directly after extrusion on the resulting microstructure and texture. This will allow to study microstructural changes as a result of dynamic processes during extrusion and additional static processes during air-cooling. Therefore two extrusion trials of magnesium alloy ZM21 were used and compared to earlier results from alloy AZ31 [1]. The intension is to study the alloying influence on recrystallization processes during extrusion.

Experiment

Two extrusion trials were carried out using magnesium alloy ZM21 for producing round bars. The parameter setting was the same with an extrusion temperature of 300 °C. One trial was carried out without any additional treatment and thus the final bar was air-cooled. During a second trial water-cooling was applied directly behind the die exit. This procedure allows to distinguish between dynamic processes during extrusion and subsequent static processes.

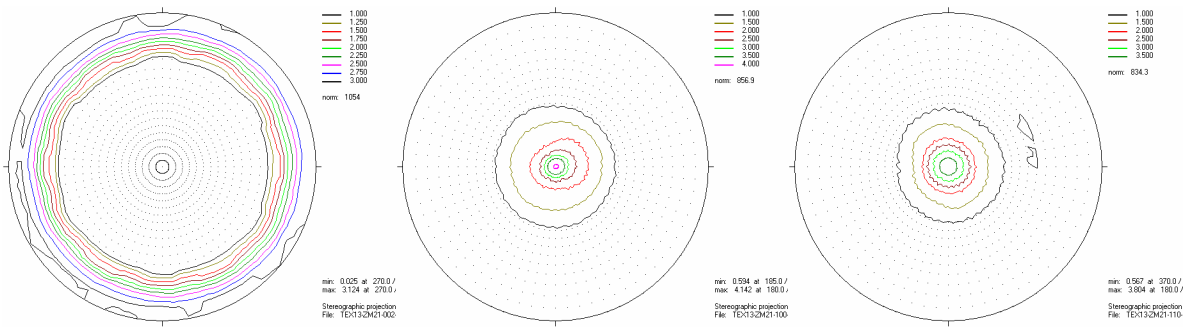


Figure 1: Pole figures of a water-cooled bar from magnesium alloy ZM21 after extrusion: a) (00.2) – max. Intensity 3.1, {10.0} – max. Intensity, 4.1 {11.0} – max. Intensity 3.8.

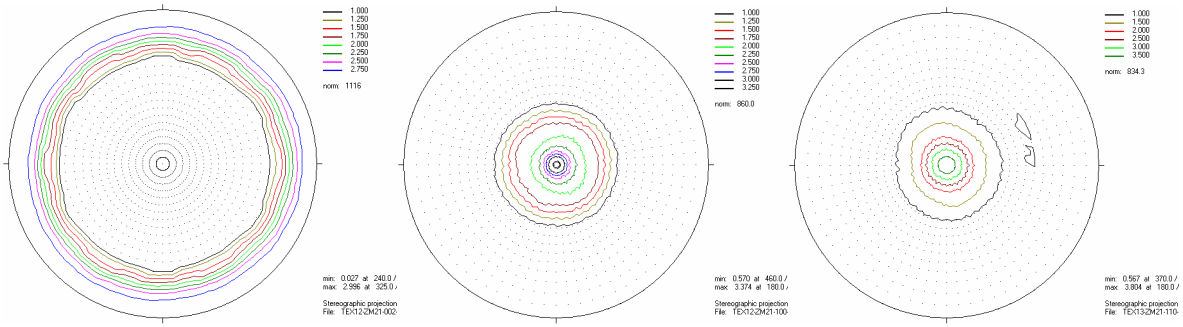


Figure 2: Pole figures of an air-cooled bar from magnesium alloy ZM21 after extrusion: a) (00.2) – max. Intensity 3.0, {10.0} – max. Intensity 3.4, {11.0} – max. Intensity 4.2.

Figures 1 and 2 show a first result of this study. Additionally, a slight coarsening of the microstructure was observed.

Achievements and Main Results

The two conditions shown in Figs. 1 and 2 are understood as two stages of the same microstructural development during extrusion. The one after water-cooling freezes the condition directly after extrusion. Compared to that the one after air-cooling received the same treatment but also an additional “heat treatment” during air-cooling. No significant differences can be found in the (00.2) pole figure after water-cooling compared to air-cooling. However, the maximum intensity of the {10.0} pole figure decreases whereas the maximum intensity of the {11.0} pole figure increases. This is in agreement with results from comparable trials with alloy AZ31 [1] where the <10.0> pole density decreases during air-cooling whereas the <11.0> pole density increases.

Future efforts will focus on a principal understanding of the influence of single alloying elements in magnesium on the recrystallization mechanisms during thermo-mechanical treatment.

Reference

[1] J. Bohlen, S.B. Yi, J. Swiostek, D. Letzig, H. G. Brokmeier, K. U. Kainer, Scripta Mat. 53 (2005) 259.

GKSS FORSCHUNGSZENTRUM in der HELMHOLTZ-GEMEINSCHAFT	**EXPERIMENTAL REPORT**	**GeNF Tex-2**

Initial texture of a friction welded Ti64 – TiAl – rod

Proposer:	**S.-J. Jin**[1,2], [1]Institute for material Science and Technology, TU Clausthal; [2]GKSS Research Centre
Co-Proposers:	**Heinz-Günter Brokmeier**[1,2]
Experimental Team:	**B. Schwebke**[1,2], **S.-J.Jin**[1,2]
User Group Leader:	**Heinz-Günter Brokmeier**[1,2]

Date(s) of Experiment:	07.06.–19.06.2005

Objectives

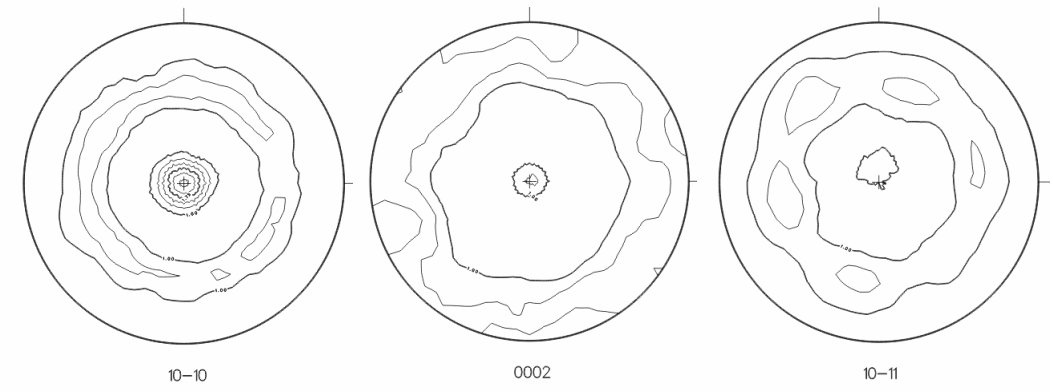
It is well known that many physical and mechanical properties of polycrystalline materials are strongly dependant on the orientation distribution of constituent crystals, namely texture. The texture is formed by the manufacturing process such as deformation, heat treatment, or phase transformation. Moreover, the properties can be modified by the texture control.
Ti-alloys are used in aerospace industries, automotive industries, medically implanted materials because of its good corrosion and high temperature creep resistance.
In the present study, we observed about the changing texture of Ti64-and TiAl-alloys during friction welding. Firstly, the texture was measured on the basic material of Ti64-alloy, far away from the heat affected zone. Further investigations deal with the phase composition in the heat affected zone and the weld.

Experiment

The texture of Ti64-and TiAl-alloys joined by friction welding was measured non-destructively using neutron diffraction in TEX-2. In order to get the bulk information an average texture of a 24 mm thick rod was investigated. Complete pole figures of (10-10), (0002), (10-11) were used to calculate the orientation distribution function (ODF) with Lmax = 22. Thereafter, the inverse pole figures in the main sample directions and some recalculated pole figures were plotted.

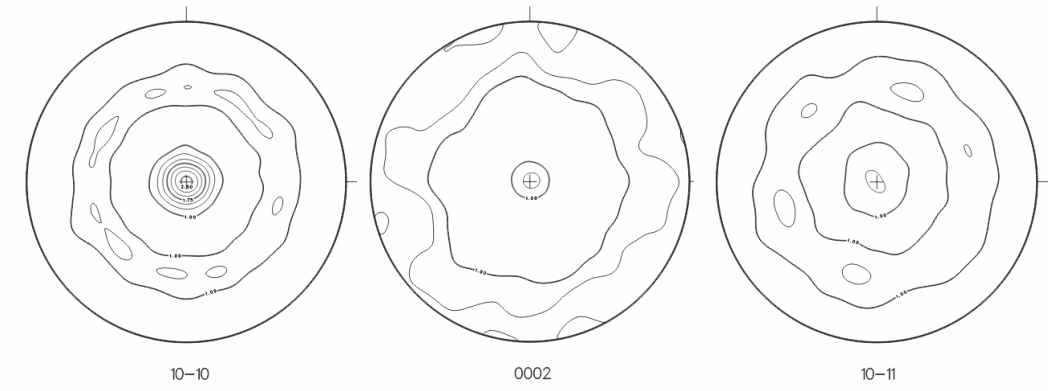
Achievements and Main Results

Figure 1 shows the measured pole figures of Ti64 alloy. It can be seen clearly, that the texture is not very strong. A medium <10-10> fiber and a very week <0002> fiber is observed. The sub-maxima inside the intensity ring of the (10-11) pole figure indicate that the rotational fiber symmetry is not ideal. Figure 2 shows the recalculated pole figure, which indicate a sufficient agreement. The inverse pole figures were calculated in three different sample direction rolling direction (RD), transverse direction (TD) and normal direction (ND) of rolling direction. Through the inverse pole figures, the texture can be easily understood for a particular direction. In the ND which is parallel to the rod axis, we observed that a medium <100> direction and weak <001>direction was developed during processing the Ti6a rod.



Pmax = 2.35 med Pmax = 1.65 mrd Pmax = 1.45 mrd

Figure 1: Measured Ti64-alloy pole figures.



Pmax = 2.59 mrd Pmax = 1.57 mrd Pmax = 1.32 mrd

Figure 2: Calculated Ti64 alloy pole figures.

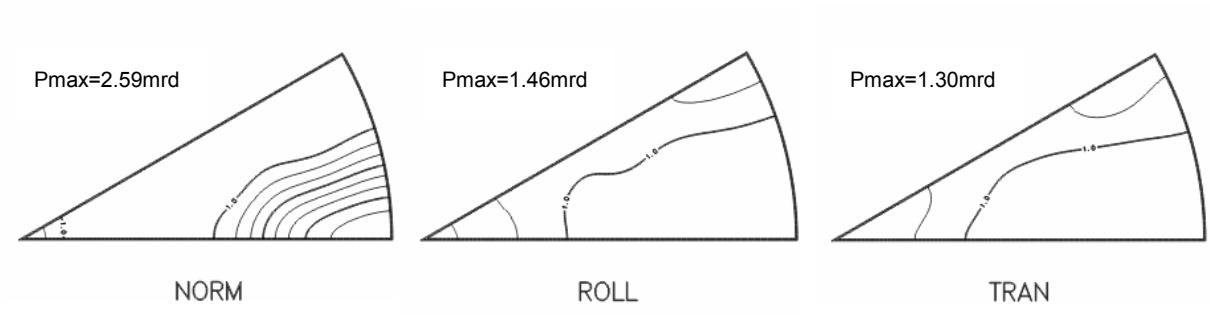


Figure 3: Ti64-alloy inverse pole figures.

Reference

Materials Properties Handbook: Titanium Alloys, 483–486 (1994)

GKSS FORSCHUNGSZENTRUM in der HELMHOLTZ-GEMEINSCHAFT	**EXPERIMENTAL REPORT**	**GeNF TEX-2**

Measurement of Textures in Low-Carbon Steels

Proposer:	**Raúl E. Bolmaro[1],** [1]Instituto de Física Rosario. FCEIA-UNR. Bv. 27 de febrero 210 bis. Rosario. Argentina
Co-Proposers:	**Heinz-Günter Brokmeier[2],** [2]Institute of Materials Science and Technology. Technical University Clausthal and GKSS-Research Centre Geesthacht Germany
Experimental Team:	**Seung Jun Jin[2], Bernd Schwebke[2]**
User Group Leader:	**Heinz-Günter Brokmeier[2],**

Date(s) of Experiment:	29–30 June 2005

Objectives

The texture development in Low Carbon Steels (LCS) is known to have a large influence in their drawability properties. It is also known that the texture development under rolling may present some heterogeneity mainly dependent on the thickness of the sheet and the in-depth position inside the sheet. We are currently pursuing a better understanding of the texture development and its connections with mechanical properties. The purpose of the current experiment is the measurement of textures in two LCS sheets by neutron diffraction and the comparison with measurements performed by X-ray diffraction techniques at different depths.

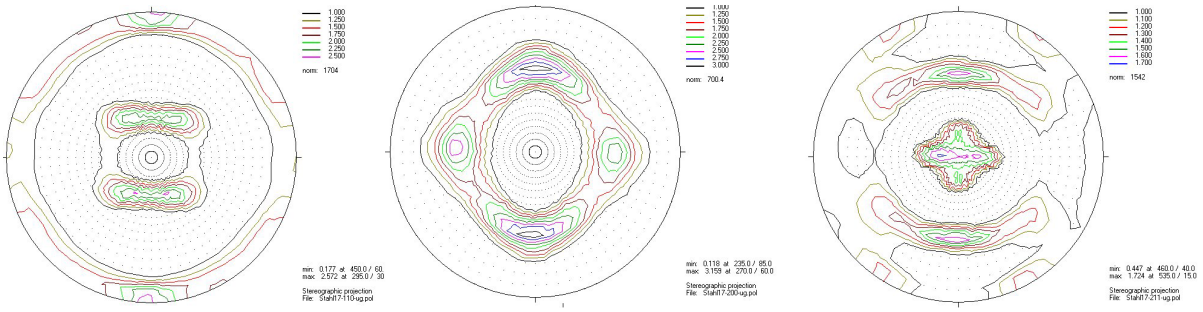
Experiment

Two composite samples were prepared by cutting 12 square shaped sheet pieces and piling and gluing to form approximately 1.5 cm^3 samples.

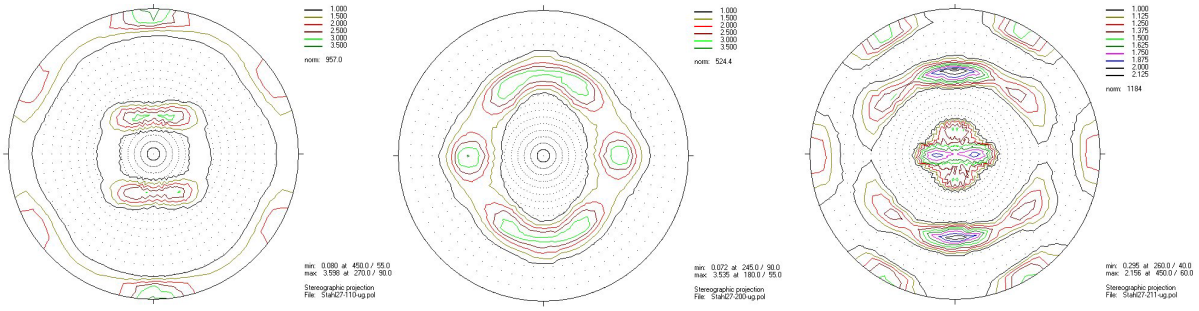
Achievements and Main Results

Results came up very close to the experimental data obtained by x-ray diffraction. Although the sample preparation was more critic in the case of X-rays because of the high absorption resulting mainly from the fluorescence of iron under Cu radiation. The surface polishing had to be done very carefully and a chemical etching was necessary to avoid residual strains and polishing perturbations influences. On the contrary, neutrons were much more reliable and will be taken as a general guide and control in further investigations.

LCS17



LCS27



References

[1] W.E. Hosford. The Mechanics of Crystals and Textured Polycrystals. Oxford Engineering Science Series 32. Oxford Science Publications (1993).

[2] U.F. Kocks, C.N.Tomé and H.-R. Wenk. Texture and Anisotropy. Preferred Orientations in Polycrystals and their Effect on Materials Properties. Cambridge University Press (1998).

[3] W.A. Backofen. Deformation Processing. Addison-Wesley Publishing Co. (1972).

[4] Recrystallization, Grains Growth and Textures. American Society for Metals. Metals Park. Ohio. Seminar of the American Society for Metals, October 16–17.1965.

[5] F.J. Humphreys and M. Hatherly. Recrystallization and Related Annealing Phenomena. Pergamon Press. (1995).

[6] W.B. Hutchinson. Development and Control of Annealing Textures in Low-Carbon Steels. Int. Met. Reviews. 29, 1 (1984) 25–42.

[7] R.K.Ray, JJ.Jonas and R.E. Hook. Cold Rolling and Annealing Textures in Low Carbon and Extra Low carbon Steels. Int. Mat. Rev. 39, 4 (1994) 129–172.

[8] R.K. Ray and J.J. Jonas. Transformation Textures in Steels. In. Mat. Reviews. 36, 1 (1990) 1–36.

[9] R.K. Ray, J.J. Jonas, M.P. Butrón-Guillén and J. Savoie. Transformation Textures in Steels. ISIJ International. 34, 12 (1994) 927–942.

GKSS FORSCHUNGSZENTRUM in der HELMHOLTZ-GEMEINSCHAFT	**EXPERIMENTAL REPORT**	**GeNF TEX-2**

Textures on FeMn Shape Memory Alloys

Proposer:	**Raúl E. Bolmaro[1],** [1]Instituto de Física Rosario. FCEIA-UNR. Bv. 27 de febrero 210 bis. Rosario. Argentina
Co-Proposers:	**Heinz-Günter Brokmeier[2],** [2]Institute of Materials Science and Technology. Technical University Clausthal and GKSS Research Centre
Experimental Team:	**Seung Jun Jin[2], Bernd Schwebke[2]**
User Group Leader:	**Heinz-Günter Brokmeier[2],**

Date(s) of Experiment:	1–2 July 2005

Objectives

Shape memory alloys (SMA) are outstanding materials where the phase transformations are closely related with the mechanical properties, both during the process and afterwards. The volume changes during the transformation, together with the crystalline reorientation, are able to drive the shape memory effect as well as stop it. The development of internal stresses, due to those volume and crystal symetry changes, can be used as internal gauges to evaluate the whole process and the importance of each phenomena.

The SMA was discovered in Au-Cd alloys by Chang and Read in 1951 [2]. Because of the possible applications numerous studies were performed and SMA, like Ti-Ni, Cu-Zn-Al, and Cu-Al-Ni were developed. Only in the eighties the ferrous alloys Fe-Pt [3], Fe-Ni-Co-Ti [4], Fe-Ni-C [5], Fe-Pd [6] and Fe-Mn-Si-(Cr-Ni) were developed [7].

Because the SMA effect strongly depends on the crystallographic orientation, a polycrystalline aggregate will not present a macroscopic SMA effect larger than the one observed in the most favorable orientation of the single crystal. The most important problem in technological applications of SMA of ferrous origin, is that the strain associated with a perfect recuperation are always less than the required (between 3 and 4 %).

Until now, dimensional recoveries observed in polycrystalline Fe-Mn-Si are too small for technological applications [5–8]. The systems based in Fe-Mn are very interesting because they show two almost overlapped martensitic transformations and two of magnetic ordering. The understanding of those transformations in the simplest systems can be considered the first steps for the understanding of multi-component alloys with technological applications, as the ones we attempt to investigate in this project.

Transformation textures in steels are usually very weak and a better averaging method for measuring them is desirable. Besides, grain boundary after thermal treatment can be too large for x-ray measurements. Neutrons are capable to gauge a larger volume and improve statistic over many grains making texture results much more reliable.

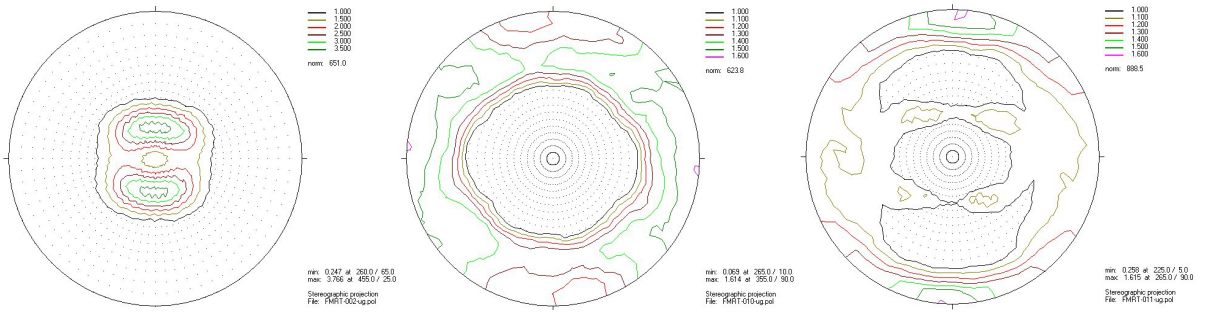
We propose to measure between 4 and 6 samples belonging to the same system and previously subject to different thermo-mechanical treatments.

Experiment

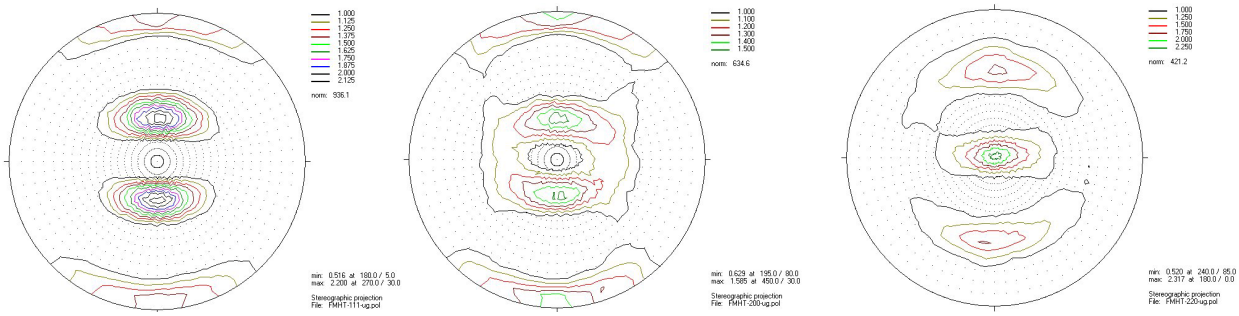
Texture measurements were performed in 10 mm x 12 mm x 15 mm bar samples cut from rolled billets. The samples are named FMRT and FMHT standing the names for Room Temperature and High Temperature (1000 °C) deformed samples, respectively.

Achievements and Main Results

FMRT



FMHT



The first striking result was that the diffraction spectra showed the presence of only one phase in both cases: HCP for the RT sample and FCC for the HT sample. Previous results obtained by X ray diffraction showed a combination of both phases. Further investigation was performed and we obtained a procedure to get rid of the “phantom phases” developed on the surface by the sole polishing procedure. We need to electro-polish the samples to eliminate the polishing produced second phases that are completely absent on the bulk sample.

References

[1] Y. C. Shu and K. Bhattacharya. The Influence of Texture on the Shape-Memory Effect in Polycrystals. Acta mater. Vol. 46, No. 15 (1998) pp. 5457–5473.
[2] Dunne P., Wayman C.; Metall. Trans. 4 (1973) 137.
[3] Maki T., Kobayashi K, Minato M., Tamura I.; Scr. Metall. 18 (1984) 1105.
[4] Kajiwara S.; Trans. JIM 26 (1985) 595.
[5] Oshima R.; Scr. Metall. 15 (1981) 829.
[6] Murakami M., Otsuka H., Suzuki H., Matsuda S.; Proc. of Int. Conf. on Martensitic Transformation ICOMAT 1986, Japan Inst. Met., p.985.
[7] Sato A., Chishima E., Soma K., Mori T.; Acta Metall. 30 (1982) 1177.
[8] Sato A., Yamaji Y., Mori T.; Acta Metall. 34 (1986) 287.

GKSS FORSCHUNGSZENTRUM in der HELMHOLTZ-GEMEINSCHAFT	**EXPERIMENTAL REPORT**	**GeNF TEX-2**

Measurement of textures in geological structures of Pie de Palo sierra, Córdoba, Argentina.

Proposer:	**Raúl E. Bolmaro[1],** [1]Instituto de Física Rosario. FCEIA-UNR. Bv. 27 de febrero 210 bis. Rosario. Argentina
Co-Proposers:	**Heinz-Günter Brokmeier[2],** [2]Institute of Materials Science and Technology. Technical University Clausthal and GKSS Research Centre
Experimental Team:	**Seung Jun Jin[2], Bernd Schwebke[2]**
User Group Leader:	**Heinz-Günter Brokmeier[2],**

Date(s) of Experiment:	3–4 July 2005

Objectives

The Pié de Palo range, adjacent to the Argentine Precordillera, is a massif of cristalline rocks shaped by a system of imbricated ductile thrusts. It is divided from west to east in three metamorphic units: the Caucete Group (CG), the Ophiolitic Unit (OU) and the Upper Units (UU), separated the last ones from the first ones by the Pirquitas thrust.
All those formations are somehow unique in the sense that they offer quartzites and calcitic rocks mixed together but still discernible in such a way that textures can provide coherent complimentary information about deformation process.
The purpose of the study is the understanding of the kinematic, deformation mechanisms and textures developed by the quartz and calcite, in the already mentioned CG and UU units, under contrasted physical conditions and analogous non-coaxial deformation regimes. Both phases were studied by X-ray and neutron texture measurements and the results were compared with texture simulations performed by Self-Consistent models. X-ray results allowed the measurement of more local kind textures but the averaging capabilities of this methods are known to be worst for rocks. In that sense neutron textures offer a better approach to geologic texture measurements.
Results show the capabilities of combined techniques, experiments and simulations, to ensure apropriate interpretations of geological data.

Experiment

The experiments were performed in three cubic shape samples 2 cm x 2 cm x 2 cm, cut following foliation and deformation directions and oriented respectful of geologic deformation characteristics.

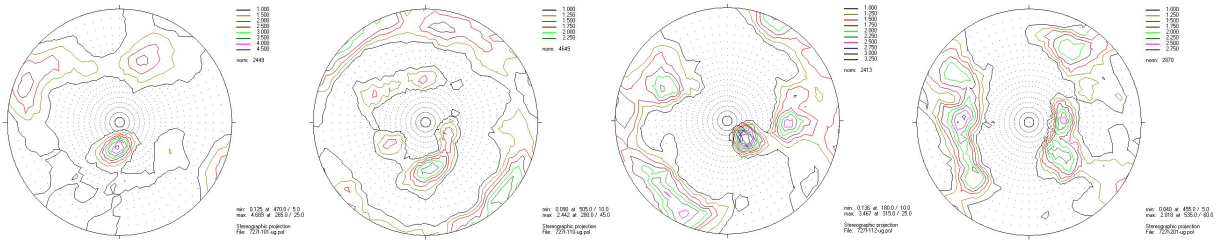
Achievements and Main Results

Two quartz veins (PP10-PP11) have already been studied together with a folded metaquartzite sample (QD 10) both obtained from the ADF. Three other quartz veins from metasedimentary cover of Quebrada de Las Flores have also been studied (724, 727 f, 727 gr). They were representative of the intense localized internal deformation on the ADF and its penetrative characteristic on the HU, product both of the very contrasting metamorphic conditions.

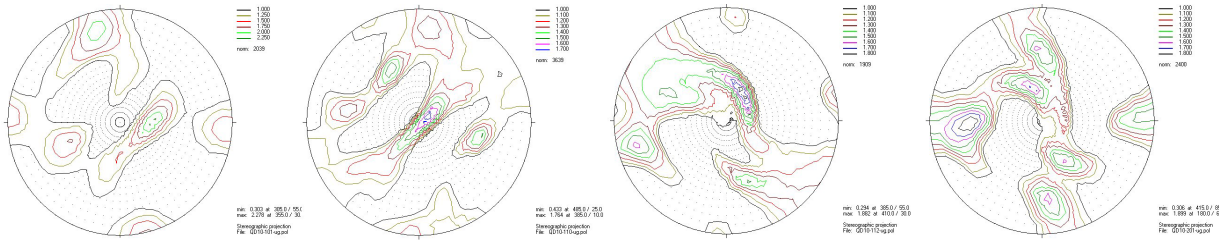
The purpose of the current project is the measurement of some samples collected from the same areas and their analysis. The goal is two-fold: a) establish cinematic relationships between the LPO and deformational structures at mesoscopic scales, either localized or penetrative. b) suggest deformation mechanisms for quartz and calcite for the region.

We re-measured QD10 and 727f region samples to check for heterogeneity and added a third sample, QD11 slightly away from QD10, to investigate deformation gradient variations along the vein. Results are under evaluation.

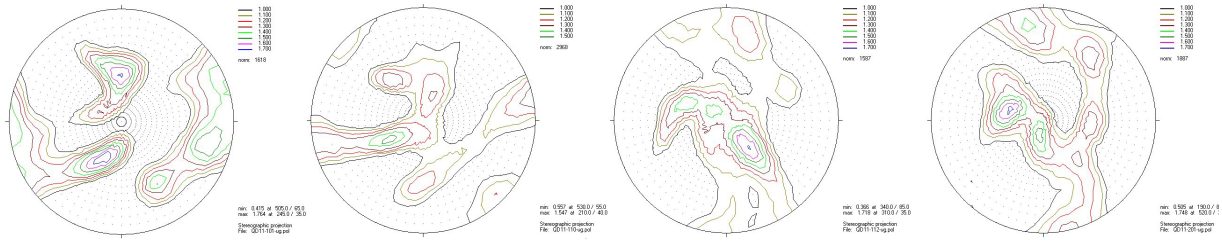
727f



QD10



QD11



References

[1] M. Pieri, K. Kunze, L. Burlini, I. Stretton, D.L. Olgaard, J.-P. Burg, H.-R. Wenk. Texture Development of Calcite by Deformation and Dynamic Recrystallization at 1000 K During Torsion Experiments of Marble to Large Strains. Tectonophysics 330 (2001) 119–140

[2] A. Barnhoorn, M. Bystricky, L. Burlini and K. Kunze. The Role of Recrystallisation on the Deformation Behaviour of Calcite Rocks: Large Strain Torsion Experiments on Carrara Marble. J. of Struct. Geology 26 (2004) 885–903

[3] Wenk, H.-R. 1994. Preferred orientations patterns in deformed quartzites. En: Hearney, P.J., Prewitt, C.T. y Gibbs, G.V. (Eds.): "Silica. Physical behavior, Geochemistry and Materials Applications". Reviews in Mineralogy V. 29, 177–208.

[4] Wenk, H-R., Canova, G., Molinari, A. y Kocks. 1989. Viscoplastic Modelling Texture Development in Quartzite. Journal of Geophysical Research 94, B12, 17895–17906.

[5] Takeshita, T., Wenk, H.-R. y Lebensohn, R. Development of Preferred Orientation and Microstructure in Sheared Quartzite: Comparison of Natural Data and Simulated Results. Tectonophysics 312: 1999, 133–155.

GKSS FORSCHUNGSZENTRUM in der HELMHOLTZ-GEMEINSCHAFT	**EXPERIMENTAL REPORT**	**GeNF TEX-2**

Texture characterisation of extruded TiAl

Proposers:	**W. Klauber[1], R. Schnitzer[1]**
Co-Proposer:	**H. Chladil[1]**
	[1]University of Leoben, Department of Physical Metallurgy and Matreial Testing, Leoben, Austria
Experimental Team:	**H.-G. Brokmeier[2, 3], B. Schwebke[2, 3]**
	[2]GKSS Research Centre, [3]TU Clausthal
User Group Leader:	**H. Clemens[1]**
Date(s) of Experiment:	29 August – 23 September 2005, 24 October – 30 November 2005

Objectives

The aim of the work was to determine the texture of a high Nb containing TiAl alloy after extrusion compared with subsequently thermo-mechanical heat treated samples. Additionally, a change of the texture was determined, due to deformation parallel or across the extrusion direction. Furthermore, the variation of the texture during different annealing times and after a massive transformation was investigated.

Experiment

The measurements were carried out on samples, which were spark-eroded form the as-extruded material and the subsequently stress-relieve annealed material. All thermo-mechanical heat treatments were conducted in a deformation dilatometer. Therefore, the samples were rather small and consequently long measurement times were needed. For each sample the 001, 110 and the 201 pole figure were evaluated, in order to calculate the orientation-distribution-function to gain the inverse pole figures.
Figures 1-4 show the measured 110 pole figures in the as-extruded state and after a deformation whereas the extrusion direction was perpendicular (Figures 1 and 2) or parallel (Figures 3 and 4) to the image plane.

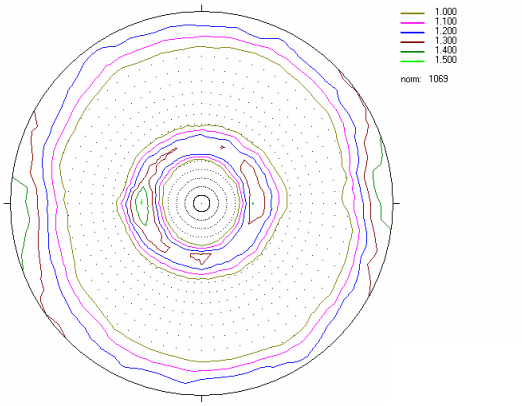


Figure 1: As extruded; 110 pole figure; extrusion direction perpendicular to plane; P_{max}= 1.507 mrd.

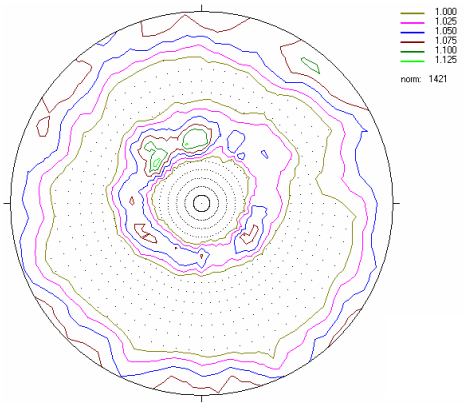


Figure 2: Deformed sample (deformed) parallel to extrusion direction); 110 pole figure; deformation direction perpendicular to plane; P_{max} = 1.138 mrd.

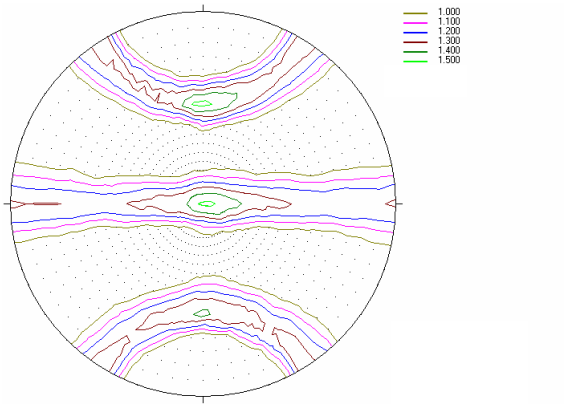


Figure 3: As extruded; 110 pole figure; extrusion direction: vertical; P_{max} = 1.536 mrd.

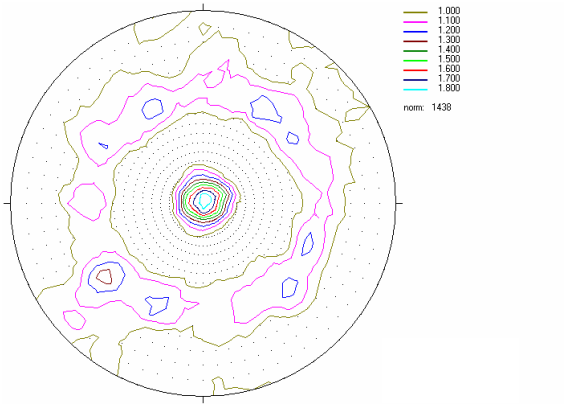


Figure 4: Deformed sample (deformed perpendicular to extrusion direction); 110 pole figure; deformation direction perpendicular to plane; P_{max} = 1.857 mrd.

Achievements and Main Results

According to H.G. Brokmeier et al. it was verified that the extrusion texture is a 111-fibre texture [1]. Furthermore, stress-relieve annealing led to a small reduction of the texture sharpness. In general, all textures showed a rather weak intensity.

The texture of the deformed samples exhibit a strong dependence of the deformation orientation in respect to the extrusion direction. In addition, the texture formation is connected to the deformation temperature and speed. However, there were only slightly changes of the 111-fibre texture after a deformation with 2 mm/s parallel to the extrusion direction at a temperature of 1290 °C (see Figures 1 and 2). Therefore, we assume that the preferred deformation mode is grainboundary-sliding. The texture of the sample deformed perpendicular to the extrusion direction showed a change from the 111-fibre (Figure 3) to a 110-fibre texture (Figure 4) (deformation temperature of 1255 °C and speed of 5 mm/s). According to Z. Jin et al. this is the preferred deformation texture for TiAl alloys [2].

Furthermore, the measurements of the samples, which were annealed at a temperature of 1275 °C and an annealing time of either 2 or 45 min, exhibited an increase of the 110-texture component.

The investigation of the massive transformed samples resulted in an unexpected rather strong 110-fibre texture and the subsequently aged samples showed two independent texture components, which might be caused by the 111-extrusion texture and the 110- massive transformation texture.

References

[1] H.-G. Brokmeier, M. Oehring, U. Lorenz, H. Clemens, F. Appel: „Neutron Diffraction Study of Texture Development during Hot Working of Different Gamma-Titanium Aluminide Alloys", Metallurgical and Materials Transactions A, Vol. 35A, November 2004, pp. 3563–3579

[2] Z. Jin, G.T. Gray III, Y.-W. Kim: "Texture evolution during α-forging of γ-TiAl alloys" Material Science and Engineering A239-240, 1997, pp. 729–735

GKSS FORSCHUNGSZENTRUM in der HELMHOLTZ-GEMEINSCHAFT	**EXPERIMENTAL REPORT**	**GeNF TEX-2**

Texture analysis of laser beam welded Al-alloys (AA5083H111 and AA6013T6)

Proposer:	**Sabine Lenser,** IWW - TU Clausthal / WFN - GKSS
Co-Proposers:	**Heinz-Günter Brokmeier,** IWW - TU Clausthal / WFN - GKSS
Experimental Team:	**Sabine Lenser,** IWW - TU Clausthal / WFN - GKSS
	Bernd Schwebke, IWW - TU Clausthal / WFN - GKSS
User Group Leader:	**Heinz-Günter Brokmeier,** IWW - TU Clausthal / WFN - GKSS
Date(s) of Experiment:	· 22 April 2005, 21–29 June 2005, 8–11 August 2005, 17–18 August 2005, 14–17 November 2005

Objectives

Aluminium is the most heavily consumed non-ferrous metal in the world. Its unique properties such as light weight, high strength and resistance to corrosion make it an ideal material for use in conventional and novel applications. Aluminium has already become important in the production of automobiles, aerospace parts and the manufacture of machinery. Aluminium users have to explore new process technologies in order to reduce production costs and make aluminium even more competitive. Laser beam welding is a new method in the handling of aluminium. However it is difficult to weld Al-sheets with high quality using a laser beam [1].

Experiment

In this report we will describe the results of texture analysis for laser beam welded sheets of rolled AA5083H111 and AA6013T6. For our samples the laser beam welding had been carried out at the rates of 1.8 m/min and 2.6 m/min and texture measurements were performed on the neutron diffractometer TEX-2 using a wavelength of 1,239 Å. At five different specimen positions, two in each individual sheet and one in the weld, the texture measurement was carried out for each welding rate. Therefore, initially the samples were prepared as a cube of 10 mm x 10 mm x 10 mm. Only the diameter of the welding seam was too small (4 mm). The size was reduced to a cube of 1.5 mm x 1.5 mm x 1.5 mm. At first the basic materials were researched. Particular in the case of AA6013T6 and in the weld coarse grains need neutron diffraction to guarantee a sufficient grain statistics. For each position three complete pole figures, i.e. (111), (200), (220), were collected. Finally a quantitative texture analysis was performed using the iterative serious expansion method up to a degree of Lmax = 22.

In the present study particular interest is focussed on the modification of the texture in the welded and the heat affected zone compared to the texture of the basic material.

Main Results

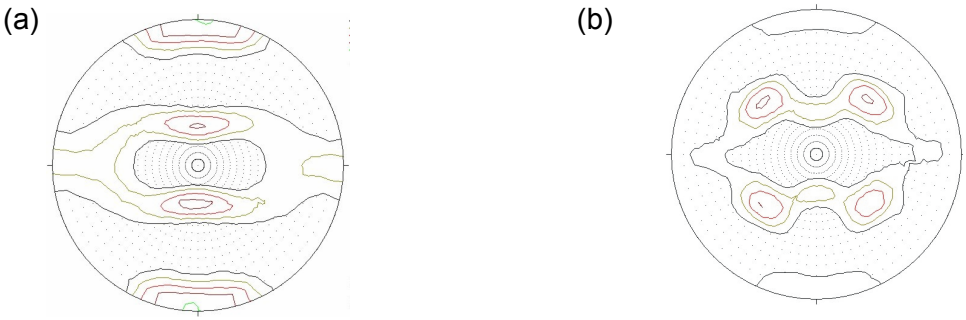


Figure 1: (111) pole figures of basic materials: (a) AA5083H111, Pmax = 1.9 mrd, (b) AA6013T6, Pmax = 2.6 mrd.

The texture of AA5083H111 is characterized by a Brass component {110} <112>, which was developed during to the rolling process. AA6013T6 shows a minor texture component directed to rolling of the sheet and a majority cube component {001} <100> [1]. The formation of the cube component indicates the heat treatment of AA6013T6. Looking on the orientation distribution function the maximum orientation degree is about 9.5 mrd in the case of AA6013T6 and about 2.6 mrd for AA5083H111.

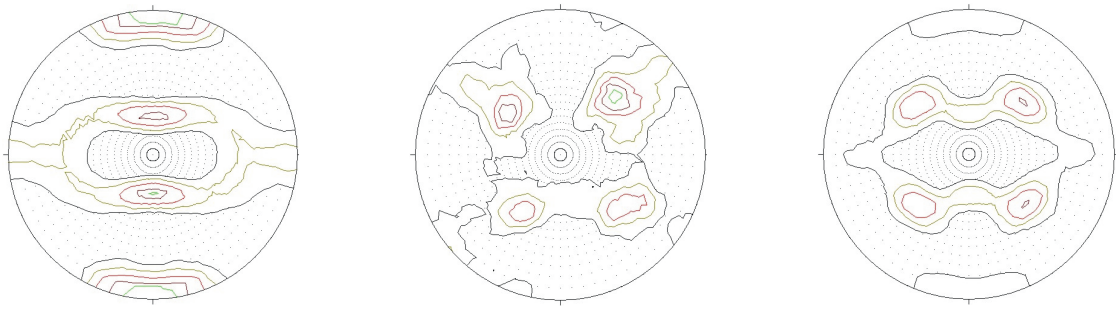


Figure 2: Texture development around the weld
(position 1 - AA5031H111; position 2 – weld; position 3 - AA6013T6).

The results we present in figure 2 are from the sheets with the welding rate of 1.8 m/min. Shown is the (111) pole figure for three sample positions: Position 1 was measured 4 mm next to the welding seam in the range of AA5031H111; Position 2 shows the pole figure in the centre of the welding seam; Position 3 was measured 4 mm next to the welding seam in the range of AA6013T6. Firstly one can recognize that there no texture change inside the basic materials. That means, the texture far away from the weld (see figure 1) and the texture close to the weld (see figure 2 postition1 and position 2) are identical. Inside the weld one obtains a pure cube texture component. This is typical for recrystallization. Additional EBSD measurements show a texture variation (texture sharpness) and the grain size variation over the cross section of the welded seam, so that the resulting neutron texture is much weaker than expected.

Reference

[1] W. Mao, “Recrystallization and Grain Growth” edited by G.E. Totton, D.S. MacKenzie, *Handbook of Aluminium*, Volume 1 (2003)

GKSS FORSCHUNGSZENTRUM in der HELMHOLTZ-GEMEINSCHAFT	EXPERIMENTAL REPORT	GeNF POLDI
Polarised diffractometer POLDI		

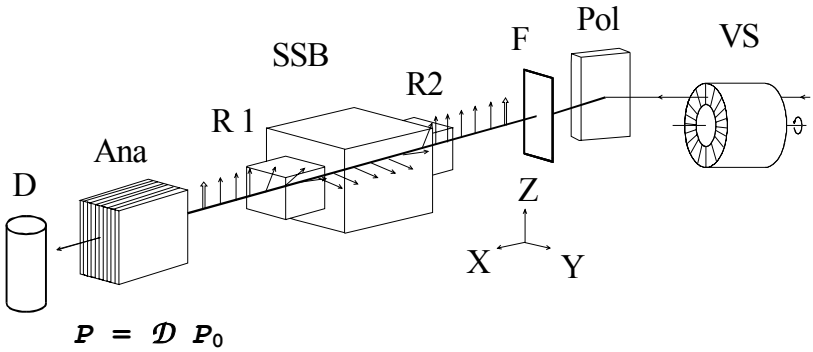
Short Instrument Description:

With the polarised diffractometer 3-D depolarisation analysis is used to investigate magnetic properties and correlations in magnetic materials. With minor modifications a time of flight option in non-polarised mode is additionally available for the purpose of dosemeter calibration.

Local Contact:

Dr. Dieter Lott
Phone/Fax : +49 (0)4152 87 – 1372 / +49 (0)4152 87 – 1338
e-mail: dieter.lott@gkss.de

Schematic View of POLDI:



Set-up for full 3-dimensional neutron depolarisation analysis in the transmitted beam.

Instrument Details:

Location at FRG-1:	beamline 7, thermal neutrons cross section 10 x 4 cm^2,
Polariser / monochromator (Pol)	Cu_2MnA (111), PG(002), Si (311) doubly focussing; helical slot selector (VS)
Take-off-angle:	$10° < 2\,\Theta_M < 65°$
Wavelength:	λ = 0.1 to 0.36 nm, 2^{nd} order suppression by velocity selector (VS)
Flux at sample position:	$\Phi_{max} = 0.8 \cdot 10^5$ cm^{-2} s^{-1} (polarised)
Analyser (Ana):	Co/Ti-supermirror
Overall polarisation:	0.94
3D depolarisation analysis in transmitted beam:	accuracy < 1 % for any component of ***D***
Sample environment fitting in the magnetically shielded sample box (SSB) for 3D depolarisation analysis:	– refrigerator T >12 K, Orange cryostat T > 1.5 K – DC magnetic field < 160 A/cm – pulsed field < 8.0 kA/cm
Detector (D):	^{3}He-counter
Instrument control / data acquisition:	remote internet PC control IEEE bus, serial bus and special interfaces

GKSS FORSCHUNGSZENTRUM in der HELMHOLTZ-GEMEINSCHAFT	**EXPERIMENTAL REPORT**	**GeNF POLDI**

Multiple reflection monochromator

Principal Proposer:	**P. Mikula** Nuclear Physics Institute, 250 68 Řež, Czech Republic
Experimental Team:	**M. Vrána[1], V. Wagner[2], D. Lott[3]** [1]Nuclear Physics Institute 250 68 Řež, Czech Republic [2]Physikalisch-Technische Bundesanstalt, Braunschweig [3]GeNF, GKSS Geesthacht
Date(s) of Experiment:	April 4–13, 2005

Using a terminology of the reciprocal lattice space, the multiple reflection effects occur when a second reciprocal lattice point (or more, generally *n* points) is brought onto the Ewald sphere. It results in reducing the intensity of a strong primary reflection or increasing the intensity of a weak primary reflection. The extreme case represents the effect of simulation of forbidden primary reflection (see Fig. 1). When these reflections are defined by the scattering vectors $\boldsymbol{g}_1$, $\boldsymbol{g}_2$ and $\boldsymbol{g}_3$ and they are in relation as $\boldsymbol{g}_1 = \boldsymbol{g}_2 + \boldsymbol{g}_3$, then, the doubly reflected beam has the same direction as the one reflected only by primary set of lattice planes. It follows from the crystal symmetry that when a secondary reflection fulfils the Bragg condition simultaneously with the primary one, there exists automatically the tertiary reflection defined by $\boldsymbol{g}_3 = \boldsymbol{g}_1 - \boldsymbol{g}_2$. It has already been experi-mentally proved on the multiple reflection effect corresponding to the peak N. 4 (see Fig. 2) that when the second and third system of reflection planes are mutually in the dispersive setting, then depending on the crystal curvature the doubly reflected beam has a narrow band-width $\Delta\lambda/\lambda$ in the range from 10^{-4} to 10^{-3} and collimation of the orders of minutes of arc [1]. It was also pointed out that such a multiple reflection effect realized in one elastically deformed crystal can possibly be used for a high-resolution monochromatization. Recently, we have tested three different cuts of cylindrically bent Si-crystal slabs set for symmetric transmission geometry in order to identify strong multiple reflection effects with the outlook of their possible exploitation for high-resolution monochromatization [2] where again the peak N. 4 related to the forbidden primary reflection was used for high-resolution powder diffraction. Part of one of the scans is introduced in Fig. 2.

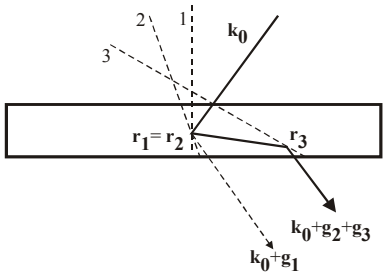


Figure 1: Schematic diagram of a two-step multiple Bragg reflection simulating a weak or forbidden reflection. The numbers 1, 2 and 3 represent the primary, secondary and tertiary reflection planes, respectively.

In the experimental search of multiple reflection effects two methods are usually used:

a. Method of azimutal rotation of the crystal lattice around the scattering vector of the primary reflection for a fixed wavelength.
b. Method of θ–$2\theta_D$ scan in the white beam for a fixed azimutal angle.

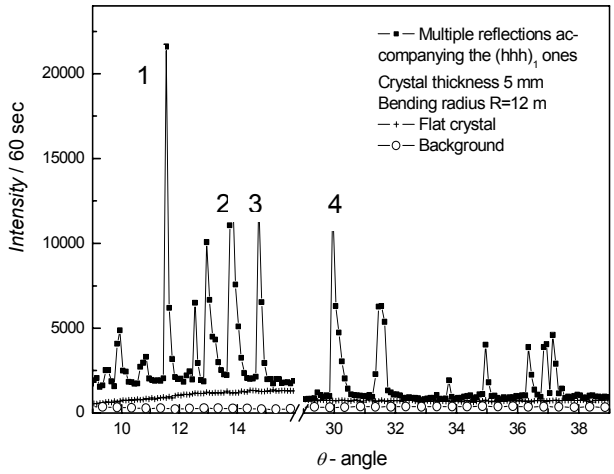


Figure 2: Parts of θ–$2\theta_D$ scan with the crystal slab (the largest face parallel to (110)) set for $(hhh)_1$ reflections in the symmetric transmission geometry.

Contrary to the earlier studies, in the recent studies we preferred the latter method of the θ–$2\theta_D$ scan when setting the cylindrically bent perfect Si-crystal slabs in the polychromatic neutron beam in the diffraction geometry for symmetric transmission. This method permitted us to determine several strong multiple reflection effects at different wavelengths (see Fig. 2). Using a calculation on the basis of the formulae introduced in the paper [2], we could determine the secondary and tertiary lattice planes contributing to the observed effects as well as the corresponding neutron wavelengths (see Tab. 1). In comparison with the studies related to the peak N. 4, in this case we focused our attention on the strong peaks N. 1 and N. 3 related to other neutron wavelengths and the allowed primary reflection. In this way it should be pointed out that contrary to the results obtained on mosaic crystals where the contribution of the multiple reflection effects is rather small [3,4], in the case of the elastically deformed perfect crystals just the choice of a suitable elastic deformation may result in a multiple reflection effect even two orders of magnitude stronger than that corresponding to the allowed primary reflection. This requirement is very important namely in cases when a multiple reflection monochromator would be envisaged for a practical employment. It is known that the integrated reflectivity of a deformed crystal is a function of the scalar product ($\mathbf{g}\cdot\mathbf{u}$) ($\mathbf{u}$ is the displacement of atoms due to deformation) [5] which may be zero for the primary reflection, i.e. ($\mathbf{g_1}\cdot\mathbf{u}$)=0 and the corresponding integrated reflectivity is independent of the deformation [6]. This is also valid in our case of cylindrical bending and symmetric transmission geometry. On the other hand ($\mathbf{g_2}\cdot\mathbf{u}$) = – ($\mathbf{g_3}\cdot\mathbf{u}$) need not be zero and the deformation can bring about a large increase of the multiple reflection effect keeping the integrated reflectivity related to the primary reflection constant. Furthermore, contrary to the dynamical diffraction on perfect crystals, for interpretation of the multiple reflection effects the quasiclassical approach can be applied [7]. According to this approach (see Fig. 1), the multiple diffraction process simulating the primary reflection in the point r_1 can be assumed as a series of successive secondary and tertiary beam reflections taking place in two different points r_2 and r_3 (which generally have different deformations), respectively. Then, on the basis of this kinematical assumption, the so-called n-beam case (which is well known in the dynamical diffraction by perfect crystals) can be considered as a simultaneous action of several independent pairs of secondary and tertiary reflections. Fig. 3 displays several diffraction profiles of a standard α-Fe solid polycrystalline sample taken with two multiple reflection monochromator performances which correspond to the effects N. 1 and N. 3. They clearly prove their applicability for high-resolution diffraction studies and the contribution of the allowed primary reflection can be considered as a background. FWHM of the diffraction profiles are however, mostly determined by the spatial resolution of the used PSD (1.5 mm) and the widths of the input and output slits situated before and after the sample, respectively (5 and 2 mm).

The presented results clearly demonstrate the feasibility of using multiple reflection effects excited in the bent perfect Si slab for high-resolution mono-chromatization of neutrons. In this case of multiple reflection monochromator, for minimizing *FWHM* and maximizing the peak intensity a special care should be paid to a proper alignment of the mono-chromator slab with respect to the incident beam axis and the scattering plane. This require-ment is especially critical when several pairs of secondary-tertiary reflections contribute to the multiple reflection effect, simultaneously. Then, any misalignment results in a decrease of the peak intensity and an increase of *FWHM*. It also brings about asymmetric peak profiles (see e.g. the peak N. 4 in Fig. 2) and enlarged as well as asymmetric $\Delta\theta$ and $\Delta\lambda$ distributions of the monochromatized beam. In the case of strong secondary-tertiary reflections even multiple peaks may appear. On the other hand, when some weak secondary-tertiary reflections do not contribute to the central peak they enlarge the tails of it. This was also partly our case, because our monochromator assembly permitted only one direction tilting of the primary set of planes with respect to the scattering plane. Important feature of such a multiple reflection dispersive monochromator is that the individual reflections can operate at large Bragg angles (even approaching the backscattering geometry) while the monochromator take-off angle can be rather low.

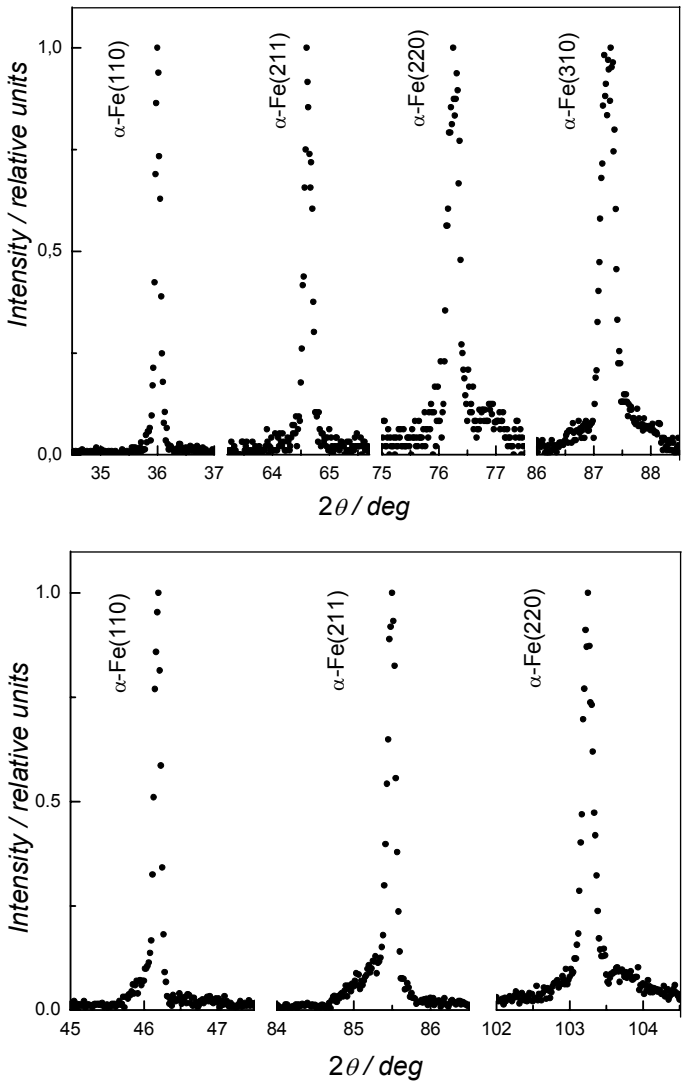


Figure 3: Examples of the α-Fe diffraction profiles taken with the multiple reflection monochromator and solid polycrystalline sample for λ = 0.1253 nm (upper part) and λ = 0.1591 nm (lower part).

References

[1] P. Mikula et al. Nucl. Instrum. Methods, 197 (1982) 563.
[2] P. Mikula, M. Vrána and V. Wagner, Zeitschrift für Kristallographie, in print.
[3] R.M. Moon and C.G. Shull, Acta Cryst. 17 (1964) 805.
[4] G. Kuich and H. Rauch, Acta Physica Austriaca, 20 (1965) 7.
[5] S. Takagi, S., Acta Cryst. 15 (1962) 1311.
[6] Yu.A. Alexandrov et al., Physica, B 151 (1988) 108.
[7] J. Kulda and P. Mikula, Phys. Stat. Sol. (a), 92 (1985) 95.

Table 1: Calculated values of the Bragg angle of the primary reflection and the wavelength related to the multiple reflections observed at the diffraction by cylindrically bent perfect crystal slab with the largest face parallel to ($\underline{1}10$) and set for $(hhh)_1$ reflections in the symmetric transmission diffraction geometry.

Peak N.	Primary reflection	Secondary reflection	Tertiary reflection	Bragg angle [deg]	λ [nm]
1	111	$\underline{5}13$	$60\underline{2}$	11.536	0.1253
1	111	$06\underline{2}$	$1\underline{5}3$	11.536	0.1253
1	111	$\underline{53}3$	$6\underline{2}4$	11.536	0.1253
1	111	$\underline{2}64$	$3\underline{5}3$	11.536	0.1253
1	111	$\underline{31}3$	404	11.536	0.1253
1	111	044	$1\underline{33}$	11.536	0.1253
1	111	$\underline{3}73$	$4\underline{62}$	11.536	0.1253
1	111	$\underline{64}2$	$7\underline{3}3$	11.536	0.1253
1	111	133	$0\underline{22}$	11.536	0.1253
1	111	$\underline{20}2$	313	11.536	0.1253
2	111	$\underline{13}3$	$2\underline{2}4$	13.763	0.1491
2	111	151	$0\underline{4}0$	13.763	0.1491
2	111	$\underline{4}00$	511	13.763	0.1491
2	111	$\underline{2}24$	$3\underline{13}$	13.763	0.1491
3	111	$\underline{1}53$	$2\underline{42}$	14.705	0.1591
3	111	$\underline{42}2$	$5\underline{1}3$	14.705	0.1591
4	222	$\underline{31}1$	513	29.956	0.1565
4	222	$\underline{3}13$	$51\underline{1}$	29.956	0.1565
4	222	$15\underline{1}$	$1\underline{3}3$	29.956	0.1565
4	222	153	$1\underline{31}$	29.956	0.1565

GKSS FORSCHUNGSZENTRUM in der HELMHOLTZ-GEMEINSCHAFT	**EXPERIMENTAL REPORT**	**GeNF POLDI**

Neutron diffraction studies on a $Fe_{50}Pt_{40}Rh_{10}$ thin film

Principal Proposer:	**P. Mani[1], D. Lott[1]** [1] MINT Center, University of Alabama, Tuscaloosa, AL, USA [2] GKSS Research Centre, Institute for Material Science
Experimental Team:	**J. Fenske[2], D. Lott[2]**
Date(s) of Experiment:	Dezember 2005

Introduction

For perpendicular recording media a high magnetic field is necessary to write the bits and a soft underlayer to provide the closure field. An interesting candidate for such a magnetic underlayer is $Fe_{50}Pt_{1-x}Rh_x$ since it becomes ferromagnetic when heated and hence helps to stabilize the recording media via exchange interactions. The advantage of $Fe_{50}Pt_{1-x}Rh_x$ compared with conventional underlayer like permalloy is that even thinner layers may be sufficient to provide the same closure field. In bulk system $Fe_{50}Pt_{1-x}Rh_x$ it was shown that a ferromagnetic to antiferromagnetic transition occurs above room temperature. First measurements on thin films indicate that there are three distinct kinds of antiferromagnetic ordering, in the (0 0 1/2), (1/2 1/2 1/2) and (1/2 1/2 3/2) direction depending on temperature and magnetic field. Here at GKSS first test measurements of neutron diffraction on a $Fe_{50}Pt_{40}Rh_{10}$ film were carried out to demonstrate the feasibility to detect the magnetic order peaks for both the in-plane and the out of plane orientation.

Results

The 200 nm thick $Fe_{50}Pt_{40}Rh_{10}$-film is deposited on a MgO(100) substrate with a Cr(3 nm)/Pt(12 nm) buffer layer, providing a good seed layer to promote $L1_0$ ordering. Finally the sample was capped with Pt(2 nm). Figure 1 shows the first test measurement on the thin film system done at zero magnetic field and room temperature. The strong MgO(002) substrate peak as well as the (002) $Fe_{50}Pt_{40}Rh_{10}$ Bragg-Peak at about 3.45$Å^{-1}$ can be detected. Moreover, also the antiferromagnetic (0 0 1/2) peak is clearly observed at about 0.85$Å^{-1}$.
For the next measurement the Q-vector was oriented in the in-plane direction of the thin film. The result is shown in figure 2. Here, the substrate Peak MgO(220) at about 4.23 $Å^{-1}$ and the (200) Peak of the in-plane component of the film at 4.58 $Å^{-1}$ are be clearly observed. On the other hand, the antiferromagnetic (1/2 0 0) peak at about 1.17 $Å^{-1}$ appears only very weak at room temperature indicating that the magnetic Q vector lies dominantly in the (001) direction at room temperature. The results of these test measurements demonstrate that the magnetic orientation even for thin magnetic films can be determined using the POLDI neutron diffractometer at GKSS.

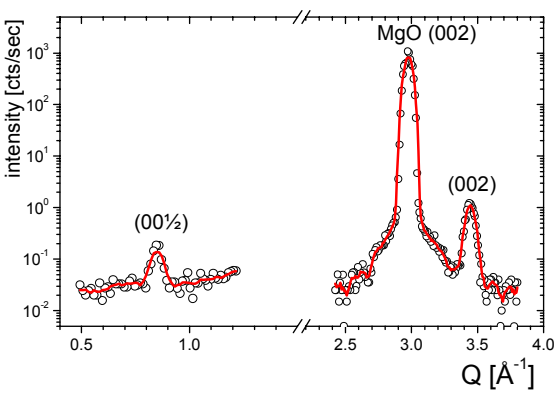


Figure 1: out-of-plane diffraction scan on $Fe_{50}Pt_{40}Rh_{10}$ at T = 295 K.

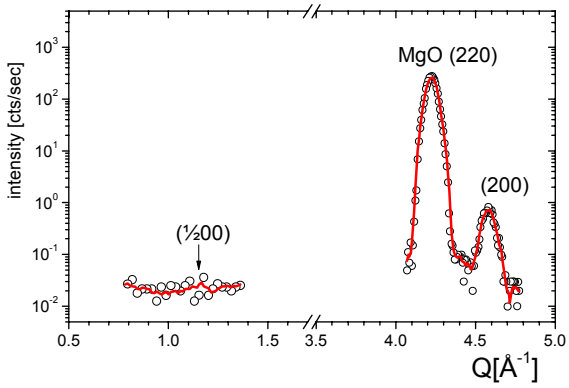


Figure 2: in-plane diffraction scan on $Fe_{50}Pt_{40}Rh_{10}$ at T = 295 K.

Outlook

Following these successful tests, the next measurements on the system $Fe_{50}Pt_{1-x}Rh_x$ are planned for various temperatures, magnetic fields and sample compositions. Therefore a cryomagnet with temperature range of 1.5 K–300 K and magnetic field up to 6 T will be set up. The antiferromagnetic peak will be measured for orthogonal directions in the reciprocal space to extract the dependence of the magnetic orientations on temperature and magnetic field. Moreover, it is expected that a transition from antiferromagnetism to ferromagnetism occurs at higher magnetic fields giving a better comprehension of the field induced antiferro- to ferromagnetic transition in general.

GKSS FORSCHUNGSZENTRUM in der HELMHOLTZ-GEMEINSCHAFT	EXPERIMENTAL REPORT	GeNF GENRA-3
Geesthacht neutron radiography facility GENRA-3		

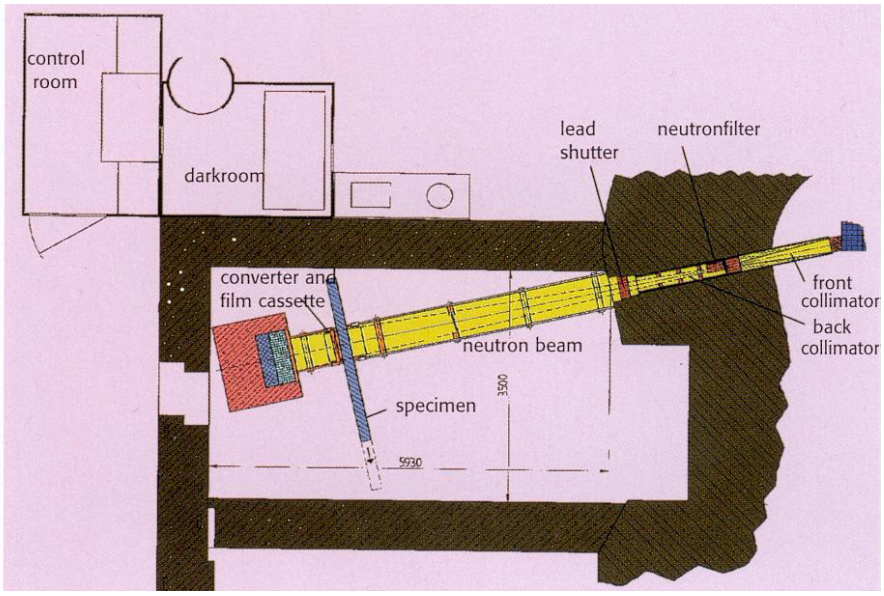
Short Instrument Description

The Geesthacht neutron radiography facility serves as an instrument for non-destructive testing and damage analysis of materials and technical structures by static and dynamic imaging. The ability of light elements, e.g. hydrogen or boron, to absorb neutrons allows unique analysis possibilities.

Local Contact:

Jürgen Vollbrandt
Phone/Fax : +49 (0)4152 87 – 1268 / +49 (0)4152 87 – 1338
e-mail: juergen.vollbrandt@gkss.de

Schematic View of GENRA-3:



Instrument Details:

Location at FRG-1:	beamline 13, thermal neutrons
Collimation ratio:	100 to 300
Flux at sample position:	$\Phi_{therm} = 1.4 \cdot 10^6$ cm^{-2} s^{-1} $\Phi_{epi} = 8 \cdot 10^3$ cm^{-2} s^{-1} with 4 cm Bi-filter at position: 2 m from beam exit available filters: 9 cm Bi-filter combined with 10 cm Be 0.2 cm Cd
max. size of specimen:	100 x 200 cm^2
Image:	15 x 15 cm^2 to 45 x 45 cm^2
Detecting: direct imaging	Gadolinium foil: max 14 x 17 inch Gd-scintillation screen connected to an image intensifier video camera
indirect imaging	transfer material: Indium, Dysprosium
Sample handling	Remote control of specimen, e.g. for scan purposes

GKSS FORSCHUNGSZENTRUM in der HELMHOLTZ-GEMEINSCHAFT	**EXPERIMENTAL REPORT**	**GeNF GENRA-3**

Insights of a methanol fuel cell – a feasibility study

Proposer:	**Regine Willumeit**[1], [1]GKSS Research Centre
Co-Proposers:	**Suzanna Nunes**[1],
	Eckhard Spohr[2], [2]Research Centre Jülich
Experimental Team:	**Heinz-Werner Schmitz**[1], **Wilhelm Müller**[1]
User Group Leader:	**Regine Willumeit**[1]

Dates of Experiment:	03.05.2005, 26.10.2005, 2.–4.11.2005

Objetives

Fuel cells are a promising alternative as a clean and effective method of energy conversion. One of the most important issues in low temperature fuel cell technology is the water management. A relevant aspect is the water distribution in the membrane electrode assembly. The membrane must contain a certain amount of water to remain highly proton conductive. On the other hand excessive water concentration in the cathode leads to catalyst flooding and hinders its contact with oxygen and thus optimal conditions for the reaction. In this study the water distribution in an existing fuel cell was determined by radiography.

Experiment

During the course of the experiment two test devices (standard stainless steel cell (1) and titanium cell (2)) designed by the FZ Jülich were used (set up chamber 1 in Fig. 1).

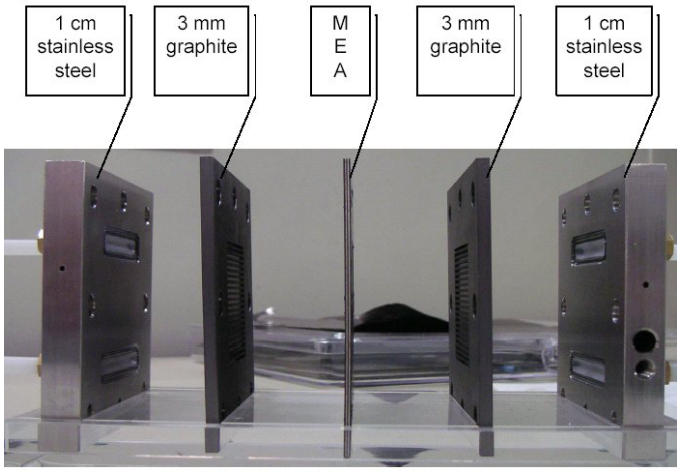


Figure 1: Test-cell 1 designed by FZJ. The dimensions are 90 x 90 x 33 mms.

In a first step the principal question whether one of the existing cells is suitable for the detection of hydrogen was answered. In static experiments information about the contrast and the spatial/time resolution were obtained. This is necessary for future experiments with the operating fuel cell. The filling of the cells on the anode side with deionised water was performed by hand until water flowed from the outlet of the cell. For contrast reasons part of the experiments were performed also with a filled anode side. The cells were then measured individually or simultaneously at position 400 (approximately 6 m from the shutter) and exposed for 20 minutes.

In a second set up the titanium cell was localized at position 200, 4 m from the shutter and a video camera monitored the experiment while water was pumped slowly through the cell. The pump rate was varied from 1.0 mL/min to 3.2 mL/min.

Achievements and Main Results

For both cell types the water distribution was detectable and it was revealed that the filling procedure did not lead initially to a homogeneous water level in the cells. This is due to wetting effects of the MEA. The longer the membrane is exposed to water the better the wetting properties become. Finally, as it was seen during the video experiment, a complete filling of cell 2 was obtained.

For cell type 1 (figure 2) it became obvious that exposure times of at least 20 minutes are necessary to detect the thin water layer in the cell because the background of the cell itself is much to high. If the cathode side is also filled with water, the anode water film can not be detected anymore. Therefore this cell is not suitable for further measurements.

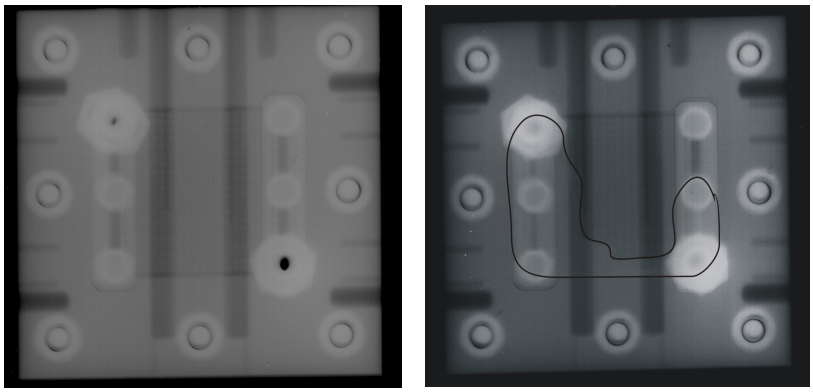


Figure 2: Cell 1 with (left) and without (right) water; exposure time 20 minutes. The distributed water is encircled in the right picture. It can be seen that by pressure-less filling of the cell the water is not evenly distributed. A complete flooding of the cell by this method was not achvied during several the tests.

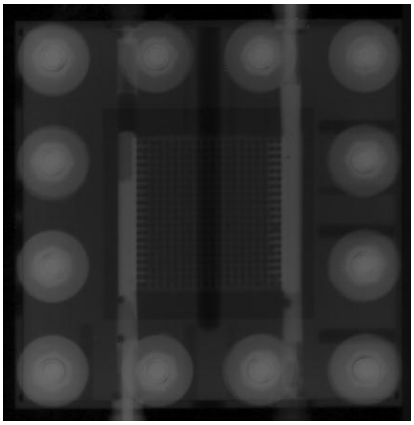


Figure 3: Fuel cell type 2 made from titanium filled with water on both sides. The labelled first few millimetres of the flow grid are filled with water on the cathode side. The anode flow field is homogeneously filled with water.

The second cell (made of titanium and almost 1 cm thinner) showed a much better transmission of the neutrons (figure 3). Therefore time resolved measurements with a video system could be performed. When the cell was measured while water was pumped through it became obvious that the cell is filled homogeneously on both sides. The filling procedure was also visible if one side was completely filled with water. Still the contrast between the water and the MEA was not sufficient to detect the thin polymer membrane. However, the setup appears to be suitable for the detection of water plugs being formed on the cathode side due to partial flooding.

Acknowledgement

We gratefully acknowledge the help of Manfred Heuer who supported this work by donation of the high precision pump.

GKSS FORSCHUNGSZENTRUM in der HELMHOLTZ-GEMEINSCHAFT	**EXPERIMENTAL REPORT**	**GeNF GENRA-3**

The New Setup for Neutron Tomography (NCT) at GENRA-3

Proposer: **Co-Proposers:**	**F. Beckmann, J. Vollbrandt, H.-W. Schmitz, T. Donath, A. Schreyer,** GKSS Research Centre
Experimental Team: **User Group Leader:**	**F. Beckmann, J. Vollbrandt, H.-W. Schmitz**
Date(s) of Experiment:	14–16 December 2005

Objectives

GENRA-3 is specialized in non-destructive testing for industrial applications. A setup for Neutron Computerized Tomography (NCT) was designed to extend this facility for three-dimensional investigations. The features of the new experimental station and first results are presented.

Experiment

The setup for neutron tomography can be installed in the irradiation chamber of GENRA-3 at different distances to the source (s. figure 1). Therefore an optimal value of L/D with respect to the size of the sample can be selected. This is required to obtain a good spatial resolution in the tomogram. The neutron beam parameters for different sample-collimator distances P are:

P [m]	0.5	1.5	2.5	4.0
Size [cm^2]	16x16	24x24	32x32	47x47
Flux [$n\,cm^{-2}\,s^{-1}$]	$7.4 \cdot 10^6$	$3.2 \cdot 10^6$	$1.7 \cdot 10^6$	$6.8 \cdot 10^5$
L/D	100	150	200	300

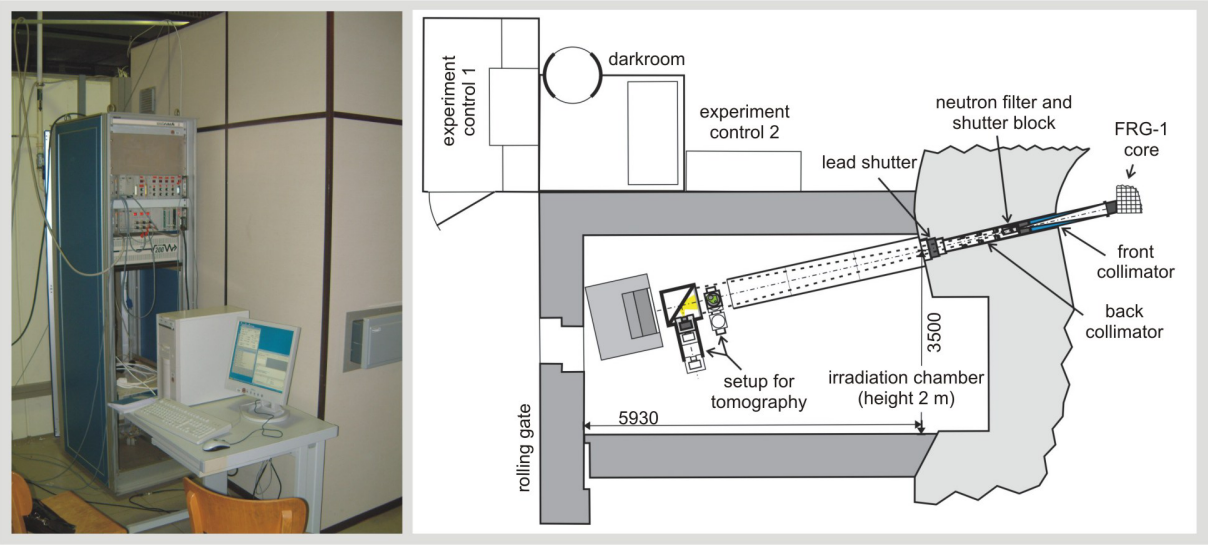


Figure 1: The experimental control used for NCT is shown on the left. It is installed at position "experimental control 2" given in the schematic view of GENRA-3 on the right. The setup for NCT setup can be installed at different distances to the source resulting in L/D from 100 up to 300.

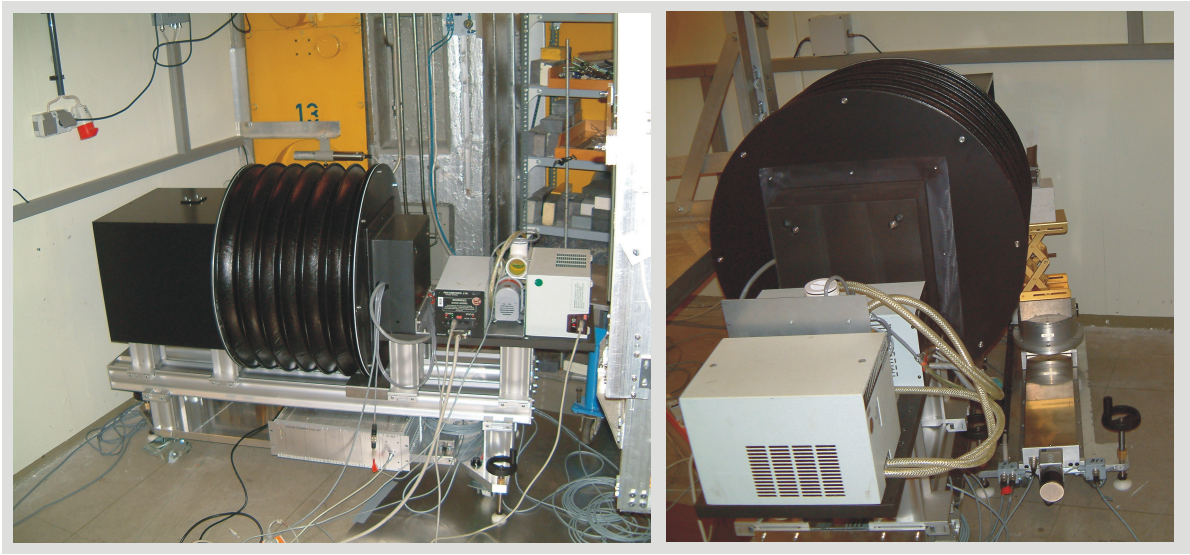


Figure 2: First installation of the setup used for NCT at position P = 0.5 m. On the right side the installation with an installed sample in front of the fluorescent screen is shown.

In figure 2 the new setup for tomography installed at GENRA-3 is shown. It consists of a 2-dimensional neutron detector and a high precision sample manipulator. The principle setup is given in the sketch in figure 3. The used components are:

CCD camera:	Kodak KAF-1400, 1320 x 1035 pixels, 6.8 µm x 6.8 µm, 12 bit digitization.
Optical lens:	Nikkor 35mm f/1.4, Nikon, Tokyo, Japan.
Optical mirror:	Plane mirror, optical surface Al covered by SiO, LINOS Photonics, Göttingen, Germany.
Fluorescent screen:	^{6}LiF/ZnS:Ag , 40x40 cm^{2}, 250µm thick, ND, green emitting, substrate 1 mm aluminum, Applied Scintillation Technologies, Harlow, UK.

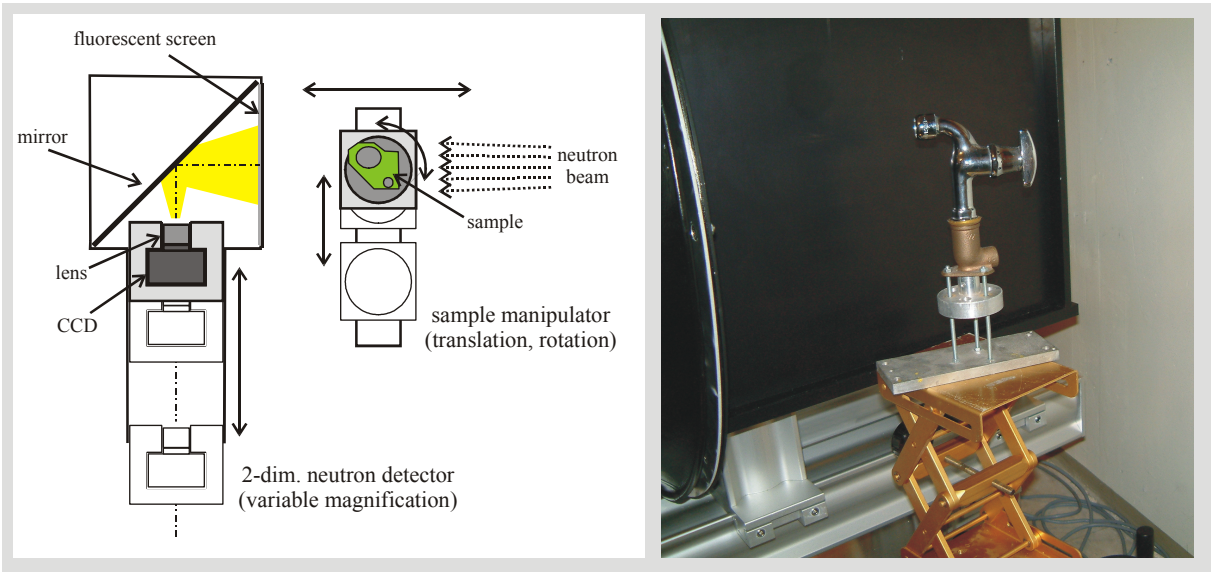


Figure 3: Sketch of the experimetal setup for NCT (left). Investigation of a water tap (right). The sample is installed on the manipulation stage in front of the fluorescent screen.

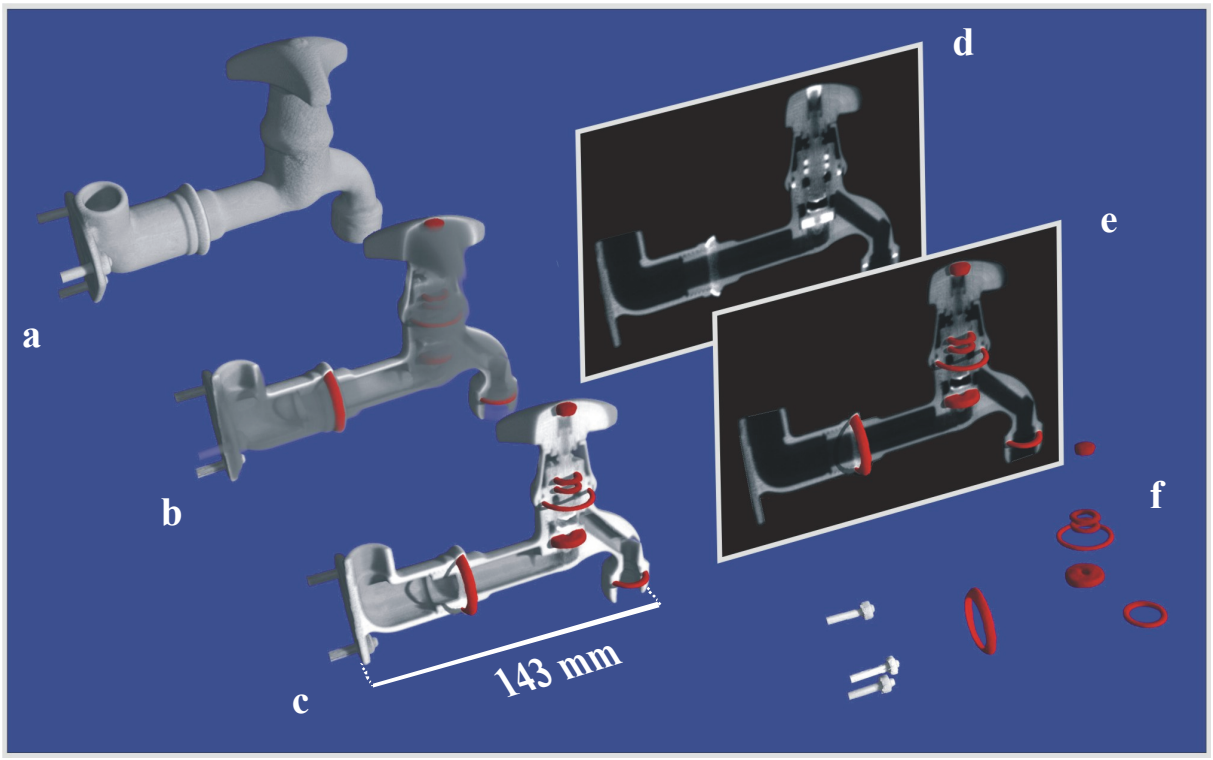


Figure 4: Volume rendering of the total reconstructed volume of the water tap (a). The high absorbing sealing rings out of rubber material are shown as white regions in the vertical cut in (d). Using the software VGStudioMax these regions are segmented and coloured in red in the 3D volume. At the position of the vertical cut, half of the metal material is visualized semitransparent (b) and transparent (c). The 3D arrangement of the sealing rings is shown in combination with the vertical cut (e) and the segmented screws (f).

Achievements and Main Results

For the first tomographical experiment at GENRA-3 we choose as a sample a water tap consisting of different types of metal and high absorbing rubber components. We set up the sample axis at 0.5 m distance from the collimator and sample-detector distance to 0.13 m (s. figure 3). The tomographical scan was performed by taking 30 flat field images (images without sample) and 720 projections at different sample rotation equally stepped between 0 and 2π. The exposure time of each image was 10 seconds. The total scan lasts 4.5 hours.
To reconstruct the sample the axis of rotation was carefully aligned by software to be perpendicular to the lines of the projections. These aligned projections then were reconstructed by using the method of backprojection of filtered projections. Each line in the projection then yields a reconstructed slice. By stacking all slices we obtain the resulting 3D dataset consisting of 498x498x611 voxel with the size of 130x130x160 mm³..
The visualization of the 3D dataset is presented in figure 4. By using the software VGStudioMax 3D-volume renderings, and virtual cuts are created. Furthermore the software is able to extract and colorize the high absorbing sealing rings of the water tap.

To test the spatial and density resolution of the setup a stepper motor (Phytron VSS 42.200.1.2) was investigated. The exposure time was set to 15 seconds and 720 projection were taken. In figure 5 a 3D-representation of the data set, a reconstructed slice and a virtual vertical slice is presented. The spatial resolution of the system is about 1 mm.

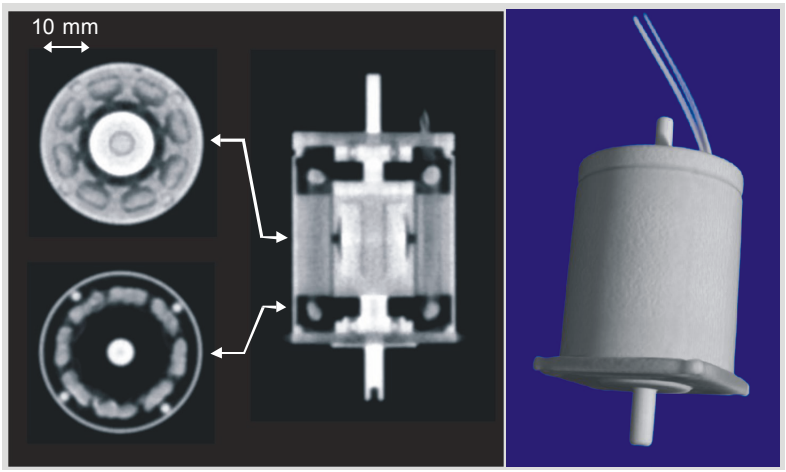


Figure 5: Investigation of a stepper motor (Type: Phytron VSS 42.200.1.2). Left: reconstructed slices and a calculated vertical slice; Right: 3D rendering.



Figure 6: Photo of a turbine blade made of stainless steel (Inconel). The total height of the sample is 107 mm.

A further tomographical scan was performed on a turbine blade out of stainless stell (Inconel). The aim of the study is the investigation of the internal cooling system. We recorded 720 projections with an exposure time of 15 seconds. The total scan lasts 5 hours. In figure 6 an optical viewgraph of the sample is given. The reconstructed data set consists of 437x437x433 voxel representing a volume of 114x114x113 mm³. Renderings of the total and sliced volume are presented in figure 7 a–c. By using the software VGStudio the voids in the blade representing the cooling canal system are segmented and visualized in blue in figure 7 d.

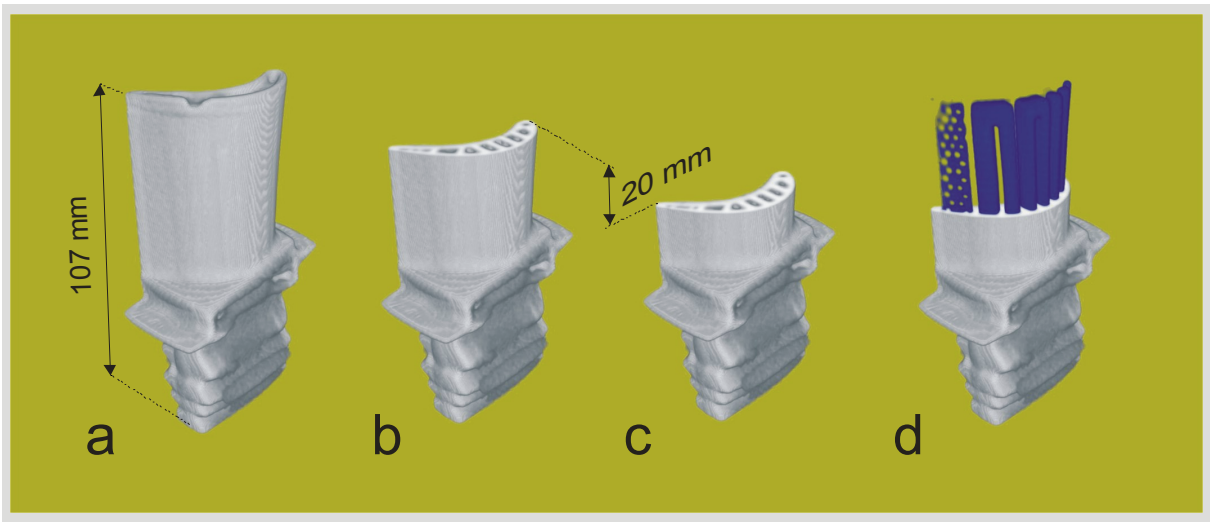


Figure 7: Volume renderings of the reconstructed data set of the turbine blade presented in figure 6. A volume rendering of the total data set is given in **(a)**. Then the volume is slice 20 mm **(b)** and 40 mm **(c)** from the top. The internal canal system is clearly visible. These voids then are segmented and coloured in blue. A combination of the cooling system (blue) and the remaining stainless steel (grey) is visualized in **(d)**.

Reference

F. Beckmann, J. Vollbrandt, T. Donath, H.W. Schmitz, A. Schreyer, "Neutron and synchrotron radiation tomography: New tools for materials science at the GKSS-Research Center", Nuclear Instruments and Methods in Physics Research A 542 (2005) 279–282.

Note

The following research projects have been supported in 2005 by the European Commission under the 6th Framework Programme through the Key Action: Strengthening the European Research Area, Research Infrastructures. Contract n°: RII3-CT-2003-505925':

M. Knaapila, L. Almasy, H. Burrows
A SANS study of water soluble polyfluorene-surfactant systems

P. Claesson
Conformational change of the polyelectrolyte in presence of surfactant studied using SANS

R. Perzynski, E. Dubois, V. Haramus
Study of the magnetic scattering in magnetic fluids and solids: dilute samples

R. Perzynski, E. Dubois, V. Haramus
Study of the magnetic scattering in magnetic fluids and solids: concentrated samples

P. Claesson
Solution Conformation of comb copolymers containing different degree of graft PEO and its interaction with the anionic detergent (SDS)

M. Almgren
Variable contrast study of coexisting fluorocarbon-rich and hydrocarbon-rich micelles

L. Vekas
SANSPOL study of organic non-polar ferrofluids stabilized by mixed surfactants

I. Skorvánek, J. Marcin
SANS study of the early stages of crystallization in the Fe-Zr-B-Cu nanocrystalline alloys

A. Manescu, A. Giuliani, F. Fiori
SANS investigation of Cu alloys for applications to technology for the restoration of ancient organs

R. Triolo, F. Lo Cels0, I. Ruffo
Fingerprinting Marbles of Archeological Interest

M. Fally, I. Drevenšek-Olenik
Light-induced phase separation in polymer dispersed liquid crystals (PDLC)

P. Mayrhofer, H. Clemens, P. Staron
Characterisation of coherent precipitates in a hard coating

D. Chernyshov, S.V. Grigoriev, K.W. Törnroos, B. Vangdal
Temperature induced spin conversion in a molecular complex as seen by SANS

V. Ryukhtin, P. Stepanek,
USANS investigations of organized nanostructuresof diblock copolymers in immiscible solvents

U. Cihak, M. Stockinger
Residual Strain Measurements within forged engineering components and model parts

H. P. Degischer, A. Pyzalla
Evolution of internal stresses during isothermal creep of an Al-Si piston alloy

P. Mikula
Multiple reflection monochromator

The support by the European Commission is gratefully appreciated by the proposers, authors and experimental teams.

Appendix I

Progress Report 2005
of the REFSANS Project

GKSS FORSCHUNGSZENTRUM in der HELMHOLTZ-GEMEINSCHAFT	**STATUS REPORT**	**GeNF REFSANS / FRM-II**

Horizontal ToF-Neutron Reflectometer REFSANS at FRM-II Munich / Germany: First Tests and Status

Proposer:	**R. Kampmann[1], M. Haese-Seiller[1], V. Kudryashov[1]**
Co-Proposers:	**C. Daniel[2], B. Nickel[3], J. Rädler[3], A. Schreyer[1], E. Sackmann[2]**

[1] GKSS Forschungszentrum, Inst. für Werkstoffforschung, D-21502 Geesthacht
[2] Technische Universität München, Physik Department, E22, D-85747 Garching
[3] Ludwig-Maximilians-Universität, Department für Physik, D-80539 München

Experimental Team:	**R. Kampmann[1], M. Haese-Seiller[1], V. Kudryashov[1]**
User Group Leader:	**R. Kampmann[1]**
Date(s) of Experiment:	2005

Introduction

In 2005 the horizontal reflectometer REFSANS at FRM-II in Munich/Germany has successfully been put into operation. It is dedicated to the comprehensive analysis of the air/water interface by means of specular and off-specular reflectivity as well as GISANS measurements [1, 2].

REFSANS and its main components

The main demands made on REFSANS are to provide excellent conditions for i) specular reflectivity, ii) grazing incidence (GI-)-SANS and iii) to allow of performing comprehensive investigations on the air/water interface for biological applications [1, 2]. To meet these demands novel and expensive components have been developed for this horizontal ToF-reflectometer.

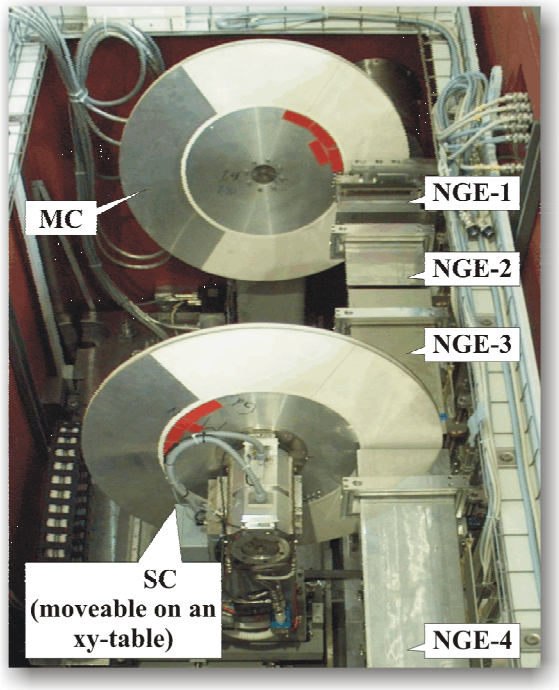


Figure 1: View of neutron guide elements (NGE), master chopper and slave chopper in the chopper chamber.

The instrument starts with the master chopper (MC) in the chopper chamber in which the slave chopper (SC) can be positioned in neutron guide gaps at distances between ~ 5 cm and ~ 2.1 m from the MC. Both choppers have double discs to adjust the transmission window between 0° and 120° (Fig. 1). They are operated with windows of equal height and the SC opens at the time t_0 when the MC closes with the result that at t_0 the neutron guide between both choppers is filled with neutrons with wavelengths $\lambda < \lambda_0$ [3]. This expensive design (Fig. 1) is needed to meet the demands of specular reflectivity and of GI-SANS comprising high and low λ-resolution.

Neutron guide elements of REFSANS as well as their mechanical support in the chopper and in the beam guide chamber are designed for realizing very different beam geometries. Standard reflectivity measurements are performed with a horizontally slit height-smeared beam

and incidence angles of the primary beam of ± 3, 12 and 48 mrad (main beam settings in REFSANS). The beam may be guided towards the sample surface from the air or through the substrate [1, 2].

GISANS geometry demands to collimate the beam horizontally and vertically. In this geometry the intensity can strongly be increased by means of focusing 13 partial beams in the detector plane at a distance of ~ 9 m from the sample (Fig. 2). This focusing is performed by means of pre-collimating the beams in radially collimating neutron guide channels in the chopper chamber (NGE-3 and -4) and by comb-like diaphragms which can be moved into the beam in between of neutron optical bodies (Figures 2 and 3) preventing mixing of neutrons in different partial beams.

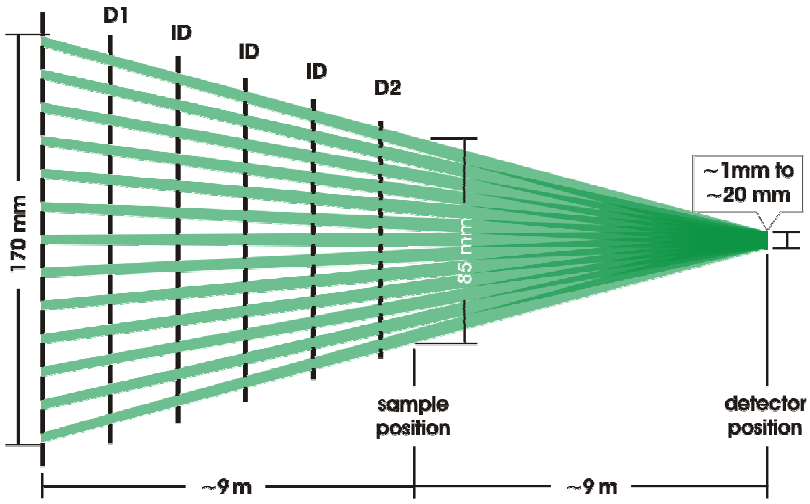


Figure 2: Schematic view of the horizontal focusing of up to 13 beams in the detector plane. The beam is pre-collimated in the radial collimator (lower channels in the 0.6 m and 1m long NGE-3 and -4).

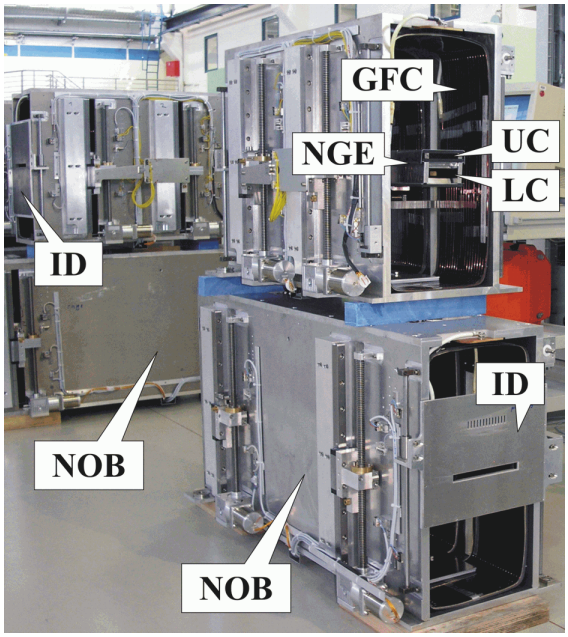


Figure 3: View of neutron optical bodies (NOB) ready for being mounted into the beam guide chamber (NGE, UC and LC: neutron guide element and its upper (UC) or lower channel (LC); GFC: guide field coil; ID: interim diaphragms).

The sample environment is designed for experiments at the air / water interface as well as at the air / solid and liquid / solid interface. In all cases one can make use of a microscope in upright or inverted position either for preparation purposes or as a complementary measuring option (e.g. fluorescence techniques). The further equipment consists of a damping table, a temperature controlled film balance and a set of translational tables (x, y, z) together with a three-axis goniometer (χ, Φ, Ω).

A 2D-position sensitive area detector with an active area of 500 mm × 500 mm and a position resolution of ~ 2 mm × 3 mm has successfully been put into operation. With its high quantum efficiency for neutrons and its very low one for gammas the detector meets all requirements for measuring low reflectivity and weak GISANS contributions [4]. Together with a new data acquisition based on the P7888 card from FAST ComTec GmbH the delay-line based 2D-detector allows of maximum count rates of ~ 10^6 n/s.

The 2D-detector can be positioned in the scattering tube at distances between ~ 2 m and ~12 m from the sample. The scattering tube can be lifted such that the specularly reflected beam passes its centre for incidence angles between ~ 0 and -100 mrad.

Status

REFSANS has successfully been put into operation, all components (chopper system, neutron optics, sample environment, 2D-detector, shielding, scattering tube with lifting system and data acquisition system) meet or even surpass their requirements. Test beams have already been guided to the sample demonstrating that the shielding is sufficiently thick. First measurements will be performed at REFSANS in spring 2006 after repairing of some broken elements of neutron guide NL-2b.

Acknowledgements

The great contribution of the technical department of GKSS to constructing and manufacturing of REFSANS components is gratefully acknowledged. The development of REFSANS has been supported by the German Federal Ministry of Education, Research and Technology (BMBF) under contracts 03-KA5FRM-1 and 03-KAE8X-3.

References

[1] R. Kampmann, M. Haese-Seiller, M. Marmotti, J. Burmester, V. Deriglazov, V. Syromiatnikov, A. Okorokov, F. Frisius, M. Tristl, E. Sackmann: Applied Physics A, 74, (2002), 249–251.
[2] R. Kampmann, M. Haese-Seiller, V. Kudryashov, V. Deriglazov, V. Syromiatnikov, M. Tristl, B. Toperverg, A. Okorokov, A. Schreyer, E. Sackmann: Physica B 335 (2003), 274–277.
[3] A. A. van Well: Physica B 180-181, (1992) 959961.
[4] R. Kampmann, M. Marmotti, M. Haese-Seiller, V. Kudryashov: Nuclear Instruments and Methods A 529 (2004) 342–347.

Appendix II

Reports of experiments carried out
at HASYLAB / DESY by GKSS personel
– GKSS outstation HARWI-II at DESY –
as responsible experimenters in support of external users.

These reports have been taken from
HASYLAB Annual Report 2005.

(reprints by courtesy of DESY, Hamburg)

ASAXS and SAXS/USAXS Investigations of Metal Hydrides for Reversible Hydrogen Storage

P.K. Pranzas[1], M. Dornheim[1], K.-F. Aguey-Zinsou[1], S. Roth[2], R. Gehrke[2], G. Goerigk[3], T. Klassen[1] and A. Schreyer[1]

[1] Institut für Werkstoffforschung, GKSS Forschungszentrum, Max-Planck-Str. 1, 21502 Geesthacht, Germany
[2] HASYLAB, Notkestr. 85, 22603 Hamburg, Germany
[3] Institut für Festkörperforschung, Forschungszentrum Jülich, Postfach 1913, 52425 Jülich, Germany

Hydrogen is one of the most interesting renewable energy sources regarding storage, transport and conversion of energy in the future. Nanocrystalline metal hydrides, like magnesium hydride or lithium alanate, offer a safe alternative to the storage of hydrogen in compressed or liquid form. MgH_2 has a high storage capacity of up to 7.6 wt.%. Absorption and desorption kinetics of hydrogen in MgH_2 and $LiAlH_4$ are subject of several studies[1-4]. Sorption properties are distinctly enhanced by the addition of metal-oxide catalysts. However, structural changes during these processes have hardly been investigated up to now and the mechanisms of the catalytic reactions are not fully understood.

The aim of this project is to study the distribution of different metal-oxide catalysts in the metal hydride matrix after high energy ball milling using anomalous small-angle X-ray scattering (ASAXS) at beamline JUSIFA, measuring at different energies close to the absorption edges of the catalyst metals. Investigations of samples with different catalysts will provide information about the influence of these additives to the evolution of the nanostructure during high energy ball milling and hydrogen sorption cycles. To obtain information about structural changes of the MgH_2 and $LiAlH_4$ matrix itself over a larger q-range, additional small and ultra-small-angle X-ray scattering (SAXS/USAXS) experiments were performed at BW4.

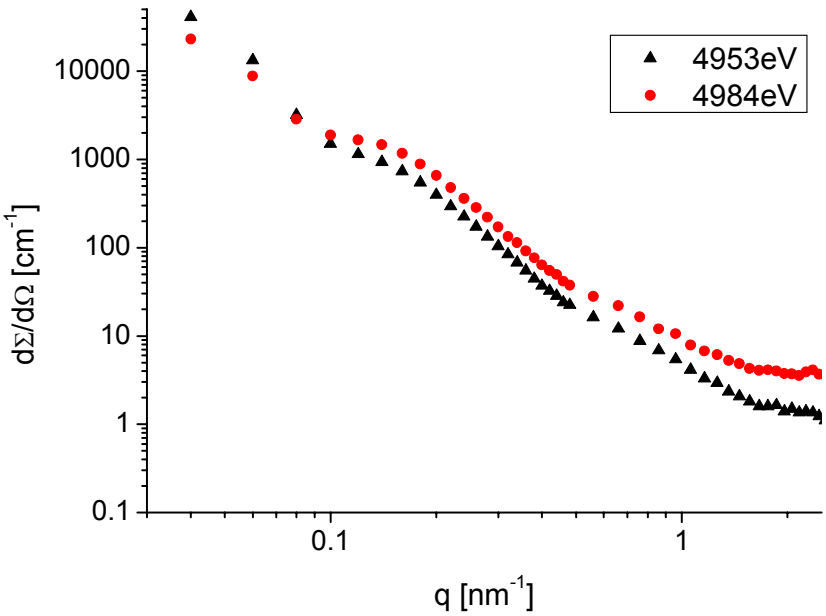


Figure 1: Total scattering curves of $LiAlH_4$ with 1 mol-% TiO_2, milled for 50 h, measured at 4953 eV, as well as at 4984 eV.

ASAXS measurements at JUSIFA were carried out at room temperature using cuvettes with thicknesses between 0.1 and 1 mm and distances between the sample and the two-dimensional detector of 935 and 3635 mm. As catalysts Fe_3O_4 and TiO_2 were used. The measurements have been performed at different energy ranges according to the K-absorption edges of the investigated catalysts metals (Ti: 4966 eV and Fe: 7112 eV). Up to 5 energies were used to obtain the energy-dependent scattering. The SAXS curves were corrected for detector sensitivity, empty beam, dark current and transmission. The macroscopic scattering cross section $d\Sigma/d\Omega$ was obtained by calibration with a reference glassy carbon sample. Figure 1 shows the total scattering curves of $LiAlH_4$ milled for 50 h after addition of 1 mol-% TiO_2, measured at 4953 eV and 4984 eV. The energies were chosen according to a measured chemical shift of 17 eV. The curves reveal an energy dependant scattering which is not fully understood yet.

Additionally, MgH_2 and $LiAlH_4$ samples were measured at BW4 to cover the large q-range from SAXS to USAXS. The measurements were carried out at room temperature using a fixed wavelength of 0.138 nm and distances between sample and detector of 2 and 12.6 m. In figure 2 selected scattering curves are shown calculated from the 2-D scattering pattern using the Fit2D program[5].

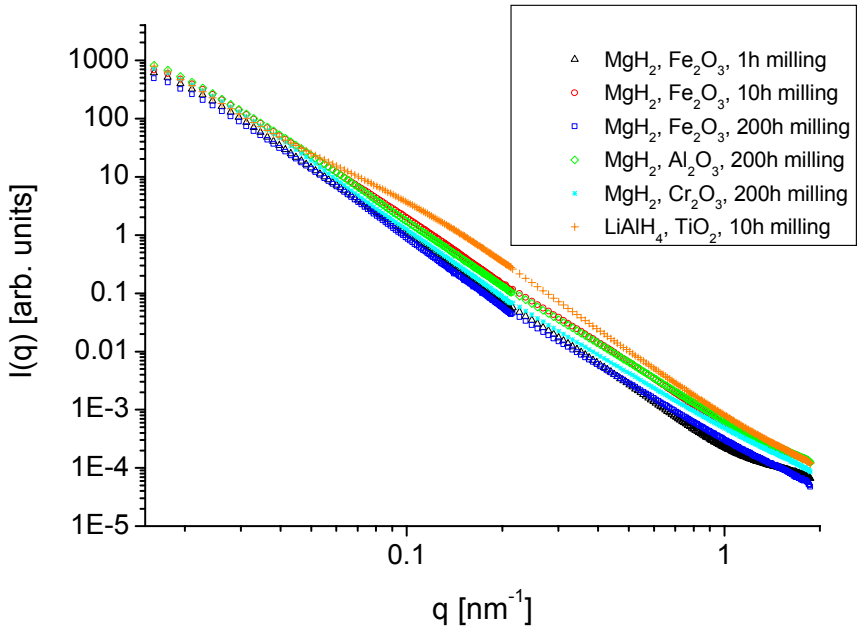


Figure 2: SAXS curves for high-energy ball milled MgH_2 and $LiAlH_4$ with different additives and using varying milling times.

Figure 2 shows combined SAXS/USAXS curves for high-energy ball milled MgH_2 and $LiAlH_4$ samples with different additives, using varying milling times. The differences in the curves exhibit structural changes in the nanocrystalline metal hydrides.

References

[1] G. Barkhordarian, T. Klassen, R. Bormann, J. Alloys Comp. 364, 242 (2004)
[2] G. Barkhordarian, T. Klassen, R. Bormann, Scripta Mater. 49, 213 (2003)
[3] W. Oelerich, T. Klassen, R. Bormann, J. Alloys Comp. 315, 237 (2001)
[4] P.-A. Huhn, M. Dornheim, T. Klassen, R. Bormann, J. Alloys and Comp., in press
[5] http://www.esrf.fr/computing/scientific/FIT2D/

Commissioning and first experiments at the Materials Science Beamline HARWI II

T. Lippmann, F. Beckmann, R.V. Martins, L. Lottermoser, T. Dose and A. Schreyer

GKSS Forschungszentrum Geesthacht, Max–Planck-Str. 1, 21502 Geesthacht, Germany

As has been reported last year [1] GKSS, GFZ and DESY are reconstructing and rebuilding beamline W2 (HARWI) in a collaborative effort. In the course of the last year the reconstruction of the beamline and the experimental hall (building 25c) were finished, so that the optics hutch and the experimental hutches could be equipped with the most important components and instruments in order to test, study and use the first beam from the new insertion device [2]. Fig. 1 shows the current interior view of the experimental hall.



Figure 1: Interior view of the experimental hall.

The optics hutch was equipped with a large monochromator tank with dimensions of 3 m in length, 2 m in width and 1 m in height (Fig. 2). Two different types of fixed–exit double–crystal monochromators will be mounted inside the tank with the option of easily changing between them without breaking the vacuum. The first one will be a Laue–type monochromator diffracting in the horizontal and providing photons between 60 and 250 keV within a beam size of 10 x 10 mm^2. The second one will provide a beam up to 70 mm in width, 10 mm in height and photon energies down to 20 keV. This monochromator will diffract in the vertical (Fig. 3). For the first tests only the horizontal monochromator was preliminarily installed in the tank, equipped with two annealed Si (111) crystals (FWHM: $\approx 6''$) and operated at 82 keV. The tank is connected to the vacuum tube of the beamline and can be evacuated to below 10^{-6} mbar.
In order to protect the downstream equipment against the 'white' beam a massive beamstop was installed behind the tank (Fig. 4). It consists of a water–cooled copper block, which is designed to



Figure 2: The monochromator tank. The beam is coming from the right.

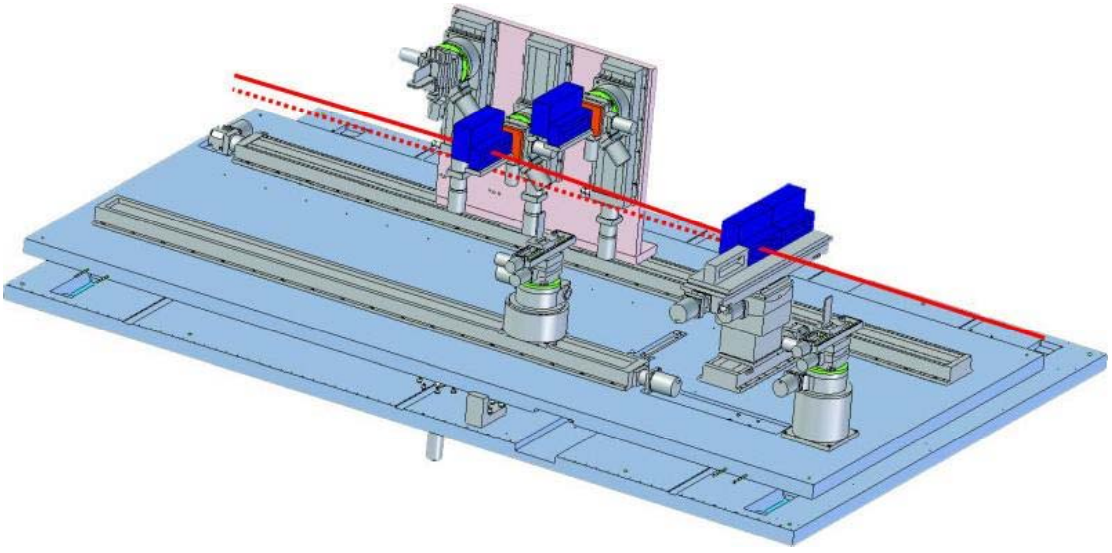


Figure 3: Sketch of the two different monochromators. The user can change between the horizontal monochromator in the foreground and the vertical monochromator in the background by moving the upper plate perpendicular to the beam (red). The whole ensemble (lower plate) can also be aligned in the vertical.

handle up to 12 kW heat load. Behind the copper, a tungsten block of 100 mm thickness absorbs the high–energy fraction of the wiggler spectrum. The beamstop has a small pinhole of 0.7 mm diameter to provide a narrow 'white' beam for experiments. Additionally, two channels for the monochromatic beams are present. Fig. 5 shows the flange at the rear end of the device. The monochromatic

channels are sealed with capton foil, whereas for the 'white' beam pinhole is covered by a glassy carbon plate of 0.5 mm thickness. The beamstop is evacuated via the monochromator tank and can be aligned using small tilt movements via remote control.

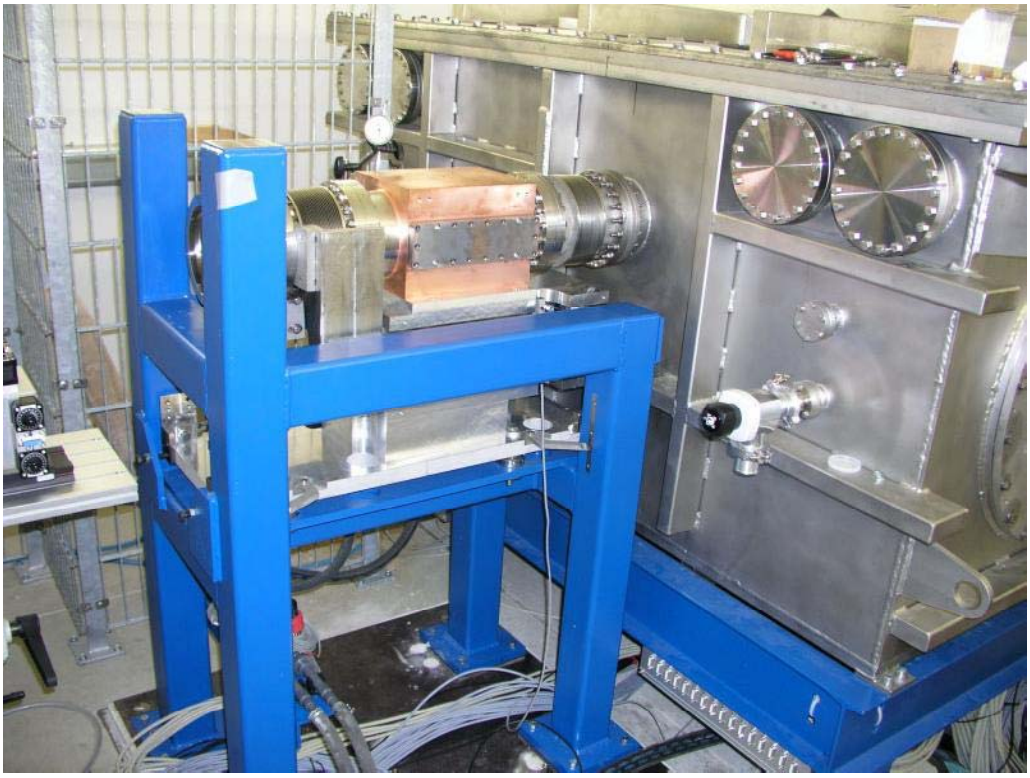


Figure 4: The beamstop for the 'white' beam.

The optics hutch equipment is completed by a beamshutter. Between the beamshutter and the beamstop there is still about 1 m remaining free beam path for a future installation of various additional devices, e.g. beam monitors and cameras, slit systems, add–on shutters and beam filters etc.
In the first experimental hutch two pits will allow to easily change between various experiments. In the first pit a large materials science diffractometer will be installed next year. The second pit (downstream) has already been equipped with two tables for heavy loads up to 3 tons. Both tables of 3 m in length and 1.4 m in width can be independently lifted into the beam (Figs. 6 and 7). On the upstream table a Eulerian cradle and an image plate scanner were preliminarily mounted for the first diffraction test experiments. As soon as the diffractometer is installed, this table will be free for other experiments. The second table is dedicated for tomography setups and measurements. A new tomography apparatus and a setup for a combined diffraction and tomography experiments is under construction and will replace the existing setup at a later stage.
First test experiments have already been performed, namely texture experiments on various samples, a strain analysis and a couple of tomography measurements. Preliminary results showed that the data quality measured at the new HARWI II beamline is already comparable to that of the existing high–energy beamline BW5, although due to limited time no optimization of the optics and the instruments could be performed so far. Thus, the first months of the next year will be needed for commissioning, optimization and characterization as well as further test experiments. After installation of the new materials science diffractometer and a new tomography setup, full user mode is expected in the second half of 2006.



Figure 5: Rear end of the beamstop.



Figure 6: Preliminary diffractometer setup on the first experiment table.



Figure 7: Tomography setup on the second experiment table.

References

[1] F. Beckmann, T. Lippmann, J. Metge, R.V. Martins, T. Dose, A. Schreyer, HASYLAB Annual Report 2004.

[2] M. Tischer, J. Pflüger, L. Gumprecht, T. Vielitz, HASYLAB Annual Report 2004.

Celebrating the first experiments at the new high-energy beamline HARWI II

On Tuesday, November 22nd, 2005, members of the three Helmholtz centers DESY, GKSS-Research Center Geesthacht and GFZ Potsdam gathered in the HARWI-II hall to celebrate a major milestone achieved at this new beamline, namely the first experiments which were successfully performed before the machine was shut down in mid November.

Following a welcome address given by Prof. Albrecht Wagner (DESY), Prof. Wolfgang Kaysser (GKSS) and Prof. Wilhelm Heinrich (GFZ) highlighted the very successful collaboration of the three research centers during the construction phase of this new materials science research facility. The characteristics of the beamline and its potential for materials science applications were illustrated by Prof. Andreas Schreyer (GKSS). Prof. Frank Schilling (GFZ) presented the new Tripple H Experiment MAX200x which allows novel experiments to study geodynamic processes.



Figure 1: Left: Address of welcome by Prof. Albrecht Wagner, DESY; Right: Introduction to the new HARWI II beamline by Prof. Andreas Schreyer, GKSS



Figure 2: Left: Greetings by Prof. Wilhelm Heinrich (GFZ)
Right: Celebrating the successful cooperation: Prof. Frank Schilling (GFZ), Prof. Andreas Schreyer (GKSS), Prof. Albrecht Wagner (DESY), Prof. Jochen Schneider (DESY)



Fig. 3: Some impressions from celebration which took place in building 25c at DESY which is the location of the HARWI II beamline.

Characterization of MgCa-bone screws by high energy texture analysis

U. Garbe, J. Fischer[2], T. Lippmann, H.-G. Brokmeyer[3], F. Beckmann and F. Witte[2]
GKSS-Research Center, Max-Planck-Str.1, 21502, Geesthacht, Germany

[2]Department of Orthopaedic Surgery, Hannover Medical School, Anna-von-Borries-Str.1-7, 30625 Hannover, Germany
[3]Institute of Materials Science and Engeneering Technical University Clausthal, Agricolastr. 6, 38678 Clausthal-Zellerfeld, Germany

Introduction

In medical technology calcium containing magnesium alloys (MgCa) are promising to replace degradable polymers or titanium as the material for small bone screws or other fixating tools. To find the best composition of Mg and Ca and the best manufacturing process, it is essential to analyse the physical and chemical properties of many series of different magnesium alloys.

The physical properties of polycrystalline materials depend on the physical properties of the crystallites of which they consist and on the orientation of the crystallites in the polycrystalline aggregate [1,2]. Hence, it is necessary to determine the orientation distribution (texture) of the crystallites. Diffraction with high energy synchrotron radiation is a new experimental method for non-destructive texture measurements. The new GKSS materials science beamline HARWI II (W2) offers an opportunity to do texture measurements in an energy range of 20 - 200 keV.

Experimental Procedure

For the first experiments on this topic, we select a MgCa-bone screw with a composition of 99.6 wt % Mg and 0.4 wt % Ca. The magnesium alloy was extruded and thread was produced by machining. For the texture measurement with high energy synchrotron radiation [3], the MgCa screw was mounted on the Eulerian cradle with a z-translation on the sample tower. Diffraction images were taken in steps of $\Delta\varphi = 5°$ with a MAR345 image plate detector. The exposure time to require a diffraction image was 30sec and the beam size was adjusted to 2*2mm. Using a special software designed for the HARWI-beamline the pole figure data were calculated from the diffraction images.

Results

For the first experiment, the measured (100)-pole figure at three different positions at the bone screw are presented in figure 1. At each measuring point (P1-P3, fig. 1) a fibre texture was investigated. The fibre axis for the (100)-reflex is parallel to the screw axis. No significant variation in intensity and orientation of the observed texture could be observed for the acquired pole figures.

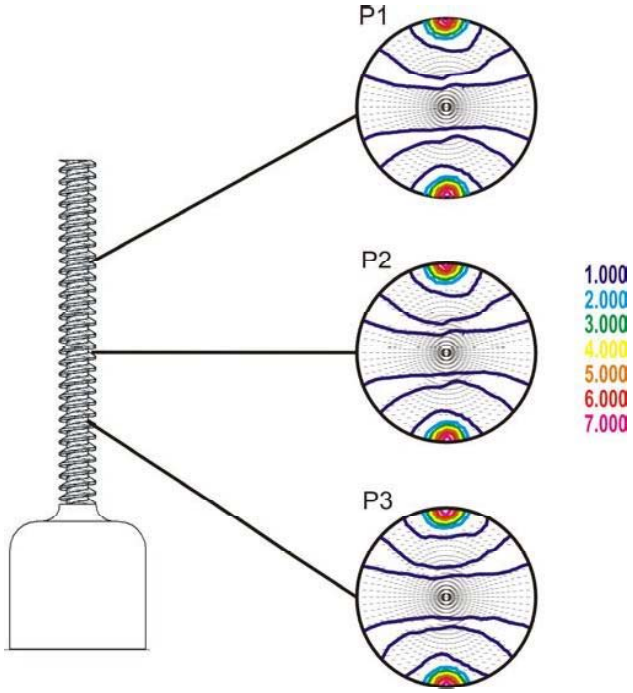


Figure 1: (100)-pole figures at different measuring points of a MgCa-bone screw.

Conclusions

Texture analysis with high energy synchrotron radiation at the new GKSS-beamline HARWI II (W2) is an excellent method to determine the homogeneity of texture with local texture measurement. The variable beam size up 100mm*5mm will allow also the investigation of the global texture in further experiments with the same beamline. The new HARWI II beamline allows to combine diffraction experiments and tomographic research at the same beamline after a short modification of the set-up. This new set-up at HARWI II provides the ability for extensive characterisation of MgCa-bone screws and other materials used in medical technology.

References

[1] G. Wassermann, J. Grewen, *Texturen Metallischer Werkstoffe*, Berlin: Springer Verlag 1962.

[2] H.-J. Bunge, *Texture Analysis in Materials Science*, Cuvillier Verlag, Göttingen 1993.

[3] L. Wcislak, H.-J. Bunge, H. Klein, U. Garbe, Th. Tschentscher and J. Schneider, *Texture Analysis with High Energy Synchrotron Radiation*, J. Appl. Cryst. (2002) **35**, 82-95.

Comparison of conventional and synchrotron-radiation-based micro computed tomography of 3D printed scaffolds for bone augmentation

S. Irsen, C. Tille, H. Seitz, B. Leukers, F. Beckmann[1], and B. Müller[2]

caesar research center, Ludwig-Erhard-Allee 2, 53175 Bonn, Germany
[1]GKSS Forschungszentrum, 21502 Geesthacht, Germany
[2]Computer Vision Laboratory, ETH Zürich, Sternwartstrasse 7, 8092 Zürich, Switzerland

New fabrication methods for the manufacturing of synthetic bone grafts are an escalating field of research during the last decade. Especially rapid prototyping techniques are promising for the generation of patient individual scaffolds based on 3D data [1]. Besides the biocompatibility, the porosity is crucial for the quality of the synthetic bone graft. Here, the internal open porosity with accessible pores having diameters between 100 and 500 μm is the prerequisite for the vascularization of the implanted scaffold [2]. Consequently, the porosity analysis of the scaffolds is one of the most important criteria for optimization. The quantification of the porosity using well-established techniques such as Hg-porosimetry and electron microscopy is problematic and does not yield a satisfying description [3] as previously uncovered for another kind of porous scaffolds for bone augmentation [4]. As the alternative to the classical techniques for porosity measurement, micro computed tomography (μCT) provides the necessary spatial and density resolution to analyze the sizes and morphologies of the open and closed pores [5].

The ceramic scaffolds were fabricated out of hydroxyapatite granulate using an experimental 3D printer [1] with a spatial resolution of about 100 dpi and a slice thickness of 200 μm. Subsequently, they were sintered to enhance their mechanical stability. Conventional μCT was performed using the Skyscan 1072 instrument at the maximal photon energy of 80 keV with a voxel size of 8 μm. Reconstruction was carried out with the software ConeRec using the Feldkamp algorithm. Synchrotron-radiation-based μCT (SRμCT) was performed at the photon energy of 24 keV with a voxel size of 4.1 μm. The 3D data sets are obtained by the standard back-projection reconstruction algoritm. The samples were scanned at two different heights because of the limited beam size. The two tomograms are subsequently merged.

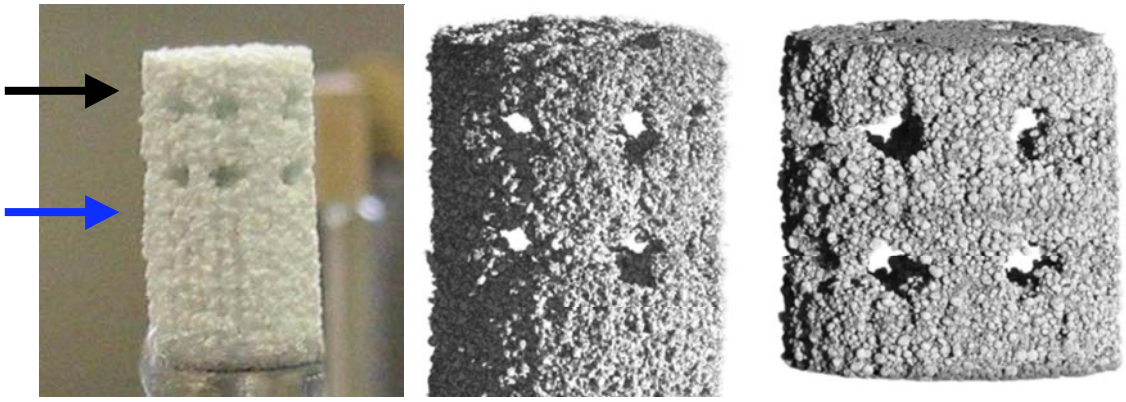


Figure 1: The 3D printed scaffolds for the structural analysis have a diameter of 3 mm and a height of 6 mm. To promote vascularization, relatively large channels with a diameter of about 0.5 mm were printed inside the structures. The images show the outer shape and are the photograph (left), the conventional μCT (center), and the synchrotron-radiation-based μCT (right).

In a first step, the results of the μCT-scans were qualitatively compared to polymer embedded and polished microsections of the samples, which are visualized by electron microscopy (REM). Figure 2 shows such a REM image, where artifacts (see black arrows in figure 2 D) of the polishing process appeared on the surface. The quantitative interpretation becomes therefore difficult. Nevertheless, the contrast of the REM images is sufficient for binarisation and subsequent porosity calculation.

As demonstrated in figure 1 conventional μCT is well suited for imaging purposes and qualitative image interpretation. Defects in the macrostructure as the result of printing or sintering can easily be uncovered. The quantitative analysis of the 3D data, however, is impossible due to the insufficient contrast and the beam hardening effects. The enhanced spatial resolution, the better contrast, and the monochromatic beam used for the SRμCT allows the automatic segmentation and binarisation of the scaffold and makes the quantitative pore analysis possible, e.g. calculating the 3D distance map [4,5]. Figure 2A and 2B show typical slices of the SRμCT data set. For comparison, a selected part of one reconstructed slice obtained with conventional μCT is represented on the same scale than figure 2B.

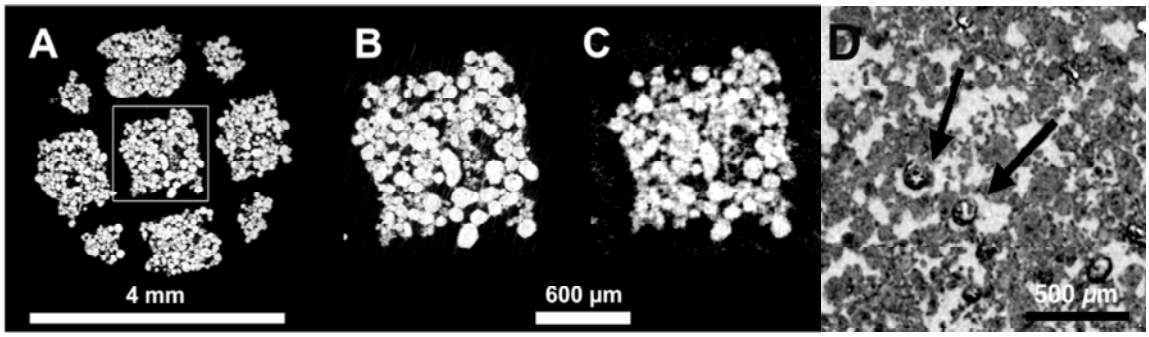


Figure 2: (A) selected SRμCT-slice, (B) central part of the SRμCT-slice, (C) slice of the same part measured with conventional μCT, (D) micrograph (REM image) of conventionally prepared sample for pore analysis. The arrows mark artifacts caused by polishing the scaffold after embedding.

The more detailed analysis of the SRμCT data offers the determination of the average porosity of the granules on the nanometer scale, the precise determination of the granules shape, the pore sizes and shapes as well as their interconnectivity on the micrometer scale, and the measurement of the generated scaffold on the millimeter scale. This is an important input for modeling vascularization and cell seeding and, therefore, for the patient specific optimization of scaffolds for bone augmentation.

References

[1] H. Seitz, W. Rieder, S. Irsen, B. Leukers, C. Tille, J. Biomed. Mater. Res. B 74, 782-788 (2005)
[2] O. Gaulthier, J.M. Boouler, E. Aguado, P. Pilet, G. Daculsi, Biomater. 19, 133-139 (1998)
[3] B. Bruckschen, H. Seitz, T.M. Buzug, C. Tille, B. Leukers, S. Irsen, Biomedizinische Technik 50 Suppl. 1/2, 1609-10 (2005)
[4] F.A. Maspero, K. Ruffieux, B. Müller, E. Wintermantel, J. Biomed. Mater. Res. 62, 89-98 (2002)
[5] B. Müller, F. Beckmann, M. Huser, F. Maspero, G. Székely, K. Ruffieux, P. Thurner, E. Wintermantel, Biomol. Engin. 19, 73-78 (2002)

Crystallographic texture of an Al90-Cu10 cold extruded composite

H.-G. Brokmeier[1,2],S.-J. Jin[1,2],S. Lenser[1,2], B. Schwebke[1,2], U. Garbe[2] and T. Lippmann[2]

[1] Institut für Werkstoffkunde und Werkstofftechnik, der Technischen Universität Clausthal, Germany.
[2]GKSS-Forschungszentrum, Max-Planck-Straße 1, 21502 Geesthacht, Germany.

An Al90-Cu10 composite was produced by powder metallurgy. Therefore, pure Al and Cu powder was mixed in the ratio 9:1 and homogenized. In a second step a pre-compacted 'green form' was pressed to a cylinder of 50mm diameter having a density of about 80%. Cold extrusion was processed after reducing the oxygen content to a deformation degree of 96% to. In extrusion direction one obtains long elongated individual Al and Cu grains and the microstructure of the cross section shows typical nearly round particles. As shown by Böcker the inner deformation degree of the individual Al and Cu fibers depend on the specific deformation behavior of each material (Al and Cu). The crystallographic texture depends on the influence of the harder Cu on Al. In laboratory X-ray texture measurement the anisotropic absorption in the direction parallel to the main orientation of the fibers and perpendicular to the fiber orientation, leads to insufficient results in the texture sharpness. A second problem occurs in texture measurement of minority phases. Both should be of minor influence by using hard X-rays.

The measurement has been performed at the new GKSS Materials Science Beamline HARWI II within the framework of first texture test experiments. Figure 1a shows an image plate picture. One can see clearly the strong texture of the materials. Furthermore, the sum pattern integrated over the whole Debye-Scherrer cone (see figure 1b, shows the partial overlapping between Cu (111) and Al (200).

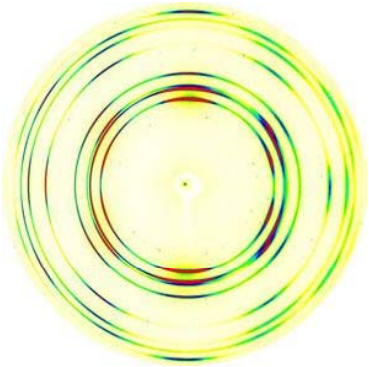


Fig. 1a: Image plate picture of an Al-Cu composite taken in 30 sec.

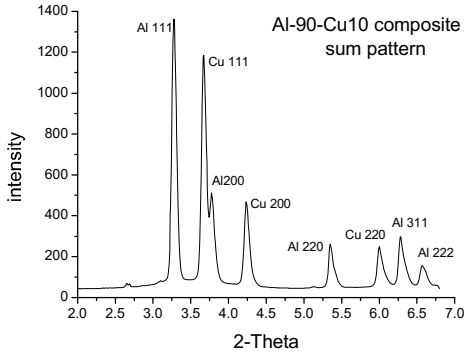
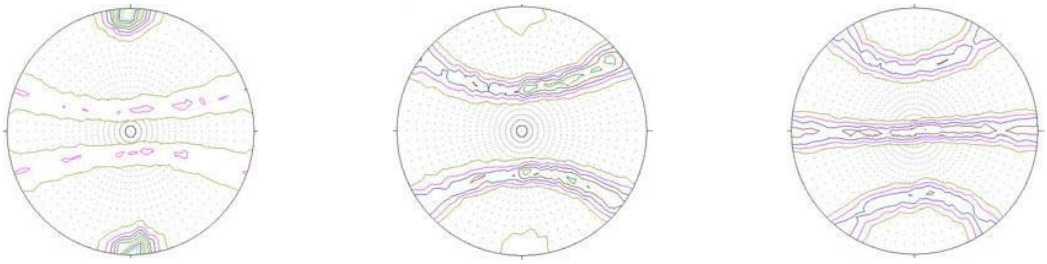


Fig. 1b: Sum patter of the Debye-Scherrer cones of Figure 1a

The texture measurement was carried out in steps of 5° in ω rotation from 0° to 90°. Integral intensities along γ were calculated to obtain a set of three pole figures for both components. Background correction and normalization to a constant photon flux for the set of individual image plate measurements were included in the data processing. Thereafter, a quantitative texture calculation using the iterative series expansion method (ISEM) was done with a series expansion degree up to L_{max}=22. Figure's 2 and 3 show the measured pole figures for Al (111), Al (200), Al (220), Cu (111), Cu (200) and Cu (220). Both metals have a strong texture.

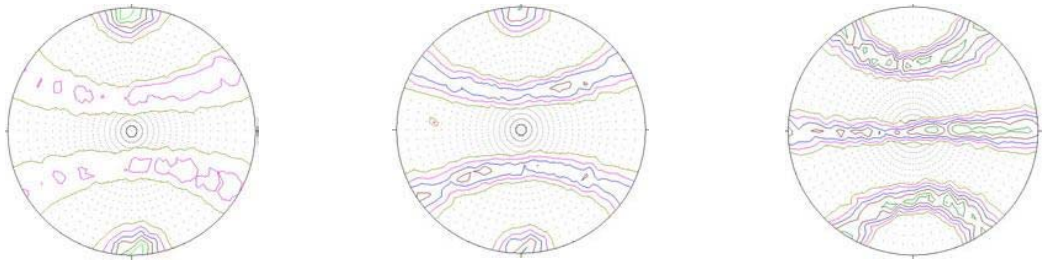
a) Al (111) pole figure b) Al (200) pole figure c) Al (220) pole figure



Pmax= 10.6 mrd Pmax = 3.4 mrd Pmax = 3.0 mrd

Figure 2: Measured Al pole figures of an Al90-Cu10 cold extruded composite

a) Cu (111) pole figure b) Cu (200) pole figure c) Cu (220) pole figure



Pmax= 3.7 mrd Pmax = 2.0 mrd Pmax = 2.3 mrd

Figure 3: Measured Cu pole figures of an Al90-Cu10 cold extruded composite

a) Al in extrusion direction b) Cu in extrusion direction

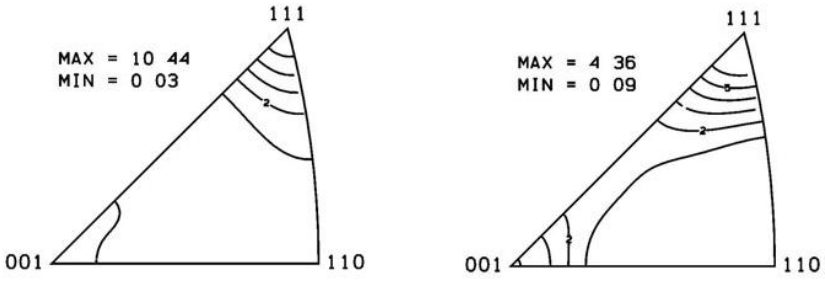


Figure 4: Inverse pole figures for Al and Cu in extrusion direction

In both components a <111> <100> double fiber is developed during cold extrusion (see figure 4). Due to differences in the stacking fault energy the <111>/<100> ratio is different between Al and Cu. The Al-texture is much stronger than the Cu texture. On one hand Cu is much harder than Al and has to deform less and on the other hand Cu is the minority phase completely imbedded in the Al-matrix. A higher Cu content will change the ratio of the texture sharpness Cu <111> to Al <111>. Further investigations are planned on Al-Cu composites with lower Cu contents, first to improve the evaluation method for texture studies in minority phases and second to investigate the influence of very small amounts of Cu on the texture development of Al.

References

[1] W. Böcker: PhD Thesis Technische Universität Clausthal 1992.

Direct corrosion measurement of Mg-alloys by SRμCT

J. Fischer[1], T. Donath[2], F. Beckmann[2], and F. Witte[1]

[1]Department of Orthopaedic Surgery, Hannover Medical School, Anna-von-Borries-Str.1-7, 30625 Hannover, Germany

[2]GKSS-Research Center, Max-Planck-Str.1, 21502, Geesthacht, Germany

The corrosion analysis of materials is an important field in materials science. There exist various classical methods such as immersion or electrochemical tests to determine the corrosion properties of materials. More sophisticated methods are needed for the analysis of local corrosion, especially if shape, depth and volume of a local corrosion site should be determined. Furthermore, the original sample is normally destroyed if the total sample has to be examined.

To evaluate non-destructively the local corrosion and to distinguish between different local corrosion forms a 3D imaging method showing high density resolution and high spatial resolution is needed. A suitable device is synchrotron-radiation based microtomography [1].

To observe corrosion processes in-situ the tomographic set-up at beamline BW2 was modified to allow for a continuous sample rotation. Thus, attenuation images can be obtained from different angles of the continuously rotating main axis over several hours.

The modification of the set-up for tomography at BW2 is shown in Figure 1. The external motor control system was replaced by a new CANBUS motor electronics [2] mounted on the rotation platform. The power supply is based on sliding contacts and the signals are transferred via a Bluetooth connection [3], thus enabling continues rotation.

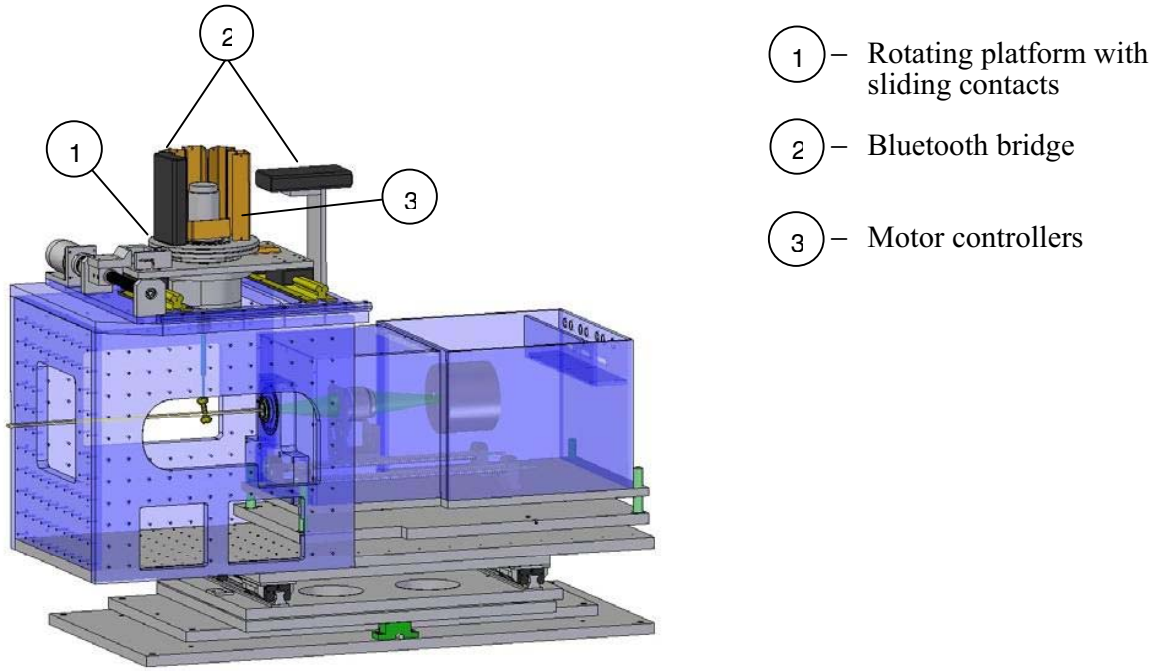


Figure 1: Sketch of modified tomographic set-up for continuous measurements.

To perform in-situ corrosion measurements a liquid cell was built out of a radiation resistant plastic (PEEK). For the corrosive sample environment during the tomographic measurements ocean water with a constantly monitored pH (according to ASTM standard) was used. The corrosive solution in the liquid cell was constantly exchanged by a peristaltic pump from a temperature monitored reservoir of two litres.

As a sample for in-situ corrosion measurements a cylindrical Mg-Apatite sample was immersed in the liquid cell and attenuation images were acquired during a period of 27 hours. Every 30 minutes a new tomographical scan was taken.

To speed up the data transfer from the CCD the tomographical scan was set to double binning of the image data. Furthermore, the normally used step-size of 0.25° rotation angle was increased to 0.5°. Thus, the overall time for a tomographical scan decreased from 2 hours to 30 minutes.

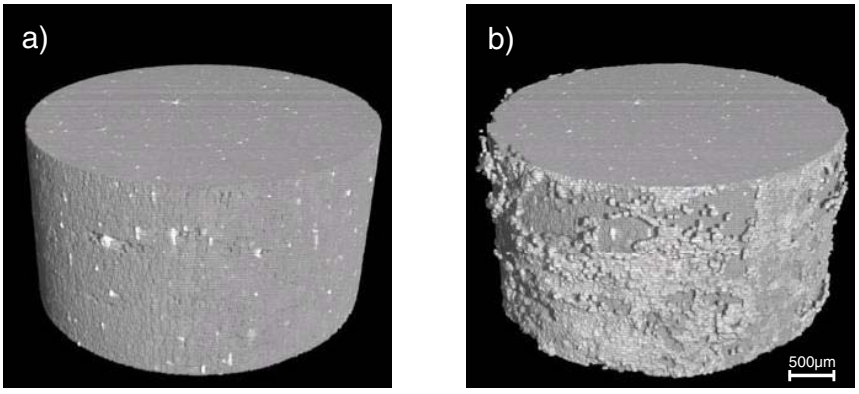


Figure 2: (a) Three-dimensional reconstruction of Mg-Apatite before corrosion.
(b) Three-dimensional reconstruction of the same sample after 27 hours. The pitting-corrosion is clearly visible.

With this method of investigation the local corrosion processes can be studied time-resolved and non-destructively in three dimensions. The corrosion parameters of many corrosive materials can be determined in this way.

References

[1] F. Witte, J. Fischer, J. Nellesen, H A. Crostack, V. Kaese, A. Pisch, F. Beckmann, H. Windhagen, Biomaterials (in press)
[2] CAN-STEPCON-1H, ESD Electronics, Hannover, www.esd-electronics.com
[3] CAN-BLUETOOTH, ESD Electronics, Hannover, www.esd-electronics.com

High Energy µCT at HARWI-II and SEM of a Cobalt / Diamond Composite

H.-A. Crostack, J. Nellesen, G. Fischer, F. Beckmann[1], T. Donath[1] and J. Fischer[1]

Lehrstuhl für Qualitätswesen, Fakultät Maschinenbau, Universität Dortmund, D-44221 Dortmund, Germany
[1] GKSS Research Center, Max-Planck-Str. 1, D-21502 Geesthacht, Germany

1 Introduction

By the combination of materials possessing different mechanical properties composites can be manufactured which are tailored with respect to macroscopical mechanical behaviour. For the prediction of the material behaviour and for the optimization of the composite micro deformation and micro damaging (like initiation and growth of micro defects) have to be understood. These micro processes take place in composites *under* load and precede a *macroscopical fracture*.

2 Materials and Methods

By water jet cutting plain dog bone shaped tensile specimens of Cobalt / Diamond were produced. This kind of composite is well-known in cutting edges for rotating tools. In order to deduce understanding about the mentioned micro processes *a* 2D analysis of the specimen's surface with SEM and a 3D analysis of real microstructure based on X-ray tomographic microscopy (XTM) at different stages of deformation with high spatial resolution were performed. At the new beamline HARWI-II CT measurements were carried out using monochromatic photons of 82 keV. The projection data set contains radioscopic images consisting of 1536x1024 pixels acquired at 720 rotation angles in the half-circle. The microstructure of the tensile specimens were imaged by tomography with a magnification $m \approx 2.4$ at different stages of deformation.

3 Results

By SR-based tomography the microstructure of a Co/Diamond composite was uncovered as depicted in fig. 1. The shape of diamonds in the bulk of the specimen can easily be recognized. A third phase was found by tomography which was afterwards identified as WC-inclusions by EDX-analysis. The specimen was deformed step-by-step and at each step a tomogram was created. The analysis of these tomograms by 3D data processing is currently in progress.

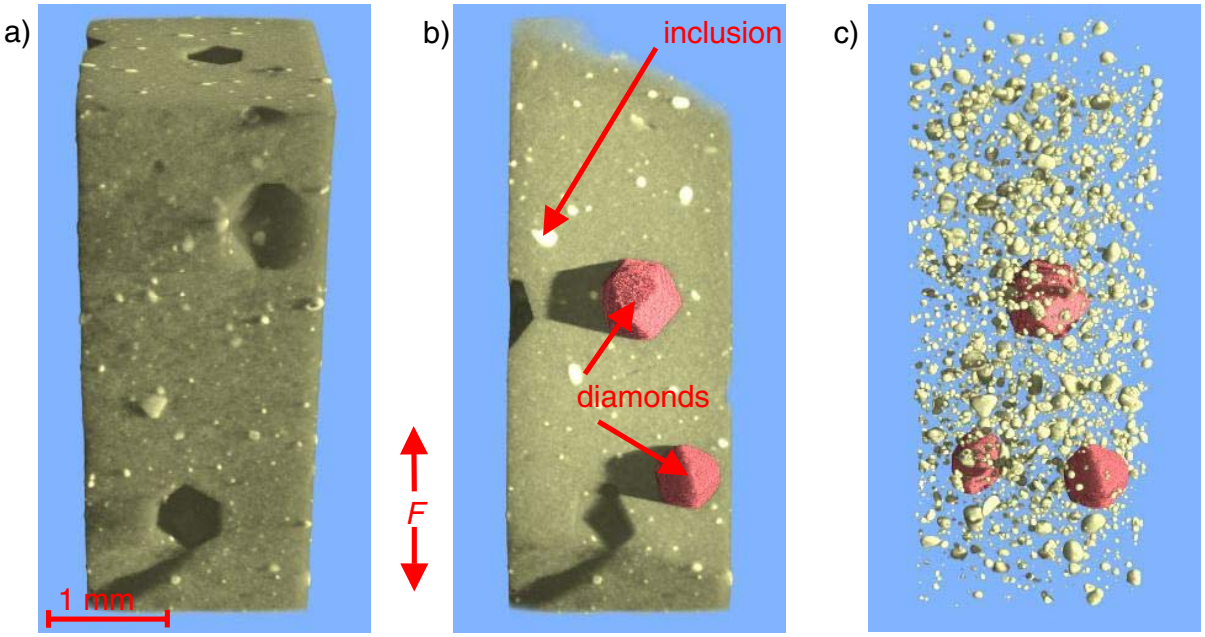


fig. 1: (a) 3D-representation of the tomogram in the undeformed stage (specimen gauge length), (b) 3D-representation of the virtually cut specimen after segmentation, diamonds cast shadows onto the cutting plane, (c) transparent representation of the Co-matrix, 3 diamond particles and tungsten carbide inclusions are visible

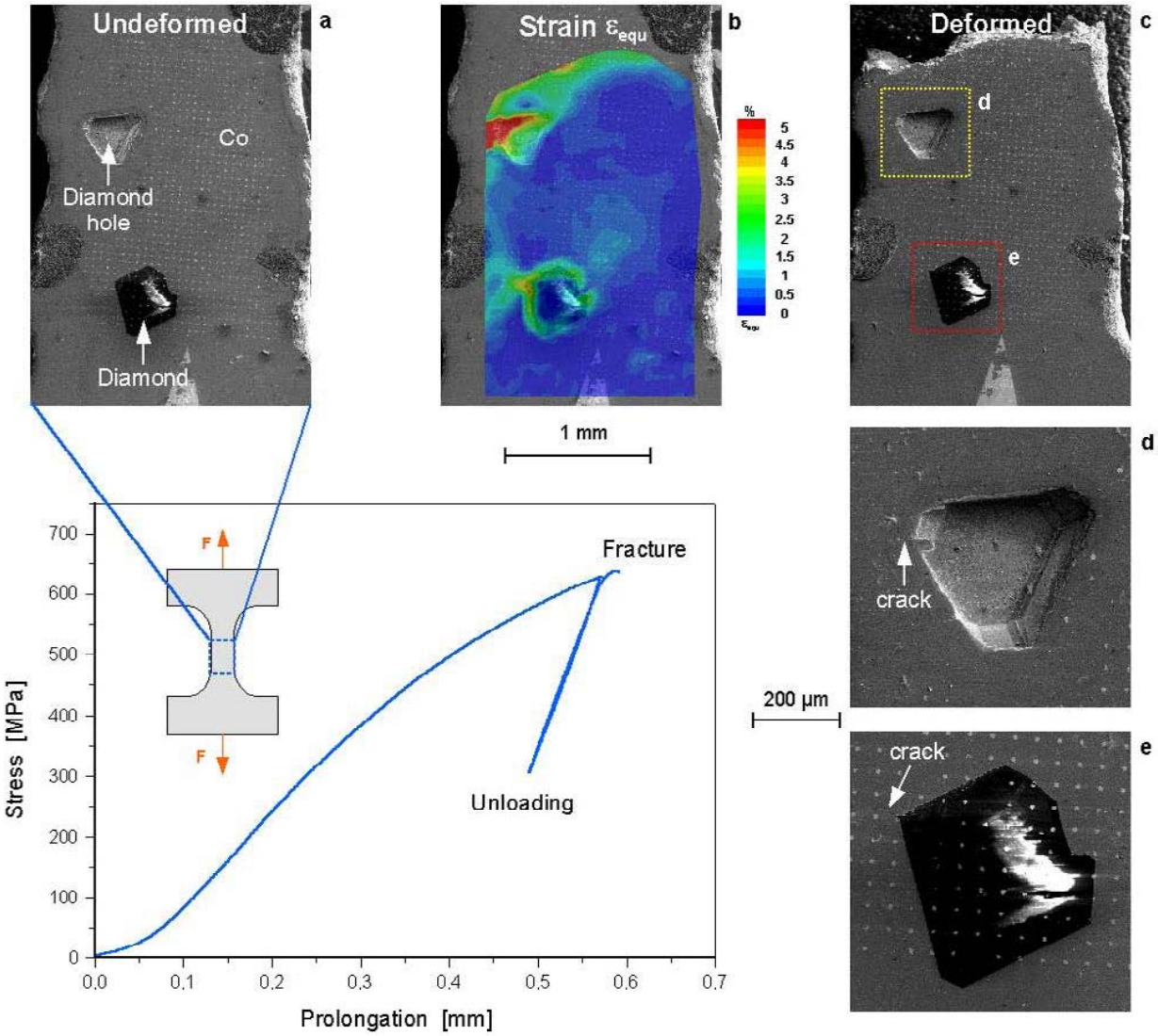


fig. 2: stress-prolongation curve and distribution of equivalent strain ε_{equ} at the specimen's surface after fracture (b) obtained by matching the SEM-images (a) and (c); relationship between high strain and cracking, see macro crack (c) and microcracks in the pictures (d) and (e)

With SEM the specimen's surface was recorded in the undeformed stage and after fracture. The surface reveals both diamonds and holes where diamonds sat (cp. fig. 2a, d, e). After fracture micro cracks orginating from diamonds resp. holes could be found (cp. fig. 2d, e). Before the tensile test the surface was artificially structured by an applied Gold dot grid as can be seen in fig. 2a and 2e to get additional gray level gradients in SEM-images. On the basis of the gray level edges an iterative matching of sub-images of different stages of deformation was carried out (image correlation). From the local transformation matrices describing this local mapping the field of equivalent strain was calculated. The field was overlaid semi-transparently on the SEM-image in fig. 2b. Strain concentrations emerge in areas of microcracks which are initiated in the neighbourhood of diamonds and holes. The results of 3D data processing on the tomographic data sets will be further fed into realistic FE-simulations (cf. [1]).

4 Acknowledgement

The financial support of this work in the scope of the research projects Cr4/111-1 is gratefully acknowledged.

5 Reference

[1] CROSTACK, H.-A.; NELLESEN, J.; BLUM, H.; RAUSCHER, T.; BECKMANN, F.; FISCHER, G.: *Analysis of the material behaviour of metal-matrix composites under tension by synchrotron radiation based microtomography and FE-calculations*, in *Developments in X-ray Tomography IV*, edited by Ulrich Bonse, Proceedings of SPIE Vol. 5535 (SPIE, Bellingham, WA, 2004), 493-504

Investigation of material flow in friction stir welds using high energy synchrotron radiation at HARWI II

T. Donath, R. Zettler, F. Beckmann, J. Fischer[1], J.F. dos Santos, D. Lohwasser[2], and A. Schreyer

GKSS-Research Centre, Max-Planck-Str. 1, 21502 Geesthacht, Germany

[1] Hannover Medical School, Anna-von-Borries-Str.1-7, 30625 Hannover, Germany

[2] Airbus Deutschland GmbH, Germany

The friction stir welding (FSW) process invented and patented by The Welding Institute of Cambridge [1] essentially relies on frictional heating and plastic deformation brought about by a rotating and non-consumable tool that is plunged into and then traversed along the join line of two abutting workpieces. In FSW the joining occurs at temperatures below that of the melting point of the materials being joined. This has demonstrated many advantages. Among these are the production of high quality joints with little preparation of the joint surfaces or post-weld dressing, relatively fast production i.e. joining speeds, high fatigue strengths, the ability to joins dissimilar alloys and the fact that distortion is relatively low when compared to conventional fusion welding processes.

To date there is no model capable of predicting the influence FSW tool geometry and welding parameters have on the formation of the joint and subsequent mechanical properties. Hence there is still a significant amount of work to do, in order to characterize and understand the process of joining and bonding. X-ray computed microtomography (μCT) was initially applied for the investigation of material flow for the FSW of an AA2024 alloy. In addition to the classical probes: macrographs, micro-hardness, strain and stress measurements, μCT delivers volume information of the 3-dimensional structure of the weld. Contrast is obtained by a marker material, which is implanted into the workpieces before welding. The welding process is then rapidly interrupted using a stop action technique which embeds the tool in the marker region of the workpieces whereby the redistribution of the marker around and behind the tool is studied.

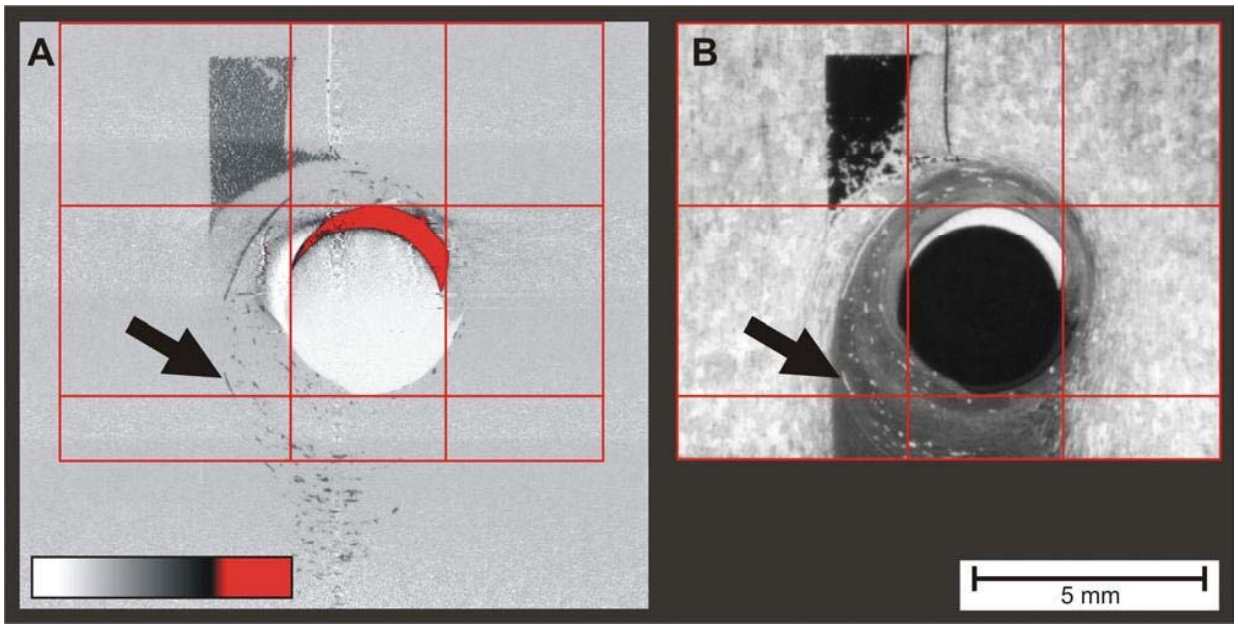


Figure 1: Tomographic cross section (A) and macrograph (B) of the same plane of a FSW sample. The Ti-marker shows up dark in the tomographic cross section and white in the macrograph. A small remainder of the pin is visible in both images. The arrow points towards the same streak of marker in both images.

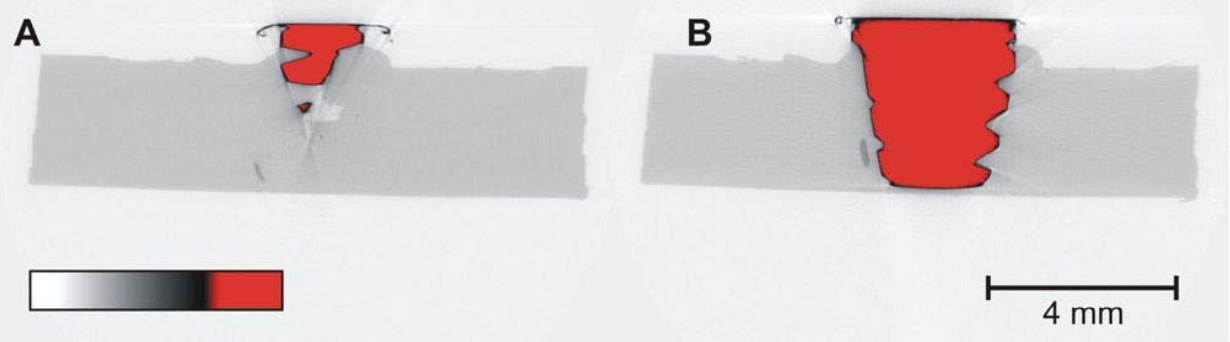


Figure 2: Tomographic cross sections (A, B) of the first friction stir weld measured at HARWI II. Using high energy X-rays of ~80 keV reconstruction of the FSW sample is possible without prior pin removal.

Investigations into marker flow commenced in 2003 on 4 mm thick cold rolled 2024-T351 aluminum sheets friction stir welded at the GKSS-Research Center, Geesthacht. Welds produced by different welding tools and varying welding parameters were studied at beamline W2 at 60 keV photon energy [2,3]. Figure 1 shows a µCT cross section in comparison with a macrograph of approximately the same plane of a weld. The shank of the pin was cut after welding and the threaded portion of the pin remaining in the workpieces carefully removed from the sample by means of spark erosion. This was necessary to avoid reconstruction artifacts caused by the strongly absorbing pin.

The project has now been continued at the refurnished beamline W2 (HARWI II). Data for a total of seven FSW samples has been recorded during the first measurement period after the beamline upgrade. Preliminary results are shown in Figure 2. High quality microtomographic reconstructions could be obtained, which allow for the segmentation of the Ti-marker. At the now available energy of above 80 keV removal of the pin from the weld is no longer necessary, as can be seen from Figure 2. This not only simplifies sample preparation, but also avoids reconstruction artifacts caused by incomplete pin removal.

We would like to thank B. Reime for assistance at the "old" HARWI beamline.

References

[1] W.M. Thomas, E.D. Nicholas, J.C. Needham, M.G. Church, P. Templesmith, C.J. Dawes: International Patent Application No. PCT/GB92/02203 and GB Patent Application No. 9125978.9, (1991).

[2] T. Donath, F. Beckmann, R. Zettler, J. dos Santos, D. Lohwasser, T. Lippman, Clemens H., and A. Schreyer: In AIP Conf. Proc. 705: SRI 03 San Francisco, 1312, (2004).

[3] R. Zettler, T. Donath, J.F. dos Santos, F. Beckmann, T. Lippmann, D. Lohwasser and A. Schreyer, Advanced Engineering Materials, accepted for publication 2005.

Investigation of Root Flaws in Friction Stir Welds

T. Vugrin, F. Beckmann[1], T. Donath[1], J. Fischer[2], A. Schreyer[1]

German Aerospace Center, Institute of Materials Research, D-51147 Cologne, Germany
[1]GKSS, Max-Planck-Str. 1, D-21502 Geesthacht, Germany
[1]Hannover Medical School , Anna-von-Borries-Strasse 1-7, D-30625 Hannover, Germany

Introduction

Friction Stir Welding (FSW) is a solid state welding process especially suitable for light weight metals. It was invented by The Welding Institute in 1991 [1]. The present investigation is focused on a possible welding flaw termed *root flaw*. The occurrence of a *root flaw* is associated with the oxide surface layer, which is always present on aluminium, and is stirred into the weld during the welding process [2, 3]. In the case of a *root flaw*, the material at the joint has undergone a thermomechanical process caused by the welding tool motion, but the material is only partially joined in the root region of the weld. It is necessary to investigate the probability of cracks initiating at the *root flaw* while a welded component is loaded mechanically. Therefore, it is necessary to characterize the three-dimensional structure of the *root flaw* throughout the weld, which is associated with the welding parameters. Since the *root flaw* is a very small feature, with dimensions of only a few hundred microns, microtomography is most suitable for the investigation of it's three-dimensional structure throughout the weld.

Experimental procedure

Three aluminium friction stir weld samples were prepared. In all three, a *root flaw* was created intentionally by a preoxidation treatment. The preoxidation treatment was applied to the edges of the aluminium plates before welding. In this way, natural aluminium surface layers of different thicknesses were formed. During the welding process, the surface layers were stirred into the welds, causing *root flaws*. One *root flaw* was very pronounced in the sample with a thick surface layer. The *root flaws* were less pronounced on the remaining two samples, because the surface layers were thinner. 1 x 1 x 20 mm^3 microtomography samples were prepared containing the *root flaw* region of the welds. The microtomography measurements were carried out at beamline BW2 using monochromatic photons of 24 keV. Projection data of 1536 x 1024 pixels with a size of 1.5 µm enabling a spatial resolution of 4.1 µm. Of each sample, a length of about 3 mm was investigated by performing 2 tomographic scans at different sample height. Each scan consisted of 720 projection equally stepped between 0 and π.

Results

Of the three investigated *root flaws*, only the most pronounced one could be imaged. The structures of the two less pronounced *root flaws* were below the spatial resolution of the current setup. Figures 1 and 2 show slices of the *root flaw*. The slice in Figure 1 is taken from a plane that corresponds to a cross section of the weld. The slice in Figure 2 lies in a plane parallel to the axis of the weld. The dark lines in the images represent the course of the *root flaw* throughout the weld. A sufficient number of slices was obtained to reconstruct the three-dimensional extension of the *root flaw* along the weld. Work is ongoing to extract a three-dimensional surface representation of the *root flaw* from the volume data.

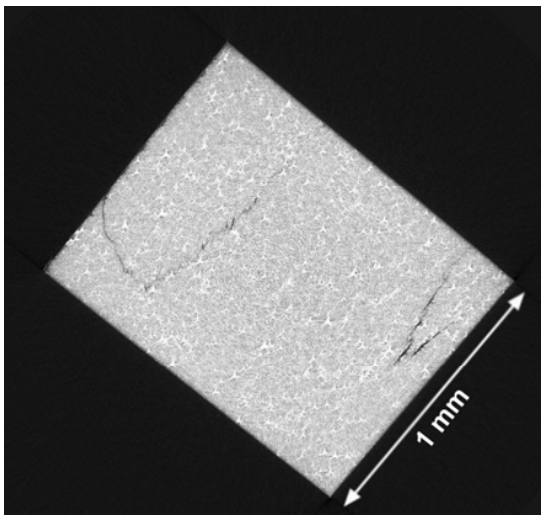


Figure 1: Cross section of the root flaw in a plane perpendicular to the welding direction.

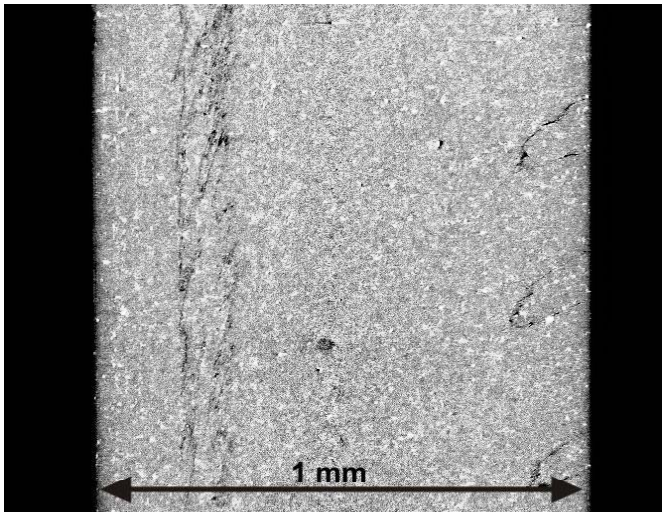


Figure 2: Cross section of the root flaw in a plane parallel to the welding direction.

References

[1] W. M. Thomas, E. D. Nicholas, J. C. Needham, M. G. Murch, P. Temple-Smith, C. J. Dawes, "Friction stir butt welding", International patent application No. PCT/GB92/02203 and GB patent application No. 9125978.8

[2] T. Vugrin, M. Schmücker, G. Staniek, Friction Stir Welding and Processing III, 277, proceedings of TMS Annual Meeting, San Francisco, California, Feb. 13-17, 2005

[3] Y. S. Sato, F. Yamashita, Y. Sugiura, S. H. C. Park, H. Kokawa, Scripta Mat., 50, 365 (2004)

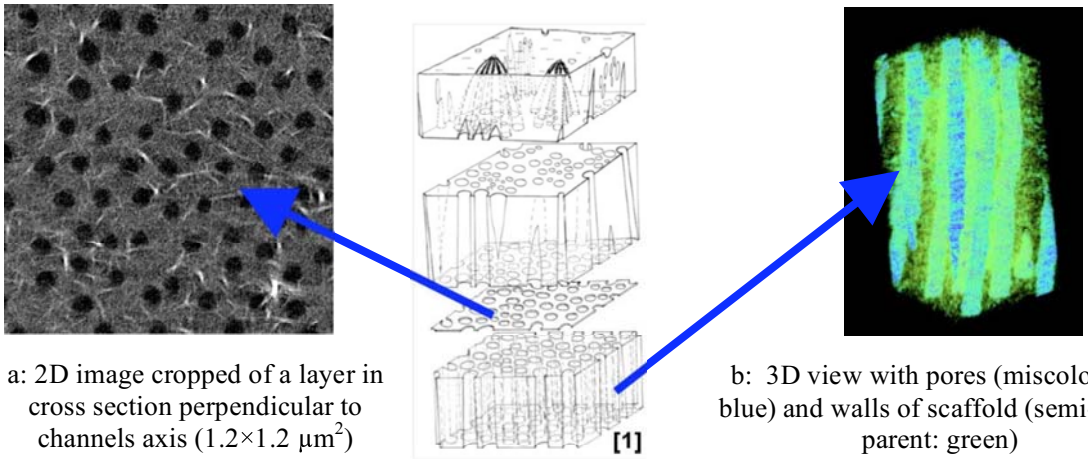
Investigations of alginate/calcium phosphate scaffolds with oriented tube-like pores by Microcomputed tomography

F. Despang, R. Bernhardt, E. Mund, R. Dittrich[1], F. Beckmann[2], G. Tomandl[1], W. Pompe, M. Gelinsky

TU Dresden, Institut für Werkstoffwissenschaft, Max Bergmann Center of Biomaterials, Budapester Str. 27, D-01069 Dresden, Germany
[1]TU Bergakademie Freiberg, Institut für keramische. Werkstoffe, Gustav-Zeuner-Str.3, D-09596 Freiberg, Germany
[2]GKSS-Research Center, Geesthacht, Germany

1 Introduction

Porous and mineralised scaffolds are required for various applications in hard tissue engineering. Scaffolds with oriented tube-like pores facilitate homogenous cell seeding, a sufficient nutrient supply during cell culture (even in big constructs) and a fast vascularisation after implantation. The phenomenon of ionotropic gelation has been known since more than 30 years which describes that alginate forms gels with capillary-like pores when covered with solutions of di- or trivalent cations [1]. This technique (Fig. 1) has now been used to develop scaffolds with tube-like and regular pores from alginate/calcium phosphate composites and to stabilise them by mineralisation with hydroxyapatite (HA) precipitated out of solution and additions of HA powder.



a: 2D image cropped of a layer in cross section perpendicular to channels axis (1.2×1.2 µm^2)

b: 3D view with pores (miscoloured: blue) and walls of scaffold (semi-trans-parent: green)

Figure 1: Principle of ionotropic gelation (center) and examples of an alginate scaffold of Manugel with 0.4 wt.% HA powder added and nano-HA precipitated out of solution (µ-CT)

2 Materials & Methods

Two types of alginate (ISP Alginates Ltd. Waterfield, Tadworth, U.K.) were investigated to form scaffolds. Manugel® DMB (MG) and Manucol® DM (MC) contain different ratios of β-D-mannuronic acid (M) to α-L-guluronic acid (G) that will give different stiffness of the calcium alginate gels. HA powder (Merck, Darmstadt, Germany, d_{50}= 4.3 μm) was dispersed in different amounts (0.2, 0.4 and 0.8 wt.% HA powder) in 98 ml di-sodium phosphate solution (Na_2HPO_4) that has been adjusted to pH 9. Afterwards 0.5 g of gelatine followed by 2 g alginate were dissolved in this sol. The gelation process was carried out using calcium chloride solution (1 M) as gelling agent. During gelation nano-crystalline HA precipitated which creates the walls of the scaffolds together with the micro-crystalline HA powder and the alginate fibers [2]. Afterwards the polymer became chemically cross-linked and freeze dried.

3 Aim of investigations by Microcomputed Tomography (μ-CT)

Variation of the M/G-ratio by choosing different alginates and adding various amounts of HA powder changed the mean diameter and length of the pores which could be proofed by sections drawn of many samples investigated in optical microscopy in wet state. 3D-μ-CT-images will reveal all information of an individual scaffold. Furthermore, the state of green body will be observed which will clarify the parameters of the crucial process of freeze drying. Interpretation of the images should be possible since the air-filled cavities will be compared to the walls being a composite of alginate (1 g·cm^{-3}) and HA (3.2 g·cm^{-3}). For each

sample 720 projections were obtained with a photon energy of 11 keV using the Beamline BW2 at HASYLAB.

4 Results & Discussion

Stacks of 790 images were taken with a resolution of 3,6 μm·vx^{-1} thus a height of 3160 μm was scanned. Lateral picture size was 1536×1536 vx corresponding to 6144×6144 μm^2. Freeze drying with exchange of solvent is indispensable. Freezing should be carried out with smaller gradient since still some cracks could be found. If the alginate scaffolds were loaded with small amounts of HA powder the wall seemed to flatten (Fig. 2d). Thus a minimal percentage of 0.4 wt.% should be applied to increase mechanical stability. The porosity as well as the mean diameter of the two comparable alginate scaffolds with 0.4 wt.% HA powder indicate that the alginate Manucol always exhibits double values (P: 30%, Ø: 125...138 μm) compared to the alginate Manugel (P: 14%, Ø= 58...97 μm) differing in the chemical nature of the polymers first of all in M/G-ratio (Manucol: 65/35, Manugel: 35/65). The focus of work will now concentrate on analysing the run of individual pores through the scaffold and their change in size over large distances (z) being tremendously important concerning ingrowth of human cells into the channel-like pores.

5 Acknowledgments

The authors are grateful to the DFG (project number PO 392/26-1) for the financial support and to HASYLAB for the financial and technical support of the SRμCT-measurements.

6 Literature

[1] H. Thiele, Histolyse und Histogenese: Gewebe und ionotrope Gele – Prinzip einer Strukturbildung, Akadem. Verlagsgesellschaft, Frankfurt a.M. (1967)

[2] F. Despang, A. Börner, R. Dittrich, G.Tomandl, W. Pompe, M. Gelinsky, Mat.-wiss. Werkstofftech. 36 (2005) (in press: DOI: 10.1002/mawe.200500961)

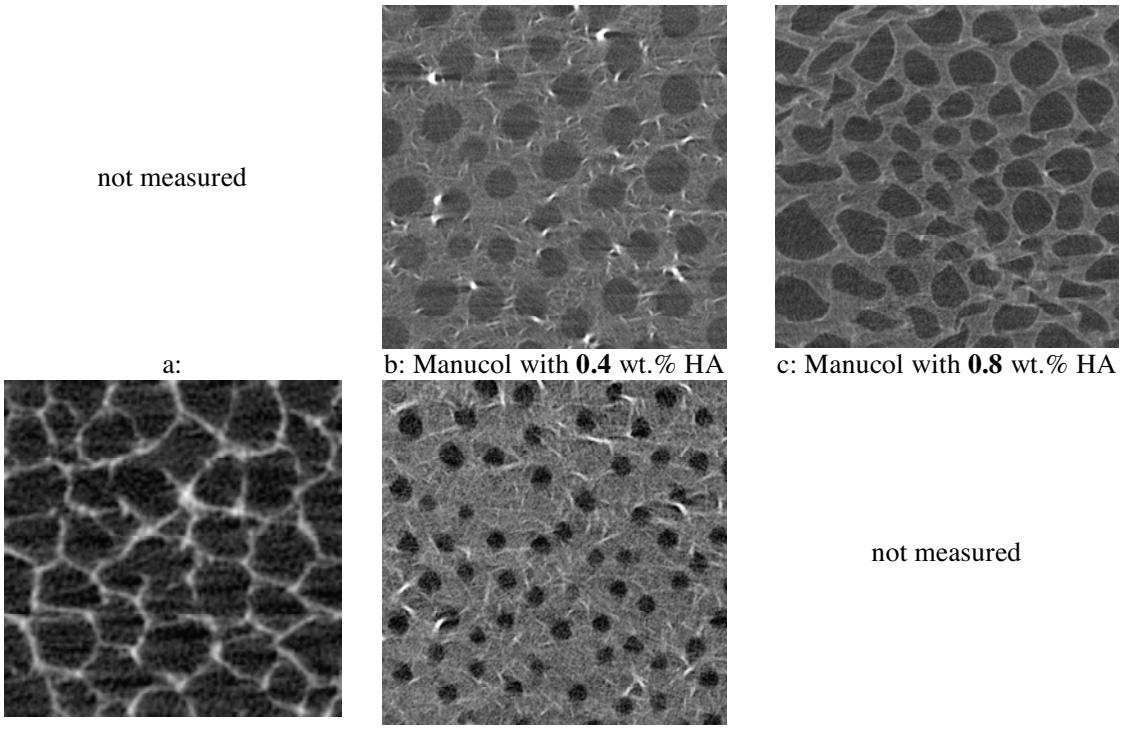


Figure 2: Cropped sections of freeze dried scaffolds (600×600 μm^2) used for analysing 200 to 600 layers depending on preparation, freezing regime or surface topography

In-vivo corrosion rates of magnesium alloys determined by synchrotron-radiation based microtomography (SRμCT)

F. Witte, J. Fischer, J. Nellesen[2], H-A. Crostack[2], T. Donath[3], and F. Beckmann[3]

Department of Orthopaedic Surgery, Hannover Medical School, Anna-von-Borries-Str.1-7, 30625 Hannover, Germany

[2]Chair of Quality Management, University of Dortmund, Joseph-von-Fraunhofer-Str. 20, 44227 Dortmund, Germany

[3]GKSS-Research Center, Max-Planck-Str.1, 21502, Geesthacht, Germany

The in-vivo corrosion of magnesium alloys can be used as a new mechanism allowing *degradable* metal-implants to be applied in muscoloskeletal surgery [1]. This would particularly be true if magnesium alloys with a predictable corrosion rate could be developed. Therefore, the in-vivo corrosion rate has to be investigated. In this approach we used absorption-contrast microtomography (μCT) to determine corrosion rates calculated from implant volume reduction during the implantation period (Figure 1). By using monochromatic synchrotron radiation a spatial resolution of a few micrometers and a high density resolution can be achieved.

Synchrotron-radiation based microtomography (SRμCT) is an excellent non-destructive method for displaying specimens with a high spatial resolution. Synchrotron sources are ideal for this tomography, since they provide a monochromatic, parallel beam with high intensity. Absorption tomography produces 3-D images of the linear X-ray attenuation coefficient μ_l which contains information about the chemical composition of each voxel. Therefore, the corrosion products compared to the metallic bulk material can be displayed in different attenuation values and can therefore be distinguish form the bulk material at various photon energies (Figure 2).

Different magnesium alloys were implanted into the femura of guinea pigs. After 18 weeks the femura were explanted and fixated in buffered formalin. At beamline HARWI I (W2) the specimens were imaged by attenuation microtomography using photon energy of 31 keV. Exposed to the parallel X-ray beam, the sample was precisely rotated stepwise 0.25° in the angular range 0-180°. After each step the absorption image was recorde. The specimens were investigated in five different positions of the z-axis to obtain a high spatial resolution. Further these separately reconstructed data were finally stacked to form an entire data set. The voxel edge size of the data set was equal to 10 μm. The residual implant volume (Figure 3) was analysed using VDStudio Max 1.2® Software (Volume Graphics GmbH, Germany). After segmentation of the gray values followed by a 3D region growing method the remaining metallic magnesium alloy was separated from the surrounding bone matrix and the corrosion layer.

Thus, the remaining non-corroded sample volume as well as the sample surface was determined in three dimensions non-destructively on a micrometer scale. Assuming a homogeneous magnesium alloy, the reduction of the implant volume could be converted into a corrosion rate by using a modification of the ASTM standard equation for weight loss, where the weight loss (W) is substituted by the reduction in volume (ΔV) multiplied by the standard density (ρ) resulting in

$$CR = \frac{\Delta V}{A \cdot t} \qquad \text{(Eq. 1)}$$

,where CR is the corrosion rate (mm/year), ΔV is the reduction in volume that is equal to the remaining metal volume subtracted from the initial implant volume, A is the implant surface area exposed to corrosion and t is the exposure time in hours.

It has been shown that synchrotron-radiation based microtomography in attenuation mode can be used as a fully three-dimensional, non-destructive technique for non-destructive local corrosion measurements on a micrometer scale [2]. This new approach to local corrosion measurements has to be evaluated in more details and compared to other local corrosion techniques.

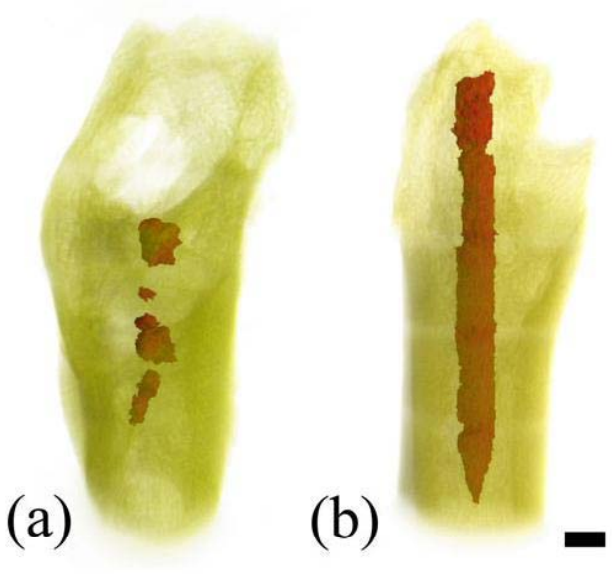


Figure 1: 3D reconstruction of remaining magnesium alloy (red) segmented from the bone matrix (brown) by region growing method [2]. (a) shows corroding magnesium alloy AZ91 after 18 weeks of implantation; (b) shows the magnesium alloy LAE442 after 18 weeks of implantation. Bar = 1.5 mm.

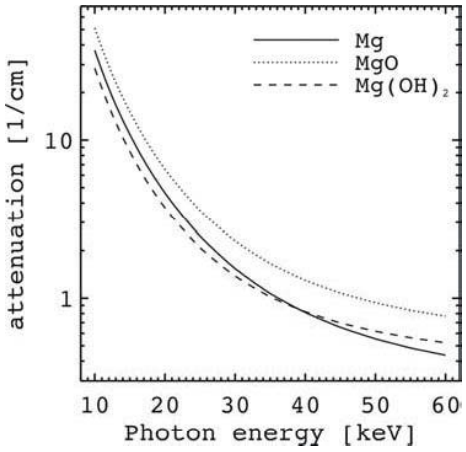


Figure 2: Attenuation of pure magnesium and its corrosion products.

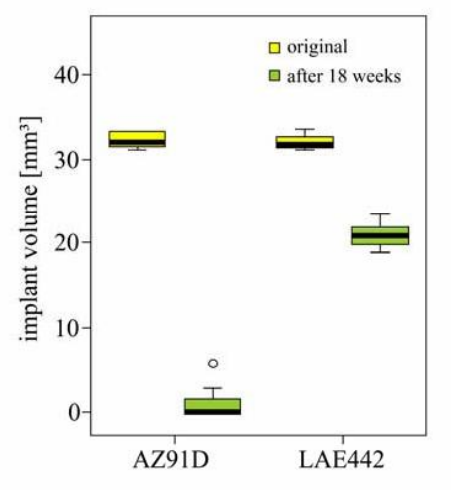


Figure 3: Reduction in implant volume after 6 and 18 weeks of implantation determined by SRμCT [2].

References

[1] F.Witte, V.Kaese, H.Haferkamp, A.Meyer-Lindenberg, E.Switzer, H.Windhagen, Biomaterials **26**, 3557 (2005)

[2] F.Witte, J.Fischer, J.Nellesen, HA.Crostack, V. Kaese, A.Pisch, F.Beckmann, H.Windhagen, Biomaterials (in press)

Measuring 3D Plastic Strain Fields Inside Metallic Materials

K. Haldrup, S. F. Nielsen[1], H.F. Poulsen, F. Beckmann[2] and J. A. Wert

Center for Fundamental Research: Metal Structures in Four Dimensions, Risø National Laboratory, Roskilde, Denmark.

[1]Risø National Laboratory, Materials Research Department, Roskilde, Denmark.

[2]GKSS-Research Center Geesthacht, 21502 Geesthacht, Germany

Finite Element Modeling (FEM) is the standard tool for predicting plastic strain fields in 3D in solid materials. The objective of the current work is to develop a complementary experimental method for mapping plastic strain fields in 3D within the bulk of plastically straining metallic components. The method is intended to be used i) in an engineering context for comparison with FEM results and, ii) in a scientific context for detecting the effects of internal microstructural features on the plastic deformation pattern in 3D. This report focuses on results primarily relevant to objective i).

The method used combines a synchrotron hard x-ray source with non-destructive micro-tomography measurements. The samples contain a distribution of markers with an x-ray absorption coefficient different from the matrix. The sample is deformed in steps, performing micro-tomography between each step; the marker motion is tracked during the course of several deformation steps. Quantitative analysis of marker motion provides a 3D map of the displacement gradient tensor, from which the 3D strain field is derived [1].

The work performed at HASYLAB has used aluminum samples with embedded W particles. The particle diameter is 5 – 10 μm and nearest neighbor particle spacing is about 20 μm. These characteristics provide a strain resolution approaching 0.01 true strain with a spatial resolution of 30 μm. The strain resolution is limited by the precision with which the center of mass of each particle can be determined; the spatial resolution is determined by the particle spacing. The sampled volume is slightly larger than 1 mm^3 and contains up to 200000 markers. Results obtained in 2005 demonstrate application of the method to strongly inhomogeneous plastic deformation fields. Three examples are described in the report.

A) Fig.1 shows the geometry of a rectangular compression sample with a circular hole, a map of the tracks of ca. 5000 particles during deformation, and maps showing the distribution of 3 displacement gradient components inside the sample. The results show that deformation in this sample is not homogeneous. An X-shaped pattern is evident already in the map of particle tracks; this pattern is quantified in the displacement gradient maps. A simple quantitative model of the X-shaped shear geometry reveals that it requires less work to be performed by the externally imposed stress than homogeneous deformation to the same macroscopic strain [2]. Work is now underway to develop an FEM model for this specimen.

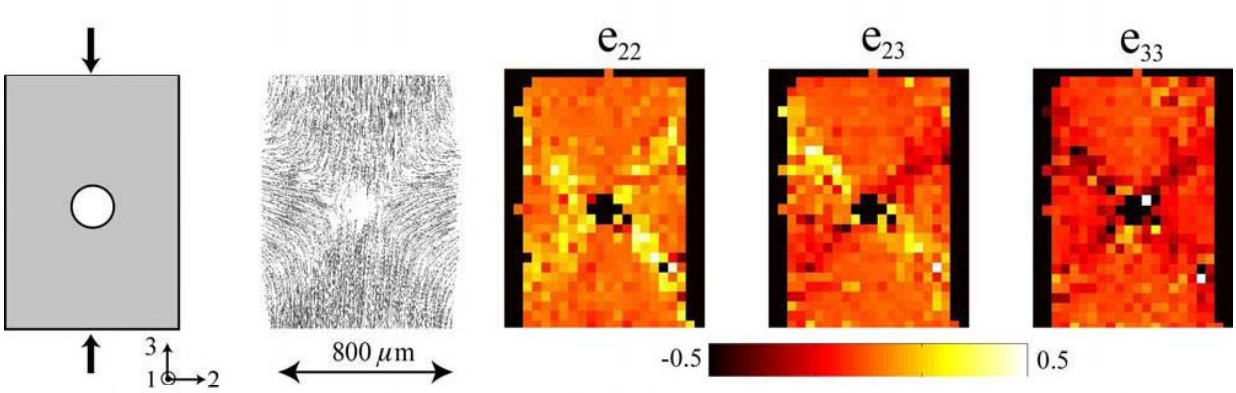


Fig. 1 Compression of a sample with a hole, a map of the marker tracks during deformation, and maps of the axial (e_{33}), transverse (e_{22}) and shear (e_{23}) displacement gradient components inside the sample.

B) The row of diagrams in Fig. 2 shows the geometry of a notched sample loaded in bending and the strain concentration at the notch tip. Variation of the through-thickness strain demonstrates the 3D character of this deformation field. This factor has long been known in the field of fracture mechanics where it accounts for the difference in fracture resistance between thick and thin specimens. Such differences between the surface and center portions of loaded plates with notch-like geometrical features or internal flaws have been calculated for decades using FEM methods and related analytical models; the strain map shown in Fig. 2 represents the first experimental 3D measurement of the effect.

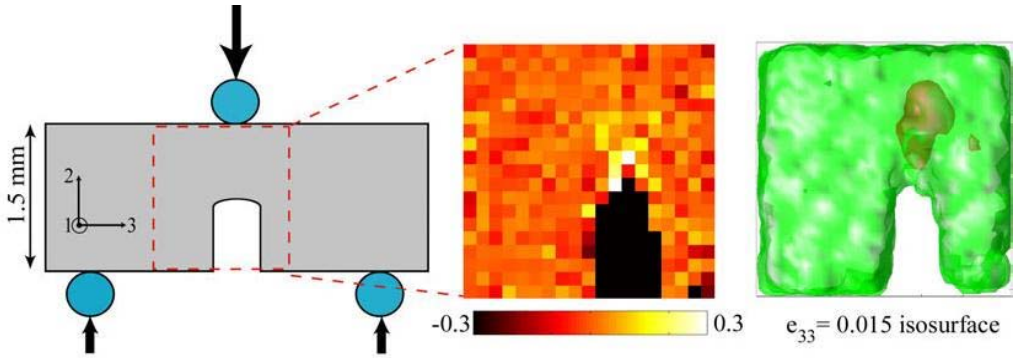


Fig. 2 A notched sample is loaded in bending. The measured strain concentration at the notch tip is represented as a 2D map of e_{33} and as a 3D semitransparent map from the same perspective.

C) The row of diagrams in Fig. 3 shows the geometry of a blind-hole sample loaded in bending and the strain concentration in zones near the hole. Although the notch and blind-hole bending samples appear to be similar in geometry, the experimental observations show the samples to react completely differently to the applied bending load. The largest stress concentration in the notch sample is at the notch tip, whereas the largest stress concentration is in the ligaments on either side of the hole in the blind-hole sample.

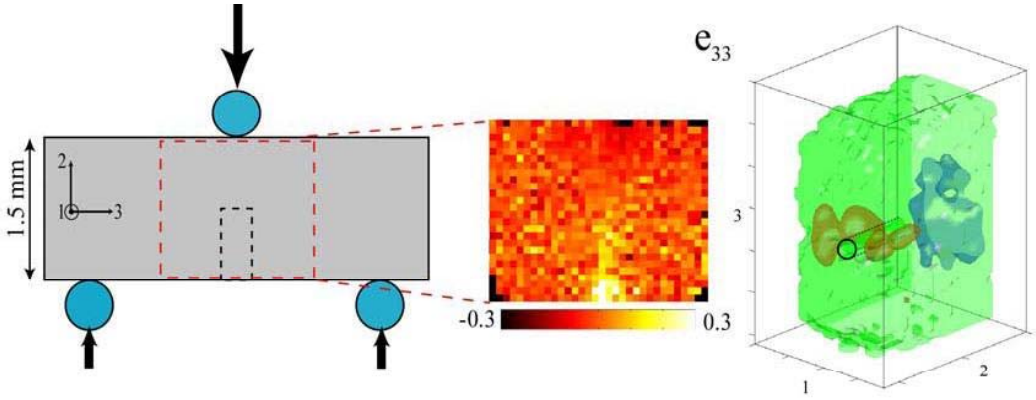


Fig. 3 A blind-hole sample is loaded in bending. The measured strain concentration in the ligaments beside the hole is represented as a 2D map of e_{33} and as a 3D semitransparent map from a different perspective. In the semitransparent rendering, red represents elongation and blue represents compression.

These recent experimental results are of a type never before obtained. Methods are still being developed to effectively display the results, which consist of maps of nine tensor components in 3D. The results are now of a sophistication that exceeds the applicability of simple deformation models; integration of the experimental results with FEM models is currently underway. Also underway are similar analyses that address the effect of internal microstructural features, such as grain boundaries, on the development of heterogeneous deformation patterns in polycrystals.

References

[1] S.F. Nielsen, F. Beckmann, H.F. Poulsen and J.A. Wert, *Mat.Sci.Eng.A*, **387**, 336, (2004).

[2] K. Haldrup; S.F. Nielsen; F. Beckmann; J.A. Wert, *Mat. Sci. Tech.*, **11**, 1428 (2005).

Microstructural Investigations on Natural Fiber Composites and Medium Density Fiberboard (MDF)

T. Walther[1], T. Donath[2], K. Terzic[3], H. Meine[3], H. Thömen[1], and F. Beckmann[2]

[1]Department of Wood Science, Hamburg University, Leuschnerstrasse 91, 21031 Hamburg, Germany
[2]GKSS-Forschungszentrum, Max-Planck-Strasse 1, 21502 Geesthacht, Germany
[3] Department of Computer Science, Cognitive Systems Group, Hamburg University, Vogt-Kölln-Strasse 30, 22527 Hamburg, Germany

Following preliminary examinations in 2004, the project I-04-100 "Microstructure of Natural Fiber Composites" started in January 2005. The project at HASYLAB is embedded in the research project "Natural Fiber Composites – An Alternative?" supported by the Arthur and Aenne Feindt Foundation, Hamburg. The aim is to reduce the amount of adhesives used for the production of the composites, to reduce production costs, and to establish more environmentally friendly products.

Laboratory MDF boards and boards with a combination of wood fibers and annual plant fibers, namely sisal and hemp were produced in a laboratory hot-press at the Department of Wood Science. The MDF boards had a density of 300 kg/m^3, 500 kg/m^3, 750 kg/m^3 and 1000 kg/m^3 and a thickness of 5 mm. Furthermore, another two series of MDF boards with the same density settings were produced and the adhesive was stained using either iodine or barium sulfate. Another set of boards contained a combination of 50% wood fibers and 50% sisal or hemp fibers.

X-ray microtomography (μCT) was performed on small samples with a dimension of 2×2×5 mm^3 at beamline BW2 at HASYLAB. The synchrotron radiation X-ray μCT-equipment operated by the GKSS was used. The photon energy for the scans was set to 12 keV to match the low absorption of the wood and annual plant fibers. 15 samples were successfully scanned during the allocated beamtime.

Figure 1 shows cross sections from the reconstructed volume data of four MDF samples of varying board densities. The different compression of the samples is clearly visible and individual cells and cavities can be identified in the low density boards.

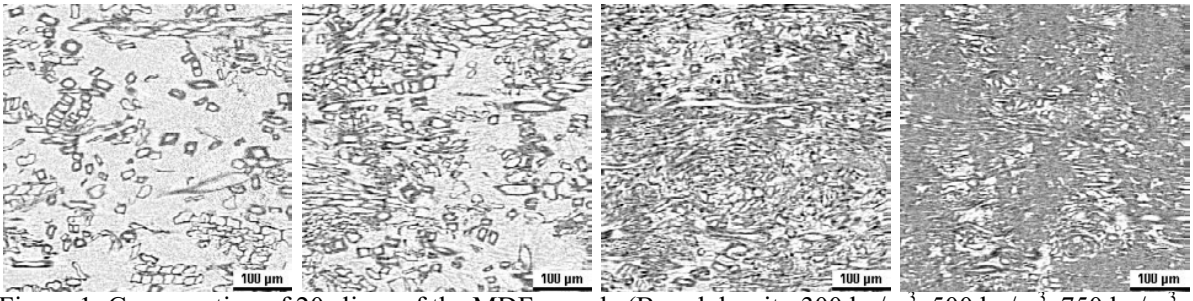


Figure 1: Cross section of 20 slices of the MDF sample (Board density 300 kg/m^3, 500 kg/m^3, 750 kg/m^3, 1000 kg/m^3 from left to right)

The 3D volume data was analyzed to gain information about the geometrical properties of the fiberboards. This is displayed using a 256×256×256 voxel sub-volume out of the 3D volume data of a low density MDF marked in Figure 2.

Figure 3 shows the different steps of the segmentation procedure. Picture A shows a rendering of the sub-volume without any segmentation. In picture B the region of low attenuation coefficient has been made transparent. The data was then segmented into air, fibers and cavities within the fibers. First the outside air was marked using seeded region growing, then the remaining voxels were separated into fibers and cavities through thresholding and subsequent seeded region growing.

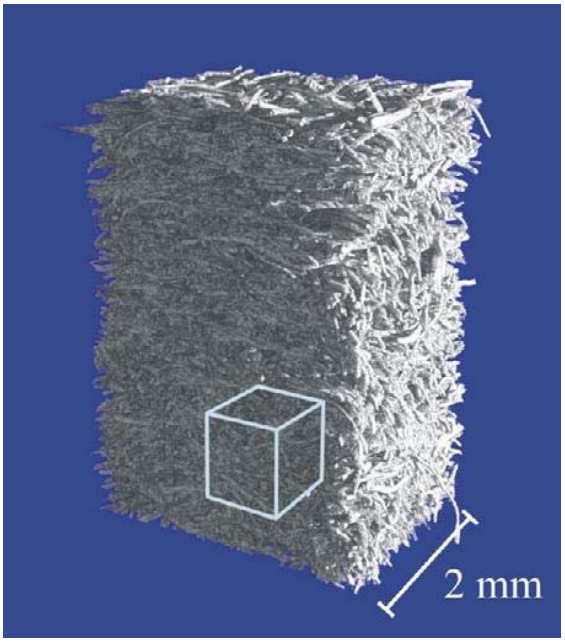


Figure 2: 3D-rendering of MDF-sample. The sub-volume used for segmentation is marked.

Picture C shows the marked cavities that have no contact to the outer air. Finally, the cavities with contact to outer air (Picture D) were separated through a series of morphological operations (erosion and dilation). Picture E shows the detected cavities in the fibers. Individual fibers were then segmented by using dilation on individual cavities and using the segmented image as a mask (Picture F).

The volumes and ratios of outer air, fibers and enclosed cavities can be calculated by counting voxels within the segmented images. The surface of the fibers is calculated by counting the contact surfaces between fiber and air. Finally, the orientation of the fibers can be obtained by performing principal component analysis on the segmented cavities.

Further investigation is planned to identify and to analyze the distribution of the stained adhesives. The gained information will be used to characterize the structure of the fiberboards and to compare the results with data from various simulations [1,2].

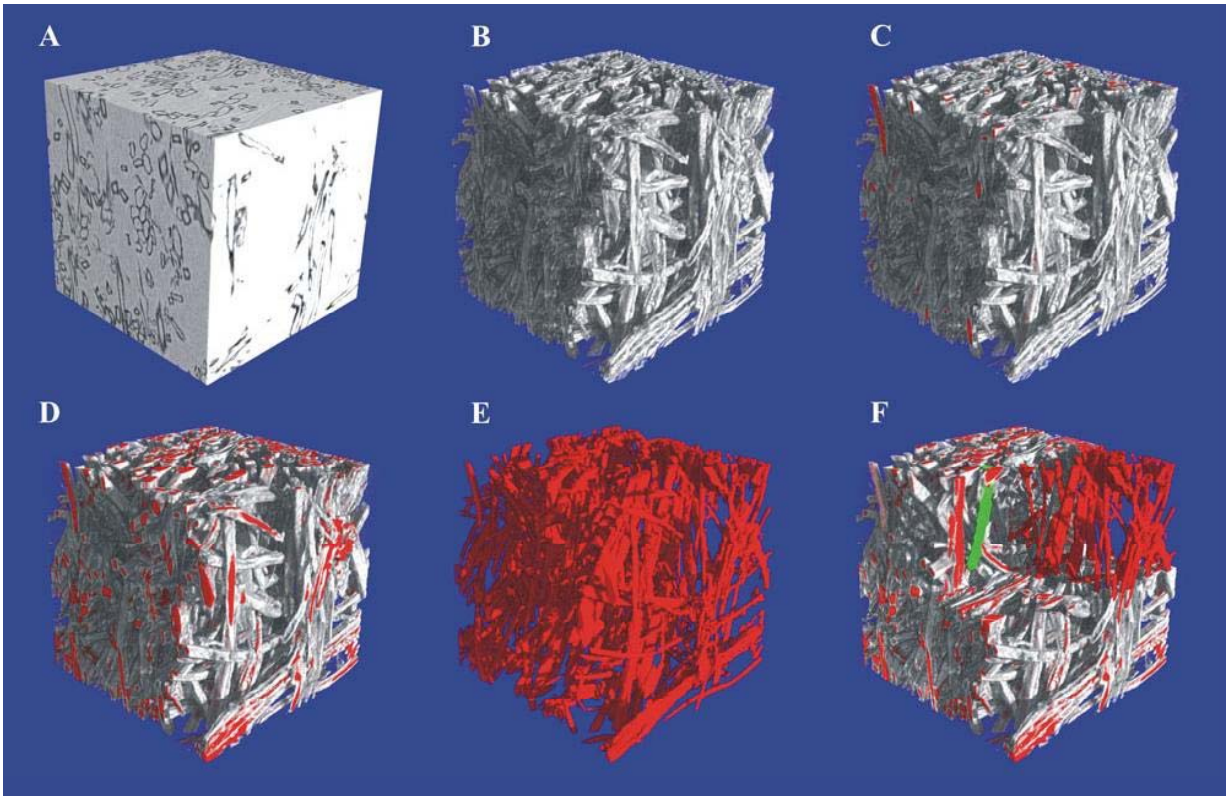


Figure 3: Segmentation steps A to F of a 256×256×256 voxel sub-volume.

References

[1] Latz, A., Wiegmann, A., Simulation der Luftfiltration in Mikrostrukturen, 7. Symposium „Textile Filter“, Chemnitz, Germany, 2.-3. März 2004

[2] Wang, H., Shaler, S.M., Computer-Simulated Three-Dimensional Microstructure of Wood Fibre Composite Materials, Journal of Pulp and Paper Science 24(10), 314-319 (1998)

Pore space analysis of soil aggregates investigated by microtomography using synchrotron radiation

S. Peth, F. Beckmann[1], T. Donath[1], J. Fischer[2], A.J.M. Smucker[3] and R. Horn

Institute of Plant Nutrition and Soil Science University of Kiel, Olshausenstr. 40, D-24118 Kiel, Germany
[1]GKSS-Research Centre, Max-Planck-Str. 1, 21502 Geesthacht, Germany
[2]Hannover Medical School, Anna-von-Borries-Str.1-7, 30625 Hannover, Germany
[3]Institute of Crop and Soil Sciences Michigan State University, East Lansing, MI, USA

Soil structure and particularly the formation of (micro)aggregates are important for long term sequestration of soil organic carbon (SOC). However, research during the last 50 years produced only a few quantitative studies that consider the interactive effects between soil biota and soil physical processes which are especially relevant on the micro-scale. Detailed knowledge of the geometry and continuity of the pore-network within soil (micro)aggregates is very important to close this gap since fluid movement (air and water) affects microbial activity in soil aggregates.

Recent advances in synchrotron radiation X-ray tomography and the development of algorithms to quantitatively describe porous media from reconstructed 3D images will greatly facilitate soil structure analysis on the micro-scale. This will contribute to understanding the mechanism involved in carbon sequestration within soil inter-aggregate pore space. For a statistical analysis of pore geometrical properties features like pore throat size, channel length and connectivity as well as pore size distributions within aggregates may be useful. Lindquist and Venkatarangan have developed a suite of algorithms assembled into a software package referred to as 3DMA to extract such geometric property distributions from 3D data sets [1]. The authors investigated the accuracy of their algorithms using a simulated image of packed hexagonal spheres. Relative errors between theoretical and numerically computed values were in general smaller than 5%. Also the analysis of microtomographic images of natural porous media (Fontainebleau sandstone) produced good results. To test the applicability of above mentioned algorithms for aggregated soil we have analysed a set of aggregates approximately 5 mm across at the synchrotron radiation source in Hamburg/Germany (DESY) (Fig. 1). From the reconstructed 3D images we extracted a brick shaped subvolume (2.50 x 2.25 x 1.60 mm) on which we determined pore statistical properties.

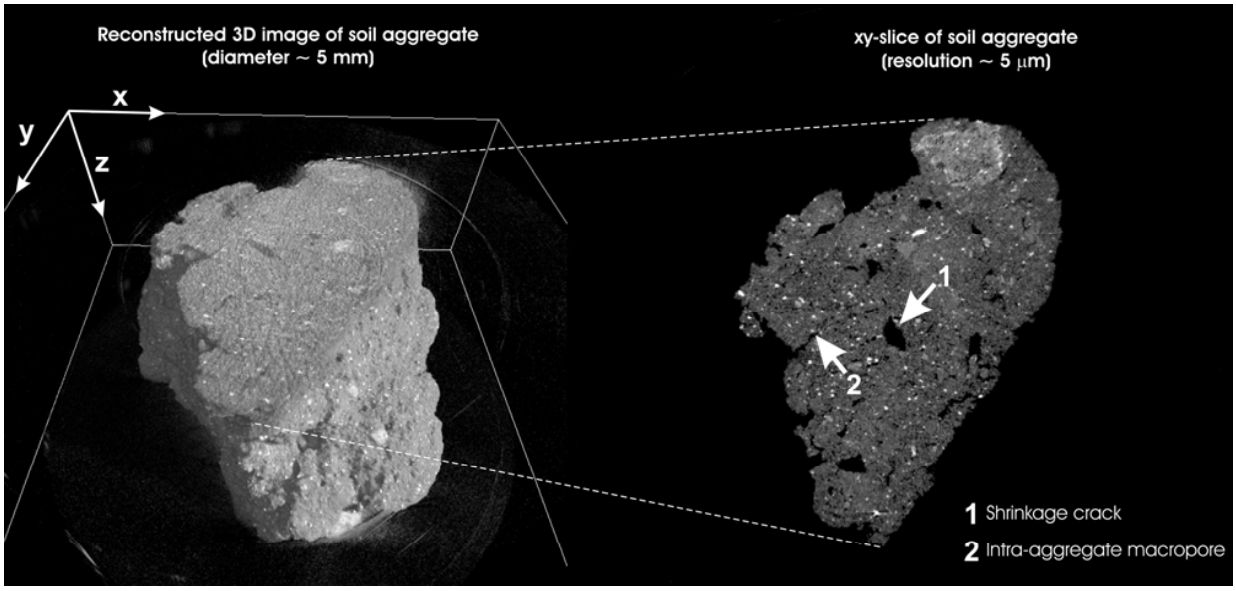


Figure 1: Reconstructed 3D image of a soil aggregate (left) and axial view on a xy-slice (right) revealing shrinkage cracks and inter-aggregate macropores. The microtomographic investigation was performed at beamline BW2 using a photon energy of 24 keV

Quantitative investigation of the geometry of the void space requires the distinction between voxels that represent solid phase and voxels that represent voids. This is achieved by an edge-finding segmentation algorithm [2] where two threshold attenuation coefficients T_0 and T_1 are chosen. Any voxel having intensity less than T_0 is identified as phase 0 (void) while voxels having intensities greater than T_1 are identified as phase 1 (solid). Voxels with intensities in the range $[T_0; T_1]$ are set using indicator kriging. Figure 2 shows the resulting segmented image which is in reasonable good agreement with the original microtomographic image.

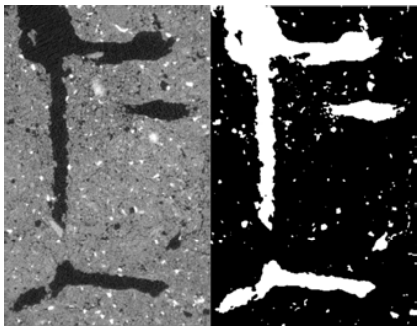


Figure 2: Original microtomographic 2D image (left) and segmented image resulting from the edge-finding algorithm (right). On the segmented image: black represents the solid phase and white the void space

To provide a representation of the network of potential flow paths the brick shaped subvolume has been skelotonized by the medial axis algorithm [1]. Apart from having a visual impression of the continuity and intersection of the flow path network medial axis construction is utilized as an embedded search structure to find specific sites such as pore throats in the object. With throats constructed, the pore space is divided into pores separated by throat surfaces from which pore-throat network statistics can be computed. Figure 3 shows a 3D view of the medial axis representing the flow network and shortest flow paths from the left to the right face of the subvolume.

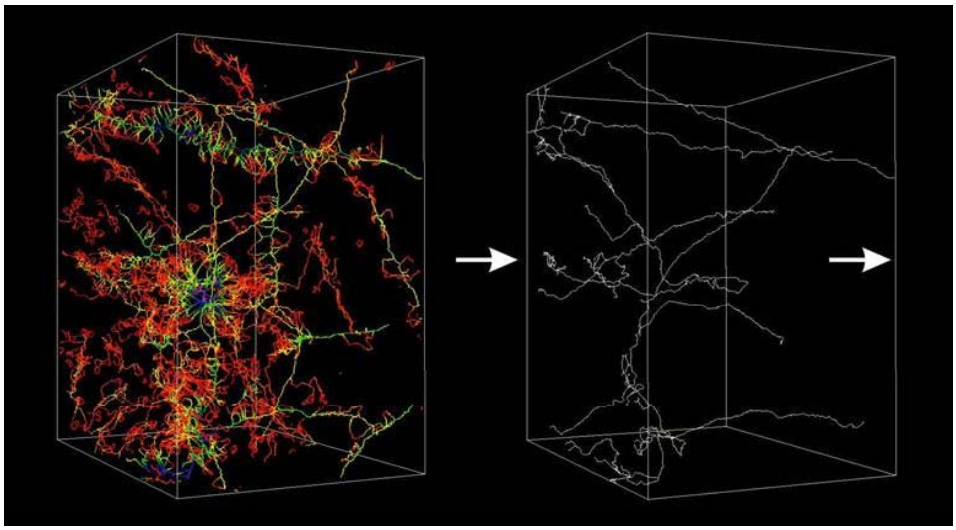


Figure 3: 3D medial axis plot showing pore channel tortuosity and connectivity (left). Shortest flow paths that connect the left and the right face of the subvolume are extracted (right)

The applied algorithms seem to be a promising tool for pore statistical analysis of soil aggregates. Further studies will focus on the effect of shrinking and swelling on changes in pore space properties.

References

[1] W. B. Lindquist and A. Venkatarangan, Journal of Geophysical Res. 105B, 21508-21528 (2000)

[2] W. Oh and W. B. Lindquist, IEEE Trans. Pattern Anal. Machine Intell. 21, 590-602 (1999)

Honeybee in 3D - Neuroimaging with µ-Tomography

M. Kuehbacher[1], J. Fischer[2], B. Gruenewald[3],

T. Donath[4], D. Behne[1], A. Kyriakopoulos[1] and F. Beckmann[4]

[1]Hahn-Meitner-Institut Berlin, Department Molecular Trace Element Research in the Life Sciences, Glienicker Str. 100, 14109 Berlin, Germany

[2]Department of Orthopaedic Surgery, Hannover Medical School, Anna-von-Borries-Str. 1-7, 30625 Hannover, Germany

[3]Institut für Neurobiologie, Freie Universität Berlin, 14195 Berlin, Germany

[4]GKSS-Research Center Geesthacht, Institute for Materials Research, Max-Planck-Strasse 1, 21502 Geesthacht, Germany

Neuroscience has benefited to a great extent from the use of animal models. The honeybee (Apis mellifera) is such an established model for research due to its distinctive behavioral traits and social instincts [1]. Like other model organisms its genome is already sequenced [2]. In contrast to the human central nervous system the brain of the investigated worker honeybee with a volume of about 1 mm^3 and a weight of about 1 mg is relatively simply structured but shows remarkable cognitive capabilities. The total number of neurons in its brain has been estimated to be 960,000 neurons [3].

Honeybees collect food from flowers, an extremely temporary food basis, and have evolved complex cognitive abilities and communication skills to optimize foraging success [4]. Their capability for associative learning is based on the need to associate a color, shape, scent, or location with a food reward. For the understanding of neurophysiologic mechanisms in the brain it is necessary to study the morphology of the wiring between and inside specific brain regions. The majority of these investigations were solved by combined staining and 2D histological sectioning techniques especially in the mushroom body, an insect brain region associated with learning and memory [5].

The development of superior 3D imaging methods was an advance for histological structural analyses. Tomography, specifically X-ray tomography, is a 3D imaging method with the advantage to be non-destructive. By the use of synchrotron radiation the spatial resolution of X-ray microtomography reaches the micrometer range. This resolution might be sufficient to visualize the projecting axons in nervous tissues. Thus, live brain imaging and 3D-neuron reconstruction within the bee brain in vivo can be obtained. These data can further be incorporated into an existing 3D-atlas of the bee brain [6].

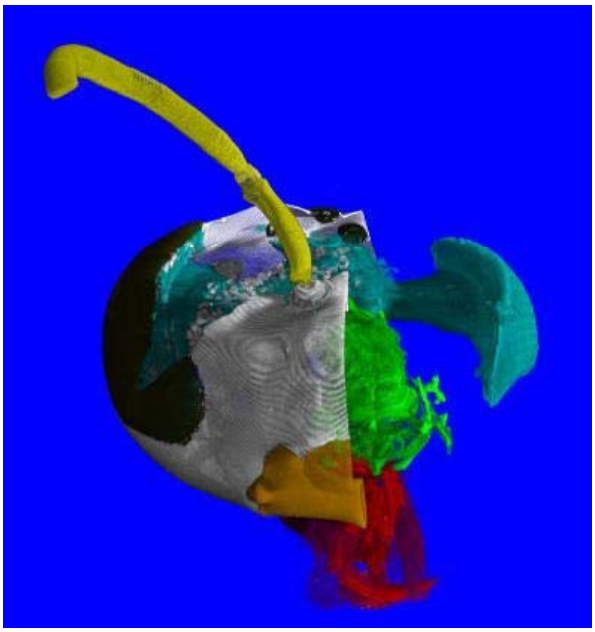


Figure 1: 3D view of a segmented and cropped head of a honeybee with a diameter of 4 mm. The different anatomical parts of the head are colorized by VGStudio Max 1.2 (Volume Graphics, Heidelberg, Germany).

In a pilot study the head as well as isolated brains of worker honeybees were investigated by synchrotron radiation-based computered microtomography (SRμCT) in absorption contrast mode at beamline BW2. The measurements were performed with photon energies of 8 and 9 keV. The voxel size was about ~1.6 μm. Figure 1 shows the segmented and cropped head of a honeybee.

The results of the successful pilot study provide valuable information about the chosen sample preparation techniques and the possibilities of 3D imaging with synchrotron radiation-based computered microtomography (SRμCT).

Acknowledgements

The authors thank the summer students Christian Taubitz and Alexey Voronov for their work of segmentation and colorization of the 3D-dataset.

References

[1] R. Menzel, M. Giurfa, *Cognitive architecture of a mini-brain: the honeybee.* Trends in Cognitive Sciences 5, 2: 62-71 (2001)

[2] http://www.hgsc.bcm.tmc.edu/projects/honeybee/

[3] W. Witthoft, *Absolute Anzahl und Verteilung der Zellen im Hirn der Honigbiene*. Z. Morphol. Tiere 61,1: 160-184 (1967)

[4] K. von Frisch, *Dance language and orientation of the honey bee*. Harvard Univ Press (1967)

[5] B. Grünewald, *Morphology of feedback neurons in the mushroom body of the honeybee, Apis mellifera*. J. Comp. Neurol. 404: 114-126 (1999)

[6] R. Brandt, T. Rohlfing, J. Rybak, S. Krofczik, A. Maye, M. Westerhoff, H.C. Hege, and R. Menzel, *Three-Dimensional Average-Shape Atlas of the Honeybee Brain and Its Applications*. The Journal of Comparative Neurology 492: 1-19 (2005)

Mikrotomographie an Biomineralien

Oleg Prymak,[a] Carsten Schiller,[a] Henry Tiemann,[b] Ilka Soetje,[b] Julia Marxen,[b] Tilman Donath,[d] Felix Beckmann,[d] Matthias Epple [a]

[a] Universität Duisburg-Essen, Institut für Anorganische Chemie, Universitätsstraße 5-7, D-45117 Essen. Fax: +49 201 183-2621; Tel: +49 201 183-2402; E-mail: matthias.epple@uni-duisburg-essen.de
[b] Universität Hamburg, Biocenter Grindel, Martin-Luther-King-Platz 3, D-20146 Hamburg.
[c] GKSS Forschungszentrum Geesthacht, Institut für Materialforschung, c/o GKSS am DESY, Notkestrasse 85, D-22607 Hamburg.

Die Bildung von anorganischen Mineralen durch lebende Organismen wird als Biomineralisation bezeichnet. Die Biominerale erfüllen die verschiedensten Aufgaben, beispielsweise findet man sie in Knochen und Zähnen der Wirbeltiere, in Schalen von Muscheln und Schnecken, aber auch in Pflanzen wie Gräsern oder Schachtelhalm. Die Biomineralisation steht aus mehreren Gründen zunehmend im Blickpunkt der Wissenschaft: einerseits ist das Verständnis der Mineralisationsvorgänge in Lebewesen hilfreich bei der medizinischen Behandlung von Erkrankungen, die auf eine Störung der Mineralbildung zurückzuführen sind (z.B. Osteoporose oder Arteriosklerose) und andererseits könnte die Nachahmung dieser hochgradig gesteuerten Kristallisationsvorgänge zu neuen Werkstoffen führen. Darüber hinaus hilft die Analyse von Biomineralen den Biologen bei der Klassifizierung von Tier- und Pflanzenarten.
Die Mikrocomputertomographie ist eine sehr nützliche Methode zur Untersuchung von Biomineralen, da sie 3-dimensionale Aufnahmen von kleinen Mineralstrukturen ermöglicht. Es ist im Gegensatz zu anderen Methoden (z.B. REM) nicht erforderlich, die Mineralpartikel aus einer sie umgebenden organischen Matrix zu isolieren, so dass keine durch die Probenvorbereitung hervorgerufenen Artefakte entstehen können.
In diesem Beitrag möchten wir die mikrocomputertomographische Untersuchung zweier unterschiedlicher Biominerale vorstellen: den Rhopalien der Meduse *Aurelia aurita* und der Schale der Schnecke *Biomphalaria glabrata*.

Rhopalien der Meduse *Aurelia aurita*

Wie alle Quallenarten orientiert sich die Tiefseequalle *Aurelia aurita* mit Hilfe von speziellen Organen, den Rhopalien, die vermutlich als Schwerkraft- und Trägheitssensoren fungieren. In diesen Organen befinden sich anorganische Kristalle, die so genannten Statolithen. Sie bestehen aus Calciumsulfat. Wir könnten mit Hilfe von Einkristall-Diffraktometrie am HASYLAB zeigen, dass es sich dabei um die Hemihydrat-Phase (Bassanit) handelt.[1] Interessant ist auch die Anordnung der Kristalle in den Rhopalien. In der mikrocomputertomographischen Abbildung erkennt man, dass eine Rhopalie dieser Qualle viele Kristalle enthält, die zusammen ein kugelförmiges Aggregat bilden (Abb. 1). Die Messung wurde an der Beamline BW2 bei einer Energie von 11.5 keV durchgeführt.

Schale der Schnecke *Biomphalaria glabrata*

Biomphalaria glabrata ist eine tropische Posthornschnecke, die als Überträger der Billharziose bekannt ist. Schnecken sind Eierleger. In den Eiern entwickeln die Embryonen bereits vor dem Schlüpfen eine Schale, die zunächst röntgenamorph ist, nach kurzer Zeit aber kristallines Calciumcarbonat enthält. Bei *Biomphalaria glabrata* liegt es in der Aragonit-Struktur vor.[2] Die Gestalt der Schale lässt sich wiederum gut mittels Mikrocomputer-tomographie beurteilen. In Abbildung 2 erkennt man, dass die Schale der Embryonen nur sehr wenige Windungen besitzt. Im Verlauf des weiteren Wachstums mineralisiert die Schnecke

Calciumcarbonat am Mantelrand, so dass die Zahl der Windungen mit der Größe der Schnecke zunimmt.

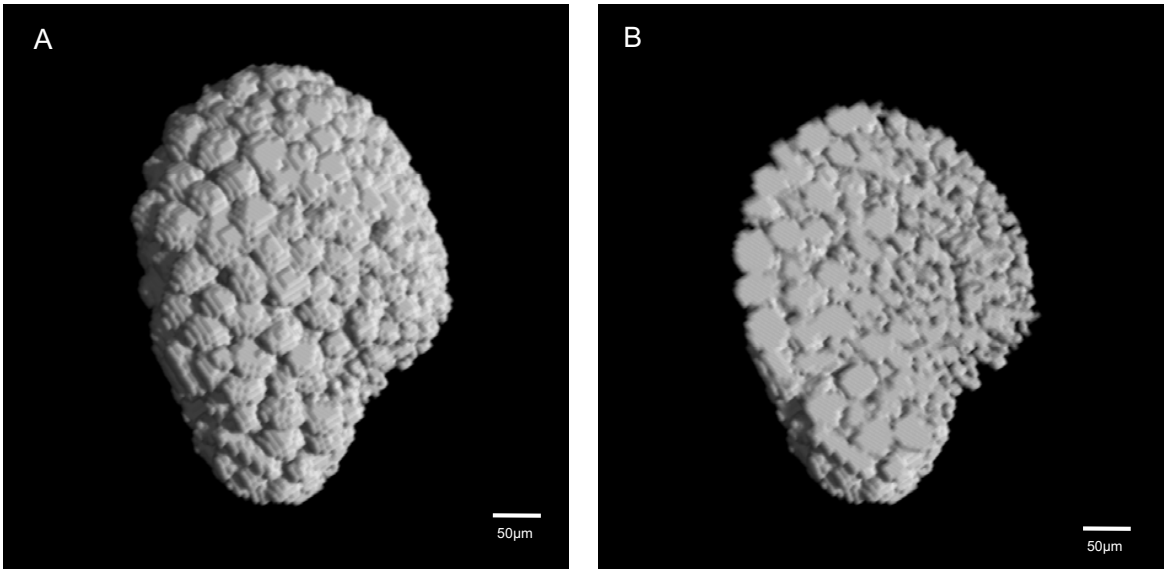


Abb. 1. Mikro-CT einer Rhopalie der Tiefseequalle *Aurelia aurita*. Bild A zeigt die Ansicht der Rhopalie von einer Seite. Man sieht, dass die kleinen Kristallen von vorne größer sind (etwa 50 µm) als die Kristalle von hinten (etwa 10 µm). Bild B zeigt die Rhopalie im Schnitt.

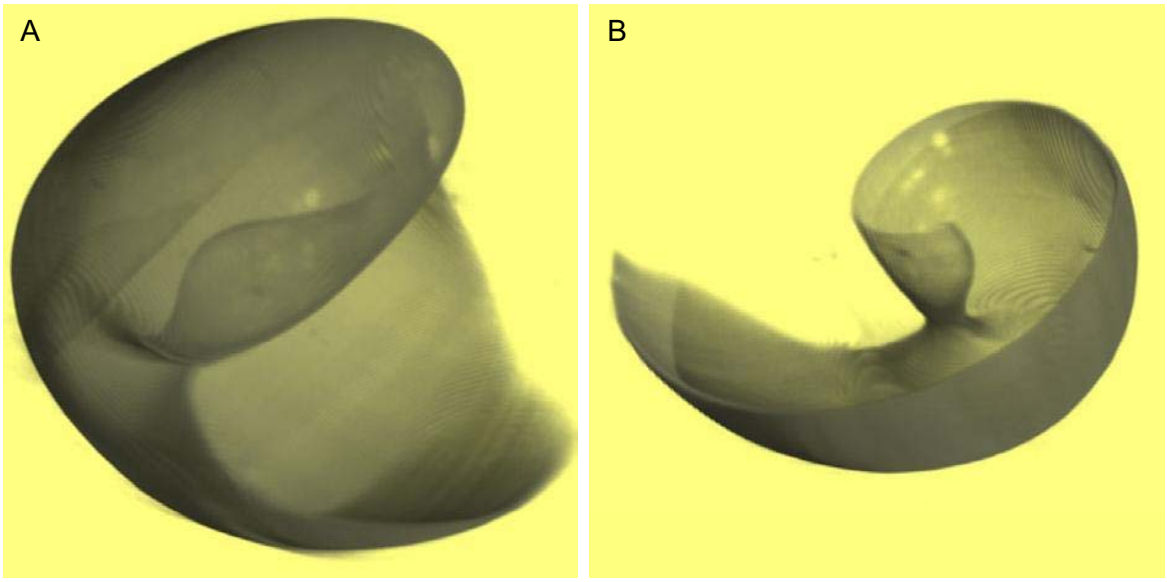


Abb. 2. Mikro-CT der Schale eines Embryos der Schnecke *Biomphalaria glabrata* im Alter von 120 h. Bild A zeigt eine Ansicht des vollen Schneckenhauses und in Bild B ist die Schale virtuell aufgeschnitten. Der Durchmesser des Schneckenembryos liegt bei ca. 0.5 mm.

Literatur

1. A. Becker, I. Sötje, C. Paulmann, F. Beckmann, T. Donath, R. Boese, O. Prymak, H. Tiemann, M. Epple, J. Chem. Soc. Dalton Trans., 1545-1550 (2005).
2. J.C. Marxen, W. Becker, D. Finke, B. Hasse, M. Epple (2003). „Early mineralization in Biomphalaria glabrata: Microscopic and structural results". J. Mollusc. Stud. 69:113-121

Quantitative morphometrics and contraction analysis of the marine sponge *Tethya wilhelma* using synchrotron radiation based x-ray microtomography and *in vivo* x-ray imaging

M. Nickel[1], J. U. Hammel[1], T. Donath[2] and F. Beckmann[2]

Department of Zoology, Biological Institute, University of Stuttgart, Pfaffenwaldring 57, 70550 Stuttgart, Germany

[2]GKSS Forschungszentrum, Max-Planck-Str. 1, 21502 Geesthacht, Germany.

Sponges (Porifera) are sessile, filter-feeding animals, mainly inhabiting the sea. In recent years interest in sponges rose the group contains a variety of interesting secondary metabolites, which could be used in pharmacology and biotechnology. Nevertheless, it became evident that a more detailed knowledge on the general biology of sponges is a pre-requisite for successful cultivation. The skeletons consist of organic substances, like collagen and its derivative spongin, in conjunction with mineral sclera (spicules) in most groups of the phylum Porifera [1, 2]. Cellular growth and synthesis of skeletal elements are connected in sponges. The main function of the skeleton is to stabilise the bodies of sponges. On the other hand the skeletal elements possess a variety of other functions in contraction and locomotion of sponges. Since these processes are slow and inconspicuous they are not well investigated. Nevertheless, they are very important in the life of sponges, since they are linked to nutrition (filter feeding activity) and to response towards environmental changes. Although sponges posses a limited number of cell and tissue types, the complexity of their body structures have long impeded to aply quantitative 3D-morphometric analyses. Our project aims to understand the functional micromorphology of sponges, by applying synchrotron radiation based micro computed tomography SR-μCT in combination with quantitative image anlysis. We performed experiments at HASYLAB beamline BW2 on dead, preserved sponges as well as on living material. In 2005 we mainly focused on *Tethya wilhelma*, an extremely contractile and locomotive specimen [3 - 5].

Morphology and morphometric analysis of *Tethya wilhelma*

By modfying an osmium tetroxide based contrasting method, generally used for TEM imaging, we were able to visualize the tissue of *T. wilhelma* at 15 keV and to distingush between tissue and mineral skeleton by density thresholding (Fig. 1A). The cavities of the aquiferous system were visualized either as cavities or by inversion as a kind of virtual 'cast'. Thorough analysis of the 3D-structure of the canal system, including virtual fly throughs, revealed a much higher degree of water recirculation probabilities in comparison to other sponges. The lacunar system cavities, forming a prominent network in the cortex, is part in the incurrent system, but also connected to the excurrent system through bypass canals. We assume that under regular conditions a part of the excurrent water is recycled to the incurrent system. During contraction of *T. wilhelma*, the flow through the bypass system might be reversed to allow faster draining of the lacunar system.

Quantiative volume and surface analysis on the image stack revealed an unequal distribution of sponge compartments. While the cortex is dominated by the aquiferous system, it shares equal volumes with the tissue in the choanoderm (Fig 1B). Nevertheless, the volume of the

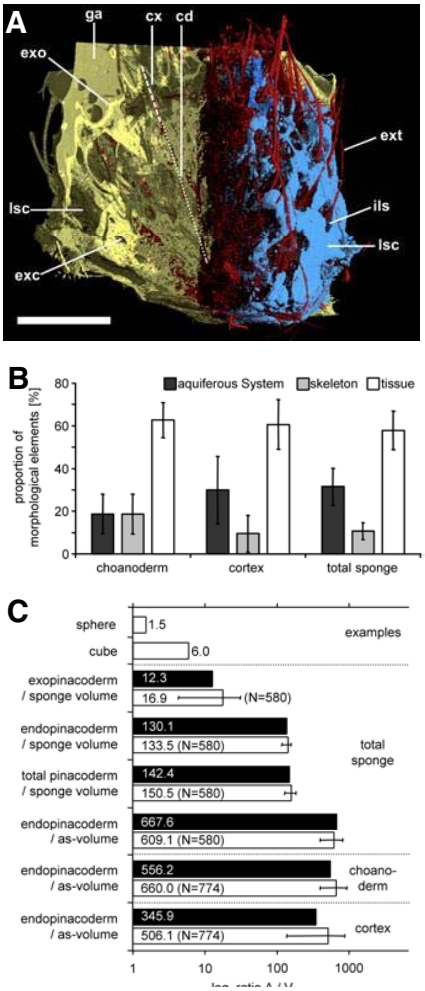


Figure 1. A. The complete morphology of *T. wilhelma*: yellow, tissue; blue, aquiferous system; red: skeleton (bar: 1000 μm). **B.** Quantification of tissue, aquiferous system and skeleton content of two distinct morphological compartments in comparison to the total sponge. **C.** Surface-to-volume rates of compartments in relation to different epithelias (pinacoderm). Figures modified from Nickel et al. (submitted).

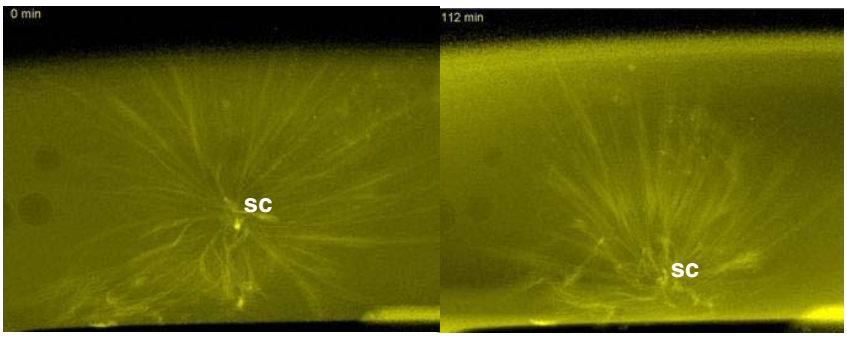


Figure 2. In vivo x-ray imaging of the radial megasclere bundles of a specimen of *T. wilhelma* during glutamate induced contraction at t=0 min and t=112 min. Note the basaly oriented shift of the skeletal centre (sc) and the change of angles between the bundles.

lacunar system together with the large excurrent canals is high enough to dominate the whole sponge. An relatively unexpected result showed up in the calculation of surface-to-volume ratios: *T. wilhelma* has a ratio of 142.4 mm-1, which outranges the same ratio of the human lung by factor of 5.7. Hence, *T. wilhelma* consits mainly of surfaces. The pinacoderm dominates the morphology of *T. wilhelma* by structural and functional means. We assume that the pinacoderm is the main mediator of contractile forces and might also be involved in signal integration processes, connected to contraction and other behaviours.

In vivo* x-ray imaging of *Tethya wilhelma

In order to test the principal possibility of *in vivo* x-ray imaging of *T. wilhelma*, we performed a static x-ray projection time series, while specifically inducing a contraction at 15 keV. We revealed a image series, which allows us to follow up structural changes of the megasclere bundle confirmation during contraction. Although the total x-ray dosis was very high, the sponge survived the experiment. However, the cells must have been seriously damaged, since the sponge lost its natural globular shape during the following days, but reorganized to a smaller globular specimen during the following weeks. Consequently we intent to develop an micro-chamber which will allow us to perform *in vivo* microtomography.
The result of this preliminary experiment itself is interesting and revealed new details of the skletal function during contraction. While the apical megasclere bundles soleyly shift their angle during contraction, the basal megasclere bundle bend strongly in addition, and even kink. As a consequence, the skeletal center and therefore the whole sponge, shifts towards the substrate.

Conclusion and outlook

Both, enhancing microtomographic imaging of fixed sponges by contrasting techniques as well as the proof of concept for in vivo x-ray imaging, are important steps towards the understanding of sponge morphology, especially the functional morphology of the aqiferous system. This is an essential prerequisite to understand the flow regime in sponges. In addition it might help to understand problems arising in complex sponge tissue culture systems. During the next experimentational stage, we will test in vivo microtomography, to understand the 3-dimensional confirmational changes of the skeleton. For the future, we will have to develop a in vivo contrasting method, which allows us, to monitor the living tissue in relation to the canal system.

Statement on animal welfare

All in vivo experiments on *T. wilhelma* comply with German and European laws on animal wellfare and have been discussed with and approved by the animal wellfare commisioner of HASYLAB, Dr. T. Wroblewski.

Acknowledgements

We thank Dr. M. Schweikert (Biological Institute, University of Stuttgart) for assitance with contrasting methodologies and Dr. T. Wroblewski for discussion of the experiments.

References

[1] P. Bergquist, Sponges. University of California Press, Los Angeles, 268 pp. (1978)
[2] T.L. Simpson, The cell biology of sponges. Springer Verlag, New York, 662 pp (1984)
[3] M. Sarà, A. Sarà, M. Nickel, F. Brümmer, Stuttgarter Beiträge zur Naturkunde Serie A 631: 1-15 (2001)
[4] M. Nickel & F. Brümmer, Bollettino dei musei e degli istituti biologici dell' Universita di Genova 68: 483-489 (2004).
[5] M. Nickel, Journal of Experimental Biology, 207 (26), 4515-4524 (2004)

Synchrotron tomography as a tool for the analysis of magnetic particle distribution in tumor tissue

O.Brunke[1], S. Odenbach[1], R. Jurgons[2], C. Alexiou[2], I. Hilger[3], F. Beckmann[4]

[1]TU Dresden, Professur für Magnetofluiddynamik 01062 Dresden, Germany

[2]Klinik und Poliklinik für Hals-, Nasen- und Ohrenkranke, Waldstraße 1, 91054 Erlangen, Germany

[3]Institut für Diagnostische und Interventionelle Radiologie, F.S.U. Jena, Erlanger Alle 101, 07740 Jena, Germany

[4]GKSS, Max-Planck-Str. 1, 21502 Geesthacht, Germany

The use of magnetic nanoparticles in biomedical applications, in particular in diagnostics [1] and cancer treatment by magnetic heating [2] or magnetic drug targeting [3] is a promising therapeutic tool. An important information for the optimization of the application of magnetic particles is their intratumoral distribution. In this context, current radiological imaging procedures are related with a variety of limitations i.e. in terms of image resolution and the applicability of histology is not suitable during the therapeutic procedure. Moreover such techniques provide either an integral information about the content of magnetic material along the beam direction or a relative local snapshot about the magnetic particle distribution limited by the number of histological cuts taken from specimen examined. Nonetheless detailed information about the particle distribution is of severe importance e.g. for the modeling of heat generation during magnetic heating and thus for an effective development of the respective therapeutic tools. For such means a three dimensional mapping of the content of magnetic particles with high spatial resolution is deeply required.

Tumor tissue of a mouse and a rabbit which both have been treated with magnetic nanoparticles have been examined by means of high resolution synchrotron tomography. The experiments have been carried out at the HASYLAB beamline BW2 at photon energies between 20 and 24 keV and and a spatial resolution range between 4 and 10 microns. In order to underline the enormous advantages of this tool in terms of spatial resolution, image quality and the possiblity to resolve density differences a direct comparison of the same samples scanned by means of conventional tomography is shown in figure (1). Due to the much higher spatial resolution of down to 4 µm and the monochromatic character of the synchrotron radiation a quantitative analysis of the density distribution of the samples becomes possible.

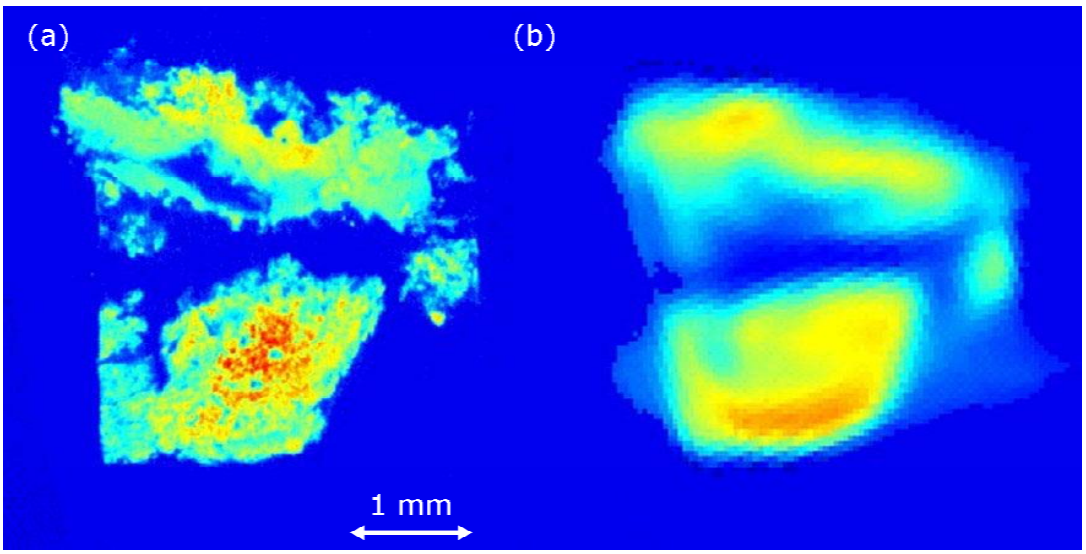


Figure 1: Comparison of the axial view of a mouse tumor examined means of synchrotron (a) and cone beam tomography

Figure 2 shows the rendered image of the part of a rabbit tumor. During the treatment the vessels system of the tissue was enriched with magnetic nanoparticles which can be observed within the tomographic dataset due to the high absorption coefficient of magnetite. The relative amount of magnetic paricles within the vessels of the tumors can be monitored with a precision of 10 µm The position and size of the vessels can be analyzed by means of 3D image processing methods as shown in [4].

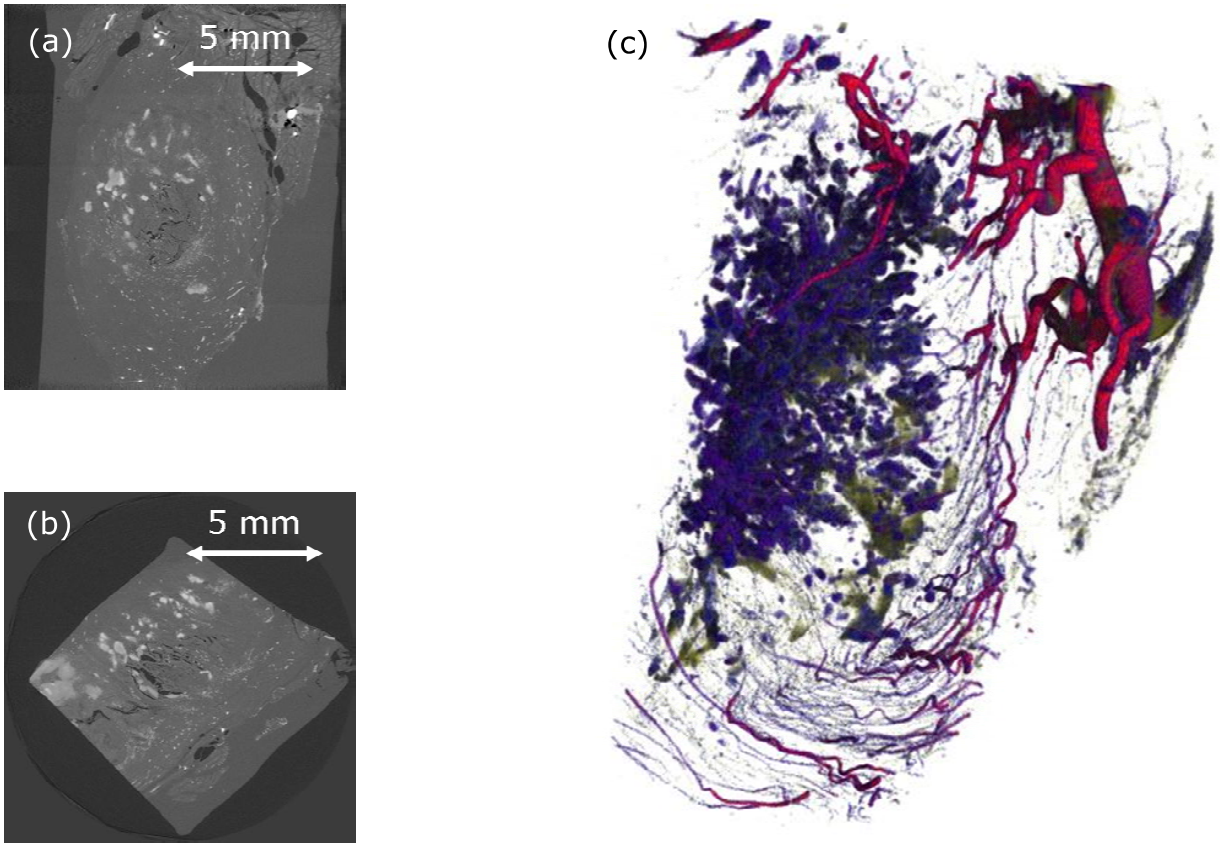


Figure 2: Sagital (a), axial (b) and rendered three-dimensional view of a rabbit tumor scanned at 20 ke and a spatial resolution of 9 µm.

References

[1] Winter P.M., Caruthers S.D., Kassner A., Harris T.D., Chinen L.K., Allen J.S., Lacy E.K., Zhang H., Robertson J.D., Wickline S.A., Lanza G.M.; Cancer Research 63 (2003) 5838-

[2] Hilger I., Hiergeist R., Hergt R., Winnefeld K., Schubert H., Kaiser W.A.; Invest Radiol. 37,10 (2002) 580-586

[3] Alexiou C., Jurgons R., Schmid R.J., Bergemann C., Henke J., Erhardt W., Huenges E., Parak F.; J. Drug Target. 11,3 (2003) 139-49

[4] Brunke, O., S. Odenbach, and F. Beckmann,. Eur. Phys. J. of Appl. Phys., 2005. 29: p. 73-81.DOI: 10.1051/epjap: 2004203

Synchrotron-radiation-based micro computed tomographic imaging of the human Organ of Corti

W. Freysinger, R. Stoffner, F. Kral, A.R. Gunkel, A. Schrott-Fischer, R. Glückert, J. Fischer[1], F. Beckmann[2], and B. Müller[3]

Medizinische Universität Innsbruck, A-6020 Innsbruck, Austria
[1]Medizinische Hochschule Hannover, D-30625 Hannover, Germany
[2]GKSS Forschungszentrum, D-21502 Geesthacht, Germany
[3]ETH Zürich, Sternwartstrasse 7, CH-8092 Zürich, Switzerland

The human hearing apparatus has found wide attention in many areas of science. Due to its anatomical, biochemical and functional complexity it is subject to intensive research. High-resolution investigations, however, cannot be performed *in vivo*. Furthermore, structural studies are *per se* destructive, histological sections are mostly used. For the immuno-histochemical, microscopic, and electron-microscopic studies the cochlea has to be destroyed; classical medical imagery has insufficient spatial resolution. Synchrotron-radiation-based micro computed tomography (SRμCT) is non-destructive and provides a spatial resolution down to the sub-cellular level. Consequently, SRμCT could be appropriate for a detailed study of the cochlea and the Organ of Corti itself with equidistant, high resolution and homogeneous spatial resolution in all coordinates.

The cochlea was explanted from a cadaver in a suitable time window post mortem, prior to the onset of autolytic destructive processes. The bony hull was drilled away as completely as possible, without destroying the cochlea itself. The specimen was further prepared and fixated in Karnovsky solution, buffered with Caco and ethanol. Preliminary SRμCT-experiments have shown that freshly explanted cochleae from untreated human cadavers do not exhibit sufficiently high x-ray absorption contrast to visualize the tiny features of the soft-tissue structures of the Organ of Corti. Therefore, the specimen was stained with 1% OsO_4 for 45 minutes and subsequently fixed in SPURR, a standard procedure in classical histology. Using the setup for tomography in absorption contrast mode at the beamline BW 2, we have obtained tomograms that reveal the complex anatomy of the human hearing organ, almost comparable to histological sectioning. It is possible to differentiate single-layer cellular membranes, inner and outer hair cells, and other structures on the micrometer scale. The osseous structure of the cochlea, specifically the center of the spiral arrangement of the cochlea, the modiolus, and the radially extending orrary structures that support and host extremely complex neural and vascular structures of the cochlea can be imaged and are shown in the figure.

Currently, we investigate the vascular system of the human cochlea, viz. at the spiral ligament and inside the lamina radialis, in detail. This will provide a better understanding of the blood supply and will allow the creation of more sophisticated models of the cochlea for educational purposes. Moreover, these studies will eventually enhance the understanding of inner ear diseases. Even more important is the visualization of the filigree membranes, which are shown in the inset of the figure. These spatially isotropic data allow creating models in 3D space and can subsequently be incorporated into physical models and advanced simulation to better decode the physics of sound perception.

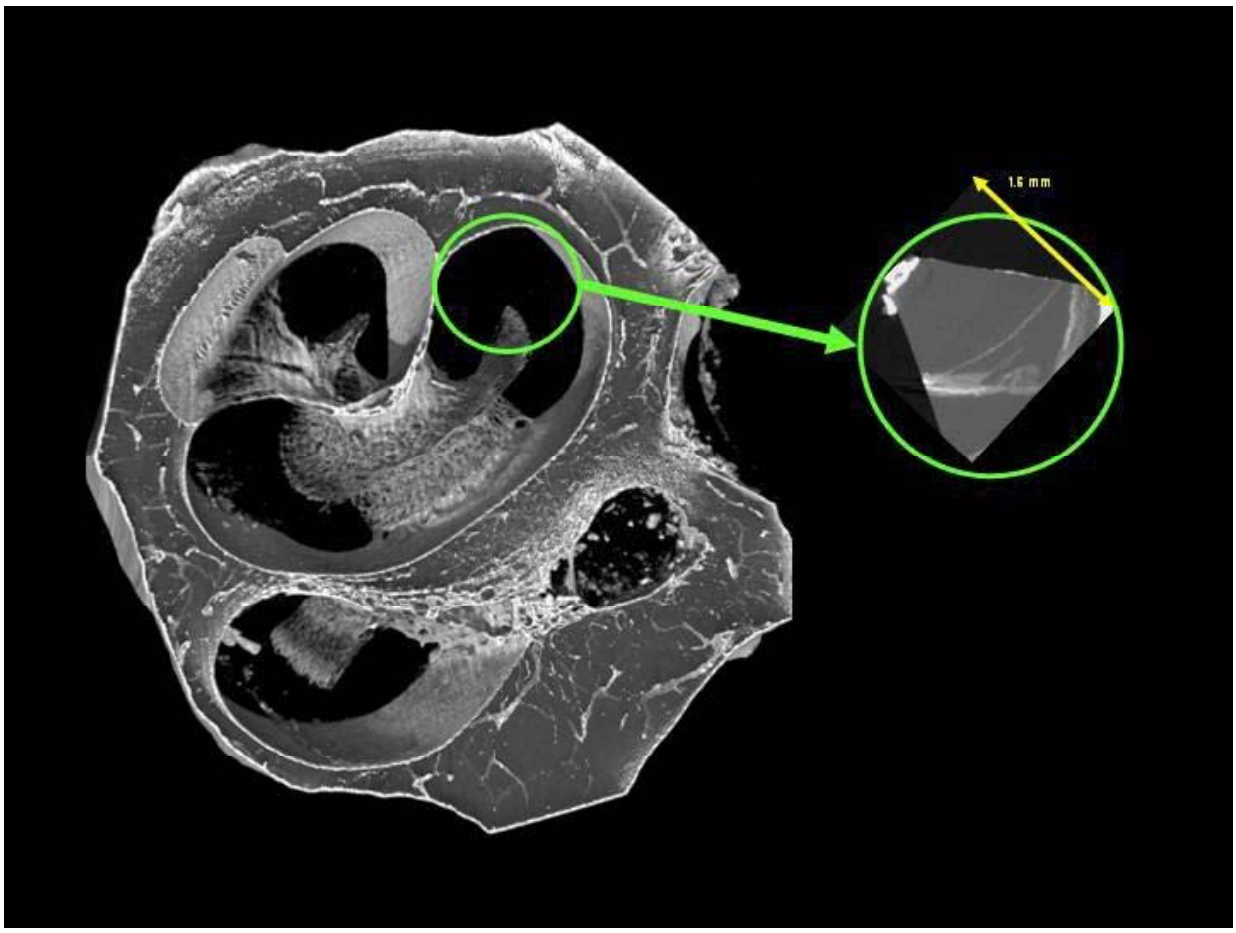


Figure: The highly detailed three-dimensional representation of the osseous structure of a human cochlea shown with SRμCT. SRμCT combined with the appropriate sample preparation allows resolving the *lamina radialis*, the radial ray-like structures pointing from the axis of the cochlea - the *modiolus*. The radio-dense structures in the petrous bone hosting the cochlea can be interpreted as nourishing vascular structures of the petrous bone.

The inset demonstrates the excellent level of detail in uncovering cellular membranes, i.e. Reissner´s membrane and other sub-structures of the Organ of Corti, viz. the tectorial membrane, supporting cells, and even Nuel´s space. These images were obtained at the photon energy of 22 keV with a spatial resolution of 2 μm; the edge length of the inset is 1.6 mm (arrow).

Three-dimensional characterization of brain tissue using synchrotron-radiation-based micro computed tomography

Marco Germann[1], Anne Morel[1], Felix Beckmann[2], and Bert Müller

Computer Vision Laboratory, ETH Zurich, Sternwartstrasse 7, 8092 Zürich, Switzerland
[1]Department of Functional Neurosurgery, University Hospital Zurich, Sternwartstrasse 6, 8091 Zürich, Switzerland
[2]Institute for Materials Research, GKSS Research Center, Max-Planck-Str. 1, 21502 Geesthacht, Germany

Performing stereotactic functional neurosurgery without penetration and physiological control requires the precise determination of the targeted lesion position solely based on magnetic resonance data. This is possible in the thalamus with desired precision even if the targeted nuclei are invisible on the acquired images using the Morel atlas [1,2]. The application of the prior knowledge to the therapy is, however, a very specific process. The current planning of the intervention, basically relying on fixed spatial relations between target areas and pre-defined anatomical landmarks can be significantly improved and generalized by taking into account the full variability of the underlying anatomical structures. One of the open issues is the establishment of anatomically meaningful correspondence between the individual structures in the training set, which is still subject of ongoing research [3,4]. Due to the very high complexity of the related model, the establishment of correspondence between stained histological slices belongs to the major challenges when trying to build the corresponding statistical shape model. Suitable algorithms allow fitting the average model to the actual patient using only structural data available from the magnetic resonance, overlaying the full set of mostly invisible, relevant nuclei.

Structure and morphology of human tissues are in general characterized on the cellular level using optical microscopy, preparing thin histological slices several 10 μm thick. The stress and strain introduced by the preparation procedure leads to deformations of the anisotropic and inhomogeneous soft matter, especially critical for mellow tissue such as brain segments. In order to get a 3D representation, the deformations have to be corrected visualizing and quantifying the anatomic features of the tissue by non-destructive methods. Synchrotron-radiation-based micro computed tomography (SRμCT) provides the necessary micrometer resolution. The density resolution, however, is expected to be problematic and maybe elaborate staining protocols have to be developed.

Human brain tissue was conserved in formalin for about 12 months. For the experiments, parts of the *pons* and the *medulla oblongata* were selected and transferred to Eppendorf tubes (volume 0.5 ml) filled with phosphate buffer. The SRμCT experiments were carried out at the beamline BW 2 by the use of the standard set-up for tomography in absorption contrast mode. The photon energy was set to 10 keV. Usually 720 projections with a size of 1536 x 1024 pixels are recorded. Using an optical magnification of 2.22, the pixel length corresponds to 4 μm. In order to improve the density resolution, the data shown in the figure were binned by a factor of 3 before reconstruction [5].

Even without any staining, several features can be uncovered in the 3D data sets. The figure shows that comparing the SRμCT data with the subsequently performed classical histology (myelin and Nissl), one can clearly identify the inferior olivary nucleus (ION), which is a conglomeration of neuronal cells (cp. cell bodies represented by violet dots in the bright field image) and which exhibits higher absorption than the surrounding tissue. The nerve fibers, best seen in the myelin and the dark field image, are hardly visible in the tomogram. The complex structures of the medulla with its fine blood vessels is not well resolved within the tomogram because of the limited spatial resolution of 5.7 μm. The holes with diameters of several 10 μm in the histological slices are attributed to the larger blood vessels. These blood vessels seem to be collapsed in the 3D configuration and presumably originate significant distortions in the histological slices. The value of the tomogram, therefore, lies especially in the possibility to non-rigidly register the different sets of histological slices. Finally, the combination of the different information on the micrometer scale offers a promising tool to improve the Morel atlas and thereby the minimally or non-invasive patient treatment.

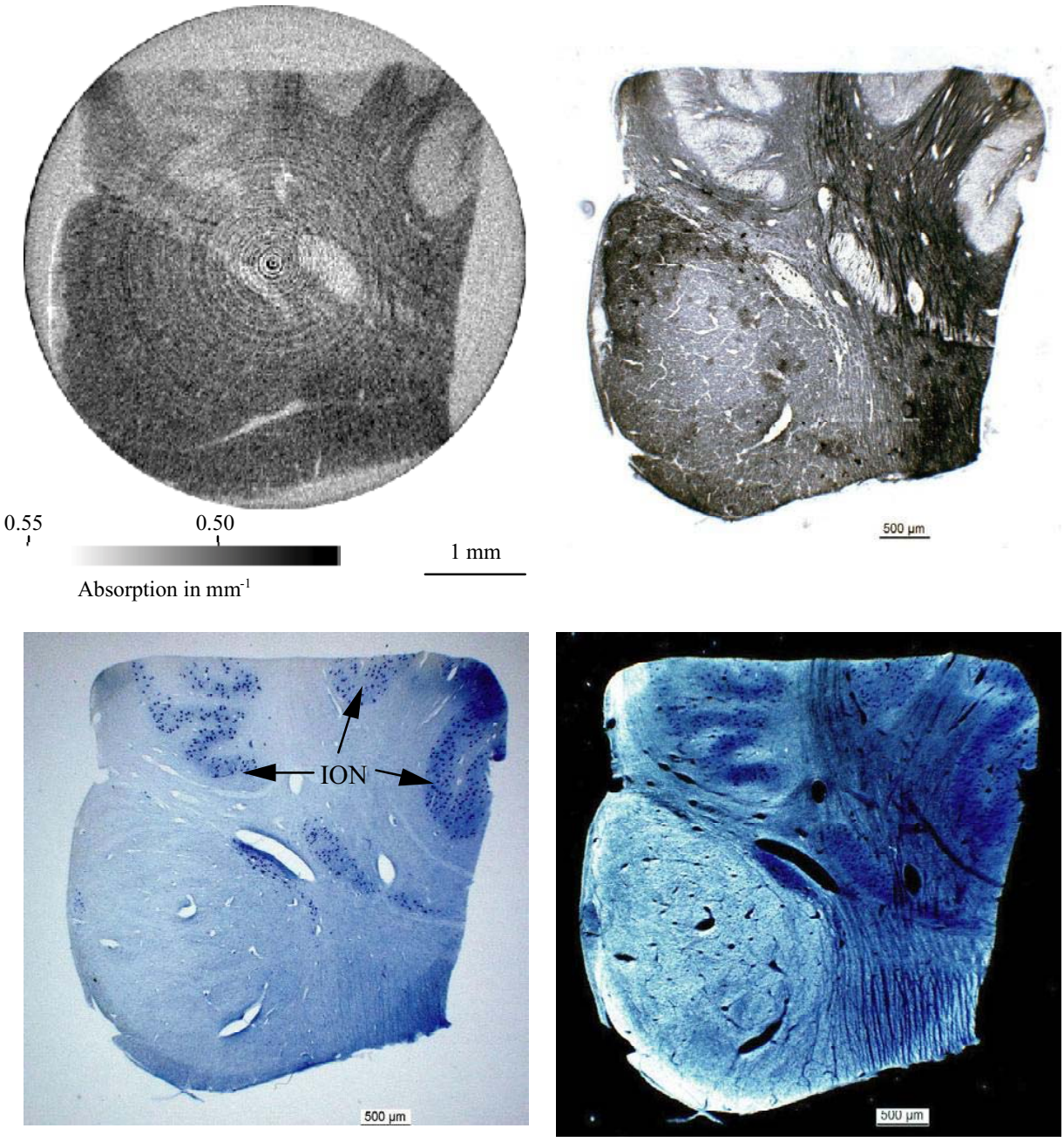


Figure: Slices of SRµCT (upper left), of myelin staining (upper right), and of Nissl staining – bright field (lower left) and dark field (lower right) show the typical anatomical features of brain tissue, here the *medulla oblongata,* including the inferior olivary nucleus (ION) with the neuronal cells, the nerve fibers, and the blood vessels.

References

[1] A. Morel, M. Magnin, D. Jeanmonod, J. Comp. Neurol. 387, 588-630 (1997)
[2] K. Niemann, V. Mennicken, D. Jeanmonod, et al., Neuroimage 12, 601-616 (2000)
[3] R.H. Davies, C.J. Twining, T.F. Cootes, et al., IEEE TMI 21, 525-537 (2002)
[4] M.A. Styner, K.T. Rajamani, L.P. Nolte, et al., Proc. IPMI'03, 63-75 (2003)
[5] P. Thurner, F. Beckmann, B. Müller, Nucl. Instrum. Meth. B 225, 599-603 (2004)

3D Bone Architecture in Osteoporosis

G.Taton, T.Rok, E. Rokita, Z. Tabor, M. Karwala-Szytula, F. Beckmann[1], T. Donath[1], J. Fischer[2]

Jagiellonian University Medical School, Department of Biophysics, Grzegorzecka 16a, Cracow, Poland
[1]GKSS-Research Center, Max-Planck-Straße 1, 21502 Geesthacht, Germany
[2]Hannover Medical School, Anna-von-Borries-Str. 1-7, 30625 Hannover, Germany

The bone mineralization process and its pathological alterations is one of the fields of interest for contemporary medicine. There are still open questions concerning the onset of its dynamics and the mechanism of being influenced by different physical or chemical factors. The aim of the project is to develop the method for precise assessment of the trabecular bone architecture allowing the investigation of the influence of different factors on the development of mineralization process. In particular, the influence of magnetotherapy on the experimental osteoporosis will be studied. The developed method will work on the basis of three-dimensional (3D) geometry and parameters describing the 3D trabecular bone architecture. The previously reported results suggest that the architectural parameters are more precise and reliable for the description of bone changes than density-related parameters [1,2].

At the current stage of the project we aimed on the choice of best bone architectural parameters allowing the estimation of subtle architecture changes. Two questions had to be answered: (1) are there parameters distinguishing between the normal and osteoporotic bones and (2) is it possible to recognize the difference between control group and bones treated with extremely low frequency magnetic field (ELFMF) [3].

The investigation is based on the rat bone model. Pregnant female rats were taken into consideration. One group was treated with ELFMF. Parameters typical for magnetotherapy in humans were utilized. The rats were also treated with their breed after the labour. The second group with their breeds were considered as a control. The young treated and control rats were killed in different age (10, 20 and 30 days). Their femoral bones were dissected and investigated. Moreover, one animal was ovarectomized in order to induce the experimental osteoporosis. The animal was killed 6 months after ovarectomy and their bones were dissected.

The bone samples were scanned with the microtomography with the use of synchrotron radiation. The beamline BW2 equipped with microtomographic scanning system was utilized. The energy of 24 or 18 keV was used depending on sample sizes. Achieved image resolution was about 10 μm for the biggest samples and about 6 μm for the smallest. Two young rat bones of the age of 20 days and 30 days as well as their control counterparts were investigated. Also the ovarectomized rat bone and its control counterpart were scanned. The proximal femoral head was taken into consideration. A set of parameters characterising the trabecular bone was calculated, e.g.: tissue volume (TV), bone volume (BV), trabecular thickness (TT), trabecular number (TN), trabecular separation (TS) and BV/TV. Also the trabecular thickness distribution (Fig. 1) and trabecular separation distribution were calculated. A reconstructed 3D image of the ovarectomized bone sample is shown in Fig. 2.

On the basis of calculated parameters it can be stated that the ELFMF treatment influences badly the bone architecture in the first stage of the mineralization process (20 d) but finally there is no big difference in measured parameters at further stages (30 d). The relative differences of chosen parameters calculated for the control and bone treated with ELFMF ((control - treated)/control) are as follows: BV/TV: -27%, TT: -10%, TN: -18%, TS: 37%. The same differences calculated for 30 d old bones are as follows: BV/TV: 3%, TT: -2%, TN: 5%, TS: 32%. The relative changes amplitude seems to be enough to investigate the influence of ELFMF on the bone architecture but the individual variability have to be investigated to draw the final conclusions.

In the case of ovarectomized animal compared to control sample TN is decreasing (-8%) while TT rises (13.5%). Surprisingly BV/TV rises (4%), but there is the same problem as in the case of

previous results. The individual variability is not known because of lack of data allowing statistical analysis.

In all cases the calculated parameters variability would be sufficient for drawing reasonable conclusions if it would be possible to compare it with the known individual variability of calculated parameters. In the present project stage additional samples should be investigated in order to allow the statistical analysis.

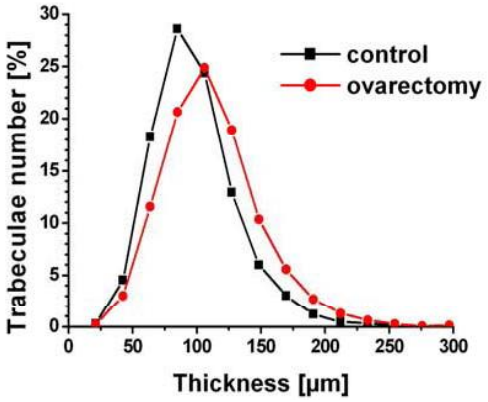


Figure 1: The distribution of trabecular thickness calculated for ovarectomized sample and control.

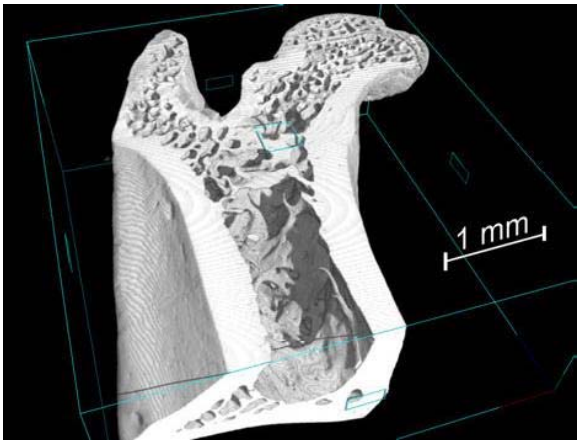


Figure 2: A sample of three-dimensional reconstruction of the ovarectomized bone sample.

References

[1] M. Stenstrom, B. Olander, D. Letho-Axtelius, J. Madsen, L, Nordsletten, G. Carlsson, J Biomech 33, 289 (2000)
[2] M. Audran, D. Chappard, E. Legrand, H. Libouban, M. Basle, Calcif Tissue Int, 69, 214 (2001)
[3] C. Sert, M. Deniz, M. Zahair Duz, F. Aksen, A. Kaya, J Bone Miner Metab, 20, 345 (2002)

Acknowledgement

This work was supported by the European Community - Research Infrastructure Action under the FP6 "Structuring the European Research Area" Programme through the Integrated Infrastructure Initiative "Integrating Activity on Synchrotron and Free Electron Laser Science" Contract RII3-CT-2004-506008.